Experimentally-informed numerical investigation of self-healing cement-based materials

Romero Rodriguez, C.

DOI
10.4233/uuid:caf37f93-e3eb-4f61-92ee-13f8f24c23a6

Publication date
2025

Document Version
Final published version

Citation (APA)
Romero Rodriguez, C. (2025). *Experimentally-informed numerical investigation of self-healing cement-based materials*. [Dissertation (TU Delft), Delft University of Technology].
https://doi.org/10.4233/uuid:caf37f93-e3eb-4f61-92ee-13f8f24c23a6

Important note
To cite this publication, please use the final published version (if applicable).
Please check the document version above.

Experimentally-informed numerical investigation of self-healing cement-based materials

Experimentally-informed numerical investigation of self-healing cement-based materials

Proefschrift

ter verkrijging van de graad van doctor
aan de Technische Universiteit Delft,
op gezag van de Rector Magnificus prof. dr. ir. T.H.J.J. van der Hagen,
voorzitter van het College voor Promoties,
in het openbaar te verdedigen
donderdag 27, Maart 2025 om 10:00 uur

door

Claudia ROMERO RODRIGUEZ

Laurea Magistrale in Ingegneria Civile,
Politecnico di Torino, Italïe,
geboren te Havana, Cuba.

Dit proefschrift is goedgekeurd door de

promotor: Prof. dr. ir. E. Schlangen
promotor: Dr. B. Šavija
promotor: Prof. dr. H.M. Jonkers

Samenstelling promotiecommissie:

Rector Magnificus,	voorzitter
Prof. dr. ir. E. Schlangen,	Technische Universiteit Delft, Promotor
Dr. B. Šavija,	Technische Universiteit Delft, Promotor
Prof. dr. H.M. Jonkers,	Technische Universiteit Delft, Promotor
Onafhankelijke leden:	
Prof. dr. ir. S.M.J.G. Erkens,	Technische Universiteit Delft
Dr. S.J. Garcia Espallargas,	Technische Universiteit Delft
Dr. ir. E. Gruyaert,	Katholieke Universiteit Leuven
Prof. dr. A. Jefferson,	Cardiff University
Prof. dr. G. Ye,	Technische Universiteit Delft, reservelid

The work in the thesis has been carried out under the auspices of the European Union's Seventh Framework Programme for research, technological development and demonstration under the ERA-NET Plus Infravation programme, grant agreement No. 31109806.0001 and the Construction Technology Research Program funded by the Ministry of Land, Infrastructure and Transport of the Korean Government under the grant 17SCIP–B103706-03.

Keywords:	self-healing concrete, self-sealing concrete, lattice fracture modelling, lattice transport modelling, 4D X-ray micro computer tomography
Printed by:	Gildeprint
Cover:	By Júlio Novaes Prado
Style:	TU Delft House Style, with modifications by Moritz Beller `https://github.com/Inventitech/phd-thesis-template`

The author set this thesis in LaTeX using the Libertinus and Inconsolata fonts.

ISBN 978-94-6496-358-8

An electronic version of this dissertation is available at `http://repository.tudelft.nl/`.

To my husband. To my family. To myself.

Contents

Summary

Self-healing concrete technology has been widely investigated in the past decade as a solution against degradation and/or loss of functionality in cracked concrete elements. Many self-healing mechanisms have been proposed and proven to work experimentally in the literature. Among these systems, the use of encapsulated mineral-producing healing agents seems to be the best working combination of components to successfully heal the cracks. The involved triggering-healing mechanisms usually consist of complex physical phenomena. Hence proper optimization of the proposed self-healing material is not possible through often resource- and time-consuming experimental campaigns. Instead, numerical modelling could be a useful tool for timely and exhaustive investigation of the self-healing mechanisms, as well as the design of appropriate experimental setups. Yet, while research on self-healing concrete seems to keep growing, comparatively the amount of modelling work devoted to the optimized design of the material has not advanced.

This thesis aims to provide a modelling framework for the study of the main aspects of a capsule-based self-healing cement-based system, namely the mechanical triggering of the self-healing system, the healing process itself and the assessment of the recovered property.

For the self-healing mechanism to work, the triggering of enough capsules along the crack is desired. Notwithstanding, this crack steering optimization comes at the expense of proper mechanical behaviour of the composite. Whereas the earlier aspect has been studied in the past, in this thesis a numerical optimization of the triggering of capsules is carried out taking into account also the achievement of acceptable mechanical performance of the material. To illustrate this, the case of self-healing cement paste with bacteria-embedded polylactic acid (PLA) capsules was selected. A 3D mesoscale lattice model was implemented herein to simulate a uniaxial tensile test on the system composed of cement paste, PLA capsule and their interface. Previous studies on the mechanical behaviour of cement paste with inclusions (i.e. capsules) have shown that the interface transition zone around the inclusion presents microstructural and mechanical properties that are totally different from those of the matrix. Therefore, a meticulous study was first conducted to obtain the mechanical properties of the interface of various types of PLA capsules with respect to bulk cement paste. Nanoindentation was performed to obtain maps of hardness and elastic modulus in the interfaces. 2D microscale lattice modelling of uniaxial tensile test on the mapped locations was performed then to obtain the overall tensile strength and stiffness of the interface. Moreover, hydrates assemblage and chemical composition around the PLA particles were studied through Backscattering Electron images and Energy Dispersive X-ray Spectroscopy. The ratios between resulting tensile strength and elastic modulus of the interface with respect to bulk paste were obtained for each PLA type which were then used as input for the mesoscale model. Cement paste samples with PLA capsules were imaged through X-ray micro Computed Tomography before and after fracture to obtain the capsules distribution to input in the mesoscale model and the fracture surface

for validation, respectively. The experimental and simulated stress-strain curves showed excellent correspondence, especially on the elastic phase, hence validating the proposed model. An exhaustive numerical investigation of the material was performed then to analyse the influence of dosage, size and shape of the PLA capsules, as well as of the interface properties on the mechanical behaviour of the composite and the triggering of the PLA capsules. The results show that interface properties close to but lower than the cement matrix do not entail substantial losses of tensile strength and elastic modulus, whereas the amount of triggered capsules is maximized. Optimum dosage, shape and size of the PLA capsules were also obtained.

To illustrate the healing process and the recovery of the functional property within the proposed modelling framework, the case of crack self-sealing in cement mortar with superabsorbent polymers (SAP) was investigated. These healing admixtures steer the crack propagation and become exposed along the fracture surface. Upon contact with ingress water they immediately absorb water and swell, thus providing a water-blocking effect and preventing harming species to further penetrate into the mortar matrix from the crack surfaces. In order to design such self-sealing systems in an efficient way, a three-dimensional mesoscale lattice model is proposed to simulate capillary absorption of water in sound and cracked cement-based materials containing SAP. The numerical results yield the moisture content distribution in cracked and sound domain, as well as the absorption and swelling of SAP embedded in the matrix and in the crack. In a first instance, the model was validated for mortar without SAP, by means of time-resolved X-ray micro Computed Tomography. Additionally, the water absorption and swelling of SAP embedded within the mortar were imaged and quantified over time to better model their role during capillary water absorption in such composite materials. The performance of the model with the presence of SAP was validated by using experimental data from the literature, as well as experimentally-informed input parameters. The validated model was then used to investigate the role of SAP properties and dosage in cementitious mixtures, on the water penetration into the material from cracks. Furthermore different crack widths were considered in the simulations. The model shows good agreement with experimental results. The obtained results show that increasing the SAP water absorption capacity, while reducing their cement solution absorption capacity improves the crack self-sealing effect more efficiently than increasing their dosage. Other guidelines for the selection of appropriate SAP are given for different crack widths. Moreover, it is suggested that capillary water absorption test in cracked concrete is sensitive enough to detect small localized changes in crack width due to the healing of the cracks.

Samenvatting

Zelfherstellende betontechnologie is in het afgelopen decennium uitgebreid onderzocht als oplossing tegen degradatie en/of verlies van functionaliteit in gescheurde betonelementen. In de literatuur zijn veel zelfherstellende mechanismen voorgesteld en experimenteel bewezen dat ze werken. Van deze systemen lijkt het gebruik van ingekapselde mineraalproducerende helende stoffen de meest effectieve combinatie van componenten om scheuren succesvol te herstellen. De betrokken activerings- en herstelmechanismen bestaan doorgaans uit complexe natuurkundige fenomenen. Daarom is een optimale afstemming van het voorgestelde zelfherstellende materiaal vaak niet mogelijk vanwege tijdrovende en kostbare experimentele campagnes. In plaats daarvan zou numerieke modellering een nuttig hulpmiddel kunnen zijn voor een tijdig en uitgebreid onderzoek naar de zelfherstellende mechanismen, evenals voor het ontwerp van geschikte experimentele opstellingen. Toch is, hoewel het onderzoek naar zelfherstellend beton blijft groeien, de hoeveelheid modellering die gewijd is aan het geoptimaliseerde ontwerp van het materiaal relatief beperkt.

Dit proefschrift heeft als doel een modelleringskader te bieden voor het bestuderen van de belangrijkste aspecten van een op capsules gebaseerd zelfherstellend cementgebonden systeem, namelijk de mechanische activering van het zelfherstellende systeem, het herstelproces zelf, en de evaluatie van het herstelde materiaal.

Voor een goed werkend zelfherstellend mechanisme is het wenselijk dat voldoende capsules langs de scheur worden geactiveerd. Deze optimalisatie van de scheursturing gaat echter ten koste van het juiste mechanische gedrag van het composiet. Terwijl dit aspect in het verleden al is bestudeerd, wordt in dit proefschrift een numerieke optimalisatie uitgevoerd van de activering van capsules, waarbij ook rekening wordt gehouden met het behalen van acceptabele mechanische prestaties van het materiaal. Ter illustratie is het geval gekozen van zelfherstellende cementpasta met polylactide (PLA) capsules, waarin bacteriën zijn ingebed. Een 3D-mesoschaal-roostermodel is geïmplementeerd om een trekproef te simuleren op een systeem bestaande uit cementpasta, PLA-capsules en hun interface. Eerdere studies naar het mechanische gedrag van cementpasta met insluitsels (zoals capsules) hebben aangetoond dat de overgangszone van het grensvlak rond de insluiting microstructurele en mechanische eigenschappen vertoont die totaal anders zijn dan die van de matrix. Daarom werd eerst een grondige studie uitgevoerd om de mechanische eigenschappen van het grensvlak van verschillende typen PLA-capsules ten opzichte van de bulkcementpasta te verkrijgen. Nanoindentatie werd uitgevoerd om kaarten van hardheid en elasticiteitsmodulus in de interfaces te verkrijgen. Vervolgens werd een 2D-microschaal-roostermodel van een trekproef op de in kaart gebrachte locaties uitgevoerd om de algehele treksterkte en stijfheid van het grensvlak te bepalen. Daarnaast werden de hydraatassemblage en de chemische samenstelling rondom de PLA-deeltjes bestudeerd met behulp van backscatter-elektronenbeelden en energy-dispersive X-ray spectroscopie. De verhoudingen tussen de resulterende treksterkte en elasticiteitsmodulus van het grensvlak ten opzichte van de bulkpasta werden verkregen voor elk type PLA en

vervolgens gebruikt als invoer voor het mesoschaalmodel. Cementpastamonsters met PLA-capsules werden voor en na de breuk in beeld gebracht met behulp van micro-CT-scans (röntgenmicrotomografie) om de verdeling van de capsules vast te leggen voor invoer in het mesoschaalmodel, en om het breukoppervlak voor validatie te verkrijgen. De experimentele en gesimuleerde spannings-rekcurves toonden een uitstekende overeenkomst, vooral in de elastische fase, waardoor het voorgestelde model werd gevalideerd. Daarna werd een uitgebreid numeriek onderzoek uitgevoerd om de invloed van de dosering, grootte en vorm van de PLA-capsules, evenals de interface-eigenschappen, op het mechanische gedrag van het composiet en de activering van de PLA-capsules te analyseren. De resultaten tonen aan dat interface-eigenschappen die dicht bij maar iets lager zijn dan die van de cementmatrix geen substantiële verliezen in treksterkte en elasticiteitsmodulus veroorzaken, terwijl het aantal geactiveerde capsules wordt gemaximaliseerd. Ook werden de optimale dosering, vorm en grootte van de PLA-capsules bepaald.

Om het genezingsproces en het herstel van de functionele eigenschap binnen het voorgestelde modelleringskader te illustreren, werd het geval van zelfafdichting van scheuren in cementmortel met superabsorberende polymeren (SAP) onderzocht. Deze helende stoffen sturen de scheurvoortplanting en komen bloot te liggen langs de scheur. Bij contact met binnendringend water absorberen ze onmiddellijk water en zwellen ze op, waardoor ze een waterblokkerend effect hebben en voorkomen dat schadelijke stoffen vanuit de scheur verder de mortelmatrix binnendringen. Om dergelijke zelfsluitende systemen op een efficiënte manier te ontwerpen, wordt een 3D mesoschaal-roostermodel voorgesteld om de capillaire absorptie van water in zowel onbeschadigd als gescheurd cementgebonden materiaal met SAP te simuleren. De numerieke resultaten tonen de verdeling van het vochtgehalte in zowel het gescheurde als het onbeschadigde domein, evenals de absorptie en zwelling van SAP die in de matrix en in de scheur is ingebed. In eerste instantie werd het model gevalideerd voor mortel zonder SAP, met behulp van tijdsopgeloste micro-CT-scans. Bovendien, werden de waterabsorptie en zwelling van het in de cementmortel ingebedde SAP in de loop van de tijd gevisualisserd en gekwantificeerd om hun rol tjdens capillaire absorptie in dergelijke composietmaterialen beter te begrijpen. De prestaties van het model met SAP werden gevalideerd met behulp van experimentele gegevens uit de literatuur, evenals met experimenteel bepaalde invoerparameters. Het gevalideerde model werd vervolgens gebruikt om de rol van SAP-eigenschappen en dosering in cementgebonden mengsels te onderzoeken op de waterpenetratie in het materiaal vanuit scheuren. Daarnaast werden verschillende scheurbreedtes in de simulaties meegenomen. Het model vertoonde goede overeenstemming met de experimentele resultaten. De verkregen resultaten laten zien dat het verhogen van de waterabsorptiecapaciteit van SAP, terwijl hun absorptiecapaciteit voor cementoplossingen wordt verminderd, het zelfafdichtingseffect van scheuren efficiënter verbetert dan het verhogen van de dosering. Verder worden richtlijnen gegeven voor de selectie van geschikte SAP voor verschillende scheurbreedtes. Bovendien wordt voorgesteld dat de capillaire waterabsorptietest in gescheurd beton gevoelig genoeg is om kleine lokale veranderingen in scheurbreedte als gevolg van het herstel van de scheuren te detecteren.

List of Figures

List of Tables

List of Abbreviations

1H NMR Proton Nuclear Magnetic Resonance.

BSE Backscattered Electrons.

CA Crystalline Admixtures.

CSA Calcium Sulfoaluminate.

DIC Digital Image Correlation.

DVS Dynamic Vapour Sorption.

E-FEM Embedded Finite Element Method.

EDS Energy-Dispersive Spectrometry.

ET Electrical Tomography.

FDD Feedback-Driven Development.

FEM Finite Element Method.

FTIR Fourier transform infrared spectrometry.

GV GrayValue.

HA healing agents.

HE Healing efficiency.

ICP Inductively coupled plasma.

LWA Light Weight Aggregate.

MRI Magnetic Resonance Imaging.

NI Neutron Imaging.

NMR Nuclear Magnetic Resonance.

PLA Polylactic acid.

PP Polypropylene.

PVA Polyvinyl alcohol.

RVE Representative Volume Element.

SAP Superabsorbent Polymer.

SCM Supplementary Cementitious Materials.

SE Secondary Electrons.

SEM Scanning Electon Microscopy.

SH Self-healing.

SHCC Strain Hardening Cementitious Composites.

TEM Transmission Electon Microscopy.

TGA Thermogravimetric Analysis.

TWS Trainable Weka Segmentation.

UHPC Ultra High Performance Concrete.

UHPFRC Ultra High Performance Fiber Reinforced Concrete.

UTT Uniaxial Tensile Test.

VOI Volume of Interest.

w/c Water-to-cement ratio.

XμCT X-ray micro Computed tomography.

XRD X-ray Difraction.

XRF X-ray Fluorescence.

I

Introduction

1

General introduction

The answers you get depend upon the questions you ask.
Thomas Kuhn

In this chapter, the background and motivation for the current dissertation are given. The objectives and the scope of the research are then layed down based on the latter. A general layout of the research methodology used throughout is also described. Finally, the dissertation outline is presented to guide the reader.

1

1.1 Background & motivation

Concrete is the most used man-made construction material [1]. Its high compressive strength and chemical stability makes it suitable for a wide range of structural applications. Nevertheless, concrete presents low tensile strength which makes it prone to crack under certain loading conditions. This is the reason why the introduction of reinforcement is necessary in structural concrete elements. Reinforcement prevents loss of bearing capacity, but small cracks will inevitably always be present. Depending on cracking extent and dimensions, cracks constitute a gateway to water and deleterious substances in solution (sulphates, chlorides, carbonate ions) into the concrete matrix, leading to either corrosion of the rebar or degradation of the matrix itself.

Much attention has been paid in the past to boost concrete mechanical properties in order to obtain better performance material-wise such as i.e. Ultra High Performance Concrete (UHPC), Ultra High Performance Fiber Reinforced Concrete (UHPFRC) [2, 3]. Technologies like concrete repair systems are an alternative to the use of expensive concrete types in massive elements, providing instead a sacrificial layer of high performance cement-based composite where the energy will be dissipated, leaving the structural part of the element undamaged or with minimum cracking [4]. In all cases, human intervention is necessary the sooner or the later while sometimes downtime might be critical for the infrastructure under repair or access to the damaged area is not even possible.

In the past decades, self-healing of concrete as a new material concept for cementitious composites has been increasingly investigated as an alternative to the above mentioned approaches to tackle degradation of concrete, thus extending its service life [5]. Concrete itself presents an autogenous ability to heal its own cracks. This phenomenon is possible due to the existence of unreacted cement pockets at the crack and surroundings and/or the diffusion of ions from the pore solution towards the crack and eventual precipitation of calcium minerals in presence of water and CO2 [6]. Experimental evidence suggests that in the best case scenarios the crack width that can be healed autogenously in cementitious materials rarely exceeds 100 μm [7].

Since larger cracks are also present throughout the service life of concrete structures, the improvement of the autogenous self-healing capability of the material has been subject of intense experimental research. Boosted autogenous self-healing has been encountered in the already existing Strain Hardening Cementitious Composites (SHCC) [8]. The use of Superabsorbent Polymer (SAP) as admixture in concrete, initially used for internal curing [9], has also been proven to be a good a self-healing booster [10–12]. Notwithstanding, since no additional healing reactants or healing agents are added on Strain Hardening Cementitious Composites (SHCC) or Superabsorbent Polymer (SAP) concrete, limiting factors of the autogenous self-healing in concrete such as the availability of calcium and carbonate ions or the need for water are not mitigated.

In order to increase the self-healing efficiency of concrete, more complex self-healing mechanisms have been devised in which healing agents (HA) are purposely incorporated as admixtures. These admixtures are designed in such a way that they can start the healing process once they are mechanically, chemically and/or physically triggered in the cracks, while at the same time remaining inactive before the self-healing needs to take place. As for the healing agents (HA) per se, there has been a plethora of proposed ones, with distinction in the literature between inorganic and organic types and their environmental implications,

as well as their compatibility with the cementitious matrix. The preliminary design and experimental study of self-healing concretes with bacteria spores [13, 14], crystalline admixtures [15], calcium bearing salts [16], etc. highlight the potential of inorganic healing products to provide efficient recovery of functionality in the material under moist exposure conditions [17].

All the above mentioned self-healing mechanisms, albeit different, have one thing in common: their working principles are the combination of multi-physical and/or chemical phenomena, as well as mechanical. Therefore, in order to optimize such materials, one has to study several parameters and under different conditions. Mechanistic and numerical modelling of the self-healing capability of these cement-based materials would certainly speed up the investigation of their performance, allowing exhaustive studies on the many involved parameters and the design of appropriate experimental setups. While extensive experimental literature can be found about self-healing mechanisms in concrete, the development of models that can be used as tools for the study of these materials is certainly outpaced with respect to the earlier as it is shown in Figure 1.1 (Data from [18]). This project aims to provide a starting point in this matter, by proposing a modelling framework for the study of some self-healing mechanisms in concrete.

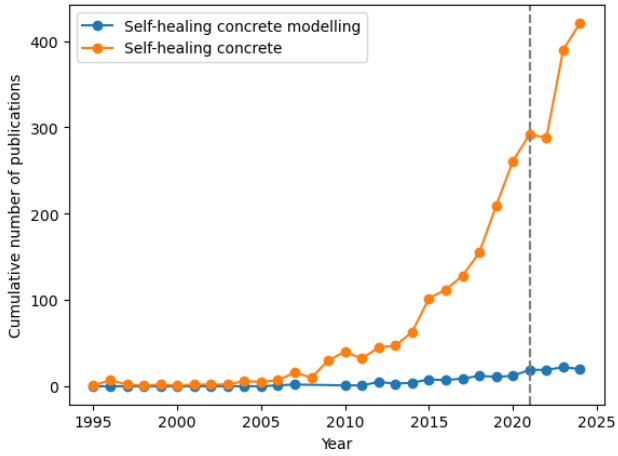

Figure 1.1: Number of total and modelling/modeling publications about self-healing/sealing concrete per year from 1995 to 2024 (data from [18, 19]). The dashed line indicates the year in which the work presented in this thesis was concluded.

1.2 Objectives and scope of the research

The objective of this dissertation is to devise a numerical modelling framework for the optimization of different self-healing mechanisms in cement-based materials. To complement the modelling framework, this thesis aims also to design robust experiments for model calibration (input) and for validation (output). The achievement of these two objectives will be performed through the execution of the following tasks relative to the different stages of a generic self-healing in concrete:

1. Triggering of a capsule-based self-healing mechanism
    - To characterize experimentally the capsule-matrix interface at the microscale.
    - To evaluate the influence of relevant design parameters of capsule-based self-healing cementitious composites on their mechanical behaviour and healing triggering through fracture mechanics modelling.
2. Physical process of crack self-sealing with SAP
    - To design relevant experiments to fundamentally understand the swelling and water absorption of SAP embedded in mortar.
    - To develop and validate a model to evaluate the influence of relevant design parameters on crack self-sealing in cement-based materials with SAP.
3. Evaluation of the healing efficiency of the mechanism
    - To propose and validate a capillary moisture transport model for the assessment of healing efficiency against water ingress in cracks.

For practical reasons, the scope of this research is limited to showcase the potential of the proposed numerical modelling framework on a few existing self-healing mechanisms. Namely, the use of capsules as healing agent carriers was investigated from its most critical aspect: crack steering and impact on the overall mechanical behaviour of the self-healing composite. Furthermore, crack self-sealing by means of Superabsorbent Polymer (SAP) was chosen to be studied in this dissertation. Nevertheless, the extension of the presented models to other self-healing mechanisms not studied is possible as discussed elsewhere in this thesis.

1.3 Research strategies

The combination of experiments and numerical modelling throughout this research allowed to satisfy the objectives mentioned in the previous section. Whereas the focus of the thesis was the development of models to study self-healing cementitious composites, the design of appropriate experiments for input and validation was as important. In addition, wherever the models could not provide explanations for certain observed phenomena, complementary experiments were performed.

To study the mechanical performance of capsule-based self-healing cementitious composites, a 3D lattice fracture model was used. The latter allowed the explicit modelling of mechanically relevant phases in the composite such as capsules, cement paste and their interface. A microstructural and micromechanical characterization of the latter was first performed through the combination of grid nanoindentation, Scanning Electon Microscopy (SEM) and 2D lattice fracture simulations. Uniaxial Tensile Test and Digital Image Correlation (DIC) were performed for validation of the 3D model. X-ray micro Computed tomography (XμCT) was used to obtain the capsules mesostructure in the sample for input and the fracture surface after uniaxial tensile test for validation.

To investigate water ingress in cracked cement-based materials, a 3D lattice transport model was developed. Input transport properties and initial conditions, such as porosity,

sorptivity and moisture content, were measured through gravimetry. In order to validate the model a 4D XμCT was developed to monitor water ingress distribution on sound and cracked mortar samples over time. The previous 3D lattice transport model was extended to model the absorbing and swelling behaviour of Superabsorbent Polymer (SAP) inside and in the cracks of cementitious materials. The virtual SAP mesostructure, characterized by irregluar particles of different sizes were generated through the particle packing model Anm [20]. XμCT was used to obtain necessary inputs relative to the swelling kinetics of SAP in the cracks.

1.4 Outline of the thesis

The outcome of the current research is given in five parts. The outline of the dissertation is shown in Figure 1.2.

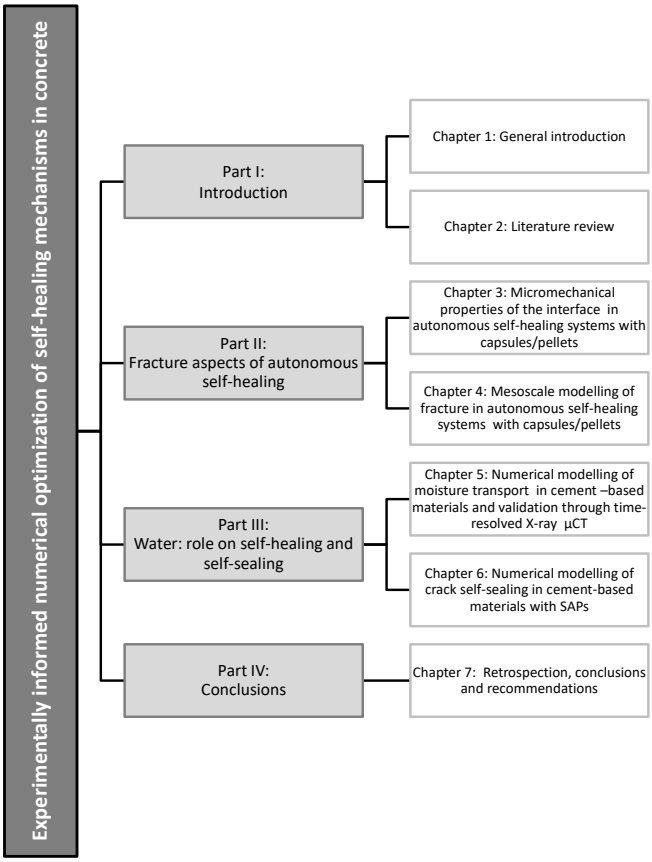

Figure 1.2: Outline of the thesis.

In the first part, the introduction of the dissertation is given. Specifically in Chapter 1, the background and motivation of the current research are explained. Furthermore, the objectives and scope of the thesis are layed down. A brief overview of the methodologies used are offered. In Chapter 2 a review of the literature regarding the main aspects of self-healing concrete is presented. Furthermore, a critical review is also performed of the existing literature on modelling of mechanically triggered healing and of healing processes.

Subsequent part two, three and four correspond to studies relative to the main stages during self-healing of cement-based materials: triggering, self-sealing and self-healing, respectively.

The second part deals with the investigation of fracture aspects of a capsule-based self-healing cementitious system, namely the mechanical behaviour of the composite and the triggering of the capsules via cracking. First a micromechanical and microstructural characterization of the interface between capsule and cement paste is performed in Chapter 3. Here, the lattice fracture model is first introduced which will be used later in the thesis as well. The obtained thickness and micromechanical properties of the interface are then used as input for the 3D mesoscale lattice modelling of uniaxial tensile behaviour in cement paste with capsules in Chapter 4. X-ray micro Computed tomography (XμCT) is introduced in this chapter, which will be used further down the thesis.

Part three is devoted to investigate the relationship between water ingress and self-healing cementitious composites. In Chapter 5 a 3D lattice transport model for the simulation of capillary water absorption in cement-based materials is presented. The model is thougth of for obtaining the cracked capillary water absorption before and after a generic healing event, thus allowing the computation of the healing efficiency related to this functionality of the material. A tailored experimental methodology, involving the use of dynamic XμCT, is used for validation and input of the previous model. In Chapter 6 the previous model is extended to investigate numerically the crack self-sealing effect provided by SAP in cement mortar.

Finally, part five includes Chapter 7, where the conclusions of this dissertation are given. Moreover, the contributions of this work are highlighted and the recommendations for future research are offered.

2

Literature review

The more extensive a man's knowledge of what has been done,
the greater will be his power of knowing what to do.
Benjamin Disraeli

In this chapter, a review of the literature regarding the main aspects of self-healing concrete is presented. Furthermore, a critical review is also performed of the existing literature on modelling of mechanically triggered healing and of the healing processes. It was identified that capsule-based mineral-producing self-healing mechanisms are the most developed, versatile and promising self-healing technology thus far. Moreover, it is advised in the literature that single-parallel-walled cracks be used for the study of self-healing efficiency in cement-based materials. Although some work has been done regarding the modelling of mechanical triggering of capsules, available optimization studies do not consider the effects of capsules on the mechanical behaviour of the self-healing composite. On the other hand, few studies are available regarding the modelling of mineral healing processes. Among the different types of models for simulating this type of healing in cracks, mechanistic modelling is the only one with predictive and descriptive capabilities. Moreover, the literature study reveals that modelling the crack carbonation in cement-based materials has not been studied thoroughly.

2.1 Introduction

The intrinsic capacity of cementitious composites to repair themselves without human intervention is defined in the literature as autogenous self-healing [21]. De Rooij et al. [7] summarized the main mechanisms behind the latter as schematized in Figure 2.1. Among these, minor contributors to the autogenous crack width reduction in cement-based materials are the deposition of fine particles, broken from the fracture surfaces or present in the water upon ingress, and the swelling of the hardened cement matrix as demonstrated in previous studies [22, 23]. The main mechanisms contributing to the crack healing are continued hydration and precipitation of calcium carbonate in the crack [24]. In the former, unhydrated cement grains available on the fracture surfaces, react with ingress water to produce cement hydrates, which occupy circa double the volume of their originating unreacted particles [25]. The latter mechanism on the other hand relies on the availability of calcium ions (Ca^{2+}), from the dissolution of Portlandite, and of carbonate ($CO_3{}^{2-}$) or bicarbonate ($HCO_3{}^{-}$) ions, from ingress carbon dioxide (CO_2) present in the atmosphere, and their reactions which are described in Equations (2.1) to (2.2) [26]. It results obvious that a different degree of healing will be obtained depending on the age at cracking, Water-to-cement ratio (w/c), crack width, exposure conditions, presence of Supplementary Cementitious Materials (SCM), type of cement, etc. [7, 24, 27–29] .

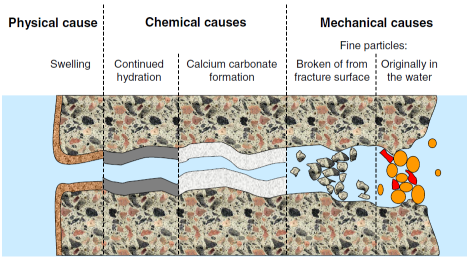

Figure 2.1: Mechanisms that may lead to autogenous self-healing in concrete [7].

$$Ca^{2+} + CO_3{}^{2-} \rightleftharpoons CaCO_3 \ (pH > 8) \tag{2.1}$$

$$Ca^{2+} + HCO_3{}^{-} \rightleftharpoons CaCO_3 + H^{+} \ (7.5 < pH < 8) \tag{2.2}$$

Inspired by the autogenous self-healing capacity of concrete and driven by the potential of increasing the efficiency of such processes and their scope, the concept of autonomous/autonomic self-healing was developed [30]. Although some contention exists regarding what is considered as an autonomous self-healing system, herein the concept defined in [7] will be used, which states that a self-healing process is autonomous when the recovery process uses material components that would otherwise not be found in the material and thus can be considered as engineered additions. In fact such smart systems can be tailored according to the different requirements for the application at hand.

In the following sections, a state-of-the-art is presented pertaining:

- Main aspects of a typical autonomous self-healing concrete.

- Modelling of the mechanical behaviour of autonomous self-healing composites.
- Modelling of autogenous and autonomous healing mechanisms.

2.2 Main aspects of autonomous self-healing concrete

Taking from [30], an ideal engineered addition for autonomous self-healing concrete should satisfy the following requirements:

1. Be compatible with concrete (i.e. its presence should not impair other functionalities).
2. Remain dormant when the concrete is uncracked.
3. Become active autonomously on repairing the damage when healing is needed.
4. Provide restoration of the previously lost property.
5. Be able to perform multiple healing events.
6. Have a long term potential activity, preferrably as long as the design service life of the concrete object.
7. Be economically feasible.

Naturally, fulfilling all the abovementioned requirements is challenging as demonstrated in previous research devoted to the development and performance of novel self-healing concrete systems. Four different aspects of such systems can be clearly defined in existing literature: 1) incorporation of the healing agent, 2) triggering of the mechanism, 3) healing process and 4) type of recovery. Usually the first three aspects and the last two are tightly interconnected among themselves. They are reviewed briefly hereafter.

2.2.1 Incorporation of healing agent

Some engineering admixtures for self-healing are added directly into the matrix. So it is the case of mineral additions such as crystalline admixtures [31–33], Calcium Sulfoaluminate (CSA) [16, 34, 35], SCM [36–38]. These admixtures do not react immediately in the matrix but their chemical activity manifests at later times. The main drawback of adding mineral additions directly is that the healing mechanism is not actuated only when damage occurs, risking the depletion of the healing agents before repair is needed at a later age of the cementitious composite. Polymeric admixtures such as SAP [39, 40] , PVA fibres [41, 42] , Polypropylene (PP) fibres [43, 44], commonly used to boost autogenous self-healing, are also added directly into the matrix. These do not impact negatively the hydration of the cement if added under a certain amount, but they may affect either positively or negatively certain mechanical properties of the material at the hardened state. The direct introduction of admixtures for self-healing of concrete presents the advantage that no extra processing is needed, thus bringing the cost down. The most common way to introduce healing agents into the cement-based composite is through micro (particles below 1 mm [45]) or macro encapsulation [46]. Encapsulation is needed when inhibition of the healing agent is

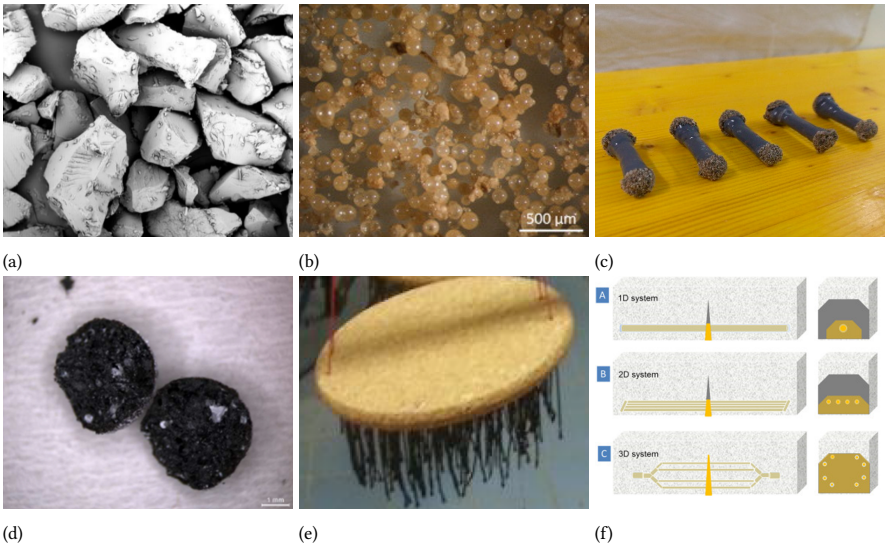

Figure 2.2: Different ways to incorporate healing agents in self-healing concrete a) directly in powder form [54], b) microencapsulated [55], c) macroencapsulated [47], d) in pellets like Lightweight Aggregates [56], e) as fibres coating [50] and f) in vascular systems [52].

necessary during mixing of concrete, as protection for the healing agents that would not survive otherwise (like bacteria spores) and/or to act as mechanical/physical triggering of the healing mechanism. Macro- encapsulation has the obvious drawback of affecting the mechanical behaviour of the overall composite [47, 48] and the survivability of the capsules is relatively low [49], while micro-encapsulation allows for more subtle disturbances of the cement-based material properties and microcapsules can survive traditional mixing processes. The main aspects of encapsulation technology, such as shape, size, capsule properties and composition, on their influence on mechanical triggering and mechanical performance of the composite will be reviewed in more detail in Section 2.3. A different way of containg the healing agent is to incorporate it as the coating of fibres [50]. Finally, more recently self-healing vascular systems are becoming increasingly popular [51], especially with the rise of additive manufacturing technology [52, 53]. The incorporation of healing agents through these networks allows the allocation of the healing agent exclusively where is needed. Furthermore, the networks can be connected to the outside for resupply of the healing agents (HA) after a healing event. Notwithstanding, the usually extensive networks need to be made of materials more brittle than the cement matrix itself (i.e. PVA), which can impact overly negatively the mechanical properties of the composite, similarly as when macro-capsules are used.

2.2.2 Triggering mechanism

Autonomous self-healing systems usually possess a triggering mechanism which can sense the existence of damage and thus set in motion the repair action. The onset of the latter can be actuated by the carrier or by the healing agent itself. Self-healing triggers can be

mechanical, physical, chemical and/or biological in nature, or a combination thereof.

Mechanically triggered self-healing concretes are the most common types when the HA are incorporated through micro or macro encapsulation [55, 57–60] in which the capsules consist of a shell with lower mechanical strength than the matrix and the healing agent is contained in the core and released upon breakage of the shell. In the case of self-healing with encapsulated bacteria presented in [61], no breakage of the capsule is needed but rather exposure of its surface, which healing agent can then be further stimulated by ingress water and oxygen. Moreover, in [62], the authors proposed a self-healing fibre reinforced concrete in which the detection of cracks through the increase of electrical resistance activates the localized heating of the healing agent.

A new generation of smart capsules has been developed in which the onset of the healing is stimulated by the penetration of harmful agents rather than by mechanical failure of the capsule. Such is the case presented in [63] where the authors developed a shell material that decomposes in presence of chloride ions. Another common stimulant of the healing onset is the use of healing additives with mutable properties upon pH changes. This trigger exploits the fact that high pH is associated with healthy concrete pore solution whereas lower pH is an indicator for carbonation or the presence of cracks with neutral to acidic ingress solutions. In this regard, different SAP with low absorption capacity in alkaline environments and high absorption capacity in neutral to acidic solutions have been developed and used for self-healing purposes [64–66]. Also capsules with pH sensitive shell/core were developed to ensure the release of the healing agent in the matrix to help repassivate the reinforcement [67] or to inhibit corrosion alltogether [68].

The use of remote self-healing triggers has been explored in [50], where induction heating was applied on bitumen-coated steel fibres inside the damaged matrix to melt the bitumen and use it as waterproofing for the crack surfaces. In a similar way [69], where the authors used ultrasonic waves to enable the breakage of the capsule without compromising the mechancial properties of the cementitious composite. Electrical current was employed in [70] on shape memory polymer tendons inside concrete to enable the crack closure of the damaged composite.

2.2.3 Healing agents and processes

Different healing agents have been proposed in the literature over the years. Among these a major distinction can be made between inorganic/mineral and organic HA. An additional requirement of organic healing agents is that their viscosity needs to be low enough to be absorbed in the crack through capillarity but high enough that it cannot be absorbed by the pores [72]. Commonly employed organic healing agents include two/three-component air-curing resins, such as epoxy [58, 73, 74] from which the main component is contained in capsules and the hardeners or hardener precursors are included in the matrix upon mixing. These epoxy resins present the disadvantage that the hardening components, added directly in the matrix, affect negatively the microstructure of the hydrated cement, often reflecting on decreased mechanical performance of control mixtures with hardener alone [74]. Another popular organic healing agents family is one/two-component polyurethane resins [47, 48, 75] which initially in liquid form, foam and solidify in presence of moisture. Cyanoacrylates have also been used for self-healing concrete encapsulated or in vascular systems [76, 77]. These adhesives cure relatively fast in presence of trace amounts of

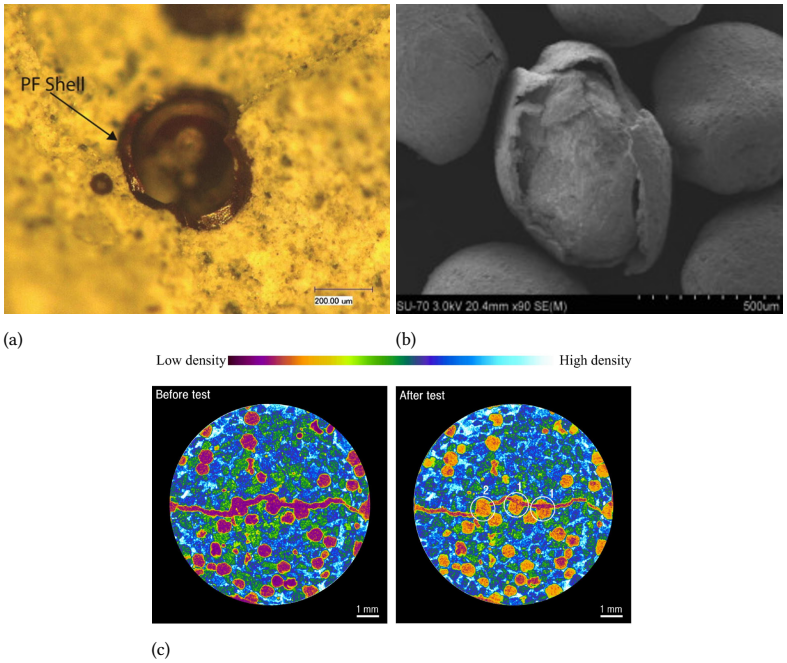

Figure 2.3: Types of triggering mechanisms for self-healing concrete a) capsules release the HA upon breakage (mechanical triggering) [59], b) pH sensitive capsules decompose rapidly when in neutral solution (chemical triggering) [67] and c) SAP absorb ingress water in the crack and swell, blocking the flow (physical triggering) [71].

moisture. Methylmethacrylate and cathalyst were separately encapsulated in [78] as healing agent. The same type of polymeric healing agent was used in [79] and injected into the crack as proof of concept for its use in self-healing concrete. A few investigations [59, 80] investigated the efficiency of self-healing concrete with encapsulated dicyclopentadiene. Specifically, the results shown in [80] pointed out at a regain in stiffness after healing. A disadvantage found generally for organic healing agents is the difficulty of preventing overflow of the initially low-viscosity healing agent into the surface of the concrete element with consequent aesthetic and functional drawbacks [81]. Furthermore, the life span of these compounds inside the concrete matrix, as well as as healing products, is limited and there is a lack of long term studies in this regard.

The alternative to the use of liquid organic healing agents in concrete self-healing is the use of mineral producing self-healing systems which are usually more compatible with the concrete matrix than their organic counterparts. Moreover, unlike the latter, the former can be used in structures subjected to moisture penetration. Due to the vast utilization of this type of healing agent and the complexity of the chemo-physical processes involved, a brief description of the main groups of mineral-producing mechanisms is given.

Boosted autogenous self-healing

Although relying on the autogenous mechanism of self-healing, in some systems admixtures are added which enhance its efficiency [82, 83]. These types of admixtures can 1) limit crack width, 2) absorbe water/calcium ions for later release and/or 3) act as nucleation sites.

There has been broad evidence of improved autogenous self-healing when fibres are added in cement-based composites. The first and more obvious mechanism for which this occurs is the ability of the fibres to limit the crack widths to some tens of micrometers and up to 150 μm. Crack width control was encountered for many types of fibres such as PVA and flax and hemp fibres in [84]. The authors found no significant difference in the crack closures after several wet and dry cycles for fine cracks of around 30 μm. In [85], cracked cementitious composites with synthetic fibres (PVA, polypropylene (PP), Polyacetal (POM) and Ethylene vinyl alcohol copolymer (EVOH)) were exposed to immersed healing conditions and their self-healing performance was studied. The results poignantly showed that PVA fibres promoted the precipitation of healing products (mainly calcium carbonate) better than the other fibres for crack widths around 300 μm, although (PP) showed improved crack closure as well. The authors explained this difference through the high polarity of PVA fibres. Similar findings were presented in [86] when comparing PVA fibres to PP and polyethylene (PE) fibres. The latest suggest that a second mechanism contributes to the improved autogenouse self-healing of concrete with syntetic fibres: the precipitation of calcium carbonate in the fibres bridging the cracks, specially so for PVA fibres. It has been also shown how these fibres not only promote crack filling but also, precipitates around the damaged fibre/matrix interface increase the frictional bond and hence the strain hardening behaviour post healing [41, 87, 88].

Admixtures like SAP, used initially for internal curing of cementitious materials [89] and to mitigate frost damage [90], have been proven to boost autogenous self-healing of concrete [11, 91, 92]. The mechanism relies on the capacity of such polymers to absorb certain acqueous solutions (i.e. mixing water, pore solution, ingressed water) which can be released in a later moment [40]. This seems to be specially advantageous when wet and dry exposure conditions are present, enabling the continuation of the healing process even when water is no longer supplied through the crack [93]. One of the driving mechanisms of absorption and swelling of SAP is osmotic pressure which enables also considerable absorption of calcium ions in the mixing water, depending on the composition of the polymer and the cross-linking level. Hence, these admixtures not only act as water sources but also as calcium sources [94], which are two species that participate in the autogenous self-healing reactions. Furthermore, the absorption of solution is accompanied by rapid and considerable swelling of the polymer. The occurence of this phenomenon in cracks has been defined as self-sealing, which provides an immediate protection to the material against water penetration and harmful species in solution [39].

The use of cellulose fibres for improving autogenous self-healing of cement-based materials was investigated by [95]. The authors attribute the modest improvement on the self-healing ratio due to the considerable water absorption of the employed cellulose fibres but further studies need to be undertaken still.

Autogenous self-healing stimulated with additional reactants

Among the limiting factors of the autogenous self-healing mechanism are the exhaustion of reactants, the slowdown of the reactions when they become diffusion controlled and the slow dissolution of atmospheric carbon dioxide. In order to overcome those, researchers have developed different self-healing systems in which additional reactants are added either directly or encapsulated. They can be divided as 1) extra reactants promoting continued hydration, 2) pozzolanic or latent hydraulic admixtures and 3) extra reactants promoting carbonation reaction.

In [96] PVA-coated pellets wtih 90 % Portland Cement and 10 % of CSA, added as 10 % of cement replacement helped seal cracks in mortar initially up to 350 μm wide after 18 days moist curing. The healing products resulted to be likely ettringite, calcium carbonate, Portlandite and gypsum.

In Huang & Ye [97], the authors studied numerically the influence of adding water capsules on the autogenous crack-filling ability of cement paste. The authors concluded that provided the use of appropriate capsules, additional water supplied can generously increase the self-healing efficiency of the studied cement paste.

According to [98] Crystalline Admixtures (CA) are hydrophilic and their active ingredients react with water and cement particles in the concrete to form calcium silicate hydrates and/or pore-blocking precipitates in the existing microcracks and capillaries. The authors suggest that the mechanism is analogous to the formation of calcium silicate hydrates and the resulting crystalline deposits become integrally bound with the hydrated cement paste. The authors further suggest that similar reactions may exist involving the calcium aluminates, but the aforementioned process is expected to prevail due to the abundance of calcium silicates. Direct evidence of improved healing of concrete through the introduction of CA has been presented in [15]. The crack healing had a more stable and reliable behaviour, specially when the samples were exposed to full or partial immersion in water. As per the composition, presence of silicium and calcium peaks were detected in the healing products when CA were added vs only calcium in the reference according to [99]. Insofar, the improved healing efficiencies in such studies remain low and their efficiency reduces with increasing age at cracking.

The influence of different Supplementary Cementitious Materials (SCM) on the autogenous self-healing of concrete has been long investigated. Some studies suggest that replacement of cement with fly ash and ground granulated blast furnace slag can extend the autogenous self-healing capacity of concrete beyond early age, due to the delayed pozzolanic activity or the latent hydraulicity of such admixtures [45]. It has been shown that large replacements of Portland cement with slag yields lower permeability of self-healed cracks when compared to replacement with fly ash [24]. Analyzing the heat production of cements with replacements of slag, fly ash and silica fume for more than 90 days in [37], the authors point out the direct correlation between heat production at late ages and thus reactivity and the increased autogenous self-healing. According to the authors at 28 and 90 days for recommended replacement levels of SCM the cumulative heat production followed the trend: Slag>Silica Fume>Fly Ash. Despite some consensus, the boost in autogenouse self-healing yielded from the replacement with SCM, the magnitude of the improvements shown in several studies depends on certain oxides contents, particle size and age at cracking, among others.

Different admixtures have been introduced with the resulting boost in calcium carbonate precipitation in the cracks. In [16, 100] the addition of CSA expansive agent boosted the precipitation of calcium carbonate. Some secondary ettringite formation and its further reaction with carbon dioxide is one of the reasons hypothesized by the authors. As another hypothesis, the formation of ettringite inside the crack would serve as nucleation sites for the precipitation of calcium carbonate. However, they listed as most likely cause the boost in portlandite dissolution. In fact, pH values were higher in mixtures containing CSA, which is related to faster dissolution rates of portlandite, which was further demonstrated from the quantification of Ca ions leached out from CSA mixtures. In contrast, in [96], when Portland cement and CSA were added in a ratio of 1:1 in pellets, the authors could identify calcium silicate hydrates, calcium aluminate hydrates, ettringite, calcium carbonate, Portlandite and gypsum among the healing products. Calcium nitrate has been suggested [101] to contribute to the formation of calcium silicate hydrate by reacting with the cementitious matrix and unhydrated cement grains when added as accelerator. But some studies devoted to the incorporation of microencapsulated calcium nitrate suggest that the majority of healing products are likely to be calcium carbonate [102, 103]. More insights into the mechanism are still needed. The introduction of the only soluble carbonate salt, sodium carbonate, for self-healing purposes was proposed in [104, 105]. The authors combined sodium carbonate-impregnated LWA with the introduction of CSA and crystalline admixtures, which proved to be beneficial for the precipitation of calcium carbonate even at significant depth from the crack mouth. In [106], the author showed that the crack closure of sodium carbonate-impregnated LWA mortar was superior to the sole self-healing capacity of a Bacillus cohnii/calcium lactate/yeast extract -based self-healing mortar during wet and dry cycles during 7 days.

Bio-mineral self-healing mechanisms

Different types of bacteria-based self-healing concretes have been proposed in the literature resulting in the precipitation of calcium carbonate to seal cracks. Although these systems differ on many aspects such as bacteria species, required nutrients, optimum environment, healing times, etc., their mechanism occurs as follows. Bacterials spores, their nutrients and mineral precursors are added to the fresh cementitious mix. When the cement-based composite cracks, water and oxygen (in the case if aerobic bacteria) penetrate through the cracks and awake the dormant spores. The latter start to germinate and grow, precipitating calcium carbonate by converting the nutrients.

Via organic carbon oxidation, certain aerobic bacteria strains are capable of simultaneously precipitating calcium carbonate and producing carbon dioxide [107]. Jonkers et al. [108] proposed the use of alkaliphilic spore-forming bacteria from the genus Bacillus (i.e. B. cohnii, B. halmapalus, B. alkalinitrilicus) as good candidate. A series of studies thereafter finetuned this self-healing system which contains bacteria spores plus a mineral precursor (i.e. magnesium acetate, organic calcium salts like calcium lactate) and organic carbon source as nutrient (yeast extract) [14, 61, 109, 110]. In the aforementioned studies the obtained crack minerals were mostly calcium carbonate-based. According to [108] in the case of calcium lactate, the bacterial metabolic conversion of the mineral precursor occurs as in the following reaction:

$$CaC_6H_{10}O_6 + 6\,O_2 \longrightarrow CaCO_3 + 5\,CO_2 + 5\,H_2O \tag{2.3}$$

As evinced from equation (2.3), although the conversion of calcium lactate results in the precipitation of calcium carbonate, a very important byproduct is the production of carbon dioxide molecules in solution, which is a limiting factor in the autogenous calcium carbonate precipitation deep in the cracks. The produced carbonate ions can then react as in equation (2.4) below:

$$5\,CO_2 + 5\,Ca(OH)_2 \longrightarrow 5\,CaCO_3 + 5\,H_2O \tag{2.4}$$

The healing efficiency of such bio-based self-healing system in combination with appropriate carriers has been investigated in different works regarding their crack filling ability. Tziviloglou et al. [111] studied the healing capacity of mortar with lightweight aggregates, impregnated with a solution of B. cohnii, calcium lactate and yeast extract. The authors subjected the 28 days old cracked specimens to 56 days of either water immersion or 12-hours wet-and-dry cycles curing, while measuring the crack permeability at different times during the healing conditioning. Cracks up to 350 μm in bacteria-containing samples were healed completely after 56 days of wet and dry cycles and 90 % after 56 days of immersed conditions. The bacteria-based mortar presented a self-healing capacity well above the autogenous one, specially in wet and dry curing conditions. A similar system was studied by [14], through crack closure light microscopy measurments. Crack locations in self-healing samples, as wide as 800 μm were successfully closed by precipitates. In [61], the authors used the same bacteria species as [111], with a different encapsulation technology (lactate derivate bio-polymer as an extra carbon source). The 28-days old cracked mortar samples were either sumerged in a water bath or exposed to 95 % relative humidity for up to 100 days while the permeability of the cracks was measured at different times during healing. Cracks up to 600 μm were completely healed when submerged, but significant healing did not happen until after 56 days when the pH of the water bath decreased from 11 to 7. In the case of samples with healing agent exposed to high relative humidity the maximum crack width that could be healed was 450 μm instead. A study performed by [110] on a similar system, showed that although self-healing efficiency in high relative humidity was as high as 90 % after 56 days of healing curing for 28-days old samples, 56-days old samples presented more unreliable healing efficiency, with a median of 35 %. Considering the difference between two different systems (one in which lactic acid derivatives are provided as precursor and one where alkanoates are used instead), the authors found a better self-healing efficiency and consistency for the latter system. Such results may suggest that at later ages, the mortars pore solution may have been acidified, thus inhibition of the metabolic activity in the case of lactic acid may have occurred. Additionally, the authors inspected the crack closure into the depth of the crakcs and observed that although a lower amount of precipitates was encountered up to 2 cm of depth for both studied self-healing systems, it was much higher with respect to reference mortars. In order to further improve the metabolic activty of bacteria spores in the crack depth, some authors have suggested the use of oxygen-releasing tablets in conjunction with this type of bacterial self-healing [112].

Several bacteria-based self-healing systems have been proposed to obtain enhanced calcium carbonate precipitation in the cracks also via bacterial enzymatic hydrolisis of urea. Alkali-tolerant aerobic ureolytic strains are known to generate the urease enzyme which acts as actalyst to decompose urea into ammonium and carbonate ions according the

equation (2.5) [45]. If calcium ions are then present in the crack solution, these dissolved carbonate ions can react with them to precipitate calcium carbonate crystals.

$$CO(NH_2)_2 + 2H_2O \longrightarrow 2NH_4^+ + CO_3^{2-} \tag{2.5}$$

In a series of studies by Wang et al. [113, 114], the authors present promising results regarding crack closure and regain of watertightness in samples with such bacteria-based self-healing system. In such studies Bacillus sphaericus is used while encapsulated in different carriers (i.e. melamine, diatomaceous earth, polyurethane etc.) in conjunction with yeast extract, urea and calcium nitrate which are directly added into the fresh cementitious mix. In [113], crack locations of the 28-days old bio-self-healing mixtures up to 970 μm are closed when immersed in water for 8 weeks and up to 600 μm when exposed to wet and dry cycles. No data regarding the depth of healing products in the crack have been published for this self-healing system. A major drawback of this system is the production of ammonia, which is toxic for the environment.

More recently, the use of denitrifying bacteria in cement-based materials has been proposed for the purpose of self-healing of cracks [115]. The advantage with respect to the two aforementioned mechanisms is that denitrifying bacteria can continue to oxidize carbon salts even in absence of oxygen by using nitrate as in equation (2.6) [45]:

$$5HCOO^- + 2NO_3^- \longrightarrow N_2 + 3HCO_3^- + 2CO_3^{2-} + H_2O \tag{2.6}$$

In [116], Diaphorobacter nitroreducens and Pseudomonas aeruginosa were used in combination with nutrients calcium formate ($Ca(HCOO)_2$) and calcium nitrate ($Ca(NO_3)_2$) in mortar specimens. The 28-days old cracked samples were submerged in water for up to 28 days and their cracks closure measured over time. The authors showed that both studied species induced complete healing of cracks initially as wide as $350-450$ μm.

A recent study has been devoted to the screening of other types of microorganisms for use as healing agent in concrete [117, 118]. In particular, filamentous fungi, such as Aspergillus nidulans, has been evaluated regarding its capacity to grow in the harsh alkaline environment found in cement-based materials. The filaments can be then calcified (be covered in calcium carbonate) through different bio-mechanisms, including increasing of carbonate alkalinity, metabolically controlling calcium ions concentration within fungal cells and binding of calcium ions with polymers contained within many cell walls. The study not only found that Aspergillus nidulans grows successfully in concrete surfaces at a considerable pace but also of precipitating massive calcite crystals on the filaments grown onto those concrete surfaces. More studies are necessary for understanding the limitations of the mechanism if any.

Other mineral self-healing mechanisms

Encapsulated sodium silicate solution and colloidal silica have been proposed as self-healing agent in several works [119–121]. Upon release the healing agent can react with Portlandite and aluminate phases to crystalline/semi-crystalline secondary calcium-silicate- and calcium-aluminate-silicate-hydrates [122]. In [121] relatively narrow cracks ($120-170$ μm) in mortar with sodium silicate-impregnated LWA were completely sealed after 28 days not only at the crack mouth but also in depth which resulted in almost pristine

flexural strength recovery of the samples. Unfortunately, the system was depleted after the first healing cycle due to the immediate release of the sodium silicate solution upon the first cracking.

Addition of expansive mineral powders for the purpose of self-healing in cementitious materials, specifically of magnesium oxide, bentonite and quicklime, has been explored in different investigations [123–125]. In [123], the authors introduced magnesium oxide as cement replacements of 2.5, 5 and 10 % by mass of cement. Cracks of 240 μm were 80 % healed after 28 days, while a combination of 5 % of bentonite and 5 % magnesium oxide completly healed cracks of similar width. As per the healing products, when employing only magnesium oxide, the authors found brucite and magnesium carbonate in the cracks. On the other hand, samples containing solely bentonite yielded healing products like ettringite and calcium aluminium silicon hydrates. In the same study, 10 % quicklime replacement yielded 90 % of crack closure in immersed conditions.

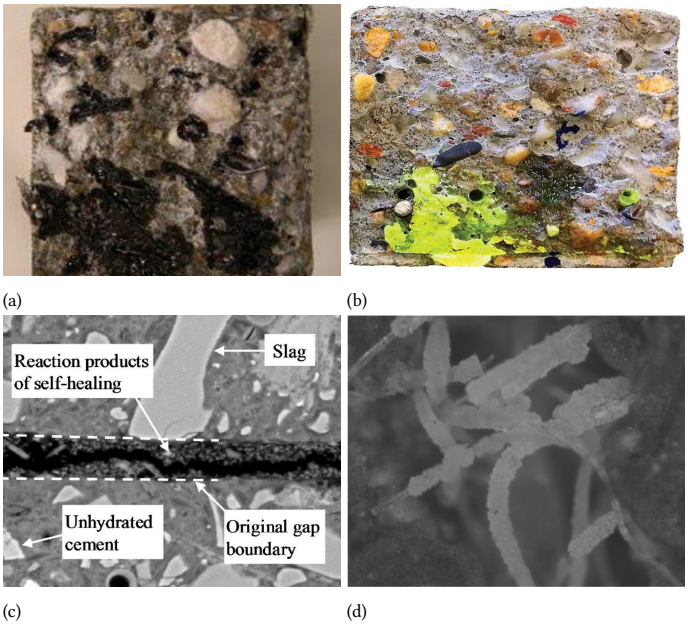

Figure 2.4: Healing products in the crack a) bitumen from steel fibre coating [50], b) epoxy resin contained in glass macrocapsules [126], c) continued hydration products in blended cement paste [27] and d) calcium carbonate in mortar with PVA fibres and SAP [11].

2.2.4 Assessment of healing efficiency

A very important aspect to correctly study self-healing concretes is the methodology for the assessment of the healing efficiency, both qualitatively and quantitatively. The choice of method depends not only on the sought-after self-healing effect, but also on the healing product properties and the availability of the experimental equipment.

Direct healing assessment tests are usually employed as proof of healing, to understand the healing mechanism or to quantify the amount of healing products. A common way to

directly evaluate the presence of healing at the crack tip or along the crack depth is the use of visualization techniques. Photo cameras, scanners or light and transmission optical microscopy, which are available at most laboratories, have been employed to monitor non-destructively the healing process of crack tips during the healing period of mineral-producing mechanisms [127–129]. Usually a certain number of marks are made along the surface of the crack path and 2D micrographs are taken of the same locations over time [126] to measure the crack widths. In these cases, the same magnification and lenses are used for every measurement and/or calibrations are performed. For a more accurate quantification of the healing products, these techniques can be used destructively upon preparation of a finite number of epoxy-impregnated (often with fluorescent dye) and polished crack cross-sections [16, 50]. Another employed visualization technique, specially for mineral-producing healing mechanisms, is Scanning Electon Microscopy (SEM), either in Backscattered Electrons (BSE) [34, 130] or Secondary Electrons (SE) [114, 131] mode, as well as Transmission Electon Microscopy (TEM) [132]. In general, for this type of microscopy the sample needs to be prepared destructively. Polished and often epoxy impreganted sections are required for performing SEM in BSE mode. The technique relies on the atomic number differences beteween mineral components in the material to provide contrast among phases, i.e between healing products in the crack and surrounding sound matrix. X-ray micro Computed tomography (XμCT) provides direct visualization in 3D of certain types of healing products in the cracks with good spatial resolution, as shown in [133–136]. Since in most experimental setups XμCT relies on the differences between attenuation coefficients of healing products and cementitious matrix to provide contrast, when it comes to quantifying healing products differential XμCT has been used. In [93, 137] mineral healing products were quantified based on the latter principle since either continued hydration products or calcium carbonate present similar gray scale values and in [138] as well because of the same lack of contrast between air (unfilled crack) and organic healing products. Recently, [139] used Nuclear Magnetic Resonance (NMR) to quantify the water absorbed and retained by SAP for later use in autogenous self-healing reactions. The use of Neutron tomography has been also investigated in [140] to visualize SAP swelling, due to the good contrast between water and cement matrix that the technique is able to provide. The authors expect to use the methodology to provide insights into crack self-sealing with SAP. Direct healing assessment can be also provided through a plethora of analytical techniques applied on the healing products such as Thermogravimetric Analysis (TGA) to quantitfy different (mineral) compounds [123, 141, 142], X-ray Difraction (XRD) for phase identification of crystalline healing products [123, 141], X-ray Fluorescence (XRF) [143] for elemental and chemical analysis of ceramic compounds, Raman spectroscopy [86] to identify molecules present in the healing products and Fourier transform infrared spectrometry (FTIR) for chemical analysis in solids, gased or liquids [123, 142]. Combination of SEM in BSE and Energy-Dispersive Spectrometry (EDS) can be used to map different chemical compounds while identifying their elemental composition [34, 123, 132, 144]. Inductively coupled plasma (ICP) has been also used for the quantification of reacting ions to estimate the amount of healing microbially produced in bacteria-based self-healing concrete [145, 146].

When direct assessment of the crack width evolution during self-healing is not possible, indirect techniques can be used to validate the existence of healed zones. Ultrasound pulse

velocity can be also used to obtain a relative crack closure in healed samples as presented in [121, 147–149]. Since ultrasonic pulses will travel faster through a sound cementitios matrix compared to when cracks are present, the technique yields intermediate velocities when going through healing products which thus reduces the travel time. Acoustic emission analysis [150–152] and Digital Image Correlation (DIC) [150, 153] have been used during post-healing mechanical tests whereby the recovery of the mechanical properties is sought. The acoustic emission source location is used to investigate the shape and extent of the fracture process zone of healed samples, which when compared to the reference test results could provide qualitative complementary evidence of the healing. Whereas from Digital Image Correlation (DIC) the derived strain field can be used to map in 2D the location of the healing products. This is possible because the healed crack presents mechanical properties substantially different from those of the original cement-based material.

Moreover, in most instances evaluating the degree of recovery of the previously lost functionality is paramount to assess the efficiency of the healing capacity of the material. Usually the healing efficiency Healing efficiency (HE) of the measured property "p" is evaluated through a formula like the generic Equation (2.7) [50, 154]:

$$HE = \frac{p_{before} - p_{after}}{p_{before}} \tag{2.7}$$

The water blocking effect of the healing products can be directly measured through permeability measurements. Different test setups have been proposed for cracked samples, the most common methods involve the use of cylindrical specimens which are cracked in splitting configuration. Usually fibres are introduced in order to prevent complete splitting of the sample [15], but also completly split cylinders can be assembled back together, glued along the lateral sides while leaving and artificial crack of desired width [155]. For the test, a water reservoir is glued above one the bases while the ingress water is measured in time. Because of the obvious difficulties of creating such samples in cement-based materials without fibres, researchers have proposed to perform permeability tests in beam samples cracked through three- or four-point bending tests. In [111, 156] a longitudinal hole is created along the span of the beam at the centre of the cross section during casting. For this setup, a hose is connected to one of the outlets of the sample hole, while the other one is sealed. For the test, the hose is connected to a water reservoir placed at a height enough to obtain the desired pressure head. A similar setup was proposed in [49] for which the cracked sample without hole is used instead. A simpler type of test to determine the sealing of cracks against water ingress are gravimetric capillary absorption tests, modified from standard sorptivity tests as presented in [126]. Both capillary absorption and permeability of cracked self-healing samples were measured through Neutron radiographs in [157–159].

More often, direct effects of self-healing on the improvement of the durability of the concrete are used as measurement of the efficiency of the healing process. The resistance against perpendicular-to-crack chloride penetration is of particular interest and methodologies like rapid chloride migration or chloride diffusion tests have been commonly used to evaluate the healing efficiency of the smart composite [160–162]. Also freeze and thaw resistancet seems to be improved when a good degree of healing is attained in cracked concrete [163] and thus can be used as a measure of the healing capacity.

For certain types of healing agents, primarily for organic types and for mechanisms promoting continuous hydration, partial or total recovery of the mechanical properties is possible. Hence, mechanical testing can be used to evaluate the degree of healing of such mechanisms. Typically, the same test employed for initial cracking is used to assess the recovery of the mechanical properties after healing has occurred, since the initial mechanical perofrmance can be used as reference.

2.2.5 Further considerations on self-healing concrete methods

In the literature the cracking of the self-healing composite before healing curing and assessment is often referred to as pre-cracking [164]. The choice of pre-cracking method depends on availability of certain mechanical testing setups, on the mechanical behaviour of the tested composite and on the desired type and quantity of cracks. The simplest pre-cracking configuration is certainly compression because of the test stability and the generally availble load control mechanical presses [144]. It can be used for plain or fibre-reinforced concrete without difficulty. Yet, such method generates multiple very narrow cracks that are commonly filled with debris and can be also healed due to the autogenous capacity of concrete of healing small cracks. All the latter makes the use of this test not entirely appropriate to understand the healing mechanism or to test the influence of crack width, and other influencing factors. Direct tensile tests are on the other hand more difficult to perform, especially in plain cement-based composites due to the need for displacement control and the influence of geometrical imperfections in the sample on the success of the test. Nevertheless, the real tensile strength of the material can be measured and parallel-walled cracks can be generated in this way [165]. Similar considerations can be made about the use of tensile splitting test, which is usually performed on cylindrical specimens. Since compression is used to split the sample, the obtained tensile strength is not entirely correct. Notwithstanding, neat parallel-walled single cracks are obtained and it is particularly appropriate when steel fibres are present [166]. Three- and Four-point bending tests are very stable tests used to generate one or multiple wedged cracks during pre-cracking of self-healing cementitious materials [166, 167]. Such type of cracks present variable width along the height of the sample and thus this pre-cracking setup is less appropriate for transport-related testing. fibre slip tests have been also used when the self-healing of the fibre/matrix interface is desired [88].

Another important aspect of self-healing mechanisms is the boundary conditions during the healing period. Factors such as temperature, relative humidity, presence of water at the boundaries, duration of the healing period and succession of wet and dry cyclic conditions play a fundamental role not only on the efficiency of the healing mechanism but more drammatically if it works or not. Among these the presence of water in any physical form is paramount for mineral producing healing systems [17, 45]. Moreover, huge differences can be observed on the healing extent depending on whether the specimens are subjected to permanent immersion in water, to wet and dry cycles or to a certain constant relative humidity as shown in[93] for SHCC with SAP.

2.3 Modelling the mechanical triggering and performance of self-healing systems with microcapsules

As elucidated above, capsules are the most advantegeous carriers for healing agents in autonomous self-healing mechanisms. In theory, the use of capsules satisfies the main requirements for healing admixtures such as: protection of the healing agent during mixing/prior to cracking and triggering of the healing process. Regarding the modification of the composite properties, special attention needs to be paid when selecting encapsulating materials that they do not affect substantially cement hydration and/or porosity. Once the latter has been verified, the fresh mix workability and the hardened composite mechanical properties can be optimized. Several studies have proposed effective solutions to counteract the decrease in workability when capsules are added in fresh cementitious mixes, the use of superplasticizer being the most effective of them all [168]. With regard to the use of capsules in self-healing cement-based materials and their influence on mechanical properties of the overall composite, there are two main competing requirements in the system: 1) breakage of the capsule is enabled upon cracking to activate the healing process and 2) introduction of a certain capsule amount does not worsen significantly the mechanical behaviour of the overall composite. Even when non mechanical healing trigger mechanisms are involved, the exposure of the capsule is usually needed for the chemical or physical mechanism to happen. Experimental optimizations require great amount of resources (high number of mix designs needed), long and time-consuming experimental campaigns. Furthermore they are limited to the studied self-healing system and consequently their results cannot be extrapolated to other types (see [169, 170]).

Few studies exist in the literature related to the numerical study of triggering of microcapsules in self-healing cementitious materials and/or of their influence on the mechanical properties of the self-healing composite. Notwithstanding the existing ones are reviewed briefly in the next sections. A distinction was made between models with implicit (i.e. Representative Volume Element (RVE) approach) or explicit modelling of heterogeneities (capsules).

2.3.1 Implicit capsule modelling

Computational homogeneization has been an attractive tool to bridge across scales the mechanical properties of heterogeneous composites such as concrete [171]. This method allows the computation of the composite mechanical response without having to refine meshes for large domains due to the small size of heterogeneities (i.e. capsules, sand grains). The computational homogeneization can be hierarchical/sequential (passing scheme input/response from micro to macro scales and viceversa) or concurrent (scales in parallel with a priori defined inelastic microscale regions) [172]. A hybrid approach was used to compute the effective elastic properties of self-healing mortar with spherical shell-core capsules (urea-formaldehyde shell and metylmethacrylate core) in [173]. The authors investigated the effect of the presence of matrix-capsule interface, the volumetric fractions of sand and capsules, and the size of the RVE on elastic modulus, shear modulus and Poisson's ratio of the cementitious composite. The choice of RVE is of paramount importance as can be seen in figure 2.5. A comparison between obtained results and Finite Element Analysis

was performed, showing differences of 8 to 30% for shear and elastic moduli and between 2 and 8% for Poisson's ratios depending on RVE size. The increase of capsules volume fractions generated decreases of all the studied properties in the composite material.

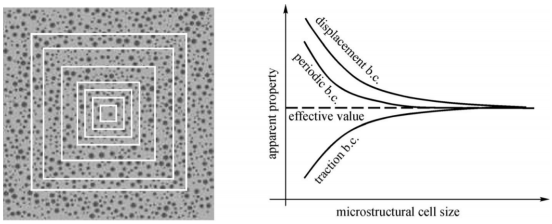

Figure 2.5: Expected trend of evaluated composite properties as a function of RVE size [174] (b.c. refers to Boundary Conditions).

2.3.2 Explicit capsule modelling

Two- and three-dimensional companion models implemented in Abaqus were used in [175] to provide insights into experimental results of delamination and debonding, respectively, between glass and concrete. The study was developed in the context of self-healing concrete with glass macrocapsules (see [49]). Extended Finite Element Method was used for the fracture zone and Cohesive Surface technique was implemented at the glass-concrete interface. The experimentally obtained bond strength and fracture energy (and confirmed numerically) were used as input for mesoscopic simulations of concrete with embedded glass macrocapsules in [176]. A three-point bending simulation of a self-healing concrete beam with two centered tubular glass macrocapsules was studied in the latter study. Again Extended Finite Element Method and Cohesive Surface as options in the commerical software Abaqus were used. Although the results were not compared to experimental ones for validations, the authors present insights into the influence of capsule-matrix interface strength, capsule number and capsule shell thickness on the load-displacement response of the beam. For this specific system the results show that thicker shells result in increased peak loads, more markedly for higher interface strength. Regarding the number of capsules, the authors found a sort of reinforcing effect when more glass capsules are added in the midspan of the beam as long as the intercapsule concrete is above a certain thickness, which otherwise increases the likelihood of concrete failure as can be observed in figure 2.6a.

In a series of studies by Mauludin et al. [177, 178] a numerical investigation was undertaken on the influence of a single circular shell-core capsule on the uniaxial tensile load carrying capacity of mortar and the breakage of the capsule. The 2D Finite Element Method (FEM) model was implemented in Abaqus with zero thickness cohesive elements interelement which allowed the input of not only the homogenized properties of mortar, shell and core of the capsule but also of their interfaces. Parameters such as shell thickness, interface capsule-mortar strength and shell-mortar mechanical property ratio were investigated. The results obtained show the great influence of the mechanical properties of the interface between mortar and capsule on the fracture patterns as well as on the composite strength. In a followup investigation Mauladin et al. [179] extended the 2D model to investigate the effect of the same shell-core capsules added in different amounts

on mortar with explicit modelling of aggregates as well. For the specific shell-core capsules studied, assumed to have weaker mechanical properties than the mortar and with bond strength, the authors found that increasing volume fractions of capsules decreased the tensile strength and increased the fracture energy of the composite. Furthermore, they found no influence of the shell thickness on the mechanical properties but rather on the success of the capsule breakage alone (see figure 2.6b). Unfortunately the results were not compared to experimental results for validation. Moreover, the influence of three-dimensional crack propagation effects was disregarded.

Lattice fracture model [180, 181] was used in [182] to investigate the mechanical triggering of tubular polymeric capsules embedded in concrete for self-healing purposes. The authors discretized a 3D homogenenous concrete cube with inside a centered single tubular capsule, distinguishing between the concrete phase and the capsule which is connected to the concrete lattice elements through so called bond beam elements. Data on the tensile behaviour of the capsule materials was used to define the constitutive law for the capsule phase, while the bond beam elements were not allowed to break. In the study, an analysis of the crack opening at the time of capsule breakage for different capsule materials of same shell thickness is performed both experimentally and through companion simulations. The study showcases the potential of lattice fracture model for preliminary screening of appropriate materials for self-healing tubular capsules.

In the same lattice fracture model framework, Huang & Ye [97] investigated the effect of dosage of spherical water shell-core capsules on the elastic modulus and tensile strength of the self-healing cementitious composite. Moreover, also a quantification of capsules encountered by the crack was obtained as to estimate the self-healing efficiency. The authors proposed then a tradeoff dosage of capsules that enables a certain level of self-healing without compromising significantly said mechanical properties of the cementitious composite.

In a more detailed work on the use of lattice fracture model to investigate self-healing composites Lv et al. [183] performed a parametric study on the mechanical triggering of shell-core spherical capsules embedded in cement paste. The authors were very careful in experimentally determining the micromechanical properties of the interlayer between capsule material and cement paste and of the former through grid nanoindentation. They used then this data as input for numerical simulations at the microscale of the interlayer to determine the elastic modulus and tensile strength of the interlayer. The distribution of capsules was imaged through XμCT and some Volume of Interest (VOI) were extracted from it and used as mesostructure for 3D mesoscale simulations as reported in Figure 2.6c. The numerically and experimentally obtained micromechanical properties of the phases: interlayer, shell and cement paste were then used as input for said 3D simulations. Although a strict validation of the obtained simulation results was not present, the authors provided a brief parametric analysis on the influence of varying interlayer strength, shell strength and capsules distribution on elastic modulus, tensile strength and capsule breakage. The authors found that stronger interlayers and/or weaker shell materials lead to a higher amount of capsules being triggered.

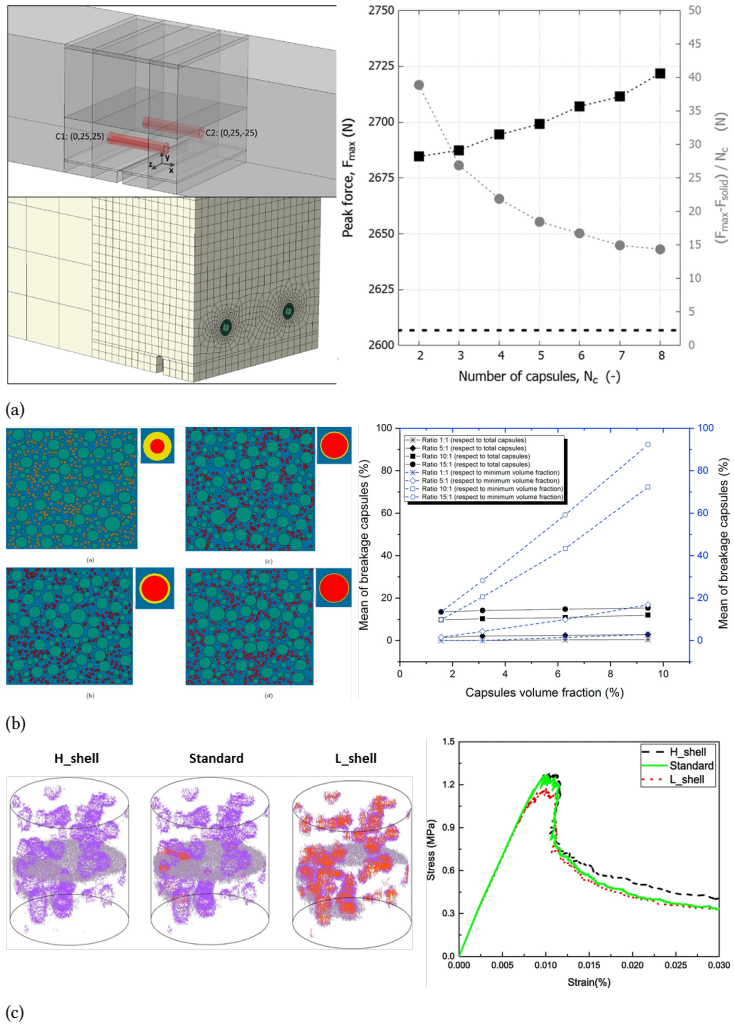

Figure 2.6: Outcomes of FEM models implemented in Abaqus: a) number of tubular capsules and obtained flexural peak force [176], b) circular capsules dosage and percentage of capsules broken for different shell thicknesses [179] and in lattice fracture model c) capsules breakage, crack pattern and load vs. displacement curve for different shell strengths [183].

2.4 Modelling healing processes in autonomous self-healing

Generally, modelling of self-healing mechanisms in cement based materials may:

- Facilitate the understanding the mechanisms in detail (through modelling different hypotheses and parameters, experimentally observed behaviours can be provided with an explanation)

- Optimize the self-healing mechanism (large number of parameters can be studied with comparatively low effort, time and material resources)
- Offer complementary information to experimental results (i.e. crack filling visualization can be related to other indirect self-healing assessment tests via modelling and viceversa)
- Help designing experiments having a priori understood the details of the mechanism.

The extent to which depends on the type of model, assumptions made, level of generalization implemented, etc.. In the following sections, advances on the modelling of self-healing processes and/or on modelling of self-healing assessment are reviewed. Distinctions between different modelling tools were made to facilitate the reader's evaluation or choice of modelling tools.

2.4.1 Stereology and analytical models

Analytical and stereological models and their combination are very useful mathematical tools that can be used to estimate the amount of healing products in the crack or certain functional properties of the self-healing material before and after healing (i.e. permeability, mechanical behaviour, etc.). They are generally user-friendly and their involved calculations are often computed manually or by means of any mathematical solver.

In [184], the authors studied self-healing of cement paste with embedded shell-core capsules containing saturated lime solution. Extending previously developed thermodynamic and transport models for continued hydration self-healing with said solution, they first obtained an analytical relationship between the amount of crack hydrates and amount of solution remaining in a 10 μm crack that has not been absorbed by the matrix at any given time. Of course such relationship needs to be calculated for every studied paste. Afterwards, the authors compute the RVE size depending on the capsule size and dosage. Then, by means of stereology and Monte Carlo simulation, the authors calculate the probability of a planar crack of hitting a given capsule. Finally the amount of solution released from hit capsules is related to the amount of crack hydrates from the first relationship. The authors obtained parametric evaluations of crack filling when varying capsule dosage and size. Despite obvious limitations on making the assumption that no crack carbonation occurs, the results showcase the potential of such model for preliminary design of a capsule based self-healing system.

The crack self-sealing effect obtained in cement-based composites with SAP has been object of investigation from a modelling standpoint in a couple of studies [185, 186]. In [185] the authors studied the equilibrium crack width reduction in a cementitious material with irregular-shape SAP through stereology. First the area fraction of SAP encountered by a planar crack was estimated depending on the particles volumetric fraction. Then, assuming that swollen SAP volumes can be calculated as dry volume plus absorbed fluid the swollen diameter was estimated. The proposed analytical formulation for the crack area reduction depends then on crack width, area fraction of SAP and relative swelling ratio of the SAP in the crack with respect to the swelling during mixing. A parametric investigation was then undertaken, providing useful guidelines to design self-sealing composites with SAP. In addition to the obvious increase of filled crack area when increasing SAP dosage

and decreasing crack width, the authors showed that it is important to limit the swelling of SAP during mixing. Nevertheless, no relation to its effect against ingress fluid in the crack and into the matrix is presented, which is not useful unless that complete blockage of the water flow is attained. Hong & Choi [186], in contrast, sought an analytical formulation to describe water flow rate reduction due to SAP swelling in the crack of mortar samples in a permeability setup. Such formulation was deduced by substracting the before- and after-sealing flow rates described by the Poiseuille law and estimating the crack volume reductions through stereology as in [185]. The flow rate reduction due to self-sealing was dependent on the crack width, depth and length, the swelling rates during mixing and in water of the SAP and on a relative crack roughness factor after sealing with respect to before. Unfortunately, the latter factor could not be physically interpreted by the authors. In fact when using relative factor equal to 1 and comparing to obtained experimental reduction of flow rates, the modeled reductions were overestimated for all the studied mortars. When fitting the relative roughness factors on the formulation to match the experiments the authors concluded that these decreased for increasing SAP volumetric fractions. Notwithstanding, the physical meaning remains a question mark and its use cannot be generalized to other SAP and crack width choices.

Tziviloglu et al. [154] presented a work on the modelling of crack filling in a bacteria-based healing system were LWA were used as carrier for the healing agents. Experimental results of crack filling visualization on a small beam sample cracked in Three-Point bending configuration were used for validation. First several mesostructure sets were digitally generated to mimick the LWA random distribution in different samples. Then an artificial wedge crack was created at the midspan and the amount if intersected carriers was determined. The sealing efficiency was calculated as volume fraction of healed crack, by calculating the volume of healing products stechiometrically as in equation (2.3) and (2.4). The authors found that the predicted sealing efficiency was overestimated. In the simplified model, the portlandite dissolution rate is not taken into account but rather the needed calcium ions are assumed to be available at all times. Furthermore, the washing out of precipitates is not accounted for in the analytical formulation. In addition, the healing agents are assumed to keep producing calcium carbonate until complete exhaustion of the nutrients, yet it has been shown in previous experiments that most likely a layer of precipitates around the carriers and on the crack walls slow down the leaching of nutrients and calcium ions, respectively, necessary for the reactions.

2.4.2 Mechanistic models

Mechanistic models use the underlying physics and biochemical principles at the root of a problem to predict or interpret the behaviour of the problem variables given the appropriate inputs. One of the advantages of this type of models is that few to no data is needed to calibrate the model. Moreover the input and outputs are physical quantities with a well defined meaning for easy interpretation of the results.

Autogenous self-healing due to continued hydration of anhydrates within cement paste is a complex mechanism involving physical and chemical processes and depending on different parameters. Just a few studies exist in the literature devoted to the modelling of such physical phenomenon. Huang & Ye [187] developed a model by coupling water transport in concrete, ion diffusion and thermodynamics to describe the further hydration of

cement particles promoted by water ingress in cracks. The author used hymostruc3d [188] to obtain the amount and distribution of unhydrated cement particles at every time step. With such data as input, the dissolution of the reactive material at the crack surfaces and embedded in the bulk matrix nearby the crack was modelled and successively, the diffusion of ions was simulated. The new concentration of ions was calculated and then the amount of reaction products precipitated in the crack is found by using thermodynamic criteria. The model was applied to a cement paste sample with a 10 μm crack in saturated and wet/drying cyclic conditions, as well as on a paste with water capsules and the healing efficiency over time was obtained for each situation. In [189] a coupled thermo-hygro-chemical model was proposed to simulate the autogenous healing of early age cement-based materials. The microstructural model STOICH HC2 [190] was used to obtain input regarding the hydration kinetics of the paste. The thermo-hygral model formulated for transport phenomena in a porous medium was complemented with a mass balance equation for the healing product. Dissolved clinker is modelled as a single solute that can be diffused and advected due to concentration and water pressure gradients, respectively. The macroscopic equilibrium equations were derived from volume averaging theorem within the hybrid mixture theory and solved spacially through Finite Element Method and in time through an implicit finite difference approximation. Results of the 2D simulations were validated using companion experiments with submerged healing conditions. The simulated healed crack area fraction was very close to that measured through experiments after 13 and 27 days, whereas after 42 days it was overestimated probably due to the contribution of calcium carbonate precipitation at that age. In [191] CEMHYD3D tool was used to simulate the distribution in the crack of hydrate phases in UHPC. An artificial crack was created in the hydrating virtual specimen and considered as porous phase saturated with water as can be seen in figure 2.7a. Different crack widths were simulated and the predicted sealing degrees over time were compared to SEM measurements from companion experiments. The authors found similar decreasing trends on the crack filling for increasing crack widths for both simulations and experiments, albeit with a slight overestimation from simulations. They attributed the overestimation to the coarse resolution of the model with respect to SEM measurements. Regarding the simulated healing products distribution, the authors found more Portlandite content in the innermost part of the crack, while CSH was found only at the crack mouths. In [192] a Lattice Boltzman single component model was proposed for simulating the continued hydration in the crack of cement paste at the mesoscale. The model makes use of a segemented microstructure obtained through light microscopy from a previous study by the authors. The dissolution rates of different phases are then computed and the transport of relevant ions are simulated in the domain using Lattice Boltzmann Method. Lastly, nucleation and growth of hydrates are calculated according to nucleation probability distribution. The model was validated using existing light microscopy experiments on 10 μm cracks (see figure 2.7b).

Regarding the autogenous self-healing due to precipitation of calcium carbonate, even fewer modelling studies have been published despite of this phenomenon being the main contributor to the healing of cracks [193]. Nevertheless, plenty of models exist to describe the main mechanisms of calcite precipitation. For instance, the leaching of calcium hydroxide in cement-based composites has been widely addressed [194], as well as carbonation in cracked concrete [195]. A model on carbonation of distributed microcracks in cement-based

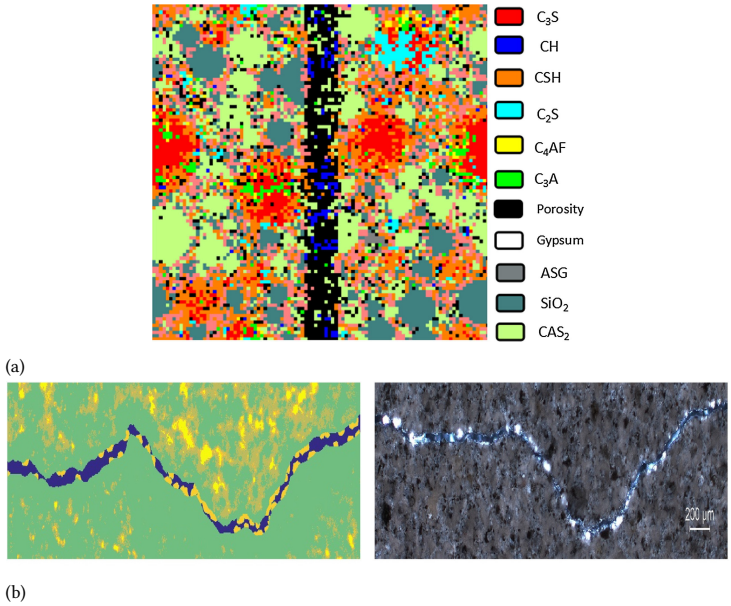

Figure 2.7: Simulated crack filling due to continued hydration a) using CEMHYD3D [191] and b) Lattice Boltzman simulations [192].

materials was presented in [196]. Calcium ions, carbonate ions and calcium carbonate are the three species considered in the model. While the calcium ions concentration is considered to be initially uniform in the saturated conditions, the carbonate ions are allowed to diffuse from the exposed surface within the pore structure according to Fick's first law. The diffusion coefficient was assumed to stay constant despite the change in porosity due to the carbonate precipitates. A first order kinetic rate is proposed for the depletion of calcium ions and the nucleation of calcium carbonate. A damage-healing approach is then used to evaluate the healing efficiency in the model. The model was implemented numerically in a FEM framework. A parametric investigation was carried out to study the kinetics and degree of healing of the simulated material while the initial damage, diffusion coefficient and reaction rate are varied. Expected trends were met by the simulations results. In [197] the development of a numerical model for the healing process induced by carbonation of a single crack in concrete was described. The authors employed Embedded Finite Element Method (E-FEM) to discretize the model equations describing transport of Ca2+ and CO2 in the crack and transport of Ca2+ in the porous bulk matrix. The use of E-FEM and consequent mismatch in mesh-physical interfaces (i.e. at the crack elements) required the introduction of a weak discontinuity in the calcium ions concentration field for finite elements where the crack is present. This enhancement allows to have the calcium ions concentration field continuous itself and a jump in the normal direction of the calcium ions concentration gradient, when passing through the crack which results in a discontinuous leakage flux that flows from the porous matrix toward the crack. This flux was used as the mass coupling term between the porous media surrounding the crack and the crack itself.

At each time step the calcite and calcium concentrations can be then calculated, as well as the calcite layer width. Since the diffusivity and conductivity tensors vary as the healing proceeds, coupling of both phenomena was considered. Electrical coupling between the transported ions was disregarded, as well as the presence of other ions.

Because crack carbonation due to bacterial activity is still not completely understood, some mechanistic models have been developed. Zemskov et al. [198] proposed a mathematical model to study the bacteria mediated calcium carbonate precipitation via organic carbon oxidation. The authors used Fick's law to model the reactive diffusive transport of the different species released by the capsule (calcium lactate, sodium glutamate, and monopotassium phosphate). By considering the boundary between limestone layer and capsule impervious, the hindering of further self-healing by deposited healing products is taken into account in the model. The bacterial density is defined over time using the Monod law of bacterial growth and consumption rates of sodium glutamate and monopotassium phosphate. Stoichiometry is then used to assess the metabolic conversion of calcium lactate. At the same time the interface between capsule and calcite layer migrates. The crack is considered to be fully saturated at all times. FEM is used for the spatial discretization of the domain with moving boundaries and the simulations were implemented in Mathematica. A typical output of the model is shown in figure 2.8. Parameters such as crack width and capsule size were varied to obtain the healing efficiency at the capsule location in the crack. In another model [199] the crack carbonation resulting from enzymatic hydrolisis of urea was studied. Diffusion of ionic species (i.e. carbonate ions, urea) was governed by Fick's first law, whereas calcium and nutrients were considered to be always available at the damaged area. One dimensional finite elements were used to discretize the domain, whereas forward finite difference was used to discretize in time. A 400 μm crack with a single capsule located at the fracture process zone was simulated. The results showed good agreement between the model and the companion SEM experiments in terms of crack mouth sealing.

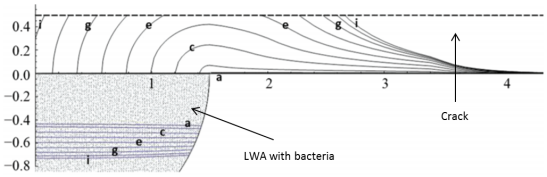

Figure 2.8: Simulated adimensional positions of the bacteria-induced carbonate layers after several time steps [198].

2.4.3 Damage-healing models

The use of damage-healing models has been widely popular in the field of cementitious self-healing materials. The reason for this may be that the output of such models is generally related to the recovery of functional properties and not only regarding crack filling efficiency. The two assessments (crack width reduction and recovery of functional property) do not always correspond, specially for properties that do not depend only on crack width, such as chloride ingress or mechanical properties.

In [200] a three-component model was proposed to simulate the mechanical regain after autogenous healing of narrow cracks ($10-30\ \mu m$) in UHPC. Firstly, the damage caused by a Three-Point bending test was simulated in a domain. Second, a hydro-chemo-mechanical model was implemented in the FEM code Cast3M to calculate the self-healing potential of a wedge crack. Third, the recovery of the mechanical properties was obtained by decreasing the local damage value due to crack filling with new hydrates. The authors emphasized the sensitivity of the second part to the input hydration rate and decided to modify it by taking out the diffusion of water from this step. In fact, they decided to divide the crack in two zones based on previous experimental works: a lower zone with C-S-H mechanical parameters and an upper zone with mechanical properties of the other hydrates. Then they varied the extents of the lower zone to understand its influence on the mechanical recovery by fitting to the experimental results. The latter analysis allowed them to conclude that the lower the location of the low zone, the stiffer the elastic branch of the healed stress-strain curve is for such small cracks. The mechanical parameters and lower crack extent were obtained through a multi-variable fitting procedure over time. Di Luzio et al. [201] proposed a more comprehensive damage-healing model for the assessment of mechanical and permeability recovery of fibre-reinforced cement based composites due to autogenous self-healing. A so-called Solidification-Microprestress-Microplane model for concrete, able to reproduce concrete time-dependent behaviour at all ages of concrete (i.e. creep, relaxation, shrinkage), was coupled with the solution of hygro-thermo-chemical problem that described the continued hydration in cracks. The model was implemented through a FEM framework. Using experimental results the model could be calibrated and validated.

In another study [202], a three-dimensional damage-healing numerical model of microcapsule - enabled self-healing cementitious material was proposed to predict the recovery of compressive behaviour of the material. The influence on the recovery of the stiffness and strength of the solidified dicyclopentadiene, as well as of the initial damage and the extent of the healing were studied. A contact constitutive model is used to represent the bond between healing product and crack surfaces. The volumetric capsule content was not explicitely modeled, but rather a homogeneization procedure was used. The model is implemented within the Discrete Element Method. Fitting of the initial and final compression simulations to experiments allowed the calibration of the undamaged and healed material properties. The authors found that the elastic regime can be extended due to self-healing, that the compressive strength increases with the strength of the healing product and the healing ratio of microcracks. Furthermore, the initial damage also influences the healed compressive strength. Although the model does not have predictive power, it allows to understand the influence of different important parameters which enable the use to make decisions on the design of this type of self-healing composite.

The self-healing of cracks in a pressurized vascular system with cyanoacrylate and its mechanical recovery were investigated in [203] by means of experiments and companion damage-healing model. The authors used the model to interpret the experimental results and to properly define the healing indices therein presented. The mean stress across the crack plane was defined as a two-component: undamaged and healed cast in terms of relative normal displacements and a scalar damage variable which are defined by damage evolution functions. A healing index referred to tensile strength and stiffness before and

after healing was used. Using then the experimental stress-strain curves for different resting times between unloading and reloading and for different crack widths the authors used the model indices to interpret the results. They found that increasing the duration of resting period increased the stiffness for all studied crack widths. Moreover, since the increase in reloading strength was modest when increasing resting periods they concluded that the healing agent did not stabilize and cure in all areas of the crack gap equally, specially for larger cracks.

A generalized damage-healing law, based on a time-dependent healing variable was enounced in [204]. The latter allows the application of the model to both coupled and uncoupled self-healing mechanisms (to the damage). A thermodynamic framework was used for the relationship between damage and strain. The time-dependent healing variables were also dependent on material properties and critical damage (i.e. for the triggering of capsules). Moreover, the authors extended classical healing theory to the generalized nonlinear and quadratic healing theories. The influence on mechanical recovery of loading history and damage, rest period between unloading and reloading and material properties (i.e. microcapsules dosage, shell thickness, healing agent strength,etc.) was investigated with the model.

2.4.4 Machine learning models

In the current era of information, generating, storing and sharing data on the field of cementitious materials becomes easier wtih each passing day, which has catalyzed the development and design of novel materials. This environment has facilitated the rise of machine learning approaches to help predict material expectations with minimal risks. In recent years, machine learning approaches have been proposed in the literature to predict the performance of cement-based self-healing materials.

In [205] a comparison is offered of the performance of different machine learning algorithms (Support Vector Regression, Decision Tree Regression, Gradient Boosting Regression, Artificial Neural Network, Bayesian Ridge Regression and Kernel Ridge Regression) to predict the crack closure percentage in non-ureolytic bacteria-based self-healing concrete. Particle Swarm Optimization is used to finetune the hyper-parameters. The algorithms were fed with several experimental datasets available in the literature for a total of 1223 specimens with different influencing variables. Only three attributes were used: number of bacteria, healing time and initial crack width. Carrier and nutrient medium are treated as affiliated parameters to the number of bacteria. A 70 % of specimens was used as training set and the rest as testing set. After the optimization of the hyperparameters for each algorithm the authors computed the mean square error and the coefficient of determination of training and testing set per algorithm. They concluded that Gradient Boosting Regression presented the best performance. Afterwards the predicted and experimental crack closure percentage were plotted for each algorithm, showing once more the better performance of the aforementioned regression. In all tested algorithms the histogram shows a tendency to overestimate the experimental values. The Gini importance of the influence of the attributes on the Gradient Boosting Regression algorithm shows that among them, the crack width is apparently the most important, while both healing time and number of bacteria are both 50 % less important. Although several limitations are present in the work (i.e. ignorance of other attributes such as curing conditions, nutrients and carrier, high scatter), it showcases

the potential of this kind of tools for studying bacteria-based self-healing concrete.

An Artificial Neural Network methodology was proposed in [206] to predict the post-healing crack width in cement-based materials with supplementary cementitious materials, bacteria, expansive minerals or crystalline admixtures. A hybrid Genetic Algorithm was used to obtain the Artifical Neural Network optimal evolution weights and biases. Afterwards, the model is trained using a feed-forward neural network along with Levenberg-Marquardt back propagation rule on predicting final healed crack width. The training set was 70 % of the database and was randomly selected, while the rest of the data points were equally divided in validating set and testing set. A total of 11 input parameters, which according to experimental studies controlled the self-healing efficiency, were used such as Portland cement dosage, water-to-cement ratio, sand, fly ash, ground granulated blast furnace slag, expansive additive calcium sulfo-aluminate, crystalline additive, lightweight aggregate and lightweight aggregate with bacteria spores contents, initial crack width and healing time. The target output was crack width reduction as a function of time. The neural network scheme is shown in figure 2.9. Predicted target output for all datasets were found to possess low error and a coefficient of determination between 0.99 and 1. An additional validation was performed with experiments carried out by the authors. The predicted values after different healing times were in excellent correspondence to the experimental results.

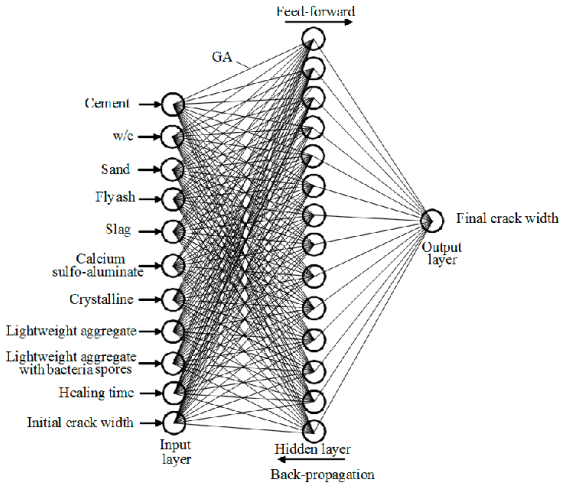

Figure 2.9: Architecture of genetic algorithm–artificial neural network model in [206].

The regain of compressive strength in cracked Ground Granulated Blast Furnace slag concrete with SAP was studied through experiments and Artifical Neural Network methodology in [207]. A multi-layer perception neural network with Levenberg-Marquardt rule of back propagation was implemented in MATLAB, with input parameters such as the dosages of slag and SAP, the age of concrete and the curing conditions. The authors concluded that the predicted compressive strength of healed samples was close to those found experimentally. It is unclear in the work how the neural network was trained and how many datasets were used for training, validation and testing.

2.5 Summary and conclusions

Based on the literature review regarding the general aspects of self-healing concrete the following conclusions can be drawn:

- Encapsulation is the most used way of introducing healing agents in cement-based materials. Such technology allows for uniform distribution of the healing agents within the composite and does not affect the fresh state workability irremediably. Different capsules can be designed for specific applications and healing agents and from various raw materials. In particular, mechanical triggering of capsules in combination with chemical triggering for the smart release of healing agents seem to offer promising results.
- Mineral self-healing mechanisms are more promising with respect to organic healing agents because of the compatibility with the cementitious paste and non-toxicity. Furthermore, in the case of bio-mineral mechanisms, the precipitation of healing products is self-sustaining and theoretically an infinite number of healing events can occur without human intervention. Most of mineral healing mechanisms aim to precipitate calcium carbonate in the cracks.
- There are many efficient experimental methodologies to assess the self-healing efficiency in concrete. Direct visualization of healing products in the crack together with analytical chemistry tools help to understand better the self-healing mechanisms. In contrast, durability tests such as chloride ingress and permeability tests help quantify the effect of crack closure on important durability issues.
- Different healing curing conditions affect self-healing efficiency differently, therefore this is an important parameter to consider when evaluating a self-healing mechanism for concrete.
- When pre-cracking samples for self-healing assessment, well-defined finite cracks are preferred. 3PB, tensile splitting and uniaxial tensile tests are commonly used to obtain realistic cracks. In particular results are easier to interpret for parallel-walled cracks.

Moreover with regards to modelling of self-healing concrete:

- Finite Element Method remains the most used tool to model numerically the mechanical behaviour of self-healing composites. Published works preliminary demonstrate the potential of FEM to optimize the mechanical triggering of healing admixtures such as capsules. Yet, published works lack validation or present incomplete analysis of relevant parameters and their combination. Moreover, available numerical optimization studies do not consider the effects of capsules on the mechanical behaviour of the self-healing composite.
- Autogenous self-healing of cement paste due to continuous hydration has been widely investigated from a modelling standpoint, albeit for narrow cracks, but the contribution of calcium carbonate precipitation has been usually disregarded. In particular, the few available studies concerning crack carbonation do not consider exposure conditions other than full saturation which is far from realistic.

- Analytical models are very user-friendly and can be used to optimize the parameters involved in simple self-healing mechanisms. However, they usually do not allow for different healing conditions or time-dependent analyses.
- Mechanistic modelling of self-healing mechanisms in concrete is useful not only for predictive purposes, but also by trying different hypotheses such models can help understanding the studied mechanisms where experiments cannot. They are computationally expensive and thus simulating cement-based materials at the macroscale may not be feasible sometimes.
- Damage-healing models are useful to evaluate the recovery of the mechanical properties after healing and to help to interpret experimental results. Nonetheless, they cannot be used for predictive purposes and have limited application on mineral-producing self-healing mechanisms.
- Machine learning models have become very attractive tools to study self-healing in concrete realized through different mechanisms. They can be particularly useful for quantifying the importance of specific parameters on the healing efficiency. On the downside, a high amount of datasets is needed to obtain statistically relevant results.

II

Fracture aspects of autonomous self-healing

3

Micromechanical properties of the interface in autonomous self-healing cement-based systems

There are very few human beings who receive the truth, complete and staggering, by instant illumination. Most of them acquire it fragment by fragment, on a small scale, by successive developments, cellularly, like a laborious mosaic.
Änais Nin

In this chapter, the interface between different types of bacteria-embedded self-healing Poly-lactic acid (PLA) capsules and cement paste is investigated. Particularly, the changes in microstructure and mechanical properties of the interface with respect to bulk cement paste were studied. First, nanoindentation was performed to obtain maps of hardness and elastic modulus in the interfaces. Lattice modelling of uniaxial tensile test on the mapped locations was performed then to obtain the overall tensile strength and stiffness of the interface. Moreover, hydrates assemblage and chemical composition around the PLA particles were studied through Backscattering Electron images and Energy Dispersive X-ray Spectroscopy. The results suggest that PLA can be tailored to optimize the physico-mechanical properties of the interface and hence, the mechanical behaviour and triggering efficiency of the self-healing system. The ratios between resulting tensile strength and elastic modulus of the interface with respect to bulk paste were obtained for each PLA type. The presented methodology can be used as input for fracture modelling of cement paste containing PLA capsules.

Parts of this chapter have been published in Cement and Concrete Research, 2020.

3.1 Introduction

Autonomous Self-healing (SH) of cracks in concrete is a smart solution to boost the durability of cement-based materials. A key feature of an autonomous system is the way that SH is triggered, which is closely linked to how the healing agents are incorporated into the composite. To this purpose, the healing agents are either specifically placed in potential crack zones of the structural element (i.e. vascular systems) [208] or randomly distributed in the cement matrix, i.e. capsules [126, 209], (coated) fibres [50], where the inclusions themselves steer the crack patterns. In the latter case, mechanical triggering should be such that the overall mechanical performance of the SH composite approaches the one of the non-SH material.

Although a huge variety of engineered SH systems for concrete have been developed in the past decades [45], there seems to be a tendency to favour encapsulation as triggering mechanism [47, 57, 60]. One such example is the introduction of bacteria spores and nutrients embedded in capsule-like particles [109, 114, 210–212]. Encapsulation of bacterial spores is needed not only as a mechanical triggering mechanism but also to protect the alkaliphilic bacterial spores during mixing of concrete, to prevent their germination prior to cracking and to contain calcium sources and activation nutrients necessary for their metabolic activity [14, 113]. Previous research on the use of bacteria-embedded poly-lactic-acid (PLA) capsules as healing agent has proven its potential to satisfy both mechanical and functional requirements of the resulting SH system [61]. The main advantage of the use of PLA as carrier for the healing agents is that its metabolic conversion by the bacteria leads to the production of CO2, which in turns results in more crack carbonation in presence of calcium cations. Since a carbon source is a mandatory inclusion in this self-healing system regardless of the carrier, the use of PLA as encapsulating matrix reduces the volume of healing particles added into concrete in order to obtain the same healing capacity [61]. Nevertheless, the biodegradable PLA partially hydrolyses in alkaline environments ultimately affecting hydration kinetics of the cement paste [213]. To what degree and extent the hydration reaction around the PLA particle is modified depends on the PLA type and should be investigated case by case. From previous studies [213, 214], it can be hypothesized that an interface zone (IZ) can be located around the PLA particle, presenting different hydration degree in comparison to the bulk paste. As a consequence modified mechanical properties of the interface zone (IZ) are expected, as well as a different mechanical behaviour of the overall SH composite.

Despite the need for the capsules to be able to steer the crack propagation and make the healing agents available at the crack location, an important requirement for SH systems is that the additives should not excessively weaken the resulting composite. In the case of PLA capsules, the thickness and mechanical properties of the IZ may have a non-negligible influence on the fracture behaviour of the self-healing system due to the microstructural changes that alterations in hydration degree may yield. Hilloulin et al. [215] verified that bond strength between PLA capsules and cement matrix is relatively low (about one third of typical tensile strengths of cement paste and one sixtieth of PLA), therefore debonding is more likely to occur than capsule fracture. These findings confirm that quantifying the interface mechanical properties is relevant to design a SH material that is tough and at the same time capable of being mechanically triggered. Furthermore, the mechanical properties of the IZ can be used as input for modelling fracture of the SH system at the mesoscale

[183]. Moreover, by changing a wide range of parameters, optimization of relevant material properties can be performed via numerical simulations [182]. The proposed approach may result in higher accuracy for optimization of SH systems than non-experimentally informed approaches [179] or stereological approaches [154, 216].

This chapter aims to provide a quantification of the tensile strength and elastic modulus of the IZ around PLA capsules, for their eventual use as input for mesoscale simulations of the SH composite. First, mapping of the elastic modulus and the hardness of the IZ around different types of bacteria-embedded PLA particles, inside cement paste, was done through grid nanoindentation. Also the bulk unaffected cement paste was tested as reference. A similar methodology was proposed in [217] to study the interface of cement-based repair systems. The nanoindentation mappings were then used as input to simulate uniaxial tensile tests through lattice fracture model. Moreover, Scanning Electron Microscopy in Backscattering Electron and Energy Dispersive X-ray Spectroscopy modes (SEM/BSE/EDS) was performed to study the hydrates assemblage distribution and chemical composition around the PLA particles. The former allowed to determine the extension of the IZ to calculate the stiffness, whereas the latter allowed to explain the possible causes of the observed variation in mechanical properties. The resulting tensile strength and elastic modulus of the IZ were compared to the values simulated for the reference cement paste and their ratios were obtained for each PLA type.

3.2 Experimental methodology

3.2.1 Materials and mixtures

Cement paste samples were produced with cement CEM I 52.5R from ENCI Netherlands, tap water and three different types of self-healing bio-polymeric particles, supplied by Basilisk (the Netherlands). All self-healing particle types were composed of a poly-lactic acid derivate matrix (PLA), embedded bacterial spores of Bacillus cohnii-related strains and growth-required nutrient inorganic salts [218]. The three types of particles differed in their production process and resulting shape, while polymer composition and dosage of nutrients and bacterial spores were the same, according to the producer. Approximate main composition of the PLA capsules can be found in Table 3.1 [218]. For the sake of nomenclature, herein reference is made to the different particles as PLA-I (irregular), PLA-II (spherical) and PLA-III (lamellar) (see Figure 3.1). Their density was measured as 1200 kg/m^3. The particle sizes were between 0.5 and 1 mm. By means of the Sauter mean diameter , measured by laser diffraction, the resulting specific surface area of particles PLA-I, -II and -III resulted $7.75x10^{-5}$, $1.11x10^{-5}$ and $15.6x10^{-5}$ cm^2/g [219], respectively. The chemical composition of the cement, obtained through X-ray Fluorescence (XRF), is reported in Table 3.2.

Four different cement pastes were designed with water-to-cement ratio (w/c) of 0.45. A mixture containing no healing particles was prepared as reference, herein referred to as CP. The other mixtures contained a certain particle type (I, II or III) with dosage of 0.6 % by weight of cement, which corresponds to 0.4 % by volume of composite. This content was chosen in order to isolate the influence of each single particle from each other on the surrounding cement paste. The investigated mixtures will be hereafter referred to as SH-I, SH-II and SH-III for pastes with capsules of PLA-I, -II and -III, respectively.

Table 3.1: General composition of bacterial PLA self-healing capsules .

Ingredient	*Weight percentage of product*
PLA	$50-80$
Bacterial spores	$0.1-2$
Nutrients	$10.5-43$
Water	$1-5$

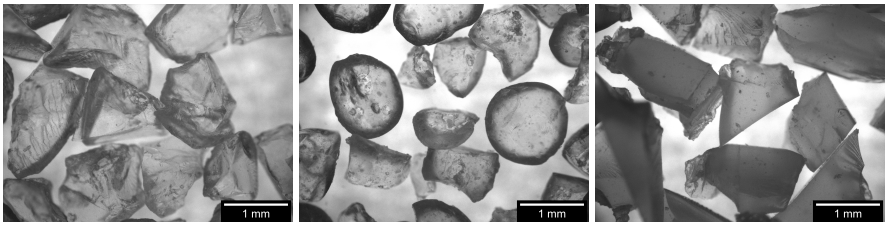

(a) PLA-I (b) PLA-II (c) PLA-III

Figure 3.1: Bacteria-embedded PLA capsules used in this work.

A Hobart planetary mixer was used to prepare the fresh pastes. All dry components (including the capsules) were mixed first for 1 minute at low speed. Water was added into the running mixer in the following 30 seconds and the components were left to mix for extra 30 seconds. Afterwards, the walls of the mixer were scraped and mixing was continued for 1 minute and 30 seconds at low speed and 30 seconds at medium speed. The pastes were poured into plastic vessels with a diameter of 35 *mm* and a height of 70 *mm*. The samples were then sealed with plastic sheet and left to harden for 24 hours at laboratory conditions. Afterwards the samples were demoulded and stored in a fog chamber with temperature and relative humidity set at $20^{\circ}C$ and 95 %, respectively until the age of 28 days.

3.2.2 Isothermal calorimetry

To determine the effect of PLA particles on the cement hydration, the heat released during the first 120 hours of hydration was monitored by means of an eight-channel isothermal calorimeter (TAM Air 3114/3236, Thermometric AB, Sollentuna, Sweden), operating at 600 mW and 20 $^{\circ}C$. For this test, a different dosage of PLA particles was selected, namely 1.3 % by weight of cement. Such choice was made in accordance with literature studied reporting on the dosage optimization for self-healing functionality [220]. The total weight of the self-healing pastes tested was of 7.565 g, whereas for the reference paste the weight was 7.25 g. Two duplicate tests were performed for each mixture.

3.2.3 Sample preparation

At the end of the curing period of 28 days, the cylindrical samples were sawn into 3-5 mm thick slices and further cut into rectangular sections with dimensions 10×10 mm^2. Selected slices, containing 1 to 3 (far apart) particles, were immersed in isopropanol for

Table 3.2: Chemical composition of CEM I 52.5R in [%] measured through XRF.

CaO	SiO_2	Al_2O_3	Fe_2O_3	K_2O	TiO_2	Other
68.7	17.4	4.1	2.8	0.6	0.3	6.1

approximately 7 days and further dried in an oven at $40^{\circ}C$ for 10 minutes. The sections were put in a desiccator for at least 24 hours. This procedure was performed to stop hydration and to dry the samples prior to preparation for the nanoindentation procedure. At the end, one section per mixture was used for subsequent measurements. The resulting sections were first ground with silicon carbide paper with a mesh grade of 1200 at 150 RPM and later polished with diamond paste (Struers) with grain sizes 9, 6, 3, 1 and 1/4 μm for 15, 15, 30 and 30 minutes, respectively, also at 150 RPM. After each respective step, the sections were put in an ethanol bath within an ultra-sonicator for 5 minutes in order to remove diamond particles and were further rinsed with ethanol prior to the next polishing step.

3.2.4 Nanoindentation

Nano Indenter (G200, KLA, USA) with a diamond Berkovich tip was used to perform grid nanoindentation on the prepared sections at 6 different locations per paste type. In the case of SH sections, for each location a grid of 5×15 indents, with a spacing of 10 μm in both directions, was performed to map hardness (H) and elastic modulus (E). The orientation of the grid was such that its short side was parallel to the boundary of the PLA particle and its origin was right at the boundary. In the case of mixture CP, the grid consisted of 5×10 indents with same spacing as the SH pastes. No preferred location or orientation was pursued for the latter. The schematics of the grid positioning within the interface are shown in Figure 3.2.

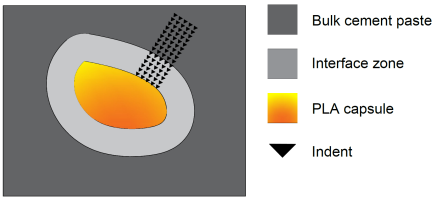

Figure 3.2: Schematics of grid nanoindentation in IZ of self-healing paste sections.

Using the continuous stiffness measurement (CSM) developed by Oliver and Pharr [221], E and H were obtained as a continuous function of the depth of penetration of the indenter. To ensure the accuracy of measurements, a standard quartz was used for the calibration of the indenter tip before each test. The surface approach velocity was 10 nm/s while the strain rate in the material was kept as 1/s. The maximum indentation depth was fixed at 1000 nm. A Poisson ratio of 0.2 was assumed for the calculation of E. The average elastic modulus and hardness were calculated in the displacement range between 500 and 650 nm to avoid the scatter of lower indentation depths where surface roughness may lead to erroneous results.

3.2.5 Scanning Electron Microscopy and Image Analysis

After nanoindentation, the same sections were coated with a thin layer of gold (10 *nm*) to ensure good surface conductivity. Scanning Electron Microscopy (SEM) in Back Scattered Electrons (BSE) mode was performed on the pastes in order to investigate the extension of the interface zones surrounding the different PLA particles. Furthermore, Energy Dispersive X-ray Spectroscopy (EDS) was performed to investigate the variation of elemental composition at the interface zones with respect to that of the bulk cement paste. An Environmental Scanning Electron Microscope (ESEM XL30, FEI, Thermo Fisher Scientific) was used at high vacuum for the acquisition of the micrographs.

For the BSE analysis, the instrument was operated with accelerating voltage of 20 kV and at a working distance of 10 mm. A magnification of 500x was employed for all SH sections, while a magnification of 550x had to be used for CP sections. The resolution of the images was 0.123 μm. Since it was of interest to investigate the interface zone, micrographs were acquired at locations where the boundary between PLA particle and surrounding cement paste was present. For statistical relevance, 30 locations were randomly chosen and two contiguous micrographs per location were acquired. The obtained 16-bit BSE images, taken at contiguous locations, were stitched through the freeware ImageJ [222]. The machine learning tool Trainable Weka Segmentation (TWS) [223] (within the same software) was used to segment anhydrous cement grains. Global thresholding was used to segment the resolved porosity.

For the EDS analysis, the accelerating voltage was set at 15 kV. The detector was a SUTW (sapphire) with a calibrated resolution of 132 eV and deadtime of around 10 %. The take-off angle was 35.3° and sample to detector distance was 10 mm. Prior to the acquisition of the spectra, the beam current was measured using a Faraday cup and a picoammeter. Per each batch type, 3 interface locations (among the ones used for BSE analysis) and 3 locations far from the particles (representative of the bulk paste) were chosen to perform point analysis. Ten points were chosen semi-randomly per analysis to exclude anhydrous cement grains and pores. The locations for the points in the interfaces were within 30 μm from the PLA particle boundary. The latter choice stemmed from the assessment of the thicknesses of the different interfaces through BSE analysis, which is reported in Section 3.4.2. After acquisition, standards based correction was performed previous to the quantification of mass and atomic percentage using the NIST DTSA-II software [224]. The mineral standards used for such corrections are shown in Table 3.3.

Table 3.3: Standards used for EDS quantification

Element	Symbol	Mineral used for correction	Chemical composition
Sodium	Na	Albite	$NaAlSi_3O_8$
Magnesium	Mg	Periclase	MgO
Aluminum	Al	Jadeite	$NaAlSi_2O_6$
Silicon	Si	Quartz	SiO_2
Phosphorus	P	Apatite	$Ca_5P_5O_{12}F$
Sulfur	S	Anhydrite	$CaSO_4$
Chlorine	Cl	Tugtupite	$Na_4AlBeSi_4O_{12}Cl$
Potassium	K	Sanidine	$KAlSi_3O_8$
Calcium	Ca	Calcite	$CaCO_3$
Iron	Fe	Haematite	Fe_2O_3
Zinc	Zn	Willemite	Zn_2SiO_4
Oxygen	O	Oxygen determined by stoichiometry	

3.3 Lattice fracture modelling

Grid nanoindentation mapping, as performed in this study, cannot lead to conclusions regarding the overall mechanical performance of the material. Hydrated cement paste is highly heterogeneous. Within each defined phase, micromechanical properties vary depending on many factors (i.e. w/c ratio, curing temperature, cement composition, etc. [225]). An approach to understand the composite mechanical behaviour is to use the output of appropriately designed grid nanoindentation, at several locations, as input for numerical fracture models [226, 227]. The chosen model should allow for imposition of local mechanical properties (measured through grid nanoindentation) in order to account for the heterogenity of the cement paste. An increasingly popular choice to simulate fracture of heterogeneous brittle materias are lattice models [228, 229]. This type of model consists in an assembly of discrete two-nodes elements (lattice beams) that represents a continuum. For the discretization of the domain, the nodes are placed pseudo-randomly inside each cubic cell of a quadrangular grid. The ratio between the specified sub-cell and the cubic cell dimensions determines the randomness of the set of nodes. Subsequently, a Voronoi tessellation is performed with respect to the previously placed nodes in the domain. Nodes belonging to adjacent Voronoi cells are joined by lattice beams. A schematic representation of the above mentioned procedure is reported in Figure 3.3a. Commonly, the elements are assigned a linear-elastic constitutive law, characterized by inputs such as elastic and shear moduli, tensile and compressive strengths [230]. It is also possible to assign non-linear constitutive laws [231].

In this work, the earlier simplification is used as the sought after properties of the interface are the elastic modulus and the tensile strength. The linear-elastic properties of each element were assigned the corresponding values obtained from grid nanoindentation. In a previous study [217] the authors suggested a mesh size below 1.75 micron for cement microstructure scale simulations. Herein a cell size of 1 micron is used with a randomness of 0.2 for the positioning of the nodes. For assigning the elemental properties, first a linear

interpolation of the grid nanoindentation elastic moduli and hardness values is peformed between the new grid nodes. Afterwards, for each lattice element with nodes i and j, the elastic modulus (E_{ij}) was calculated as if the element was composed of two springs in series with moduli E_i and E_j, respectively [232]:

$$\frac{1}{E_{ij}} = \frac{1}{E_i} + \frac{1}{E_j} \tag{3.1}$$

Consequently, the shear modulus of the element (G_{ij}) was obtained through Equation 3.2. A Poisson ratio (ν) of 0.2 was used.

$$G_{ij} = \frac{E_{ij}}{2(1+\nu)} \tag{3.2}$$

The ratio between measured hardness and tensile strength ($f_{t,ij}$) used was taken as 12, as suggested in [233] and further confirmed in [234]. The elemental tensile strength was then calculated as suggested in [232]:

$$f_{t,ij} = min(f_{t,i}; f_{t,j}) \tag{3.3}$$

The compressive strength ($f_{c,ij}$) to tensile strength ratio was taken as 10 which has been experimentally confirmed for such length scales in [235].

After discretization and assignment of input properties, lattice fracture model was used to simulate uniaxial tensile test on the 2D meshes. The tensile test was simulated on the PLA-pastes by fixing all degrees of freedom on the origin of the IZ (at the boundary with the PLA particle) and by imposing a unitary displacement on the opposite side. Same boundary conditions were used for the simulations on the bulk cement paste but the choice of the side for nul degrees of freedom was done arbitrarily. Typical uniaxial tensile configurations for PLA-pastes and bulk CP meshes are shown in Figure 3.3b.

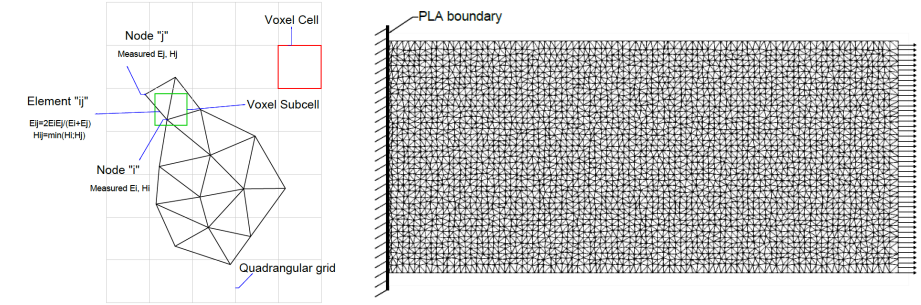

Figure 3.3: Lattice model discretization procedure a) and simulated loading condition in uniaxial tensile mode b).

3.4 Results

3.4.1 Kinetics of hydration of cement paste with PLA particles

In a work by [213], it was observed that similar PLA capsules, as in this study, interferred in the hydration of cement paste. According to a study of [236], organic PLA undergoes alkaline degradation into molecules containing α-hydroxy carboxyl group which can be very absorbing and therefore retarding. Notwithstanding, contradictory discussions can be found in the literature regarding the effects of PLA on hydration kinetics [237]. Some studies report acceleration and other, retardation. Therefore it is relevant to understand how and to what extent the studied PLA particles modify the hydration kinetics of the surrounding paste when compared to a reference containing no PLA capsules (Figure 3.4). The reported curves correspond to one of the test duplicates for each mixture as no relevant differences were found among replicates.

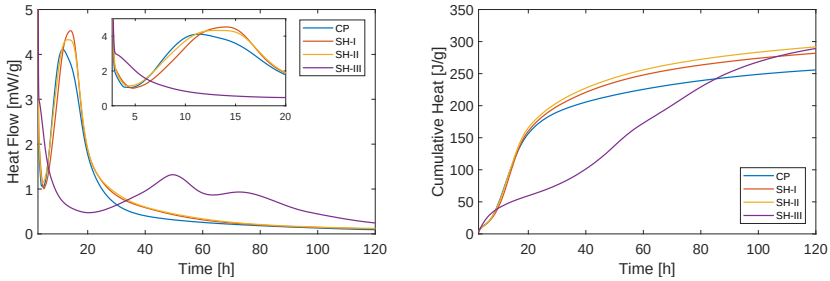

(a) (b)

Figure 3.4: Heat flow a) and cumulative heat b) of the studied hydrating cement pastes CP, SH-I, SH-II and SH-III from first 3 to 120 hours of hydration.

As can be observed in Figure 3.4a, the induction period is slightly prolonged for SH-I and SH-II of about 60 and 20 minutes, respectively. In the case of SH-III, the induction period occurs 17 hours later than the reference paste and releases considerably more energy. Since induction period seems to be associated most likely to ionic concentration in the solution [238], this may suggest that dissolution of PLA/nutrients is causing the retardation. As for the differences between the PLA capsule types, shape seems to be the only differring factor with resulting surface areas as follows PLA-II<PLA-I<PLA-III. Furthermore, production processes may have affected the solubility of the bio-polymer.

Acceleration of hydration occurs at a similar rate as the reference for SH-I and SH-II, yet the maximum of the heat flow is higher for II and I, respectively. Furthermore SH-II presents a flatter peak than SH-I and the reference. The acceleration rate of SH-III is quite lower than CP and the peak is delayed 35 hours with respect to the reference, denoting very slow nucleation of hydrates on the cement grain surfaces. Moreover the peak heat flow is 4 times lower than the reference. A possible explanation for the behaviour of SH-III is still the low dissolution rate of cement grains, which cannot compensate timely for the nucleation and growth of hydrates.

At the onset of the respective deceleration periods the cumulative heat of hydration

for the studied pastes had the following trend: SH-III<CP<SH-I<SH-II. After the primary acceleration peak, SH-III presented a secondary peak (or broad shoulder) in the heat flow curve. Further studies should be carried out to understand what the cause of this anomaly is.

To summarize, while PLA-I and PLA-II provoke moderate changes in the cement hydration kinetics, PLA-III seems to dramatically affect cement hydration in the first 120 hours.

3.4.2 Chemical and physical properties of the interface zone

Degree of hydration and porosity

In Figure 3.5, an example of the SEM/BSE gray-valued (GV) micrograph of the interface zone of SH-III is reported, as well as the resulting segmentation of the anhydrous and hydrates phases through Trainable Weka Segmentation (TWS) in b) and the segmentation of pores through thresholding in c). By defining the position 0 of the IZ as the particle-paste boundary, a MATLAB code was developed and used to shift all pixel rows to start at such position 0, making possible the calculation of the degrees of hydration and porosity at different distances from position 0.

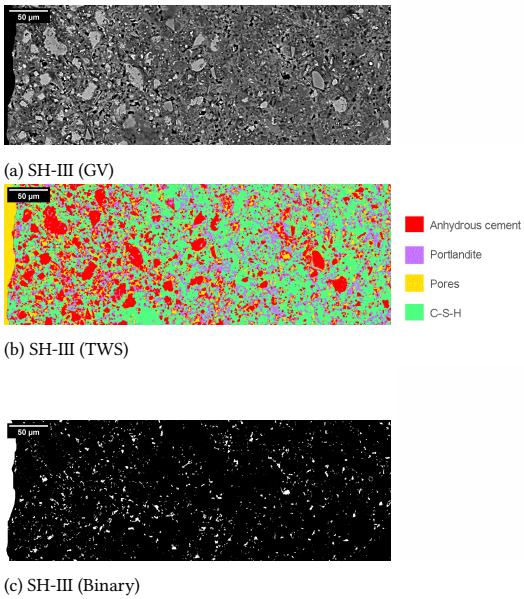

(a) SH-III (GV)

(b) SH-III (TWS)

(c) SH-III (Binary)

Figure 3.5: BSE image of the interface zone of SH-III (PLA particle at the left) in Gray-Value a), after Trainable Weka Segmentation b) and after pore thresholding c).

The degree of hydration (α) was estimated according to Powers & Brownyard [25] assumption that the volumetric fraction of hydration products (F_{hp}) is 2.1 times that of their originating unhydrated grains (F_{up}) through:

$$\alpha = \frac{F_{hp}/2.1}{F_{hp}/2.1 + F_{up}} \tag{3.4}$$

The linear-traverse and point counting methodology [239] was employed to assess the volumetric ratios of F_{hp} and F_{up}. Linear-traverses were chosen in correspondence of every pixel column of the segmented images. Hydration products and anhydrous grains pixels alike were counted and the degree of hydration and porosity were computed per linear-traverse.

The graphs shown in Figure 3.6 report the degrees of hydration and porosity profiles along the direction perpendicular to the PLA boundary in SH-I, -II and -III, in order to define the extent of their respective interface zones. The error bars represent the standard deviation among the different micrographs for each relative position. The limit values for the bulk zone, obtained from CP micrographs, are reported in each graph in relation to degree of hydration or porosity. In this regard, it is worth mentioning that, due to the different magnification used to image CP bulk zones (550x), values cannot be rigorously compared. A higher resolution image will yield better defined boundaries of the phases and more accurate quantification of their area, whereas the opposite applies to lower magnifications. This applies specially to small phases (like pores) where the surface to volume ratio is higher.

From the profiles of porosity no clear trend could be found. This is somewhat logical since all the porosity cannot be resolved at these magnifications. The profiles of degree of hydration were chosen for the selection of the interface zones length instead. The degree of hydration was observed to be the lowest at the position 0 for all interface zones, namely 0.68, 0.70 and 0.42 for IZ-I, -II and -III, respectively. The IZ limit was chosen as the point where a plateau is reached in the degree of hydration profile. Thus, the IZ thicknesses were estimated as 110 μm, 130 μm and 260 μm for IZ-I, -II and -III, respectively. These thicknesses are quite larger than typical mechanical interfaces forming around inert additions such as regular aggregates [240] and even those in overlay systems and around recycled aggregates [217, 241]. The values of the degree of hydration beyond the IZ were similar to those in bulk CP ($\alpha_{ave} = 0.82$) for SH-I and -II, whereas for SH-III there seems to be a more widespread modification of the paste with values of α beyond the IZ of around 0.60.

Elemental analysis

In the bar graph reported in Figure 3.7a, the average elemental atomic concentrations, normalized to the calcium concentration, are shown for each studied interface and their respective bulk pastes.

The most striking feature observed in Figure 3.7a is the highly heterogeneous nature of SH-III CSH composition. Furthermore, negligible differences were spotted between interface zone and bulk paste of SH-III. The latter confirms the hypothesis formulated in the previous section regarding the more widespread interference in hydration of PLA-III. Traces of phosphorus were detected in both interface and bulk paste of SH-III, whereas none were detected for SH-I or SH-II. The presence of phosphates in portland cement has been proven to retard hydration and to cause long-term decrements of compressive strength [242, 243] which could explain the retardation of early reaction in SH-III and long term lack in hydration degree. Sulphur was also found in relatively high concentrations for

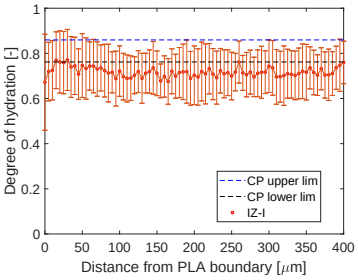

(a) IZ-I (α)

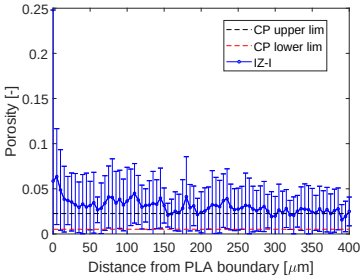

(b) IZ-I (porosity)

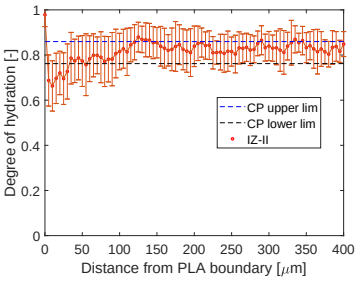

(c) IZ-II(α)

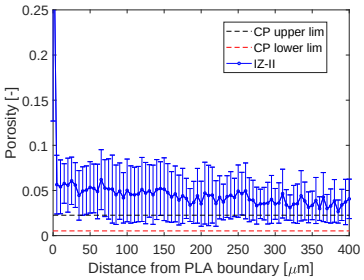

(d) IZ-II (porosity)

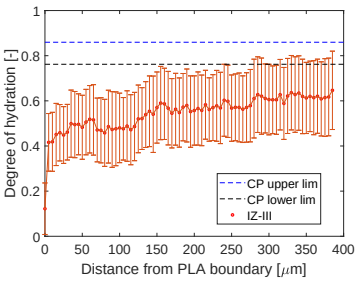

(e) IZ-III (α)

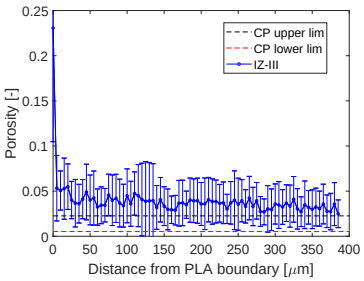

(f) IZ-III (porosity)

Figure 3.6: Degree of hydration profiles from PLA boundary of the IZ of SH-I a), -II c) and -III e) and porosity profiles from PLA boundary of the IZ of SH-I b), -II d) and -III f). The error bars represent the standard deviation among the different micrographs for each position.

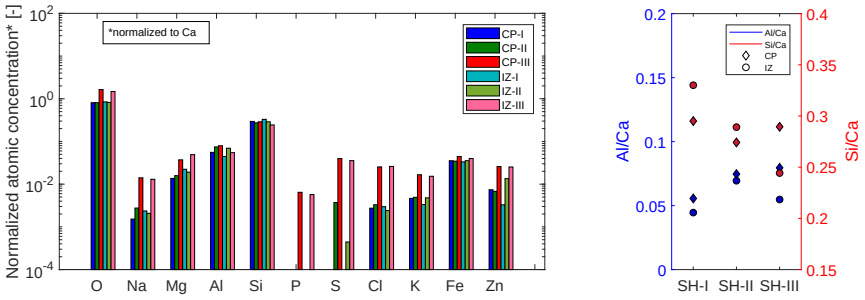

(a) (b)

Figure 3.7: General elemental atomic compositions a) and aluminum and silica atomic fractions b) normalized to Ca atomic ratio for the interfaces SH-I, SH-II and SH-III and bulk cement paste beyond the IZ, CP-I, -II and -III.

interface and bulk paste of SH-III. Smaller concentrations were found for SH-II, specially so for its interface zone, and none for SH-I. Considerably higher concentrations of Cl and alkalis Na and K were detected in SH-III when compared to the references and interfaces of SH-I and SH-II.

Since Ca, Al and Si make the bulk of hydrates in cement paste, Al/Ca and Si/Ca ratios are also reported in Figure 3.7b relative to the interfaces and respective reference bulk pastes. With respect to the references, Si/Ca ratio was higher for interfaces I and II which may indicate a slight localized decalcification of the IZ. For IZ-III instead there was a significant decrease in Si/Ca when compared to the three references. Coherently, also Al/Ca was lower for SH-III interface when compared to the reference bulk paste, which may suggest a higher concentration of Ca in the gel at the interface. A slight decrease in Al/Ca ratio was also found for IZ-I, whereas, no changes in Aluminum concentration could be spotted for the IZ-II with respect to bulk cement paste.

3.4.3 Mechanical properties of cement-PLA interface

2D mapping of micromechanical properties at the interface zone

In Figures 3.8-3.11, the maps of elastic modulus and hardness, resulting from the grid nanoindentation, are shown for 6 different locations (a-k) per each of the studied pastes SH-I, -II, -III and CP, respectively. The locations of PLA-pastes in Figures 3.8-3.10 are displayed in such a way that the boundary of the PLA particles (not mapped) is at the left of the map. The contour legend of E modulus map captures the whole range of measured values: 0-60 GPa whereas for the hardness maps the colour legend was scaled to the range 0-4 GPa.

Since the depth of indentation, chosen for the computation of the elastic modulus and hardness, is relatively high, the resulting values are indicative of a volume of interaction mostly bigger than individual phases in the hydrated cement pastes. For this reason, the individual indentation values do not correspond rigorously to the micromechanical properties of such phases. Nevertheless, as described in Hughes & Trtik [244], high contrast in these properties can be found between anhydrous grains and hydrates, and clearly pores. From literature, typical values of hardness and elastic modulus for clinker are found to

be between 3 and 6 GPa and between 60 and 120 GPa [245], respectively. For CSH„ there exists a further distinction between Low- (LD) and High-Density (HD) CSH with values of H and E ranging between 0.4-1 GPa and 18-39 GPa, respectively, with increasing values for increasing density of the CSH phase [245]. Similarly, Portlandite (CH) hardness and elastic modulus values range from 1.5-2 GPa and from 40-50 GPa [245]. Such indications seem to consistently order the phases by values of hardness or elastic modulus as Clinker>CH>HD-CSH>LD-CSH>Pores. And therefore herein, such indications could also be used to roughly describe key features of the different IZ studied.

From the mappings of both elastic modulus and hardness, it can be observed that more extensive blue zones (i.e. indicating lower stiffness) are present in IZ-III, suggesting that the porosity is high and highly connected when compared to the reference CP. IZ-I and -II do not present such large porous areas but rather uniformly distributed smaller defectuous zones. As observed from SEM/BSE analyses, also from the micromechanical mapping, interface zones of the PLA-pastes present lower degrees of hydration when compared to the reference bulk cement paste, as evinced from the presence of more hubs with values of properties close to those of clinker. The latter seems specially true for IZ-III and less so for IZ-I. In general, IZ-II presented higher hardness values of (likely) CSH phases when compared to IZ-I and IZ-III, but similar values to the bulk cement paste. Similar observations can be made regarding the E modulus.

Uniaxial tensile 2D simulations of the interface zone

In Figure 3.12 the cracking history of location 1 of IZ-I is reported, overlapped with the mapping of tensile strength assigned to the lattice elements and alone with the respective load versus displacement response in i. In the curve, the same cracking history events have been annotated. First cracking occurred even before reaching the peak, at a load of around 0.06 mN. Such event it is not reported in Figure 3.12. The initial cracked elements were not located at the edges. The peak load was only attained when one of the cracked spots got connected to one of the edges (as observed in a)) at approximately 80 μm from the PLA boundary, which is located within the interface zone as measured from SEM/BSE analysis in section 3.4.2. The next relevant event was the nucleation of another crack in the opposite edge of the mesh (b), this time further away from the particle boundary at circa 120 μm. The nucleation of the latter crack was expected to occur due to the imposed uniform displacement. Both cracks nucleated in zones with low local tensile strengths (in red). Next, the latter crack and then the first crack propagated along the direction perpendicular to the load in turns. The latter propagation required an increase of the applied force in c) since the second crack had encountered local elements with higher strength. After event d), the load necessary to proceed with the cracks propagation was rapidly decreased probably due to the reduction of the bearing section to less than half of the pristine section. After point f), the bearing section got reduced to one third of the original one at the two cracks locations. The second crack propagated all the way to the other edge (h) with subsequent lower load due to low local tensile strength near the edge. Since the crack outside of the nominal interface provoked the final failure, the failure was considered to occur in the bulk cement paste and not the interface in this instance.

For the other tested locations, similar developments of cracking events were observed. In Figure 3.13, some examples of crack patterns at failure are reported for specific locations from the different simulated pastes. The examples refer to widely observed behaviours of

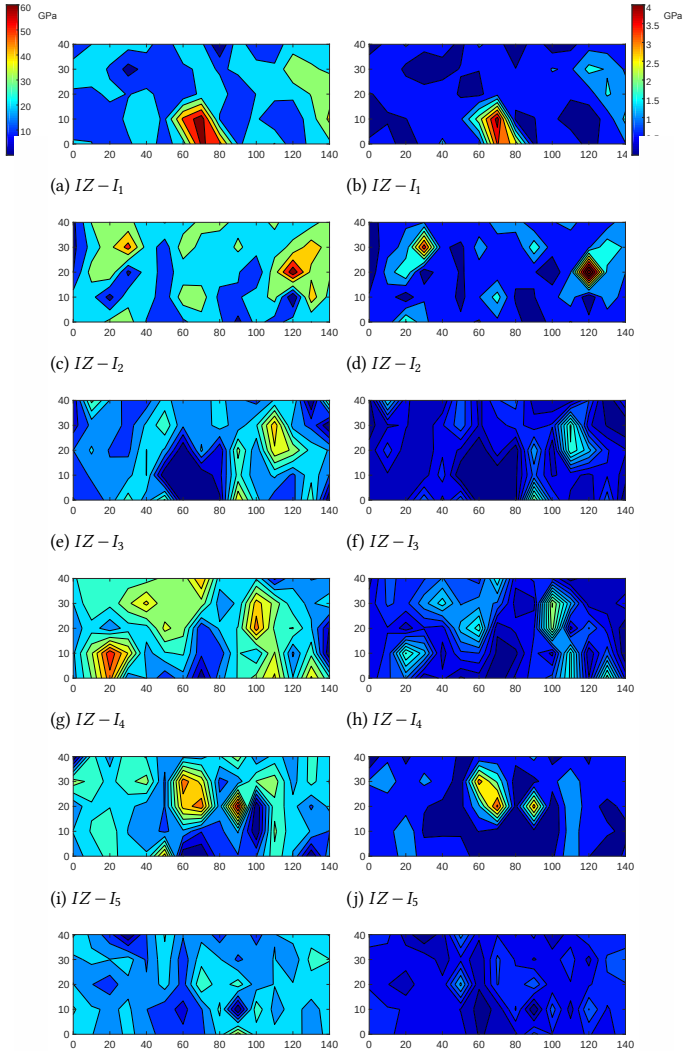

(a) $IZ - I_1$ (b) $IZ - I_1$

(c) $IZ - I_2$ (d) $IZ - I_2$

(e) $IZ - I_3$ (f) $IZ - I_3$

(g) $IZ - I_4$ (h) $IZ - I_4$

(i) $IZ - I_5$ (j) $IZ - I_5$

(k) $IZ - I_6$ (l) $IZ - I_6$

Figure 3.8: E modulus (left) and hardness (right) maps obtained from grid nanoindentation for 6 locations at IZ-I (grid axes in μm).

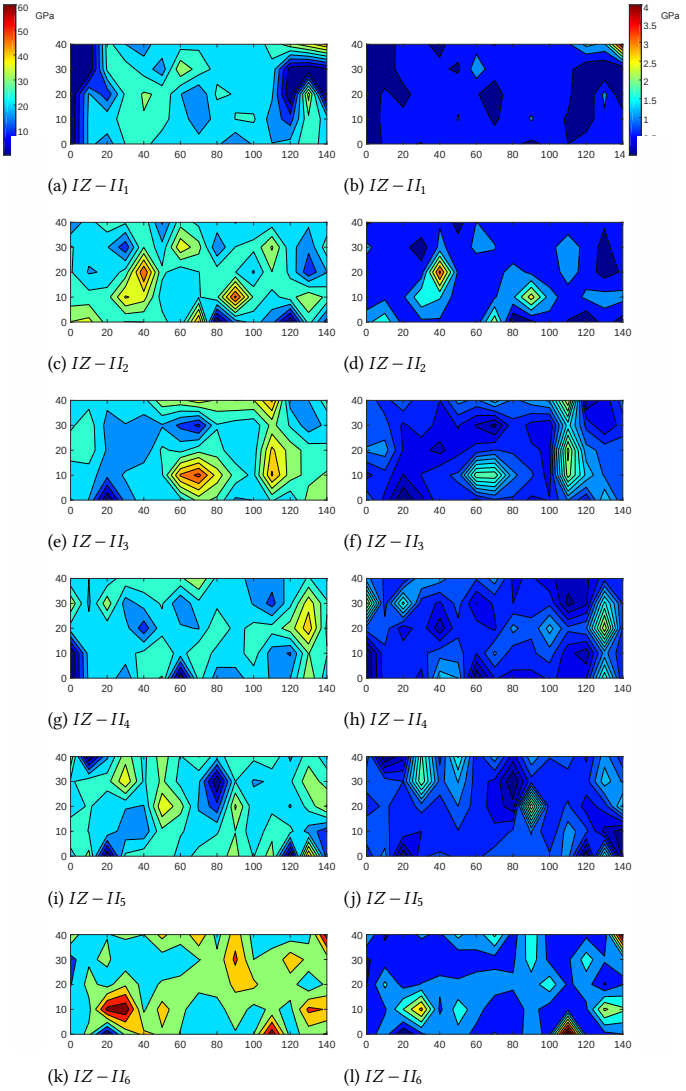

(a) $IZ - II_1$ (b) $IZ - II_1$

(c) $IZ - II_2$ (d) $IZ - II_2$

(e) $IZ - II_3$ (f) $IZ - II_3$

(g) $IZ - II_4$ (h) $IZ - II_4$

(i) $IZ - II_5$ (j) $IZ - II_5$

(k) $IZ - II_6$ (l) $IZ - II_6$

Figure 3.9: E modulus (left) and hardness (right) maps obtained from grid nanoindentation for 6 locations at IZ-II (grid axes in μm).

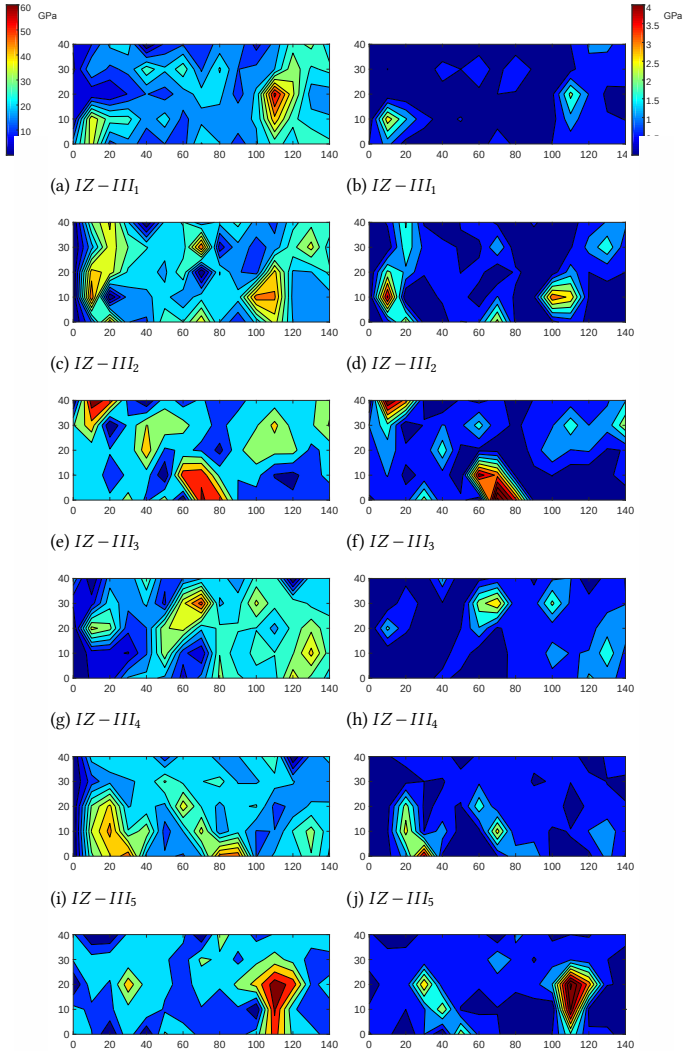

(a) $IZ - III_1$ (b) $IZ - III_1$

(c) $IZ - III_2$ (d) $IZ - III_2$

(e) $IZ - III_3$ (f) $IZ - III_3$

(g) $IZ - III_4$ (h) $IZ - III_4$

(i) $IZ - III_5$ (j) $IZ - III_5$

(k) $IZ - III_6$ (l) $IZ - III_6$

Figure 3.10: E modulus (left) and hardness (right) maps obtained from grid nanoindentation for 6 locations at IZ-III (grid axes in μm).

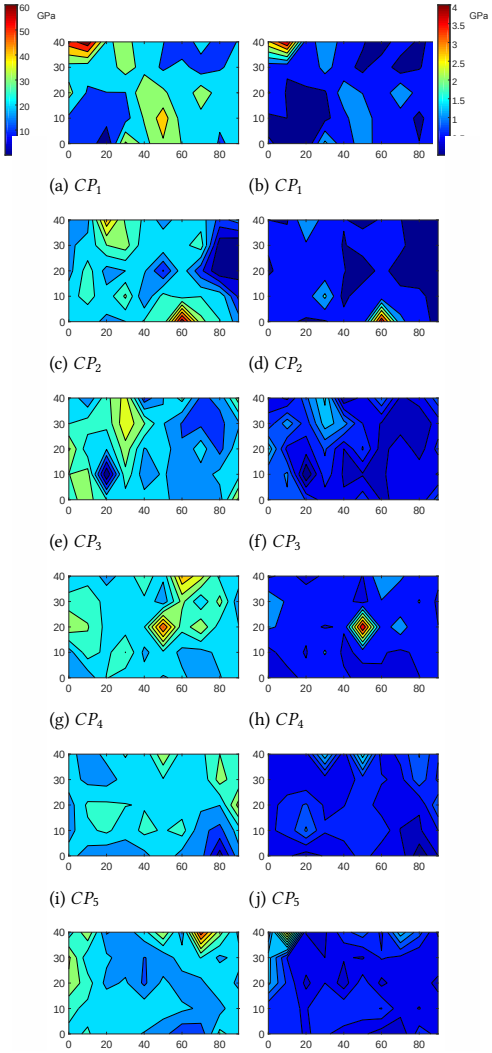

(a) CP_1 (b) CP_1

(c) CP_2 (d) CP_2

(e) CP_3 (f) CP_3

(g) CP_4 (h) CP_4

(i) CP_5 (j) CP_5

(k) CP_6 (l) CP_6

Figure 3.11: E modulus (left) and hardness (right) maps obtained from grid nanoindentation for 6 locations in bulk CP (grid axes in μm).

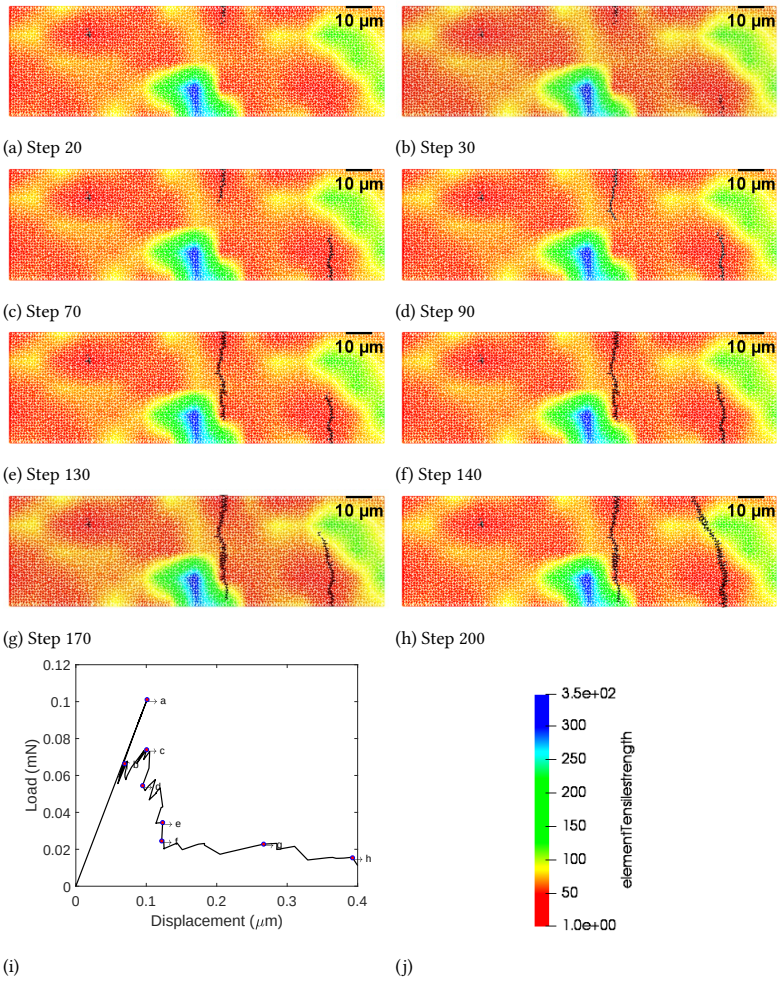

(a) Step 20 (b) Step 30

(c) Step 70 (d) Step 90

(e) Step 130 (f) Step 140

(g) Step 170 (h) Step 200

(i) (j)

Figure 3.12: Cracking history of location 1 of IZ-I (a-h) (cracked elements are reported in black), annotated Load vs. displacement curve (i) and contour colour legend (j) of the tensile strength mapping.

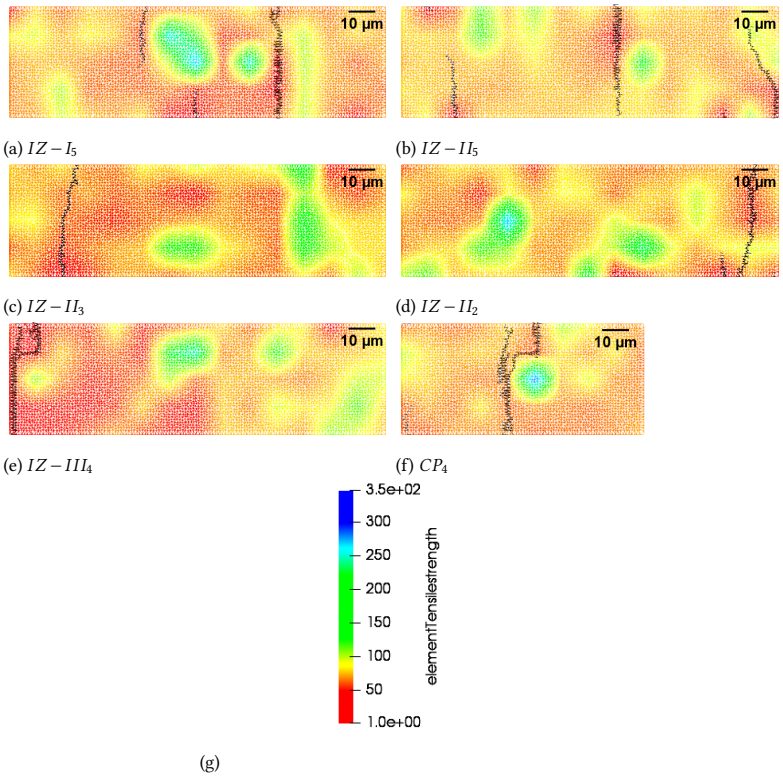

(a) $IZ - I_5$ (b) $IZ - II_5$ (c) $IZ - II_3$ (d) $IZ - II_2$ (e) $IZ - III_4$ (f) CP_4 (g)

Figure 3.13: Common simulated crack patterns at failure of mapped interfaces and bulk cement paste regions.

the different interfaces and bulk cement paste. Multiple cracking was observed for several locations of IZ-I and IZ-II, as shown in a) for $IZ - I_5$ and b) for $IZ - II_5$, probably due to the presence of many closely distributed low-tensile-strength hubs from where cracks could easily nucleate, but at the same time the existence of stronger hubs where cracks got trapped during their propagation. Where weaker zones were interconnected, one single crack nucleated and propagated all the way through to the other edge, as was the case reported in c) for $IZ - II_3$. As in the case shown in Figure 3.12, in Figure 3.13d the other single case of fracture outside of the IZ is reported. In contrast, for IZ-III all locations failed in the IZ and specifically, more failures occurred near the PLA boundary where large weaker zones were commonly present, as shown in e). Finally, the crack pattern at failure of location CP_4 is shown in f). As in the case described in Figure 3.12, two cracks nucleated at either side of the section and propagated in turns while diverting around stronger local elements. It is worth mentioning that the choice of boundary condition at the left side, as schematized in Figure 3.3b, results in stress concentration at the same border due to the blocked contraction in the vertical direction. However, with exception of IZ-III, this stress concentration did not seem to influence the location of final failure for the rest of the studied IZ or bulk paste, likely due to the generally low stiffness at that location.

The simulated load versus displacement responses of the different tested locations are

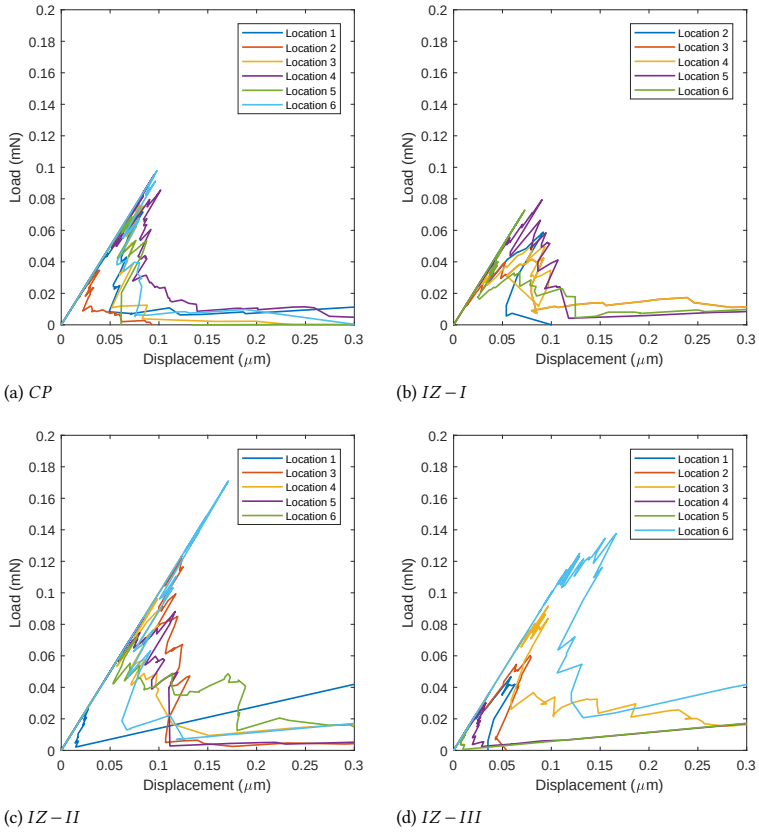

(a) CP (b) $IZ-I$

(c) $IZ-II$ (d) $IZ-III$

Figure 3.14: Simulated load vs. displacement curves for tested locations of bulk cement paste (a) and interfaces (b-d).

reported in Figure 3.14a-d for CP, IZ-I, -II and -III.

3.5 Discussion

From each curve in Figure 3.14, the tensile strength was calculated as the peak load divided by the area of the section with width of 41 μm and depth of 1 μm (as the cell size). The stiffness of the overall location was considered as equivalent to that of two springs (IZ and bulk cement paste) in series as suggested in [217]. The stiffness of the IZ (E_{IZ}) was calculated considering that the ratio between total area (A_{tot}) and simulated stiffness (E_{tot}) is the sum of the ratio between the area of the IZ (A_{IZ}) and the sought after E_{IZ} and that between the area of the remaining section corresponding to the bulk cement paste ($A_{bulk} = A_{tot} - A_{IZ}$) and the simulated stiffness of the bulk cement paste (E_{CP}) as reported in Equation:

$$\frac{A_{tot}}{E_{tot}} = \frac{A_{IZ}}{E_{IZ}} + \frac{A_{bulk}}{E_{CP}} \tag{3.5}$$

In Figure 3.15, box plots for tensile strength and stiffness of the different interface zones and bulk cement paste are shown. The box plots summarize the samples statistics. The red line inside the boxes is the median value and the bottom and top of the boxes are the 25^{th} and 75^{th} percentile values. The outliers are represented by a + sign and the whiskers extend to the lower and upper values not considered as outliers. A value was considered as outlier if it was more than three scaled median absolute deviation (MAD) from the median. The scaled MAD is defined as $c * median(|A - median(A)|)$, where $c = -1/(\sqrt{2} * erfcinv(3/2))$.

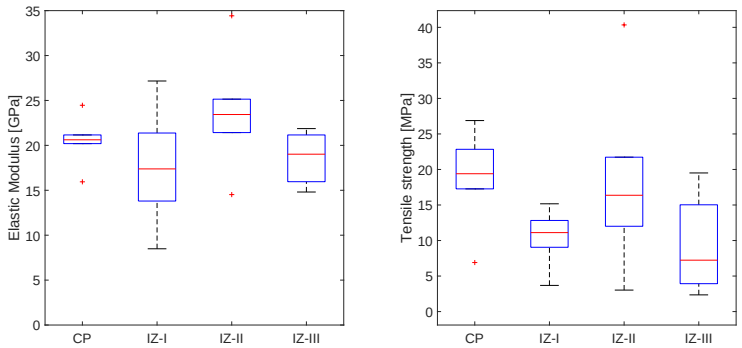

(a) (b)

Figure 3.15: Summary of stiffness a) and tensile strength b) values obtained from uniaxial tensile simulations of the tested interface and bulk paste locations.

First of all, the range of tensile strength values obtained for the reference cement paste ($17 - 26\ MPa$), as well as those of elastic moduli ($20 - 22\ GPa$), are consonant with those found for similar pastes with water-to-cement ratios between 0.4 and 0.5, hydrated for 28 days [246, 247].

Regarding tensile strength of simulated IZ locations, the results point towards a decrease in median values for the interface zones when compared to the reference bulk paste. The ratios between median tensile strength of each interface and that of cement paste were found to be 0.65, 0.89 and 0.38 for IZ-I, -II and -III, respectively. As reported, the effect of PLA type on the mechanical properties of their respective interfaces varied significantly, which suggests that PLA capsules can be tailored to modify the interface and therefore the triggering efficiency and the overall mechanical performance of the self-healing material. The different ratios seem to correlate quite well to the distribution of weaker regions of low hardness (thus high porosity) in the 2D hardness maps obtained form grid nanoindentation (section 3.4.3). For example, IZ-III maps presented very extensive weak zones, specially near the boundary with the PLA capsule, which could also be confirmed by the low degree of hydration in the interface zone of SH-III as observed from BSE analysis. The microstructure of this interface can be explained by the modifications in hydration brought in by the capsules PLA-III, such as dramatic delays of hydration at early age, as shown from the

heat flow curves. These microstructural features explain also the positive skewness of the distribution of tensile strength for IZ-III, which emphasizes the greater likelihood of obtaining lower values of strength. In contrast, the other interfaces IZ-I and -II, as well as the CP, presented seemingly normal distributions of tensile strength. Hardness maps of CP, IZ-I and -II showed smaller and well-distributed weak hubs, specially so for IZ-II, which coincided with higher median tensile strength with respect to IZ-III. Decreases in alumina content were also observed in the interfaces IZ-I and IZ-III. From the interquartile ranges of the box plots, it is also possible to notice that both IZ-II and IZ-III tensile strength distributions presented more data dispersion than CP and IZ-I which may be related to the increase of heterogeneity in these interfaces. A similar observation could be made about the higher scatter of the tensile strength values for IZ-II and -III, as denoted from the separation of the whiskers in the plot.

Concerning the stiffness of the simulated locations, median values were in a narrow range, between 17 and 24 GPa, which denotes a weak influence of the PLA particles on the elastic response of their respective interfaces. This is coherent with established research [247] stating that elastic modulus is much more dependent on the continuity of the solid phases rather than on the presence of porosity. The latter seems to be considerably different among the interfaces and bulk cement paste as shown in the hardness and E modulus mapping. Yet, variation on the median values of stiffness were observed. As CP, all the interfaces presented normal distribution of the elastic moduli. When comparing the median values of elastic modulus among the different location types, it is noticeable that IZ-I presented the lowest stiffness, followed by IZ-III and IZ-II, respectively. Decalcification in IZ-I CSH, as seen from EDS point analysis, may have been the cause of the loss of stiffness in the interface phase as it has been reported in [248]. In contrast, no decalcification was observed at the interface II and even an increase in calcium content was identified for IZ-III. The latter may have been negatively compensated by the presence of large zones with low stiffness present at the IZ-III which disrupts the continuity of the solid phases. Notwithstanding, it cannot be ruled out that different types of PLA may change the proportions of HD-CSH and LD-CSH, which can be also responsible for differences in stiffness of the interface with respect to the reference bulk paste. In general, data dispersion and scatter of simulated stiffness were greater for interface locations when compared to bulk CP. The increased variability of both stiffness and tensile strength values for interfaces suggests that although these zones are definitely affected chemicallly, physically and mechanically, there is higher heterogeneity than in the bulk paste and therefore, their mechanical properties are more variable.

3.6 Conclusions

In this chapter, a quantification of the tensile strength and elastic modulus of the interface zone (IZ) between bacteria-embedded PLA capsules and cement paste was provided for their eventual use as input for mesoscale simulations of the self-healing concrete. In order to do so, mapping of the elastic modulus and hardness of the IZ around different types of PLA capsules, embedded in cement paste, and of the bulk unaffected reference cement paste was done through grid nanoindentation. The outcome was then used to simulate uniaxial tensile tests on several data sets through lattice fracture model. Moreover, Scanning Electron Microscopy in Backscattering Electron mode (SEM/BSE) was performed

to study the hydrates assemblage distribution around the PLA particles and therefore to determine the extension of the IZ zone. Chemical analysis was performed through EDS to identify differences in elemental composition at the interfaces. The following conclusions can be drawn from the results presented herein:

- The studied PLA capsules interfere with reaction kinetics in the first 120 hours of hydration of cement paste. The influence of the additive varies in magnitude in accordance to particle morphology and (alleged) different production processes.
- PLA capsules used in this study definitely modify the long-term hydration of cement paste in the vicinity of the capsules as evinced from the extensive interface zones inferred from the degree of hydration profiles measured through image analysis of BSE images. Mechanical interfaces are typically smaller than 40 μm as reported in the literature [240], whereas in this study interfaces for different reactivity grades of PLA were found to range between 110 and 260 μm.
- Porosity profiles along the interfaces, as measured from BSE images, yielded no definitve trend. On the other hand, from grid nanoindentation results, differences were observed in terms of amount of low stiffness indents, between different zones of the grid themselves and between the IZ and the bulk.
- Traces of phosphorus were found via EDS point analysis in the interface zone and bulk paste of certain PLA type contained in cement paste. This correlated to dramatic short and long term hydration hindrance in the cementitious paste, with consequent worsened mechanical properties.
- Grid nanoindentation could provide a qualitative comparison among the degrees of hydration of the different interfaces, via characteristically high values of hardness and elastic moduli of anhydrous phases.
- The ratios between the tensile strength of the PLA interface zones and the bulk cement paste resulted 0.65, 0.89 and 0.38 for SH-I, SH-II and SH-III respectively. These results suggest that PLA can be tailored to optimize the physico-mechanical properties of the interface and hence, the mechanical behaviour of the SH system.
- Average values of stiffness for the interface zone of SH-II and SH-III were close to those of unaffected cement paste. The interface IZ-I showed significantly reduced stiffness which seemed to correlate with decalcification of the interface locations as observed from EDS analysis.

Various limitations of the methodology employed here are to be taken into account when interpreting and using the results of this study. One important matter is to consider that on selecting the indented locations, uncracked areas were preferred, therefore the effect of bigger defects in the interface could not be reflected on the statistics of simulated mechanical properties. Regarding the numerical simulations, it has been shown in the literature [226] that elastic moduli and tensile strengths obtained from 2D lattice fracture simulations are consistent with those found for 3D cases. Nonetheless, the distribution of 2D strength was found to be askew towards values up to 30 % higher then their 3D counterpart,

which may suggest that the 2D analyses overestimate this property. Notwithstanding, the ratio between this property in bulk cement paste and interfaces should not be affected, as shown in other studies [249].

In the next chapter, the results obtained herein, i.e. ratios between properties of the interface and bulk paste, are to be used as input for fracture simulations at the mesoscale of the self-healing concrete.

4

Numerical investigation of fracture mechanics of self-healing cement-based systems

A fear of weakness only strengthens weakness.
Criss Jami

In this chapter, a 3D mesoscale lattice model is proposed to simulate uniaxial tensile test of a self-healing system composed of cement paste, bacteria-containing poly-lactic acid (PLA) capsules and their interface. The ratios between tensile strength and elastic modulus of the interface with respect to bulk cement paste, obtained in the previous chapter for three different PLA types, were used as input for the mesoscale model. The self-healing and reference cement pastes were imaged through X-ray micro Computed Tomography before and after fracture to obtain the capsules distribution to input in the mesoscale model and the fracture surface for validation, respectively. The experimental and simulated stress-strain curves showed excellent correspondence, especially in the elastic phase, hence validating the proposed model. An exhaustive numerical investigation of the material was performed then to analyse the influence of dosage, size and shape of the PLA capsules, as well as of the interface properties on the mechanical behaviour of the composite and the triggering of the PLA capsules. The results show that interface properties close to but lower than the cement matrix do not entail substantial losses of tensile strength and elastic modulus, whereas the amount of triggered capsules is maximized. Optimum dosage, shape and size of the PLA capsules were also obtained.

4.1 Introduction

Microcapsules are the most commonly employed healing agent carriers in autonomous self-healing cement-based materials [47, 57–60, 63–66]. Such particles protect the healing agents during mixing and also hinder the onset of the repair when no cracking has yet occurred. Furthermore their uniform distribution within the composite facilitates the availability of healing agents in all locations of the concrete element. Finally, capsules are the main actuators of the triggering of the healing process [55, 67, 68]. In this regard, leaving aside the type of triggering mechanism (chemical, physical or mechanical), for healing to begin capsules must either break or at least be exposed in the crack [7]. This means that the capsules need to steer the crack propagation in the self-healing material. On the other hand, the addition of capsules in cementitious materials for the purpose of self-healing must not impair significantly the mechanical properties of the composite. Hence, the design of a capsule-based self-healing cementitious system must respect two (often competing) requirements.

In [250] an experimental investigation of the effect of different dosages of urea - formaldehyde shell capsules with average diameter of 200 μm on the compressive strength and elastic modulus of mortar was presented. The results showed reductions of the compressive strength of 5.8, 13.5 and 20 % for 5, 10 and 15 % of added capsules. For the elastic moduli, a similar trend was found whereas the strain at the peak seemed to increase of 6.5, 12.9 and 19 %, respectively. In addition, the authors measured the healing rate of the aforementioned properties after a certain period of healing and found proportional linear increases of the compressive strength after healing as the amount of capsules was increased by 5 %. On the other hand, the peak strain decreased after healing took place yet also linearly proportional to the increase of capsule dosage in the mortar. In another study by Kanelloupoulos et al. [169], the compressive strength, E modulus and healing efficiency of mortar with solid shell - liquid core capsules were investigated. The authors added volume fractions of 300 μm capsules from 4 to 32 % with 4 % increments. It was found that the compressive strength of cubes followed a decreasing trend when the dosage of capsules was raised from 12 % on with decreases between 17 and 27 %. Yet for the lowest volumetric fractions, the strength drop was negligible. The authors suggested that this peculiarity was due to the size of the capsules. Regarding the Young's Modulus, the results showed no specific trend but large fluctuations were found on the values obtained for different volume fractions of capsules present in the mortars. Finally, the healing efficiency of the system, measured from crack mouth width reduction and healed depth, was shown to increase linearly with the dosage. Milla et al. [251] investigated the effect of three different dosages (0.25, 0.50 and 1.00 % by weight of cement) and average diameters (22, 50 and 109 μm) of shell-core microcapsules on the mechanical properties and healing efficiency of concrete. The influence of the microcapsules on the elastic modulus was highly dependent on the diameter of the capsules and the dosage, suggesting the existence of an optimal combination thereof for 50 μm capsules in a dosage of 1.00 %. With regards to the compressive strength, a decrease was found for increasing dosages of microcapsules, whereas among the studied capsule sizes no noticeable strength differences were found. The recovered compressive strength seemed to decrease for increasing particle size while no clear trend was observed for the studied dosage range. Similar studies were presented in [80, 113, 252, 253] for different self-healing systems with high variability on the results

regarding the influence of the studied capsule sizes and dosages. Relevant studies on the parametric study of mechanical properties and triggering of capsule-based self-healing concrete through a modelling methodology have been reviewed in Chapter 2. Some of the reviewed works preliminary demonstrate the potential of FEM to optimize the mechanical triggering of healing admixtures such as capsules. Yet, published works lack validation or present incomplete analysis of relevant parameters and their combination. Moreover, available numerical optimization studies don't consider the effects of capsules on the mechanical behaviour of the self-healing composite.

It is therefore evident that numerical fracture models could be an efficient way to optimize the design of capsule-based autonomous self-healing cementitious composites. In particular, through lattice fracture model exhaustive studies of relevant design parameters are possible while saving time and resources that would be otherwise necessary through an experimental approach. Specifically, such model is developed and used herein in the context of self healing cement paste with addition of Poly-lactic acid (PLA) capsules containing bacteria.

Preliminary research on the use of bacteria-embedded poly-lactic-acid (PLA) capsules as healing agent have been presented in [61]. Some peculiarities of the microstructure and local micromechanical properties of cementitious composites with PLA capsules have been discussed in Chapter 3. In the literature, increasing the dosage of PLA particles seems to result on reductions of the compressive and tensile strength [61, 110, 214] but as in the case of other capsule-based self-healing cementitious composites, no exhaustive investigation of the influence of capsules on the mechanical behaviour of the composite exists thus far.

In this chapter, 3D fracture lattice model is used to study the mechanical behaviour and healing triggering of cement paste with bacteria-embedded PLA capsules. Self-healing and plain reference cement paste samples were imaged through X-ray micro Computed Tomography (μCT) before and after fracture via Uniaxial Tensile Test. In the case of the self-healing cement paste, the imaged capsules distribution was used as input for simulating Uniaxial Tensile Test (UTT) on the self-healing system composed of PLA capsules, bulk cement paste and their interface (influence zone). The tensile strength and elastic modulus ratios of the influence zone relative to the bulk cement paste, obtained in the previous Chapter 3, were used as input. Experimental and simulated elastic modulus and tensile strength were in excellent agreement when capsules and influence zone were assumed to be fully in contact. The simulated post-peak behaviour could not match the experimental one as expected due to the adopted simple linear-elastic constitutive law for the lattice elements, and the assignment of uniform micromechanical properties in the bulk cement paste. The validated model was then used to perform a parametric investigation considering the influence on mechanical behaviour and healing triggering of capsules size, shape, dosage and influence zone properties within certain ranges and the combinations thereof.

4.2 Experimental Methods

4.2.1 Raw materials and sample preparation

Ordinary Portland Cement CEM I 52.5 R (ENCI, the Netherlands), tap water and self-healing capsules containing bacterial spores (Basilisk, the Netherlands) were used for the preparation of samples. The chemical composition of the cement, obtained from XRF

measurements, was reported in Chapter 3. The self-healing capsules were composed of a Polylactic acid (PLA) derivates matrix and embedded bacterial spores of Bacillus cohnii-related strains and growth-required nutrients [218]. From the results presented in Chapter 3, capsule type PLA-II was chosen to be used herein as explained in Section 4.1. The density of the particles was 1200 kg/m^3 and the particle sizes were between 0.5 and 1 mm. Using the Sauter mean diameter [219], measured by laser diffraction, the resulting specific surface area of particles PLA-II was $1.11x10^{-5}$ cm^2/g .

Two cement paste types were prepared with water-to-cement ratio (w/c) of 0.45. One mixture containing no healing particles was prepared as reference, herein referred to as CP. The other mixture, SH-II, contained 4.1 % of PLA-II capsules by volume of composite.

A Hobart planetary mixer was used to prepare the fresh pastes. In the case of SH-II, cement and capsules were first mixed for 1 minute at low speed. Water was added into the running mixer containing cement powder (and capsules) within 30 seconds and the components were left to mix for other 30 seconds. Then, the walls of the mixer were scraped and mixing was continued for 1.5 minutes and further 30 seconds at low speed and medium speed, respectively.

After casting, the samples were sealed with plastic foil and left to harden for 24 hours at laboratory conditions. Afterwards they were demoulded and stored in a fog chamber with temperature and relative humidity set at $20^{\circ}C$ and 95 %, respectively until the age of 28 days. Prior to testing the samples were kept at laboratory conditions for 72 hours to reduce the influence of moisture content on the tensile behaviour of the material.

4.2.2 Uniaxial Tensile Test and Digital Image Correlation

Uniaxial Tensile Test (UTT) was performed by means of a servo-hydraulic press Axial Tension-Compression Systems, model 8872 from Instron (High Wycombe, UK). Three reference samples (CP) and three samples containing capsules (SH-II) were prepared from cubes with approximate sizes of $10 \times 10 \times 10$ mm^3. Two identical notches were sawn in the samples as shown in Figure 4.1a. A thin layer of white paint was applied on one side of the sample and random black dots were marked in order to perform Digital Image Correlation (DIC) during the UTT. The samples were glued to the loading plates using a two-component glue (X60 consisting of a power Plex 7742 and a fluid Pleximon 801) while in load control with a small compression load of 20 N to prevent precracking due to the shrinkage of the pleximon glue. The average vertical displacement of two Linear Variable Differential Transformers (LVDT) between the two loading plates was used to control the test at a rate of 15 nm/s. The LVDT's were positioned in the same plane as the notched faces of the samples. The loading plates in the used configuration had high rotational stiffness with respect to the bending stiffness of the specimen, hence rotation of the faces bond to the steel plates was not allowed [254, 255]. In Figure 4.1b the configuration described above is shown.

For each tensile test Digital Image Correlation (DIC) analysis was performed in order to track the sample surface displacements and to capture the crack nucleation and propagation. The digital images were acquired at 10 frames per minute during the test. The digital camera used was a Canon EOS 6D, with a nominal resolution of 20.2 megapixel and a MP-E 65mm f/2.8 1-5x Macro Photo lens. The open source software Ncorr[256] was used for the 2D digital image correlation analysis.

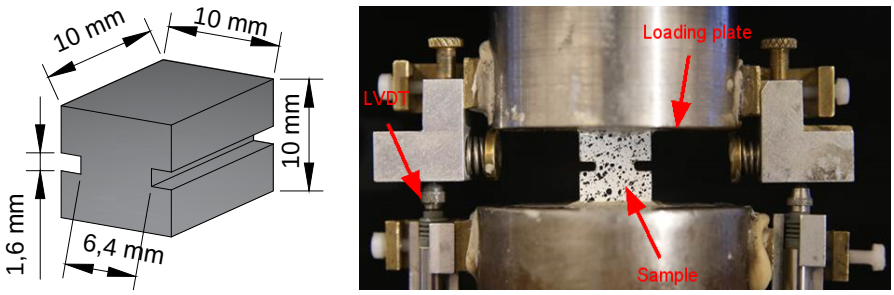

(a) (b)

Figure 4.1: Sample scheme in a) and UTT configuration in b).

4.2.3 X-ray micro Computed Tomography

The 3D fracture surfaces obtained after UTT of reference and self-healing paste samples were acquired by means of X-ray micro Computed Tomography (μCT). In the case of SH-II samples, the samples were also scanned before the UTT to obtain the capsules distribution to be used as the material mesostructure for fracture simulations, as it will be explained in Section 4.3.

The samples were scanned using a Micro CT-Scanner (Phoenix Nanotom, GE, Germany). The X-ray tube was operated at 140 kV and 160 μA. A number of projections (1441) were acquired by a digital GE DXR detector (2288×2304 pixels). Each projection was the resulting average of 4 radiographs with an exposure of 500 ms in order to minimize noise. The voxel resolution under these conditions was 11 μm.

The projections were calibrated with dark and bright field images and 3D reconstructed by means of the software Phoenix datos|x Reconstruction 2.0. Spot and beam hardening artifacts were corrected with the same software during reconstruction. Reconstructed scans of SH-II samples after fracture were registered with respect to the sound ones through the opensource software DataViewer (Bruker). This allowed for the spatial correspondence of each voxel of the scanned volume before and after UTT in a same sample. Image treatment and analysis was then performed using the freeware ImageJ [222] and MATLAB.

4.3 Lattice fracture modelling

For the discretization of the 3D domain, a cell size of 100 μm and a randomness of 0.2 for the positioning of the nodes were used. A schematic representation of the above discretization is reported in Figure 4.2. Although any type of constitutive laws can be assigned to the single lattice beams [231], linear-elastic behaviour of the finite elements is also accepted when modelling brittle materials and for which only elastic and shear moduli, tensile and compressive strengths are needed as elemental inputs [230]. The latter approach relies on the mesh randomness and presence of heterogeneities to simulate the post-peak behaviour of the studied materials at a small scale. The limitations of this approach have been thoroughly discussed elsewhere [257, 258]. In this work we used the latter simplification, mainly to speed up the computations, which makes possible the study of a large array of relevant material parameters.

One advantage of lattice models is the possibility of explicitely modelling the influence of material heterogeneities on the fracture process. In the specific case of self-healing cement paste with PLA capsules, phases such as bulk cement paste, PLA-II capsules, influence zone between capsules and cement paste (IZ-II), etc. present different mechanical properties as shown in [259]. A 3D material mesostructure is first obtained from X-ray micro Computed Tomography or digitally computed through softwares like Anm [20] (in the case of irregular particles) or spheres parking procedure [260]. The result of such procedure is the assignment of a certain material phase to each of the cells of the lattice mesh and thus to the nodes. Lattice beams with nodes belonging to the same phase are tagged as such, while elements bridging both phases are distinguished as interface elements (Figure 4.2).

After discretization and assignment of input properties, lattice fracture model was used to simulate uniaxial tensile test on the 3D meshes. The boundary conditions at the bottom boundary of the domain were imposed by constraining all the degrees of freedom. On the other hand, at the top boundary, a unitary vertical displacement was imposed on the nodes.

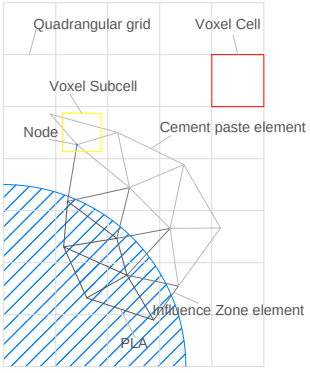

Figure 4.2: Lattice model discretization procedure for the 2D case (modified from [260]).

4.4 Results

4.4.1 Experimentally-informed input parameters

Reference cement paste sample (CP)

The linear-elastic properties of the bulk cement paste lattice elements were fitted from UTT lattice simulations emulating the experimental Stress-Strain curve, which methodology was detailed in Section 4.2.2. A lattice mesh consisting of 939386 nodes and 7138143 elements was generated to simulate the uniaxial tensile behaviour of a CP sample with dimensions as in the scheme shown in Figure 4.1a. From X-ray CT results, the air void size distribution of the scanned CP samples (see Figure 4.3a, 4.3b, 4.3c) was obtained and shown in Figure 4.3d. As a consequence, a mesostructure with 0.3 % by volume of randomly distributed spherical air voids, was digitally generated.

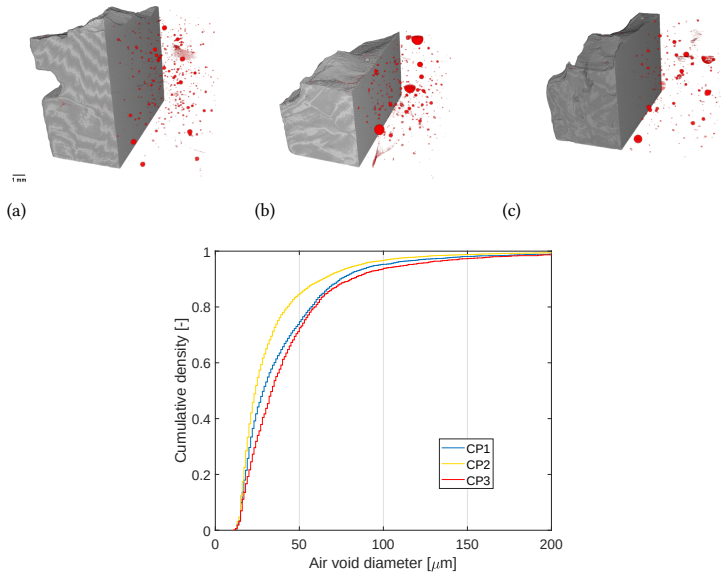

Figure 4.3: Segmentation of airvoids in cement paste samples imaged from X-ray CT (a), b) and c)) and airvoid size distribution d).

The beam elements with both nodes belonging to the air phase were eliminated. Whereas the elastic modulus was fitted from the Stress-Strain curve, the shear modulus of the element (G_{ij}) was obtained via Equation 3.2. A Poisson ratio (ν) of 0.2 was adopted.

The compressive strength ($f_{c,ij}$) to tensile strength ratio was taken as 10 which has been experimentally confirmed for such length scales in [235].

In Figure 4.4a the experimental Stress-Strain curve as well as the best fit simulated curve are reported. The latter was obtained by assigning linear-elastic properties to the cement paste elements as shown in Table 4.2. For the fitting of the elastic modulus, the secant method was chosen. The latter was calculated as the slope of a line drawn from the origin to a point on the experimental Stress-Strain curve corresponding to a 40% of the peak stress [261]. On the other hand, the experimental peak load was used as target for obtaining the elemental tensile strength. Experimental and simulated tensile strength and elastic modulus are reported in Table 4.1.

Table 4.1: Summary of mechanical properties obtained from experiment and fitting simulation.

Sample	E [MPa]	f_t [MPa]
CP exp	11698	2.1029
CP sim	10979	2.0951

Whereas the linear elastic behaviour of simulated and experimental samples match

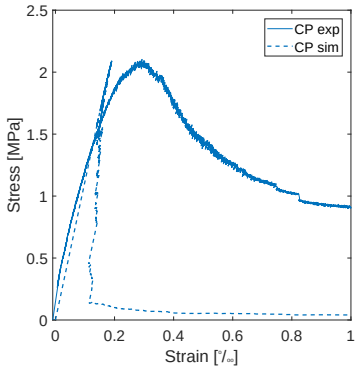

(a)

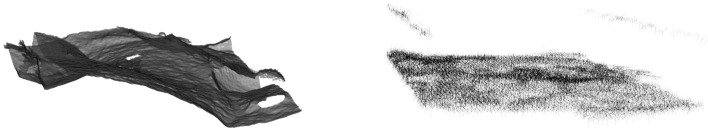

(b) (c)

Figure 4.4: Comparison of experimental and lattice simulated UTT for sample CP a) Stress vs. Strain curve, b) experimental fracture surface and c) simulated fracture surface.

well, differences between the two curves arise shortly before the achievement of the peak stress. In fact, in experimental curves it is canon to observe a non-linear elastic behaviour before the maximum load is achieved [262]. The latter is attributed to widely distributed microcracking within the specimen, due to the existence of defects that may act locally as stress concentrators [261]. Although in the simulated results, cracking of certain lattice elements occured prior to the achievement of the peak stress (as it will be shown shortly), the pre-peak nonlinearity is negligible in the Stress-strain curve. This behaviour was expected because in the simulated specimen the cement paste lattice elements were all assigned uniform elastic properties and mechanical strength. In reality, plain cement paste presents micro defects, as well as heterogeneous phases with different mechanical strength [263], that can locally lead to failure before the tensile strength of the overall composite is achieved. The coalescence of microcracks at a certain location of the affected section then gives rise to the creation of a fracture zone around the peak stress attainment [264]. In the post-peak zone of the curve, both simulated and experimental specimens undergo a softening behaviour but some crucial differences are present. Typically for this loading configuration and sample size additional deformation of the fracture zone occurs while the rest of the specimen is elastically unloaded. In agreement with the latter in the experimental specimen, the fracture zone deformation was achieved by a slowly

progressive smaller stress when compared to the simulated softening. In the simulated case, the same deformation is achieved at a significantly lower stress thus presenting a more brittle performance. The linear elastic constitutive law adopted for the lattice elements and the lack of heterogeneity in the micromechanical properties of the lattice elements in the cement paste are the leading causes of the steeper decrease of the stress in the post-peak obtained in the simulations. It has been largely agreed that the existence of heterogeneities in cement-based materials does result in a more tortuous crack path and a large number of micro-cracks around the main crack, which is directly related to increased fracture energy [265]. The latter can be further confirmed when comparing the final fracture surface obtained via CT (Figure 4.4b) scan and the simulated one (Figure 4.4c).

A direct comparison of experimental and simulated crack nucleation and propagation provides further insight into what to expect from the modelling results presented in this study. In Figure 4.5, the 2D map of vertical strains at different relevant moments during the test of the CP sample obtained via DIC are shown in comparison to the simulated displacement 3D map on a generic CP sample. Four different stages along the Stress-Strain curve were selected: 1) in the linear elastic phase at around 40% of the peak stress, 2) in the nonlinear elastic phase circa 95% of the peak stress, 3) at 50% of the stress drop before the plateau in the softening branch and 4) right before failure. For each of these stages, an experimental DIC frame and the corresponding simulation render are reported in Figure 4.5 from top to bottom. In stage 1) the DIC analysis of the vertical strains indicates the presence of some high strain zones (in yellow and red) which are distributed throughout the sample face. In contrast, the simulations show that damaged lattice elements have appeared only along the notches edges, due to the geometry-induced stress concentration at those locations. At the nonlinear-elastic zone, the DIC analysis shows similar conditions as in stage 1), while the simulated fracture process points at increased damage along the edges notched. In stage 3), both physical and virtual samples show well localized fracture zones. Specifically, the DIC results show two clear high strain fracture zones at both notches with the left one being predominant, plus some damage near the top base of the sample where the latter is glued to the actuator. In the simulations, after the peak fracture at the lower edges of both notches propagates, but the fracture at the right notch becomes predominant in stage 3) and propagates steadily from that point on until reaching the other notch.

Observing the differences between experiments and simulations it is evident that a faithful-to-experiments post peak behaviour is not expected to be validated and therefore, any quantitative evaluation of the the fracture energy will not be correct in absolute terms. This is due to the simplifications made on the model, as explained before. On the other hand, these preliminary results suggest that the simulations can correctly predict the modulus of elasticity and tensile strength of cement paste if average micromechanical properties of the cement paste are used as input.

Samples with capsules of type PLA-II (SH-II)

In the study presented in Chapter 3, the tensile strength and elastic modulus of the influence zone relative to PLA-II (IZ-II) were obtained. There, mapping of the elastic modulus and hardness of the IZ around different types of PLA capsules, embedded in cement paste, and of the bulk unaffected reference cement paste was done through grid nanoindentation.

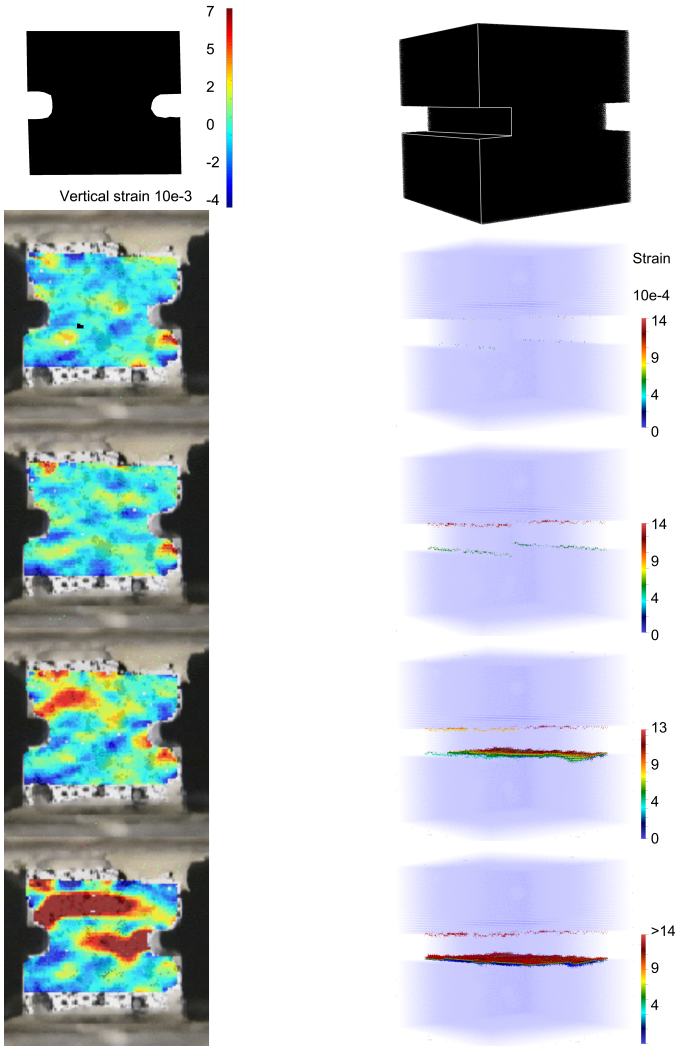

Figure 4.5: Crack propagation from vertical displacements a) in DIC analysis and b) in the simulations.

The outcome was then used to simulate uniaxial tensile tests on several data sets through lattice fracture model. An upscaling procedure exists to successively use the outcome of lower scales as input for lattice elements at the next scale [232, 257]. Nevertheless, the latter requires that a statistically signifcant number of locations are tested, namely 10 as shown in [266]. In Chapter 3 only 6 data sets were used. Furthermore, this upscaling procedure is usually enacted by using input obtained by simulating virtual samples at the prior scale with the same dimensions as the elemental size of the upper scale. Because of the aforementioned reasons, in this work the ratio between properties at the IZ-II and in the bulk cement paste is used instead as input. This has been done before in [217]. The

ratios were used to obtain the linear-elastic properties of IZ-II relative to those fitted for the CP as explained above (see Table 4.2).

Table 4.2: Properties of CP, IZ-II and PLA-II lattice elements.

Phase	Samples total	Sample	E [MPa]	ν	G [MPa]	f_t [MPa]	f_c [MPa]
CP	1	1	5800	0.2	2417	2.75	27.5
PLA-II	1	1	4400	0.3	1692	50	50
IZ-II	6	1	4204	0.2	1752	0.4428	4.428
		2	6990	0.2	2913	3.1814	31.814
		3	6757	0.2	2817	2.7044	27.044
		4	6353	0.2	2647	2.0891	20.891
		5	6040	0.2	2517	1.7580	17.58
		6	9249	0.2	3854	5.9069	59.069

Via μCT, the mesostructures of SH-II samples were segmented via grey-scale thresholding. In this way, air content and PLA-II capsules were separately distinguished from the cement paste phase. The segmentation results are reported in Figure 4.6. The volume fraction of PLA-II capsules was 3.72, 4.35 and 3.86% for SH-II 1, 2 and 3, respectively.

Regarding the properties of PLA-II elements, in this chapter, values found in the literature for similarly produced PLA [267] are used, which are reported in Table 4.2.

4.4.2 Validation of the model

A lattice mesh consisting of 942400 nodes and 7167154 elements was generated to simulate the uniaxial tensile behaviour of the sample SH-II 2 with dimensions as in the scheme shown in Figure 4.1a. An overlay procedure as described in Section 4.3 was used to model the segmented mesostructure of sample SH-II 2. Since the resolution of the μCT was 11 μm whereas the lattice nodes resolution is 100 μm, the reconstructed scans where downscaled with interpolation, which resulted in a reduction of total volumetric fraction of PLA-II capsules from 4.35 to 3.5%.

Different scenarios were considered for the simulation of fracture in capsule-based self-healing cement paste to understand the mechanical interactions between the different mechanical phases considered. For benchmark case 1, the capsules were considered to not be physically bonded with the cement paste and the existence of the influence zone is neglected. In terms of lattice discretization this was enacted by eliminating the lattice elements in correspondence of the capsules as if they were macropores. In case 2, the capsules were still modelled as macropores, but this time the influence zone generated around the capsules was considered. As explained in the previous section, the micromechanical properties of 6 influence zone locations were obtained in the previous Chapter. These 6 datasets were assigned randomly to the elements surrounding the void where the PLA-II capsule is considered to be. The last case (3) considered the capsule to be in contact with cement paste and the existence of the influence zone. In terms of lattice discretization, the discrete elements belonging to the capsule domain were assigned PLA properties and the interface elements between capsule and cement paste were assigned the IZ-II datasets as explained for case 2. The experimental Stress-Strain curves and the simulated ones for the three

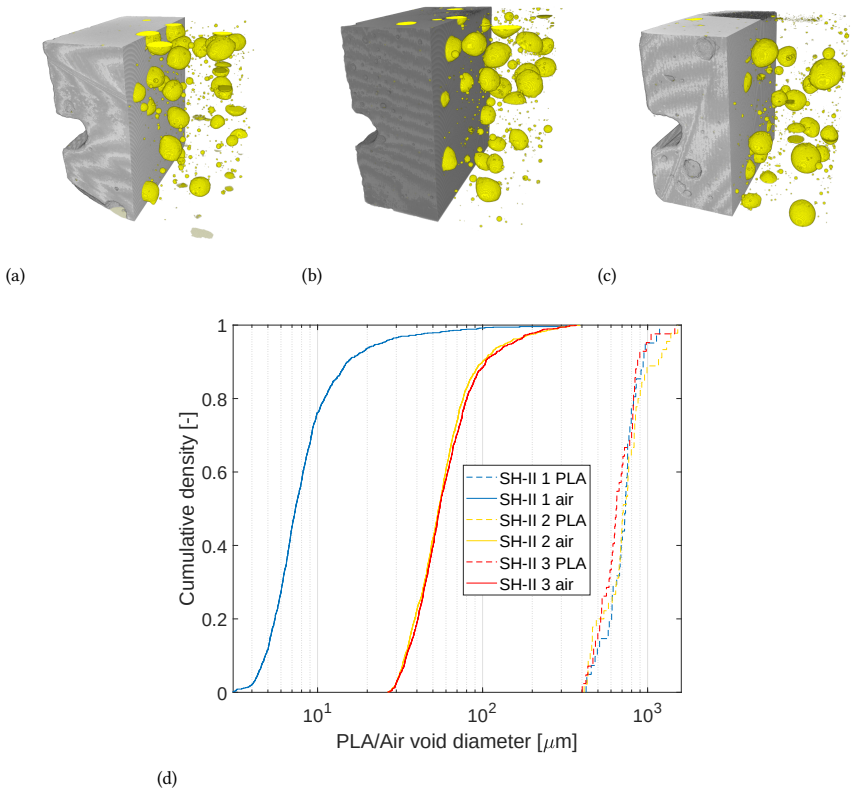

Figure 4.6: Segmentation of airvoids and PLA capsules in SH-II samples imaged from X-ray CT (a), b) and c)) and airvoid size distribution d).

aforementioned scenarios are reported in Figures 4.7a, 4.7b and 4.7c, as well as a summary of tensile strengths and elastic moduli is shown in Table 4.3.

Table 4.3: Summary of mechanical properties obtained from UTT experiments and simulated cases for validation.

Result type	Sample	Notes	E [MPa]	f_t [MPa]
Experimental	1	-	6920	1.942
	2	-	10371	2.288
	3	-	9300	1.998
Simulated	2	void (sim 1)	10471	1.810
		void + IZ-II properties (sim 2)	10566	1.873
		capsule + IZ-II properties (sim 3)	10891	2.071

From the experimental results it can be observed that the average tensile strength of SH-II samples (2.076 MPa) is only slightly lower than the reference CP (as reported

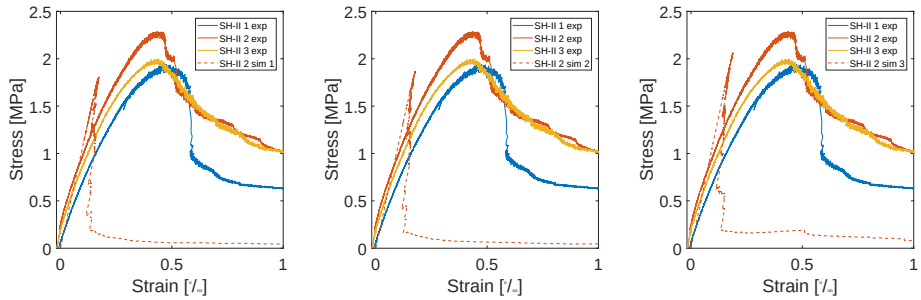

Figure 4.7: Comparison of experimental UTT for samples SH-II 1, 2 and 3 and lattice simulated UTT for sample SH-II 2 for benchmark cases a) 1, b) 2 and c)3.

in Table 4.1). A decrease on the average elastic modulus was also found for SH-II when compared to CP. Although, since only the mesostructure of SH-II 2 was chosen randomly to simulate the UTT, the following discussion pertains to the comparison between the experimental results of SH-II 2 and the different simulated case scenarios.

The simulated moduli of elasticity seem to be slightly overestimated with respect to the experimental results for all considered cases ($0.9 - 5\%$). But as in the experiments, the simulated secant moduli of elasticity decrease when either voids or PLA-II capsules are present in the cement paste for the studied dosage, compared to the CP sample. This holds also when the IZ-II properties are used as input for the interface elements. It has been largely established theoretically and empirically that there exists a direct relationship between the density of the components of heterogeneous materials and their static elastic modulus [268, 269]. This is accurately captured in the lattice simulated results in the cases 1 and 2 due to the presence of discretized voids that overall decrease the stiffness of the mesh. In case 3, the decrease in stiffness with respect to the simulated cement paste is mainly due to the assignment of the E modulus of the PLA-II for the respective lattice elements, which is lower than the E modulus assigned for cement paste elements. Among the different considered scenarios, the E moduli followed the trend $E_1 < E_2 < E_3$. Although in both cases 1 and 2, the PLA capsules were considered as detached from the cement paste and not contributing mechanically to the overall behaviour, differences were observed among the resulting elastic moduli. In fact, when the interface elements surrounding the capsules voids were assigned the IZ-II properties (in average stiffer than the reference cement paste), the obtained elastic modulus modestly increases by 0.9%. If cases 2 and 3 are compared instead, it can be seen that the inclusion of the capsules leads to a further increase in the elastic modulus of 3%, again related to the substition of the void by PLA-II type elements which provide additional stiffness to the lattice mesh in contrast to the presence of voids. The simulated case scenarios 1, 2 and 3 seemed to underestimate the tensile strength of SH-II 2 by 21.6, 18.1 and 9.5%, respectively. Furthermore, the simulated tensile strengths seem to be at least slightly lower than the tensile strength of the reference cement paste. The results point out that the assignment of IZ-II micromechanical properties to the interface elements surrounding the capsules, considered as voids, leads to an increase

of 3.5% in the tensile strength of the self-healing composite in simulated case scenario 2, when compared to that of case 1. Finally, it is shown that when the PLA-II capsules are considered to contribute mechanically to the tensile response of the composite in simulated case 3, the strength is increased by 10% with respect to case 2. Furthermore, the explicit modelling of influence zone and PLA particles resulted in a higher residual stress relative not only to case 1 and case 2, but also to the simulated reference cement paste.

When comparing the crack nucleation and propagation derived from each individual simulated case (Figures 4.8b-4.8d) to the DIC analysis (Figure 4.8a), some insights into the mechanisms of failure can be proposed. In the linear elastic phase, damage occurs in several isolated lattice elements exclusively along the edges of the notches of the virtual sample modeled as in case 1, followed by concentration of damage at the same location in the nonlinear elastic part of the curve. In this benchmark situation, in which the material is considered to be isotropic, it was expected that the crack nucleation was triggered by geometric stress concentration. On the other hand, in both case 2 and case 3 the first damaged elements are located at the interface between voids (in case 2)/ capsules (in case 3) and the cement paste. In the latter cases, after the aforementioned damage, more stress concentrates along the edges of the notches as can be understood from the widespread cracking in elements at that location at the onset of the nonlinear elastic phase. Since some interface lattice elements present micromechanical properties which are lower than those of the surrounding cement paste elements, some microcracking occurs in this phase first in the simulated sample. Notwithstanding, the critical location from which a well localized crack is developed is the notch edge as in case 1. In the DIC analysis of the experimental sample, the same behaviour is observed.

In the DIC results, after the peak stress two cracks are developed at different moments on opposite notches and propagation occurs from one and the other alternatively until no more load-carrying area is available. It is worth noticing that in the DIC analysis, both cracks seem to deviate around a PLA-II capsule, as it can be observed in the final 3D fracture (Figure 4.8e). The post-peak crack propagations for case 1 and case 2 are very similar: one crack propagates steadily from one of the notches showing little tortuosity across the voids (representing the capsules). When capsules are explicitely discretized, like in case 3, first a main crack developes from one of the notches, branching through the interface elements and around the capsules (with higher elemental tensile and compressive strength than cement paste or IZ-II) and thus presenting a more tortuous crack pattern. This main crack still propagates mainly in a plane perpendicular to the imposed displacement direction and the crack deviations occur exclusively around capsules that encounter such plane. In the softening plateau, more damage concentrates around a specific capsule which upper interface is located in the crack path. A secondary crack develops and propagates from the lower interface elements before the main crack further propagates until failure.

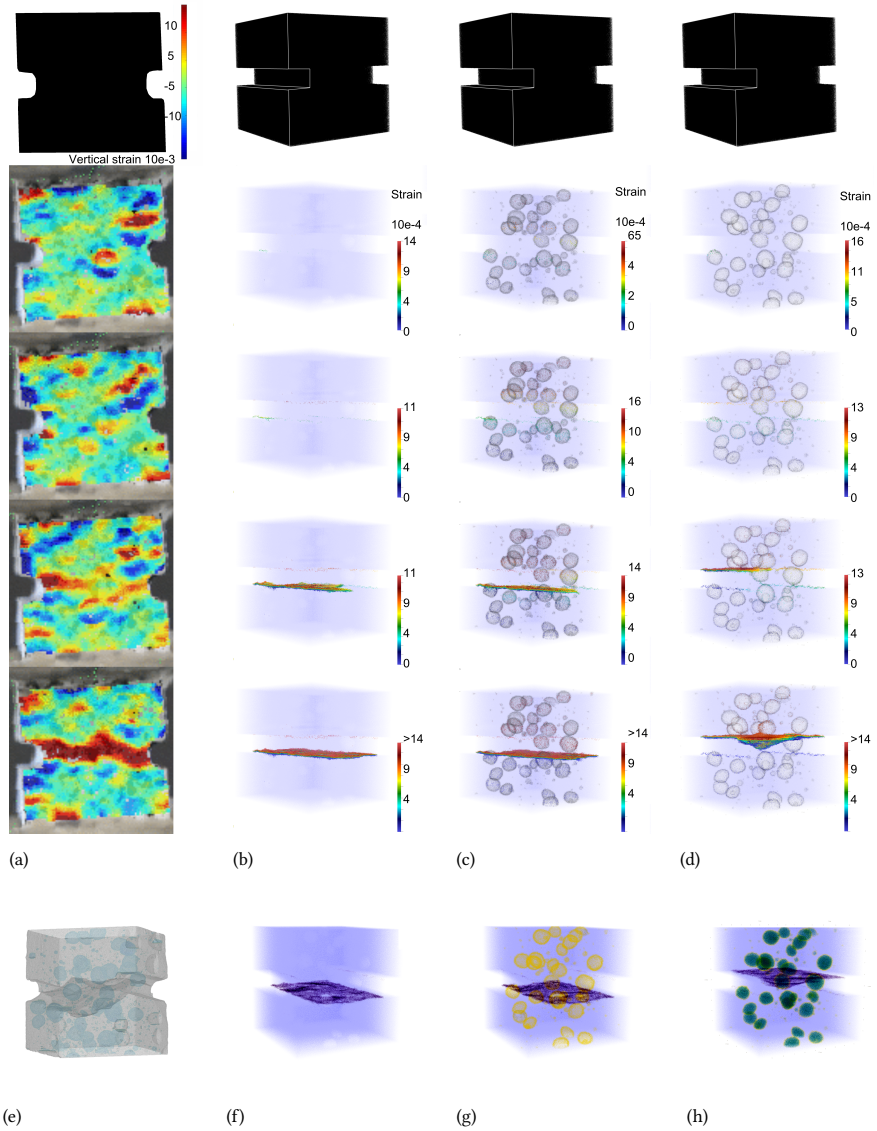

Figure 4.8: Crack propagation in SH-II 2 from vertical displacements a) in DIC analysis and in simulations for b) case 1, c) case 2 and d) case 3 and final fracture surfaces from e) μCT, f) simulated case 1, g) simulated case 2 and h) simulated case 3.

Among the different simulated scenarios, it results obvious that case 3 better approximates the behaviour of SH-II 2 if both the elastic modulus and the tensile strength are used as validating properties. Therefore the hypothesis of full contact between PLA-II capsules and surrounding cement paste is assumed for further analyses.

4.5 Parametric study

In this section a numerical investigation of the validated capsule-based self-healing cement paste material is undertaken. The influence of capsules dosage, size, shape and influence zone micromechanical properties on the uniaxial tensile behaviour of the composite as well as on the exposure of said capsules is studied. Specifically on the mechanical behaviour of the heterogeneous material, the Stress-Strain curve, microcracking and final fracture are analyzed and discussed based on a specific parameter that is being varied. In an analogous manner, also the amount of particles encountered by the final fracture is quantified. Only a limited combination of parameters is studied in this section to better focus on the influence of individually analyzed parameters. A more complete parametric analysis is offered in the following section instead.

For a better understanding of the analyses, the virtual samples have been named following the formula PLAxsydzpw, where:

- PLA stands for the shape of the particle and x assumes value 1 or 2 for irregular or spherical, respectively.
- s stands for the size range and y assumes value 1, 2 or 3 for the smallest, medium and largest particle size ranges herein studied, respectively.
- d stands for the dosage and z assumes value 1, 2 or 3 for the smallest, medium and largest dosages herein studied, respectively.
- p stands for the influence zone properties set and w assumes value 1, 2 or 3 for $IZ-I$, $-II$ and $-III$ as obtained from Chapter 3, respectively.

4.5.1 Influence of dosage

The dosage of capsules is of paramount importance when designing a self-healing system. The amount of healing agent in the capsules needs to be sufficient to perform the prescribed amount of healing cycles. Nevertheless, an optimized capsules dosage is needed to limit the cost per kg of material and to minimize the reduction on the mechanical properties. A particle packing algorithm was implemented in MATLAB to park non-overlapping spheres in a quadrangular grid with characteristic size of 100 μm and cubic domain of 10 mm side as in the meshes used for the simulations. Equal parts of spheres from sieves with diameters $1201-1400$ μm, $1401-1600$ μm, $1601-1800$ μm and $1801-2000$ μm were generated. An overlay procedure followed to assign the micromechanical properties to elements belonging to the spherical PLA-II particles and influence zone IZ-II as described in Section 4.3. Three mesostructures with different capsule dosages were studied, namely 1.3, 2.6 and 3.9 % by weight of cement, equivalent to volumetric fractions of 1.52, 2.99 and 4.42 %, respectively. Such optimal dosages were suggested by [220] who studied bacteria-based self-healing effect in mortar with the studied capsules.

In Figure 4.9 the results from simulated uniaxial tensile test on the three mesostructures are presented. In Figure 4.9a and 4.9b, the Stress-Strain curves and a zoom in of the vicinity of the peaks are shown. Instead, the simulated mesostructure, pre-peak microcracking and final fracture are shown in Figures 4.9c to 4.9k. The simulated E moduli, tensile strength and number of cracked elements at the peak stress and at a strain of 0.25 ‰, for the influence zone and the cement paste phases, are summarized in Table 4.4.

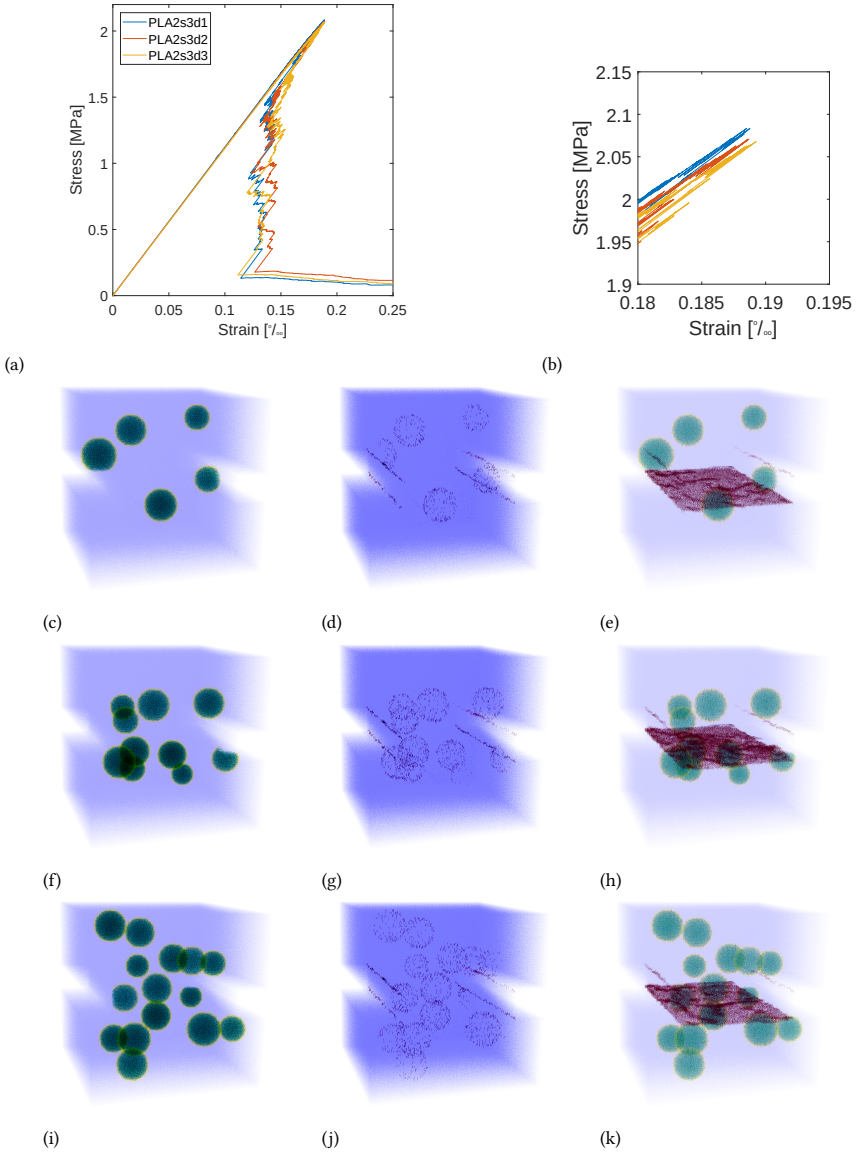

Figure 4.9: Simulation results for cement paste samples with PLA-II spherical capsules with diameter $601-1000\ \mu m$ for different dosages: Stress-Strain curve a); mesostructure c, f, i, microcracking at the peak load d, g, j and final fracture e, h, k for capsules dosage of 1.3, 2.6 and 3.9 % by weight of cement, respectively.

It can be seen from the mesostructures shown in Figure 4.9c, 4.9f and 4.9i that the random parking of the spherical capsules can result in uneven or even spatial distributions which can well represent what would happen in a real cement paste sample. Depending on the notched section and capsule dimensions, it is expected that the amount of capsules at that location is more or less the same above a certain dosage, as it seems to be the

Table 4.4: Summary of mechanical properties obtained from simulations on virtual samples with different capsules dosages.

Sample	E [MPa]	f_t [MPa]	Elements cracked at peak		Elements cracked at $\varepsilon = 0.25$ ‰	
			CP	IZ	CP	IZ
PLA2s3d1p2	11036	2.083	1680	757	42242	1486
PLA2s3d2p2	10974	2.071	1660	1690	46447	3053
PLA2s3d3p2	10927	2.068	1732	2214	41484	2847

case for PLA2s3d2 and PLA2s3d3. Regarding the pre-peak behaviour among samples with different dosage of the PLA-II capsules, a few differences can be observed. It can be said that increasing the amount of said capsules with same dimensions and influence zone mechanical properties results in more widespread microcracking before the peak stress is achieved (see Figure 4.9d, 4.9g and 4.9j). Distinctions between cracked elements for different phases (Table 4.4) show that whereas the amount of failed lattice elements in cement paste (mainly localized along the notches edges) does not change significantly when adding more capsules, the amount of cracked influence zone elements swiftly increases.

For the modulus of elasticity, it was found that increasing the dosage of PLA-II capsules slightly decreases the stiffness. As of the tensile strength, it is noticeable that although the inclusion of increasing capsules dosages up to 3.9 % (by weight of cement) results in consistent tensile strength drops with respect to plain cement paste, this amounts to less than 2 % for the highest dosage herein investigated. Due to the linear-elastic constitutive law herein used and the choice of homogeneous mechanical properties for the cement paste phase, the post-peak behaviour of all simulated samples is characterized by a steep strain-softening branch. The latter effect is less marked as a higher number of influence zone elements is cracked in the post peak stage as it can be deduced from Table 4.4. The residual stress at a strain of 0.25 ‰seems to follow the opposite trend instead.

As the bacteria-embedded PLA capsules just need to be exposed (breakage is not needed), herein it is considered that the crack propagation along the influence zone elements is sufficient to activate the self-healing mechanism. Under this criterion a total of 2, 3 and 3 capsules were exposed in the crack surface according to the simulations for PLA2s3d1p2, PLA2s3d2p2 and PLA2s3d3p2, respectively. Although the specimen is quite small compared to the capsule size, it clearly shows that with the increase in capsule number, more capsules are exposed, which is expected and in line with the literature [184].

4.5.2 Influence of capsule dimensions

The choice of capsule dimensions is less of a self-healing concrete design constraint and more of a technological one. Notwithstanding, its effect on the mechanical behaviour of the composite is usually important [251], with influence levels depending on the capsule properties. Same sphere packing algorithm was used in this section to generate three different mesostructures with 3.9 % of PLA-II capsules by weight of cement. Three different particle diameter ranges were used for the mesostructures: $200-601$ μm, $601-1200$ μm and $1201-2000$ μm. For each diameter range, equal volume fractions were graded every 200 μm.

In Figure 4.10 the results from simulated uniaxial tensile test on the three mesostructures are presented. In Figure 4.10a and 4.10b, the Stress-Strain curves and a zoom in of the vicinity of the peaks are shown. Furthermore, the simulated mesostructures, pre-peak microcracking and final fracture are shown in Figures 4.9c to 4.10k. The simulated E moduli, tensile strength and number of cracked elements at the peak stress and at a strain of 0.25 ‰, for the influence zone and the cement paste phases, are summarized in Table 4.5. As shown in the mesostructures in Figure 4.10c, 4.10f and 4.10i, using smaller capsules for the same dosage increases the likelihood of having more particles, thus more specific surface area, at the location which is prone to crack (in this case the notched section). As the peak stress is reached, a comparison of microcracking extent can be drawn for the samples with different particle size ranges (Figure 4.10d, 4.10g and 4.10j). As the particles become smaller, there seems to be a more even distribution of microcracks at the influence zone. Moreover, as can be observed from Table 4.5, the number of cracked elements at the influence zone until the peak stress is reached increases by a factor of 1.7 from PLA2s3d3p2 to PLA2s2d3p2 and it is doubled up to PLA2s1d3p2. Regarding the elastic moduli, there seems to be no clear trend as the average particle size is increased. It is worth noticing that adding 3.9 % of PLA-II as in PLA2s1d3p2, PLA2s2d3p2 and PLA2s3d3p2 resulted in an increase of the E modulus when compared to the simulated SH-II (Section 4.4.2), where a wider size range ($200 - 1000\ \mu m$) was used. Instead the influence of particle size PLA-II capsules on the tensile strength results more substantial. Increasing the average particle size from 400 to 900 μm already results in a decrease of 5 % of the tensile strength, while further increasing the average particle size to 1600 μm does not result in additional tensile strength changes. When comparing the tensile strength of PLA2s1d3p2 and PLA2s2d3p2 to the SH-II paste, it can be said that tending to uniformly smaller capsules leads to higher tensile strength. As for the post-peak behaviour, the particles average size seems to be a significant parameter. It is noticeable that the residual stress at a strain of 0.25 ‰increases for smaller PLA-II particles. A clear trend is found among the simulated mesostructures through the number of cracked elements in the influence zone from the peak strain to a strain of 0.25 ‰. The number of failed elements in the post-peak increases significantly as the simulated particles become smaller which indicates a higher work of fracture.

The potential volume of healing products for this self-healing system is proportional to the volume of the particles as described in [154]. Furthermore, since the average particle size is different for the studied mesostructures studied in this section (PLA2s1d3p2, PLA2s2d3p2 and PLA3s3d3p2), the volume of the PLA-II particles exposed in the crack is used to estimate the influence of particle size on the potential efficiency of the self-healing mechanism.

The number of exposed particles was 18, 14 and 3 for PLA2s1d3p2, PLA2s2d3p2 and PLA3s3d3p2, respectively. The latter is equivalent to a volume of particles in the crack of 0.6, 5.34 and 6.43 mm^3. For the simulated mesostructures, the results point out that increasing the capsules size in the studied range potentially increases the volume of healing agents, which is in agreement with the results found in [252]. Notwithstanding, while increasing the particles diameter from 400 μm to 900 μm, for a dosage of 3.9 % of PLA-II by weight of cement, the healing potential increased eightfold. A further size increase from 900 μm to 1600 μm may not change the healing potential as much (20 %).

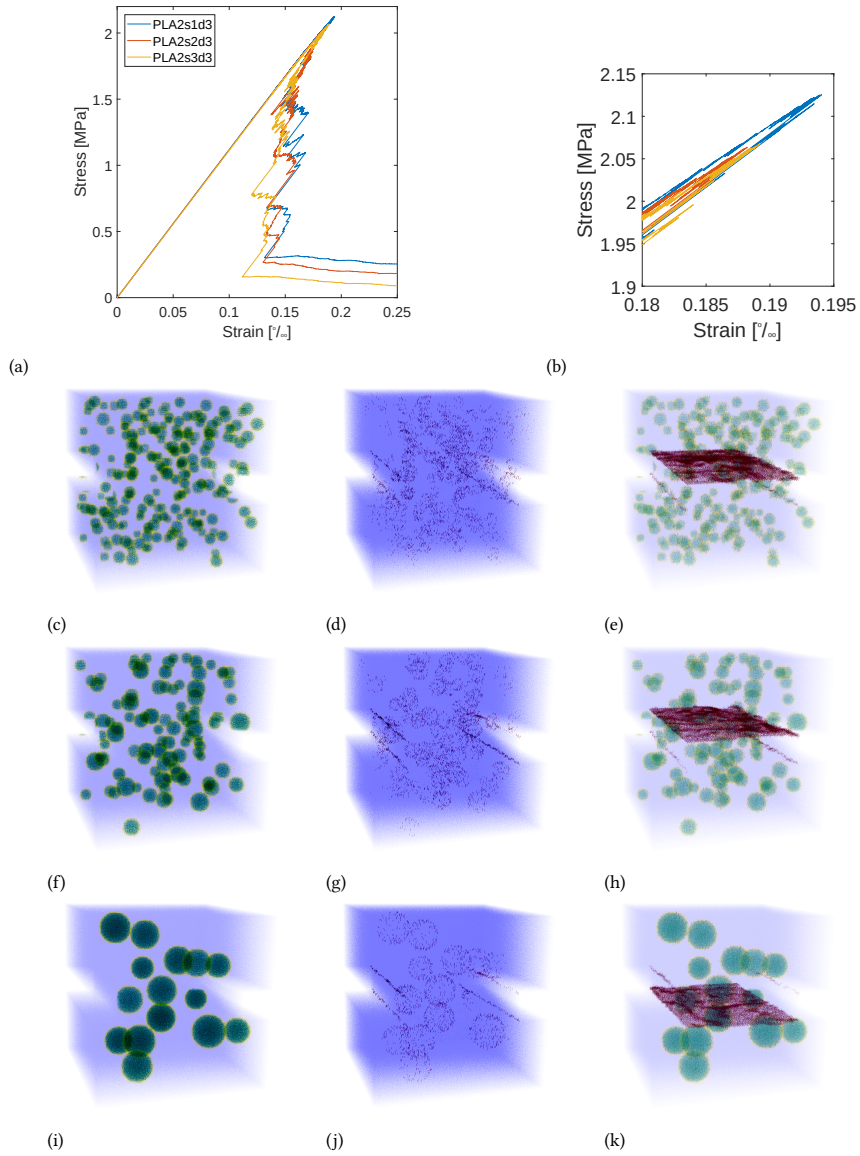

Figure 4.10: Simulation results for cement paste samples with PLA-II spherical capsules with dosage of 3.9 % by weight of cement for different diameter ranges: Stress-Strain curve a); mesostructure c, f, i, microcracking at the peak load d, g, j and final fracture e, h, k for capsules diameter ranges $200-600\ \mu m$, $601-1200\ \mu m$ and $1201-2000\ \mu m$, respectively.

Table 4.5: Summary of mechanical properties obtained from simulations on virtual samples with different capsules dimensions.

Sample	E [MPa]	f_t [MPa]	Elements cracked at peak		Elements cracked at $\varepsilon = 0.25$ ‰	
			CP	IZ	CP	IZ
PLA2s1d3p2	10953	2.125	1980	5077	45057	8739
PLA2s2d3p2	10964	2.064	1601	3781	40724	6676
PLA2s3d3p2	10927	2.068	1732	2214	41484	2847

4.5.3 Influence of interface properties with respect to bulk properties

The interface transition zone is typically referred to as the often-disturbed cement paste or mortar around sand grains or coarse aggregates, respectively. These regions, ranging between $30-50$ μm thickness, have been throughly studied in the literature and characterized with respect to their porosity, hydration degree, micromechanical propeties, etc., as well as their influence on the overall mechanical behaviour of mortar and concrete [270, 271]. In an analogous way, the region surrounding capsules in self-healing cementitious materials needs to be studied and characterized to more accurately describe the mechanical behaviour of the self-healing composites. In the case of bacteria-embedded PLA capsules, it has been shown previously in [259] that this transition zone, herein called influence zone, can be far more extensive (up to 350 μm). In this section the same mesostructure containing 3.9 % of spherical capsules by weight of cement and diameter in the range $1201-2000$ μm was used to simulate uniaxial tensile test for different sets of properties of the influence zone according to the results presented in Chapter 3. The same procedure described in Section 4.4.1 was used here to obtain 6 sets of input properties for each influence zone I and III, which results can be found in Table 4.6.

As discussed in Chapter 3, the values of tensile strength of the influence zone for different particle types presented high scatter in general, more so for IZ-II and IZ-III when compared to bulk cement paste and IZ-I. Furthermore, the median of the relative tensile strengths (with respect to CP) indicated the following trend: $f_{t,IZ-III} < f_{t,IZ-I} < f_{t,IZ-II}$. Regarding the modulus of elasticity of the different influence zones, the trend was instead: $E_{IZ-I} < E_{IZ-III} < E_{IZ-II}$. The scatter of this property was more relevant for IZ-I and IZ-II when compared to CP and IZ-III.

In Figure 4.11 the results from simulated uniaxial tensile tests on the three simulated samples are presented. In Figure 4.11a and 4.11b, the Stress-Strain curves and a zoom in of the vicinity of the peaks are shown. As usual, the simulated mesostructure, pre-peak microcracking and final fracture are shown in Figures 4.11c to 4.11k. The simulated E moduli, tensile strength and number of cracked elements at the peak stress and at a strain of 0.25 ‰, for the influence zone and the cement paste phases, are summarized in Table 4.7.

Some similarities and differences can be observed among the pre-peak behaviours of a same mesostructure when using different sets of properties for the influence zone. As can be noticed in Figure 4.11d, 4.11g and 4.11j, the distributions of cracked elements are very similar, with cracks occurying mainly along the notch edges and around the capsules in correspondence of the interface elements. Notwithstanding, it is evident that a far greater

Table 4.6: Properties of IZ-I and IZ-III lattice elements.

IZ type	Sample	E [MPa]	ν	G [MPa]	f_t [MPa]	f_c [MPa]
IZ-I	1	5991	0.2	2496	2.2210	22.210
	2	7165	0.2	2985	1.8776	18.776
	3	2756	0.2	1149	0.5393	5.393
	4	4207	0.2	1753	1.3249	13.249
	5	5010	0.2	2087	1.6677	16.677
	6	5165	0.2	2152	1.5867	15.867
IZ-III	1	5339	0.2	2225	0.9113	9.113
	2	4189	0.2	1746	1.2071	12.071
	3	6187	0.2	2578	2.2003	22.003
	4	4514	0.2	1881	0.5750	5.750
	5	5422	0.2	2259	0.3443	3.443
	6	5987	0.2	2495	2.86	28.6

number of interface influence zone elements failed at the peak stress for PLA2s3d3p2 and PLA2s3d3p3 when compared to PLA2s3d3p1 (also observable from Table 4.7). The latter trend can be correlated to the trend followed by the tensile strength lower limits of the different influence zones. Moreover, clear fracture localization can be observed at the left notch of both PLA2s3d3p1 and PLA2s3d3p3 where the damaged elements at the notch edge and around neighbouring capsule influence zone have coalesced.

Regarding the elastic modulus the composites exhibited the following trend: $E_{IZ-III} < E_{IZ-I} < E_{IZ-II}$. If the latter trend is compared to that followed by the average and median elastic moduli of the influence zones obtained in [259], it can be observed that the trend is reversed between PLA2s3d3p1 and PLA2s3d3p3. These results suggest that the elastic modulus of the capsule-containing composite is more influenced by the upper limit of the elemental elastic modulus rather than by the average value. The different IZ types had a noticeable influence on the tensile strength of the composites. The same trend followed by the median tensile strengths of the influence zones was found for the cement paste with PLA capsules. Namely, PLA2s3d3p1 and PLA2s3d3p3 had very similar tensile strength, which was about 3 % lower than that of PLA2s3d3p2. Also the post-peak behaviour of the simulated samples are influenced by the properties of the influence zone. In particular, from the number of failed elements in the cement paste and influence zone phases in Table 4.7, it can be observed that to propagate the fracture a larger number of cement paste elements had to fail in PLA2s3d3p1 and PLA2s3d3p3, with respect to PLA2s3d3p2. Furthermore, the presence of a stronger interface in the latter sample corresponded to a smaller number of failed influence zone elements relative to the other two samples with IZ-I and IZ-III. Moroever, among the latter samples the number of failed elements in the postpeak increased of a 12 % from PLA2s3d3p1 to PLA2s3d3p3.

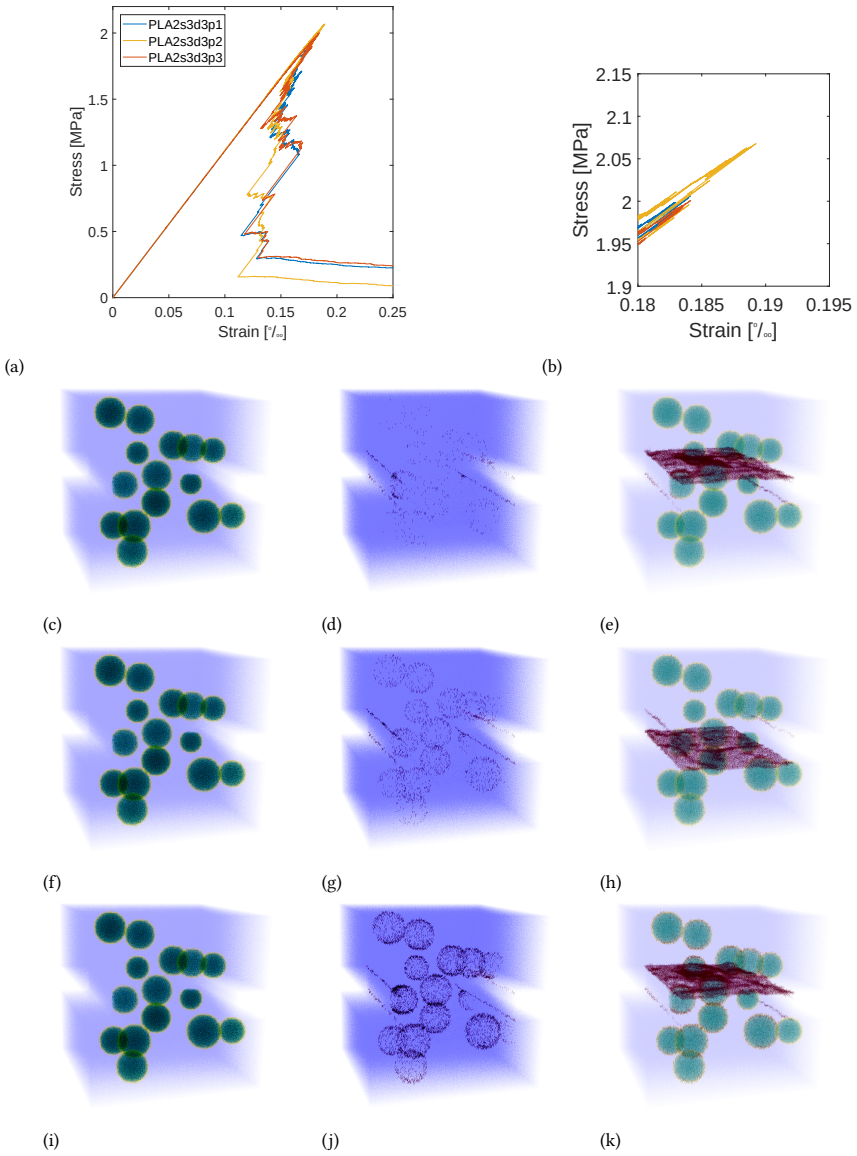

Figure 4.11: Simulation results for cement paste samples with spherical capsules with dosage of 3.9 % by weight of cement, with diameter $1201-2000\ \mu m$, for different influence zone properties: Stress-Strain curve a); mesostructure c, f, i, microcracking at the peak load d, g, j and final fracture e, h, k for properties of the influence zone IZ-I, IZ-II and IZ-III, respectively.

Four, three and five capsules were exposed in the crack in PLA2s3d3p1, PLA2s3d3p2 and PLA2s3d3p3, respectively. The latter results suggest that the higher energy dissipation in the post-peak stage corresponded to longer crack paths around more and more capsules with interfaces IZ-I and IZ-III, respectively.

Table 4.7: Summary of mechanical properties obtained from simulations on virtual samples with different influence zone properties.

Sample	E [MPa]	f_t [MPa]	Elements cracked at peak		Elements cracked at $\varepsilon = 0.25$ ‰	
			CP	IZ	CP	IZ
PLA2s3d3p1	10897	2.006	1444	1310	43041	5197
PLA2s3d3p2	10927	2.068	1732	2214	41484	2847
PLA2s3d3p3	10867	2.001	1307	8376	43104	12767

4.5.4 Influence of capsule shape

The shape of the capsules, specially for PLA, is more often a consequence of production process rather than a design choice. Nevertheless its effect on the mechanical behaviour of the self-healing composite deserves attention. It has been shown in the literature [272] that the shape of aggregates influences some mechanical properties of concrete. Two different mesostructures were studied in this section to investigate numerically the influence of PLA-II shape on the tensile behaviour of the composite. The latter mesostructures contained the same dosage of PLA-II particles (2.6 %) and characteristic size range ($601 - 1200\ \mu m$). The first mesostructure, PLA1s2d2p2, was generated using the algorithm package Anm [20]. The package is composed of various databases for irregular sand particles, of which the crushed sand EN196-1 (666 particles) was used in this work. From such database, Anm can extract all sort of 3D geometrical properties and modify the particles depending on the specified sieve sizes and dosages. A complex non-overlapping parking procedure follows the previous step, for which scaling and rotation allow the creation of a tailored mesostructure of irregular particles. Specifically for PLA1s2d2p2 one unique sieve size was created with range as specified above. The second mesostructure, PLA2s2d2p2 was generated using the spherical particles parking algorithm from which a description was offered in a previous section.

In Figure 4.12 the results from simulated uniaxial tensile test on the two simulated samples are presented. In Figure 4.12a and 4.12b, the Stress-Strain curves and a zoom in of the vicinity of the peaks are shown. As usual, the simulated mesostructure, pre-peak microcracking and final fracture are shown in Figures 4.12c to 4.12h. The simulated E moduli, tensile strength and number of cracked elements at the peak stress and at a strain of 0.25 ‰, for the influence zone and the cement paste phases, are summarized in Table 4.8.

From the pre-peak microcracking, shown for the different mesostructures in Figure 4.12d and 4.12g, and from the values in Table 4.8 it can be inferred that a more distributed and higher amount of lattice elements failed prior to the peak stress in PLA1s2d2p2. A logical explanation is the existence of a higher surface area of PLA particles and thus of influence zone element number. Again the pre-peak failed cement paste elements were roughly the same in both mesostructures as they exclusively concentrated along the edges of the notches. The elastic moduli and tensile strengths were very similar for both samples, with PLA2s2d2p2 having slightly lower values than the PLA1s2d2p2. It has been found before that the shape of coarse aggregates does not influence the latter properties for weak regular interfaces, whereas for strongly bonded aggregates concrete with irregular shaped aggregates presented higher values of both E modulus and tensile strength [272].

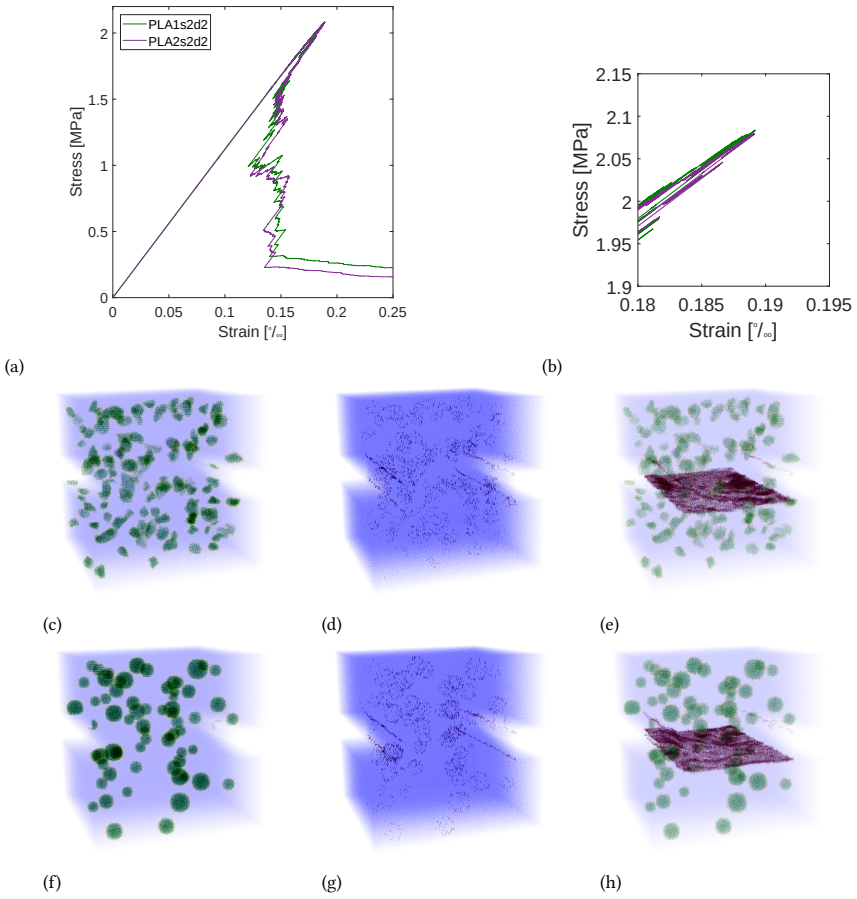

Figure 4.12: Simulation results for cement paste samples with PLA-II capsules with dosage of 2.6 % by weight of cement and with sieve diameter $601 - 1000\ \mu m$ for different capsule shapes: Stress-Strain curve a); mesostructure c), f), microcracking at the peak load d), g) and final fracture e), h) for irregular and spherical-shape capsules, respectively.

Important differences were found among the studied mesostructures when it came to the post-peak behaviour. The residual stress at a strain of 0.25 ‰ seemed to be substantially different with the paste containing spherical PLA particles presenting a residual stress 23 % lower than that of the paste with irregular PLA particles. Furthermore the number of elements failed after the peak until a strain of 0.25 ‰, which could be correlated to the amount of dissipated energy during fracture propagation, seems to be significantly higher for the cement paste with irregular PLA particles, not only due to dissipation at the influence zone but specially in cement paste elements. This simulated behaviour represents well the increased fracture path encountered in heterogeneous materials where the surface area of the heterogeneities is higher.

Regarding the exposed self-healing particles, the paste with irregular particles had 9 PLA particles along the fracture against 8 for the paste with spherical aggregates. The

difference is not substantial and could be altered by the distribution of the particles in real samples. Yet the number of failed influence zone elements in Table 4.8 directly correlates to the surface area of particles directly exposed in the fracture which very likely influences the dissolution kinetics and thus the rate of release of the healing agents.

Table 4.8: Summary of mechanical properties obtained from simulations on virtual samples with different capsule shapes.

Sample	E [MPa]	f_t [MPa]	Elements cracked at peak		Elements cracked at $\varepsilon = 0.25$ ‰	
			CP	IZ	CP	IZ
PLA1s2d2p2	11015	2.084	1663	3309	46501	6297
PLA2s2d2p2	11001	2.080	1608	2828	41161	4889

4.5.5 Discussion

In the previous sections an analysis was offered of the influence of individual parameters on the mechanical behaviour and particles activation in self-healing cement paste containing bacteria-embedded PLA capsules. Namely, the dosage, dimensions and shape of the capsules, as well as the properties of the interface between paste and capsule were studied one at the time. The former analyses apply only to the specific combination of multiple parameters used and can be regarded as showcase on how the presented model can be used to study capsule-based self-healing systems. In this section, a more extensive parametric study is presented on the mechanical behaviour of the composite material until the peak stress for all combinations of the studied parameters (within the previous limits). Analysis of the post-peak behaviour as well was not pursued due to the extensive computational time needed to carry out all simulations.

The surface plots of the simulated elastic moduli for different combinations of dosage and size of the PLA particles are shown in Figure 4.13a, 4.13c and 4.13e when PLA with IZ-I, -II or -III are used, respectively. In general, the properties of the influence zone modestly influence the elastic modulus. For the studied ranges of the parameters, E can decrease as much as 4 %, or increase up to 1 % when compared to the reference cement paste. Regarding the trends encountered when different influence zone properties sets are used, some similarities and differences can be found. Although in different proportions, for all studied influence zone properties sets, the elastic moduli either stays the same as the cement paste or slightly increases when the smallest particles and lowest dosage of PLA is used. It is expected that a lower dosage of (less stiff) PLA particles leads to smaller changes on the elastic modulus of the composite with respect to that of plain cement paste. On the other hand, logic would dictate that smaller particles, for the same (lowest) dosage, would entail a higher number of influence zone lattice elements. The latter elements had large standard deviation on the elastic moduli for all the studied PLA particles as shown in [259]. Furthermore, median and average elastic moduli for IZ-I and IZ-III were lower than the median and average value for cement paste. The fact that higher composite stiffness was obtained for the smallest PLA particles for the low dosage, points out that the influence zone properties do influence the overall elastic modulus of the composite. Moreover, the results point out a heavier influence of the maximum stiffness of the influence zone rather

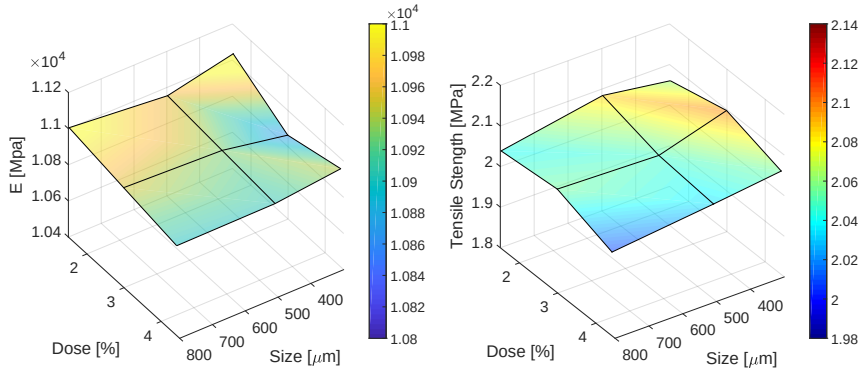

(a) IZ-I (b) IZ-I

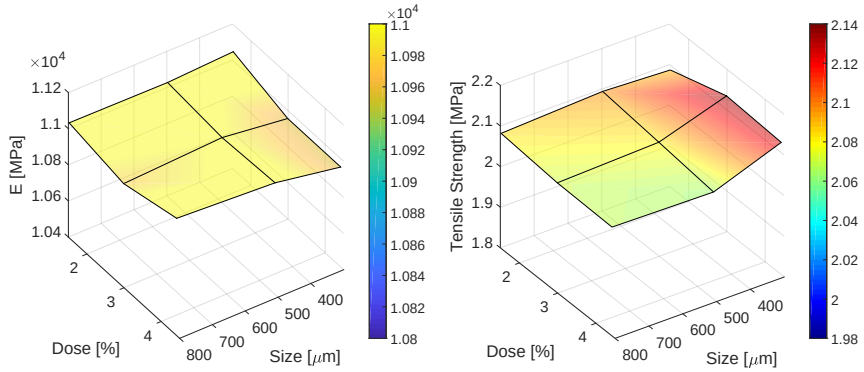

(c) IZ-II (d) IZ-II

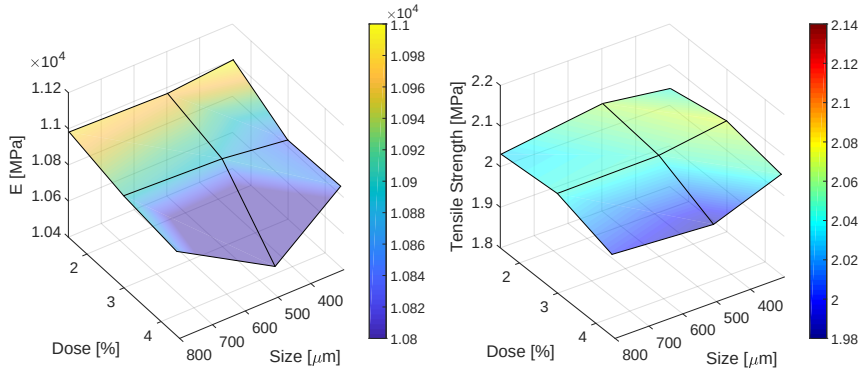

(e) IZ-III (f) IZ-III

Figure 4.13: Parametric plots of mechanical properties E (a, c and e) and f_t (b, d and f) as a function of spherical PLA particles dosage and size for IZ-I, -II and -III, respectively.

than of the median or average values. As explained in [247], the elastic modulus of a heterogeneous brittle material is more influenced by the stiffness of the bridge between phases rather than by the less stiff links. Analyzing the results across the different studied influence zone properties sets, it seems that for a specific size range the elastic modulus tends to decrease for increasing dosage of the particles. The latter behaviour is more and more accentuated when using PLA with IZ-I and PLA with IZ-III, respectively. In fact, both interfaces IZ-I and IZ-III present lower median and average elastic moduli when compared to the cement paste and IZ-II. Specifically, IZ-I presented way higher upper limit of the elastic modulus when compared to IZ-III which may be the reason why the elastic modulus of the composite with PLA with IZ-III is more sensitive to particle dosage and size variations than its counterpart with PLA with IZ-I. For each given dosage, regardeless of the type of IZ simulated, E seems to exhibit a slight minimum or maximum for particles with average diameter of 900 μm. Nevertheless, these results may represent fluctuations due to the close particle sizes herein studied. Comparing the average elastic moduli of composites with different PLA IZ types, it can be observed that $E_{CP+IZ-III} < E_{CP+IZ-I} < E_{CP+IZ-II}$.

In a similar fashion Figure 4.13b, 4.13d and 4.13f report the surface plots of the simulated tensile strengths obtained for the combination of dosage and size of the PLA particles when PLA with IZ-I, -II or -III are used, respectively. As for the elastic modulus, also the tensile strength has been influenced by the introduction of the PLA particles. Due to the higher tensile strength of the PLA particles, reductions on tensile strength of the self-healing composite are limited and mainly due to the presence of the influence zone around such particles. Given the ranges of the studied parameters, the tensile strength was decreased as much as -6% and increased up to 2%. For all IZ properties sets, maximum tensile strength was obtained for a volumetric dosage of 3 % and the smallest studied particles. The minimum tensile strength was achieved when the highest studied dosage and size range were employed. The trends found as the studied parameters were varied depended highly on the type of particle included. Namely, the sensitivity of the tensile strength values for varying dosages and sizes of the PLA particles was greater for pastes with PLA with IZ-III and IZ-I, respectively, when compared to the paste with PLA with IZ-II. For each given size range, either the tensile strength has a local maximum at the mid dosage (as seen for particles with average diameter of 400 μm and 1600 μm) to then decrease at the highest dosage or the strength decreases for increasing dosage. The latter findings suggest that the inclusion of PLA particles in cement paste increases to a certain extent the tensile strength of the composite until a threshold dosage, afterwhich the influence zone properties (in general lower than that of cement paste) overcome the positive effect of the PLA. A similar trend is found for a fixed dosage of particles when increasing the size range of the particles (be it with IZ-I, -II or -III). In fact, the tensile strength of the composites either reaches a maximum for medium sized particles when the dosage is kept at the studied minimum, or slowly decreases when bigger PLA particles are used. Moreover, as shown in Section 4.5.2, a more distributed micro-cracking was encountered in pastes with smaller particles which allowed a delay on the coalescence of damage and propagation of the main crack. In general the average tensile strength for the cement paste with different PLA particles were: $f_{t,CP+IZ-III} < f_{t,CP+IZ-I} < f_{t,CP+IZ-II}$, same trend followed by the elastic modulus. A direct proportion is thus found between influence zone median/average tensile strengths and that of the corresponding composite cement pastes.

4.6 Conclusions

The following conclusions can be drawn from the results presented herein:

- The use of a linear-elastic constitutive law for cement paste elements with uniform material properties yields correct values of the elastic modulus and the tensile strength. The experimentally-observed post-peak behaviour of cement paste is not accurately represented in the simulated results due to the latter constitutive law but also due to the homogeneity of the virtual sample. As a consequence also the simulated fracture surface differs from the experimental one in terms of decreased surface roughness.

- When modelling the tensile behaviour of PLA-containing cement paste, the interface and PLA particle properties need to be explicitely modeled in lattice model context, which suggests good bond between PLA and cement paste, as well as non-negligible impact of the influence zone properties. The ratio between influence properties and bulk cement paste derived from previous study [259] resulted in good agreement between the experimental and simulated elastic moduli and tensile strengths. The explicit modelling of influence zone and PLA particles resulted in a higher residual stress.

- Pre-peak cracking extent is inversely proportional to the lower limit of the tensile strength of the influence zone, while the elastic modulus is higher as the upper limit of the influence zone stiffness increases. The tensile strength of the composites follows the same trends as the median/average values of the elemental tensile strength of the influence zone.

- The effect of the influence zone properties on the post-peak behaviour is non negligible: residual stress at a strain of 0.25 ‰ decreases, less exposure of PLA particles occurs and less lattice elements fail for stronger influence zone and viceversa.

- The influence of dosage is heavily affected by the size of the used PLA capsules and viceversa. In general, the lowest tensile strength and elastic modulus among the studied ranges of the parameters and for all PLA types corresponded to the biggest size and the highest dosage.

- For a specific size range of the PLA particle the elastic modulus tends to decrease for increasing dosage of the particles. On the other hand, for the tensile strength, an optimum dosage of PLA particles seems to exist for which the tensile strength is the highest. The latter suggest that the inclusion of PLA particles in cement paste increases to a certain extent the tensile strength of the composite until a threshold dosage, afterwhich the influence zone properties (in general lower than that of cement paste) overcome the positive effect of the PLA. No significant differences on the amount of exposed PLA capsules in the crack was encountered for sample size to particle size ratio of 3.

- For a specific dosage of PLA particles, both elastic moduli and tensile strength seem to either decrease with increasing particle size or to achieve maximum values at

the intermediate particle size range studied herein. A wider range for the analyzed parameters is needed to investigate this trend and its possible causes. Regarding the post-peak behaviour, the addition of smaller capsules seems to decrease the slope of the post peak branch and to increase the residual stress. Also, the use of gradually larger PLA particles seems to increase the potential volume of healing products, yet this increase tends to be smaller for big enough capsules.

- The studied shapes of PLA particles did not impact the elastic modulus or tensile strength of the self-healing composite paste in a relevant way for the studied particle size, dosage and influence zone properties. Only the residual stress in the strain-softening plateau of the Stress-strain curve was influenced by the shape of the particles with the paste with irregular particles achieving a higher residual stress when compared to its counterpart with spherical capsules.
- The parametric analysis can serve as tool for the design of a self-healing system with bacteria-containing PLA capsules. Yet, the methodology used herein can be applied to other capsule-based self-healing composites.

It is useful to remark the various limitations of the methodology used in this study. As mentioned before, the use of homogeneous micromechanical properties for the cement paste elements and the use of a linear-elastic constitutive law for the elements do not allow the correct representation of the post-peak behaviour of cement paste with or without capsules. Moreover, the rate of the metabolic process or internal limiting factors of the bacteria-based self-healing process were not taken into account in estimating the amount of potential healing from the exposed PLA particles.

III

Water: role in Self-healing and Self-sealing of cement-based materials

5

Numerical modelling of moisture transport in cracked cement-based materials and monitoring through time-resolved X-ray micro Computed Tomography

Use a picture.
It's worth a thousand words.
Arthur Brisbane

In this chapter, capillary water absorption in sound and cracked mortar, with and without superabsorbent poymers is investigated. A 3D lattice transport model for the simulation of capillary water absorption in sound cement-based materials is presented. The model is intended for obtaining the cracked capillary water absorption before and after a generic healing event, thus allowing the computation of the healing efficiency related to this functionality of the material. A tailored experimental methodology, involving the use of dynamic XμCT, is used for validation and input of the previous model. Through the experiments, local effects within the moisture uptake process were observed. Furthermore, the morphological properties of the cracks and the wetting front position and water content at saturation were correlated for cracked samples. The validated model was used to perform a parametric study on the role of porosity and initial moisture content on the capillary moisture transport within the sound mortar.

5.1 Introduction

The ingress of water in cement-based materials is unavoidable due to their intrinsic porosity. When cracks are present in the concrete elements, the kinetics of moisture absorption are further accelerated as water can rapidly fill the cracks and the area exposed to moisture is increased. Species such as chlorides, sulfates, etc. can be transported in solution into the (un)cracked concrete and initiate the chemical degradation of either the cementitious matrix or the reinforcements within. On the other hand, moisture transport is at the basis of mineral producing autonomous self-healing mechanisms, not only within the crack boundaries but also its transport from the crack towards the matrix and from the matrix to the cracks. The transport in the former direction determines the volume of composite surrounding the crack, from which healing agents and other species can eventually travel from to participate in the healing process. Whereas the latter direction enables that fundamental species participating in the healing process (i.e. dissolved from healing agents) can travel to the crack location via diffusion. Therefore understanding how the moisture transport occurs in cracked cement-based materials is paramount for the design of self-healing cement-based materials where acqueous reactions are responsible for the production of healing products. Furthermore, water transport within the cracks and from cracks to the mortar matrix, in the form of permeability or capillary water absorption measurements, respectively, have been successfully used in experimental works to assess the self-healing efficiency of all types of self-healing cementitious systems. Henceforth, the correct modelling of such processes are as important as the modelling of the self-healing process itself to understand in practical terms what a certain crack sealing may mean for the recovery of watertightness in the cracked material

The absorption of water by the porous concrete is in most of the cases driven by capillarity. The latter is characterized by a capillary pressure, which is a strong function of the water content in the pore network, as well as on the characteristics of the pore structure itself. At low water saturations, water occupies the smallest pores and throats in the material while at higher water contents, fluid flows linking all configurations. In both cases the aim is to attain a uniform hydrostatic pressure of the liquid phase throughout [273]. The water transport has long been theoretically described departing from the Darcy's law by defining the flow rate (permeability or hydraulic conductivity) as a function of the water content to account for unsaturated flow. Based on this, simplified models to describe water flow in unsaturated cement-based materials have been proposed . These models have been proven very useful to predict the behaviour of cementitious composites, i.e. durability, when combined with the use of experimentally-informed inputs of the material properties and the initial conditions. Experimentally, the transport properties of the cementitious materials are used to describe their proclivity to absorb water (sorptivity, permeability test, tortuosity, porosity and pore size distribution). These can in turn be later used as input to model chloride ingress, carbonation etc. Another methodology to study moisture transport in cement-based materials is to directly visualize the dynamic process through different physical principles. Direct visualization techniques can be used to study transport processes in cement-based materials with admixtures that may alter the physics of such processes. It is obvious that for these composite materials, characterization by means of average properties overlooks the local effects potentially caused by these admixtures on the moisture transport. In turn, observations of the composite behaviour at the local level

may aid the design of models in an informed manner. In the literature both 2D and 3D (tomography) imaging have been used as it will be briefly reviewed as follows.

Neutron Imaging NI is the most obvious visualization tool for this purpose. In summary, the object to be studied is irradiated with a highly collimated and moderated neutron beam. After converting the passing neutrons to visible light and digitalization, a 2D greyvalued image is obtained. Because of the large scattering produced by hydrogen atoms when interacting with neutrons, relative to that of calcium-based minerals in the cement-based matrix, high contrast between moisture and surroundings can be attained [274]. In fact, many works in the literature have been devoted to monitoring the capillary moisture transport through 2D NI in sound cement-based materials to study the role of w/c ratio and age of mortar [275], to investigate the role of air entrainment and initial moisture content [276] on the transport process, to study the kinetics of the moisture exchange between young repair system and old mortar susbtrate for different initial moisture saturations [277], etc.. Some authors have used 2D NI to study the capillary moisture transport in cracked samples as well to study the moisture absorption and desorption of multiply cracked SHCC with or without hydrophobizing agent [278] and to study the effect of self-healing on moisture penetration in mortar with differen healing agents (SAP, polyurethane, metylmethacrylate) [279–281]. It is worth noticing that in these studies a small sample thickness was necessary to avoid excesive in-depth heterogeneity due to the 3D nature of the cracks. Furthermore, other chemical and physical processes for which moisture transport happens as collateral effect could be studied through NI as well, such as the moisture redistribution actuated by internal curing of cement paste with SAP (in 2D) [282], and the moisture migration due to thermally-induced drying of concrete exposed to elevated temperatures [283] (in 3D). In the aforementioned studies the temporal resolution ranged from tens of seconds for 2D imaging to 1 minute for tomographic acquisition. Regarding the spatial resolution, this was maximum 57 in 2D and 200 μm in 3D, depending on the chosen field of view and temporal resolution which is considered coarse in the context of moisture transport within the fine pore structure of cementitious materials. Additionally, due to the costly construction and maintenance and the necessary highly qualified manpower, there is a limited number of NI facilities around the world [284].

Few literature is available regarding the use of Proton Nuclear Magnetic Resonance 1H NMR to map 1D moisture transport in cementitious materials. The technique exploits the sensitivity of the spin angular momentum of hydrogen nuclei (abundant in water inside concrete) when a strong static magnetic field is applied. To spatially resolve the samples, magnetic gradients systems are commonly used. As an example, [285] presented one-directional saturation profiles over time of initially dry mortar in contact with a water reservoir at one of the free boundaries. In [286], the authors present one dimensional profiles of evaporable moisture content at various drying periods in samples of different maturity. Because water physically bonded within cement-based materials present different characteristic relaxation decays, it is possible through NMR to discern between capillary and gel pores water absorption. This was used in [287] to study the moisture reconfiguration during thermally-induced drying of concrete with and without PP fibers. In general, NMR imaging of moisture transport in cement-based materials is limited to coarse spatial resolution and 1D visualizations.

In recent studies, Electrical Tomography ET has been proposed as alternative to

radiation-based tomography to map the moisture transport in cementitious materials, due to the wide accessibility in comparison to the other methods. There exist different types of ET: Impedance-, Resistance- and Capacitance Tomography based on the property reconstructed [288]. The first two reconstruct conductivity/resistivity through the measurement of the voltage and current and of voltage with knowledge a priori of the currents, respectively. Whereas the third type of tomography reconstructs permitivity. In all cases, measurements are generally taken at the boundaries of the samples through an array of electrodes. The measured quantities are quite sensitive to the presence of moisture in the pore structure and thus ideal to monitor its transport. Several works are available on the progressive development of Electrical Resistance Tomography for the imaging of moisture absorption in concrete first in 2D [289] and later in 3D [290], which was also shown to work when artifical and natural cracks are present in the material [291]. Lately, the use of Electrical Capacitance Tomography has been favoured to monitor moisture transport at later stages to overcome artifacts encountered in the other electrical tomography types and also for attempting to quantify the moisture content [292, 293]. Although with a coarse spatial resolution ET can monitor the position of the wetting front correctly as seen from comparing to NI, XμCT and numerical simulations. Yet, to this date the correct quantification of the water content distribution remains unattained.

In lab-based X-ray radiography or tomography, an X-ray beam is generated through the acceleration of electrons which then hit a target from which X-ray photons are emitted and collimated. The resulting conical beam photons interact with the studied sample by either photoelectric effect or scattering, depending on the photons energy and the atomic number of the atoms in the sample. The passing X-ray photons are then converted to visible light by a detector positioned behind the sample, which results in the generation of 2D radiographs consisting of an array of "interaction intensities" or GrayValue (GV). When it comes to imaging of moisture transport, X-ray micro Computer Tomography has been long disregarded due to the relatively weak interaction between X-ray photons and hydrogen in the water, when compared to the solid phases. But lately, the use of differential images with respect to an initial state of the sample can be used to monitor even minor GV changes in the voxels over time [294]. To quantify moisture content per pixel through the depth of the cementitious sample via 2D X-ray radiography, the Beer-Lambert law (which relates the attenuation of light to the properties of the material) was used in [295, 296]. This has been successfully used for applications such as the exchange of moisture between young SHCC repair and old mortar substrate in [297] and the study of moisture uptake in the same type of material presenting multiple cracking [298]. The latter work highlighted the duality of the technique to image with relative high resolution the cracks and also the uptaken moisture. It is until recently that XμCT started being used for in-situ monitoring of moisture absorption in cementitious materials. The difficulty mainly resides on the availability of flow cells transparent to the X-rays, quality of the scanner and spatial-temporal resolution trade-off. Yang et al. [299] used cesium cloride as doping agent and performed an analysis of the wetting front position over time in dry cement pastes samples exposed to water from the bottom with a temporal resolution of 30 minutes. In a more advanced study, Oesch et al. [300] monitored and quantified the capillary moisture transport in sound concrete samples over a period of 24 hours with relatively coarse spatial and temporal resolutions. In the study, an ad-hoc artifact correction algorithm was proposed to reduce the measurement

errors. The authors in [301] studied the drying and moisture migration in concrete exposed to heat with a temporal and spatial resolution of 10 minutes and 160 μm, respectively. Given the relatively high elastic and inelastic expansion of the samples, the authors proposed the use of digital volume correlation to obtain uniequivocally corresponding material voxels at each time step.

Among the aforementioned visualization techniques, differential XμCT seems to be the most promising to monitor moisture transport in cementitious materials. Firstly, with the use of differential scanning, the technique allows for moisture content quantification despite not being able to resolve all of the porosity of the material. Secondly, the high attenuation of X-rays by the cementitious matrix enables the imaging of admixtures (usually less dense) and cracks, which may considerably influence the moisture transport. Although the use of in-situ XμCT is not new, this methodology has not been used to study in detail the influence of cracks and self-healing admixtures on the water absorption of cementitious composites.

In Section 2.2.3, it was reported how SAP are used in cement-based materials to provide a crack self-sealing effect and to boost autogenous self-healing. SAP are three-dimensional network of crosslinked polyelectrolyte chains which can absorb large quantities of solution with respect to their own weight. The main pressures contributing to the swelling of SAP are of osmostic nature, due to both the elevated packing density of network strands and the difference in ionic concentration between the external solution and solution retained in the gel [302]. The dispersion of the polyelectrolytes is limited by their elastic deformation capacity and by acting external forces [303]. The polyelectrolyte gel reaches swelling equilibrium when pro-swelling and counteracting pressures are in equilibrium.

In this chapter, capillary water absorption in sound and cracked mortar is investigated, as well as in mortars containg SAP. A 3D lattice transport model for the simulation of capillary water absorption in sound and cracked cement-based materials is presented. The model is thought of for obtaining the cracked capillary water absorption before and after a generic healing event, thus allowing the computation of the healing efficiency related to this functionality of the material. A tailored experimental methodology, involving the use of dynamic XμCT, is used for validation and input of the previous model. Through the comparison between experiments and numerical results, local effects within the moisture uptake process were discerned. Moreover, the model was used to perform a parametric study on the role of porosity and initial moisture content on the capillary moisture transport within the sound mortar. Furthermore, the morphological properties of the cracks and the water content distribution were correlated for cracked samples.

5.2 Methods

5.2.1 Experiments

Sample preparation

Mortar mixtures with different water to cement ratios and Superabsorbent Polymers were prepared according to the mix designs in Table 5.1. CEM I 52.5 R from ENCI Netherlands and quartz sand with particle size 0.125/2 mm were used in all the mix designs. The mixtures workability was adjusted with water-reducing admixture from MasterGlenium 51 to match the mini-cone slump flow diameter of mix R0.55, measured as $185-190$ mm. The

Table 5.1: Mix design of mortars in kg/m^3

Component	R0.55	R0.45	R0.35	F0.5
CEM I 52.5 R	501	527	557	499
SAP	-	-	-	2.5
Water	275	237	195	224
Additional water	-	-	-	50
Superplasticizer	-	1.2	12.68	1.2
Aggregates 1-2 *mm*	502	528	556	500
Aggregates 0.5-1 *mm*	422	444	468	420
Aggregates 0.25-0.5 *mm*	355	374	395	354
Aggregates 0.125-0.25 *mm*	355	374	395	354

SAP powder used in this study was a commercially available SAP Floset 27cc, a cross-linked copolymer of acrylamide and acrylate, supplied by SNF SAS (Andrezieux - France). The resulting particle size distribution was determined by laser diffraction in ethanol and it is shown in 5.1. Since the SAP absorb water during mixing, additional water was added to the mix F0.5 to account for the surplus needed. To quantify the extra water, different water dosages were tested in the mortar. The mortar flow was evaluated 10 minutes after mixing until achieving the flow of the reference mortar [168]. In [304], the authors employed the same type of SAP and estimated an absorption during mixing of 20 g_{water}/g_{SAP}, which was in agreement with that measured in this work.

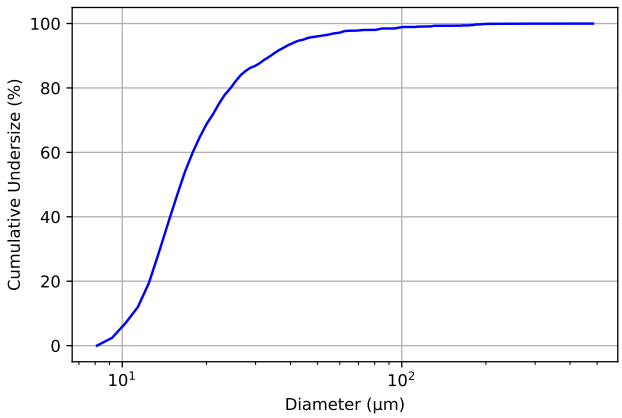

Figure 5.1: Particle size distribution of dry SAP

The mixtures were cast into moulds consisting of grooved mortar cylinders of 16 *mm* diameter, with two diametrically parallel prismatic grooves of 2 *mm* side, and a height of 30 *mm*. The samples were cured in an environmental chamber at 21°*C* and 95 % of Relative Humidity. At the age of 21 days two 10 *mm* high samples were obtained from each of the

Table 5.2: Experimental Series

Code	w/c_{tot}	w/c_{eff}	SAP [$\%w.cem$]	Crack width [μm]
R0.55	0.55	0.55	-	-
R0.45	0.45	0.45	-	-
C175	0.45	0.45	-	175
C300	0.45	0.45	-	300
R0.35	0.35	0.35	-	-
F0.5	0.55	0.45	0.5	-
FC175	0.55	0.45	0.5	175

grooved cylinders by means of a diamond saw and the resulting specimens were returned to the curing chamber until the age of 28 days. Sucessively, the samples were weighed and their dimensions measured before being put in a ventilated oven at $40^{\circ}C$ until constant mass attainment. The dried samples were then wrapped in plastic and kept in the oven until testing age to favour a uniform moisture distribution and to prevent further carbonation.

For the samples to be studied at the cracked state, cracks were introduced in Brazilian Splitting configuration by means of a Kamrarth & Weiss mini-tensile-compression testing machine. The two halves were kept together by wrapping the sample prior to the splitting in order to avoid loss of material. Artifical crack widths of 175 and 300 μm were generated within the groove of the split samples as follows. The two halves of the discs are fixed together by gluing them at the edges of the grooves. The desired crack width was steered by inserting prismatic bars with width equal to the groove width plus the desired crack width. Dimensions and scheme of the split cylinders can be observed in Figure 5.2. Prior to testing, the lateral surface of the samples was sealed with polypropilenic tape.

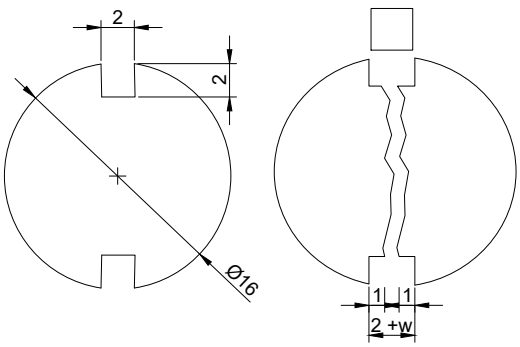

Figure 5.2: Generation of artificial cracks with desired width (dimensions in mm)

Three samples were tested for each series which are summarized in Table 5.2.

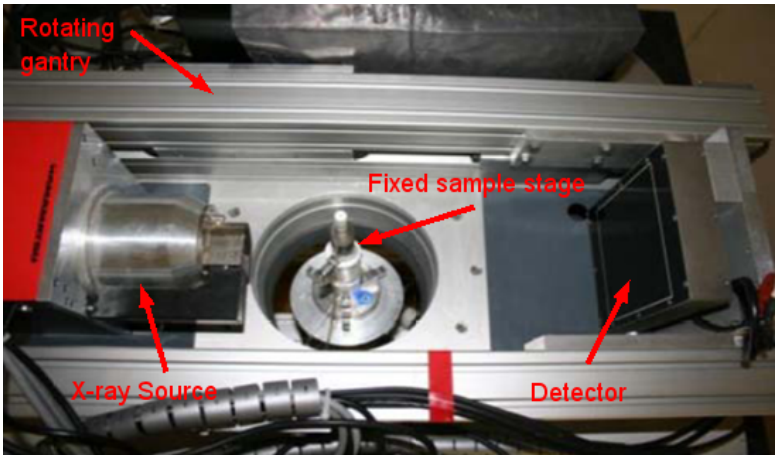

Figure 5.3: Environmental Micro Computerized Tomography scanner (adapted from [307]).

X-ray Micro Computed Tomography

The Environmental Micro-CT (EMCT) at the UGCT in Ghent University [305] was used to monitor the dynamic process of capillary water absorption in the samples. The device consists of a standard directional microfocus X-ray source operated with up to 130 kV, maximum power output of 39 W and a minimum spot size 5 μm. The system is doted with a CMOS flat-panel detector (1316 $\times$ 1312 pixels with a 100 μm pitch) with a thick structured CsI scintillator. The scanner is mounted on a horizontal gantry which allows the rotation of the X-ray source–detector assembly as can be seen in Figure 5.3. This configuration enables the installation of a large number of add-on modules such as flow cells, pressure stages, temperature stages, etc. in a convenient static vertical position without limitations for tubes and wires, as well as inertial effects of flowing water. Furthermore, the components of the gantry enable fast and continuous CT scanning at up to 5 full rotations per minute (12 s per scan). The scanner source-detector combination, together with the applied smooth-scanning acquisition, allows for fast scanning of dynamic processes [306].

A capillary absorption cell was designed in such a way that a constant water head at the bottom of the sample was obtained and that the top surface of the specimen was at room environmental conditions at all times. The Polymethylmethacrylate (PMMA) cell was connected at the bottom to a hose through a screw-type watertight connection. The hose was attached to a water pump. The sample was fixed in the cell by means of a hollow cylinder from above with internal diameter slightly smaller than that of the sample and from below by resting on two cylindrical bars affixed horizontally to the cell walls. The latter was important in order to minimize sample movements during the experiment. In Figure 5.4 a scheme of the cell and sample setup is shown.

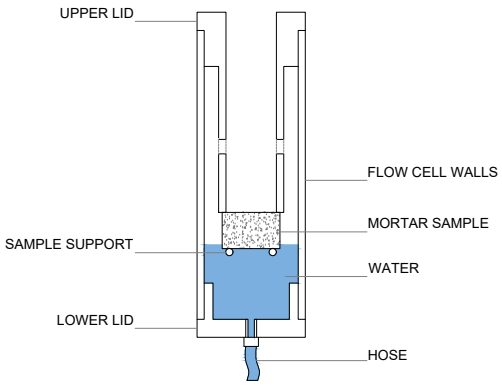

Figure 5.4: Scheme of the cell used for the monitoring of water absorption in mortar through time-resolved X-ray microtomography.

As it will be explained in Section 5.2.2, in this study the moisture transport in the samples is monitored by means of X-Ray differential imaging. This implies that scans are performed before and during the capillary absorption experiments. The scans settings were optimized to maximize spatial and temporal resolution. This was achieved by employing two scanning modes. High resolution scans were performed at the dry state of the samples, where high temporal resolution was not required. For scans performed during the capillary absorption experiment, shorter exposure times and a lower number of projections had to be used. The lowest nominal spatial resolution obtained was 28 μm and the temporal resolution of fast scans was 18 s. The scanning sequence employed in the study can be summarized by means of Table 5.3.

Table 5.3: Scanning seettings during capillary absorption experiments.

Settings	Slow Scans	Fast Scans
Voxel size [μm]	14	28
Total time scan [s]	720	18
Binning of the detector	No	Yes
Exposure time [ms]	4x80	1x30
Projections number	2200	600
Source-Detector-Distance [mm]	364.27	364.27
Source-Object-Distance [mm]	51	51
Tube Accelerating Voltage [kV]	120	120
Tube Current [μA]	80	133
Step-and-Shoot Dry State scan	Yes	Yes
Smooth Wet State scan	No	Yes (0-10 min)
Step-and-Shoot Wet State scan	Yes (64 min)	Yes (20, 30, 40, 50, 60 min)

Some 100 dark field images and 120 flat field images were taken before every capillary absorption experiment and for each scan setting. These images were used to correct the beam profile, scintillator, taper or detector imperfections.

Gravimetric analysis

The initial moisture content of the samples was calculated via gravimetry from Equation 5.1.

$$\theta_0 = \frac{m_{sat} - m_0}{m_{sat} - m_{imm}} \tag{5.1}$$

Where m_0 is the mass of the samples prior to the capillary absorption test, m_{sat} is the mass of the sample after water saturation under vacuum for 24 hours and m_{imm} is the hydrostatic weight of the sample. Likewise, the porosity acessible to water was estimated via the formulation in Equation (5.2):

$$p = \frac{m_{sat} - m_{dry}}{m_{sat} - m_{imm}} \tag{5.2}$$

Where m_{dry} is the mass after drying till constant weight attainment in an oven at $105^{\circ}C$.

Special attention was given to obtaining a properly dry surface during the measurements, due to the small sample size.

5.2.2 Imaging post-processing

The acquired radiographs were reconstructed into 3D volumes by using the Tescan XRE reconstruction software Octopus Reconstruction©. Prior to the 3D reconstruction the projections were corrected with spot and ring filters. A third-order polynomial beam hardening correction was applied on the reconstructed stacks.

The software Dataviewer from Bruker was used to register stacks obtained at different times of the same sample. Due to the difference in pixel size between slow dry and fast wet scans down-sampling was necessary, hence the final resolution of the stacks resulted 55 μm.

X-ray attenuation method

In order to obtain the water saturation for each voxel, the additivity rule of linear attenuation coefficient is used here[295, 308, 309]. According to this rule, the attenuation of a single voxel at the dry state can be defined as:

$$\mu_0 = \mu_{cem} w_{cem} + \mu_{air}(w_{por} - w_0) + \mu_{wat} w_0 \tag{5.3}$$

Where μ_{cem} and w_{cem} are the attenuation coefficient and volume fraction of hydrated cement paste and μ_{air} and w_{por} the ones for the pores (filled with air at the dry state). The aggregates are considered impervious as it could be verified after treatment of the data.

While the attenuation coefficient of the same voxel at any wet state can be defined as:

$$\mu(t) = \mu_{cem} w_{cem} + \mu_{air} w_{air}(t) + \mu_{wat} w_{wat}(t) \tag{5.4}$$

Where μ_{air} and $w_{air}(t)$ are the attenuation coefficient and volume fraction of the air in the pores and μ_{wat} and $w_{wat}(t)$ the ones for the water saturated fraction of the porosity.

The sum of $w_{wat}(t)$ and $w_{air}(t)$ should yield $w_{por}(t)$ at all times, assuming that temperature and pore structure do not change during the water absorption experiment. The output of the reconstructed tomography is however given in GV . Strictly speaking, only if all scanning settings remain unvaried, a proportion can be established between attenuation coefficient and obtained GV. In order to account for unavoidable changes in beam intensity between the initial scan and the time-progressive ones, the slight changes in time of GV of pure water and air (also monitored within the field of view) were used for correction. Taking all this into account, one can obtain a volume fraction of water in each voxel as:

$$w_{wat}(t) = \frac{GV(t) - GV_0}{GV_{wat}(t) - GV_{air}(t)} + w_0 \tag{5.5}$$

The calibration of the volumetric moisture content was done by quantifying the initial moisture content w_0 gravimetrically and the porosity accessible to water of the sample through the Archimedes method.

Image segmentation

Prior to all further image analysis the registered stacks were applied a median filter with radius of 1 pixel to mitigate noise propagation.

Segmentation of the mortar phase, SAP macropores, airvoids and cracks was performed on the stacks obtained prior to moisture absorption. A simple thresholding procedure was used for this as the contrasts between air and mortar, dry SAP and mortar and dry SAP and air were very high. To further separate air voids and SAP macropores, a morphological segementation was performed by selecting only objects with circularity between 0.8 and 1 as the air voids. The binary masks containing one phase at the time, with gray scale value of 1 (i.e. mortar, SAP macropore, crack, etc.) were later used to segment the moisture content in the respective phases.

Technically, no segmentation procedure was employed to segment the moisture at different time steps since each voxel moisture content was directly obtained through the methodology explained in Section 5.2.2. Nevertheless, in samples containing SAPs or cracks, the moisture absorbed by the admixtures or in the crack were further segmented from the overall moisture distribution by multiplying the relative binary masks to the overall moisture stack.

Further difficulties arose near the bottom of the sample containing open objects (i.e. crack tip, sawn macropores, etc.) which could not be directly obtained through the binary masks. In the case of cracks segmentation, two planes were drawn manually at the crack tips in the dry stacks and GV outside the two planes were discarded as belonging to the air phase (above) or the water pool (below). The latter operation although not rigorously precise had no influence on quantification of moisture absorption as it occurred outside of the mortar and SAP phases.

5.2.3 Numerical Model of water transport

To validate the proposed methodology and to study certain parameters highlighted by the experimental results, a numerical model of capillary water absorption in porous media is proposed herein. First, a brief derivation of the governing equation is given, followed by the numerical implementation within the context of lattice transport model.

Theory of unsaturated water transport in sound and cracked cement-based composites driven by capillary absorption

Starting from the two mass balance equations for air and water and Darcy's extended law for the flow velocity, one can arrive at the two-phase formulation of immiscible flow in homogeneous porous media. The resulting system can be simplified if certain conditions are met, leading to the Richards equation for the unsaturated water flow in porous media [310]. The conditions for the validity of Richards equation in cementitious materials have been reported in [311]. In sum, isothermal conditions around $20^{\circ}C$ ensure the correctness of the assumption of uncoupling the water and air transport if they are assumed to be continuous throughout the pore space. Equation 5.6 reports the potential form of such equation:

$$C(\theta)\frac{\partial \phi}{\partial t} = \nabla(K(\theta)\cdot\nabla\phi) + S(\theta) \tag{5.6}$$

Where ϕ is the hydraulic potential $[L]$, sum of the water head (q) , capillary (ψ) and gravitational (z) potentials; $S(\theta)$ contains sinks or sources; $K(\theta)$ $[LT^{-1}]$ is the unsaturated permeability function and $C(\theta)$ $[L^{-1}]$ is the so-called capacity or storage coefficient described in Equation 5.7:

$$C(\theta) = \frac{d\Theta}{d\phi} = (\Theta_s - \Theta_i)\frac{d\theta}{d\phi} \tag{5.7}$$

Where $(\Theta_s - \Theta_i)$ represents the difference between volumetric water content at saturation and at the start, which in a way represents the porosity accessible to water of the material, p $[-]$, and θ is the pores water saturation $[-]$.

If gravitational and waterhead potentials are considered to be negligible with respect to the capillary potential and the hydraulic diffusivity, $D(\theta)$ $[L^2T^{-1}]$, is defined as in Equation 5.8:

$$D(\theta) = \frac{K(\theta)}{C(\theta)} \tag{5.8}$$

Equation 5.6 can be transformed into:

$$\frac{\partial \theta}{\partial t} = \nabla(D(\theta)\cdot\nabla\theta) + s(\theta) \tag{5.9}$$

The advantage of the PDE formulated as in Equation 5.9 lies on the fact that $D(\theta)$ can be approximated, for the case of undamaged mortar, as [273]:

$$D(\theta) = D_0 e^{n\theta} \tag{5.10}$$

Where n has been proven to lay between 6-8, varying little among materials [273]. In this work, n is assumed to have value 6. D_0 can be estimated from sorptivity experiments with good results, as proposed in [312]:

$$D_0 = \frac{n^2 S_0^2}{(\Theta_s - \Theta_i)^2[e^n(2n-1) - n + 1]} \tag{5.11}$$

And the sorptivity S_0 being defined as the slope of the best-fit line of the curve cumulative water absorption vs. $[T^{1/2}]$ for initially dried samples.

In the case of cracked mortar, the values of the hydraulic diffusivity in the cracked domain, $D_{cr}(\theta)$, are known to be much higher than those measured for the sound domain [298]. Using the definition of $D(\theta)$ and $C(\theta)$ given in Equation 5.8 and 5.7, respectively one can estimate the earlier as in the work of [313]:

$$D_{cr}(\theta) = -K_{cr}k_{cr}(\theta)\frac{dp_c}{d\theta} \tag{5.12}$$

In Equation 5.12, the crack relative permeability $k_{cr}(\theta)$ and the water retention curve $p_c(\theta)$ are assumed to follow Mualem [314] and van Genuchten [315] analytical formulations respectively, calibrated for cracks by [313]. The saturated permeability of the cracked domain, K_{cr} is estimated by Poiseuille equation, assuming a laminar flow and a planar crack.

The system of equations describing the water absorption in unsaturated cement-based materials results then in the parallel implementation of Equation 5.9 and Equation 5.10 (or Equation 5.12 for the cracked domain).

For the problem of simulating capillary absorption of water in mortar the following boundary and initial conditions can be posed:

$$\begin{aligned} &\theta = 1 && \text{on } \Gamma_1 \\ &\frac{\partial\theta}{\partial n} = 0 && \text{on } \Gamma_2 \\ &\theta(t=0) = \theta_0 && \text{in } \Omega \end{aligned} \tag{5.13}$$

Being Ω the entire domain and Γ_1 and Γ_2, two boundaries of Ω. θ_0 is the initial moisture content of the porous medium.

Numerical implementation

As done in Chapter 3 and 4, lattice network models are widely used to simulate mechanical behaviour of cementitious materials [228]. Lately, they have also found applications in mass and ionic transport in such materials (i.e. moisture, water, chlorides) [260, 313]. This type of model consists in an assembly of discrete two-nodes elements (lattice beams) that represents a continuum. For the modelling of transport, the lattice approach treats the transport as occurring along the beam elements in the lattice mesh. Other studies [316] defend the implementation of the transport in cracked materials occurring along the facets of the Voronoi polygons (in 2D). Herein, the transport is regarded as along the lattice beams.

For the discretization of the domain, the same methodology explained in Section 3.3 is employed.

If Equation 5.9 is discretized by using Galerkin method, in the context of lattice model its weak formulation in matrix form results:

$$M\frac{\partial\theta}{\partial t} + K\theta = F \tag{5.14}$$

Where the M and K are the mass and diffusivity matrices, respectively. F is the forcing vector, in which the Neumann-type boundary conditions and any sink/source terms are dumped. The elemental matrices and vectors described above are reported in Equations 5.15, 5.16 and 5.17 for the ij element in its local reference system:

$$m_{ij} = \frac{A_{ij} l_{ij}}{6\omega} \begin{bmatrix} 2 & 1 \\ 1 & 2 \end{bmatrix} \tag{5.15}$$

$$k_{ij} = \frac{D_{ij}(\theta) A_{ij}}{l_{ij}} \begin{bmatrix} 1 & -1 \\ -1 & 1 \end{bmatrix} \tag{5.16}$$

$$f_{ij} = \begin{bmatrix} f_i \\ f_j \end{bmatrix} \tag{5.17}$$

A_{ij} and l_{ij} are the elemental area and length. While ω is a correction parameter for the volume of the single element, defined as the ratio between the total volume of the lattice elements in the mesh and the volume enclosed by the mesh boundaries. It has been proven that for three-dimensional meshes ω equals 3 [317].

Crank–Nicholson scheme is used for the time discretization.

$$(M + \frac{1}{2}\Delta t K^{n-1})\theta^n = (M - \frac{1}{2}\Delta t K^{n-1})\theta^{n-1} + \Delta t f \tag{5.18}$$

An iterative algorithm is avoided by calculating θ of the current time step (n) using the K matrix calculated at the previous step ($n-1$). Although an error is introduced in the solution of the system, it is small for appropriately short time steps. Such a procedure was used by [318] to model the drying of cementitious materials with good results.

5.3 Results and discussion

5.3.1 Capillary water absorption in sound mortar

Sorptivity and wetting front position

Due to the small sample size used for the 4D XμCT, validation through gravimetry could not be possible. In [319] it was shown that the sorptivity value measured in differently sized samples stops changing beyond a certain sample size where the effects of surface water adhesion become negligible with respect to the absorption within the core. Therefore, herein the lattice transport model is used to complement the experimental results obtained through 4D XμCT. A mesh size of 0.25 mm was used to discretize a domain with dimensions $20 \times 5 \times 5$ mm^3, which resulted in 32000 nodes and 225750 lattice elements. A time step of 0.25 min was selected from previous studies [320]. The input values of porosity accessible to water and initial moisture content were obtained gravimetically as described in Section 5.2.1. Whereas, the sorptivity (S_0) values were obtained from the cumulative absorption I versus square root of time obtained from the 4D XμCT experiments. For the computation of I, the following equation was used:

$$I(t) = \frac{m_{water}(t)}{A \rho_{water}} \tag{5.19}$$

Where $m_{water}(t)$ is the water uptake measured at each time step, A is the exposed area of the studied volume of interest. Once the sorptivity S was obtained the value was further normalized to account for the initial nonzero moisture content as proposed by Lockington et al. [312]:

$$S_0 = S\left(\frac{e^{n\Theta_s}(2n(\Theta_s-1)-n\Theta_s+1}{e^{n\Theta_s}[2n(\Theta_s-\Theta_0)-1]-e^{n\Theta_0}[n(\Theta_s-\Theta_0)-1]}\right)^{\frac{1}{2}} \tag{5.20}$$

The porosity, initial moisture content, resulting sorptivity, hydraulic diffusivity and air void content of the studied samples are reported in Table 5.4. In Figure 5.5, the experimental curves of I vs. $\sqrt{t}$ are shown for R0.35, R0.45 and R0.55. Three samples were tested for each series except for R0.55, for which only one sample could be successfully monitored. Along with the experimental results, also the simulated cumulative absorption vs square root of time was reported.

Since the sorptivity input was obtained from the 4D XμCT the simulated curves correspond well with the experimental ones. It is possible that the high initial moisture uptake (1 and 5 minutes) is due to the low signal to noise ratio at those time steps, as the imaging noise may be of the same order of magnitude as the real water uptake. As expected, the sorptivity increases with increasing water-to-cement ratio. Yet the difference between R0.35 and R0.45 is noticeably smaller than the one between R0.45 and R0.55. In fact, when factoring in the influence of porosity and initial moisture content through the hydraulic diffusivity, R0.35 and R0.45 have very close rates, which are almost double for R0.55. This is somehow understandable since the increase in porosity is not linear among the studied w/c ratios, with faster growing porosity for higher w/c ratios. In addition, it has been shown in the literature that the increase of porosity comes accompanied with decreased tortuosity and higher pore connectivity which results in increased permeability of the material [321, 322].

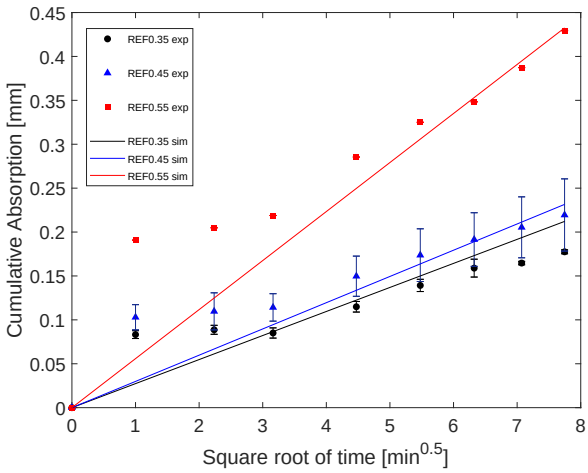

Figure 5.5: Comparison of simulated and experimental cumulative water absorption vs. square root of time.

Table 5.4: Gravimetry-measured porosiy and initial moisture content and derived sorptivity and diffusivity and XμCT-measured air void content for mortars with different w/c ratios.

w/c	p [-]	θ_0	S_0 $[mm/min^{1/2}]$	D_0 $[mm^2/min]$	Airvoid content [%]
0.35	0.124 ± 0.006	0.242 ± 0.005	0.025 ± 0.001	6.09×10^{-4}	2.61 ± 0.40
0.45	0.147 ± 0.006	0.213 ± 0.013	0.031 ± 0.006	6.16×10^{-4}	1.87 ± 0.25
0.55	0.177 ± 0.01	0.178 ± 0.003	0.059	11.3×10^{-4}	1.95 ± 0.22

A comparison between the wet front position obtained through the experiments versus the simulated ones was then used to validate the methodology. In Figure 5.6, the experimental and simulated vertical moisture profiles for one sample from each series R0.35, R0.45 and R0.55 are shown. To obtain a precise moisture content distribution, the height of any given voxel column was ajusted with respect to the height of the first voxel in contact with the water pool (at the bottom of the sample). In this way, the effects of uneven and/or non-straight sample surface were eliminated.

In all experimental vertical profiles the presence of depressions in the moisture content at well defined heights are coincident with the presence of "horizontal layers" of aggregates which absorb little to no moisture, specially for short absorption times. This can be seen directly from the renders at different elapsed times (1, 30 and 60 minutes) presented in Figure 5.7, where the segmented moisture is overlayed with the segmented mortar phase. In fact the water does not percolate into the material homogeneously. Clear dry objects are seen enclosed by the moisture, which correspond to the aggregates. As expected, the average moisture content per slice increases with increasing porosity accessible to water from R0.35 to R0.55. Furthermore, the advance of the wetting front is faster for increased porosity from R0.35 to R0.55. Nevertheless, R0.35 and R0.45 present similar penetration depths for each time step, as already foreseen from the similar hydraulic diffusivities. Airvoids were quantified from the reference stacks and reported in Table 5.4. It was found that the mortars airvoid content increased as the water-to-cement ratio was decreased. Since the workability of the three mortars was kept constant, the increasing addition of superplasticizer for decreasing water-to-cement ratios may be responsible for the latter trend.

A common feature in the different series, when compared to the numerical results, is that due to the small sample size, and relative large aggregates, a perfect correspondence of the moisture content obtained through XμCT and that obtained from the simulation of a homogeneous mortar is not possible due to local effects (i.e. wet front deviation around aggregates, no absorption in the aggregates, etc.). In the series R0.35, the experimental and simulated positions of the wetting front are very similar. During the first 5 minutes, it seems that in the experiments the position is more advanced than in the simulations but after 10 minutes this is no longer a problem. After 1 hour of capillary water absorption both experimental and numerical results indicate the position of the wetting front to be between 3.75 and 3.95 *mm*. For R0.45, the positions of the wetting front at different elapsed times resulting from the simulation correspond very well with those encountered in the experiments. One hour into the capillary water absorption experiment, the position of the wetting front seems to be between 3.5 and 3.75 *mm* from both experiments and simulations. For the series R0.55, the simulated results seem to be lagging behind the experimental

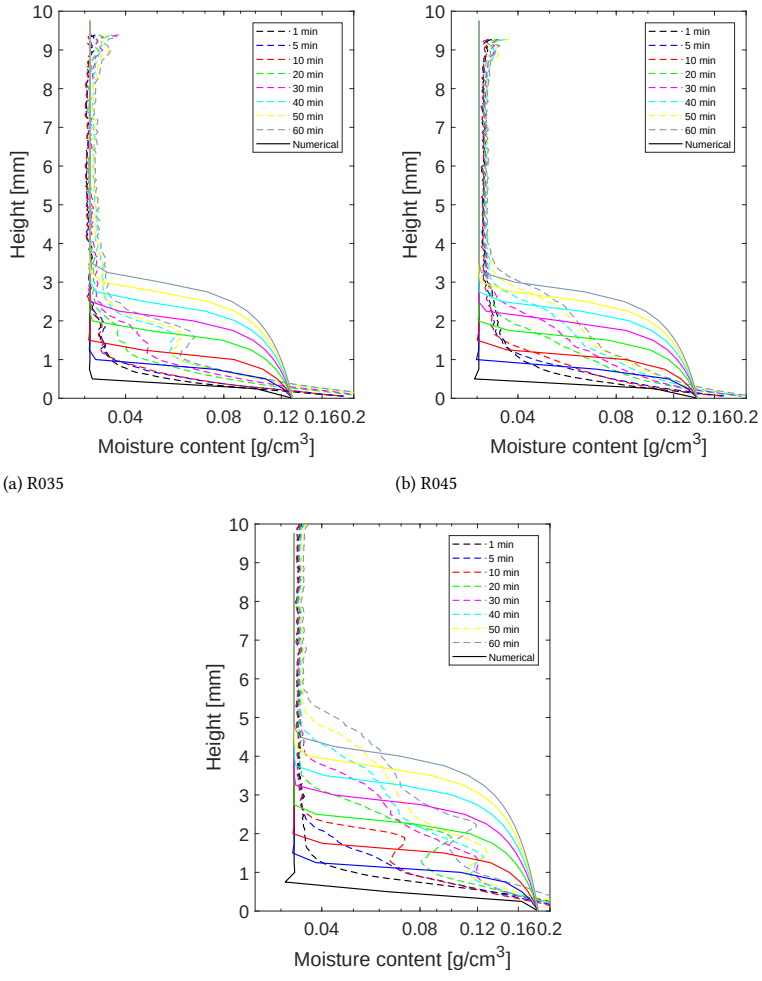

(a) R035

(b) R045

(c) R055

Figure 5.6: Vertical moisture profiles for mortars with w/c ratios a)0.35, b)0.45 and c)0.55.

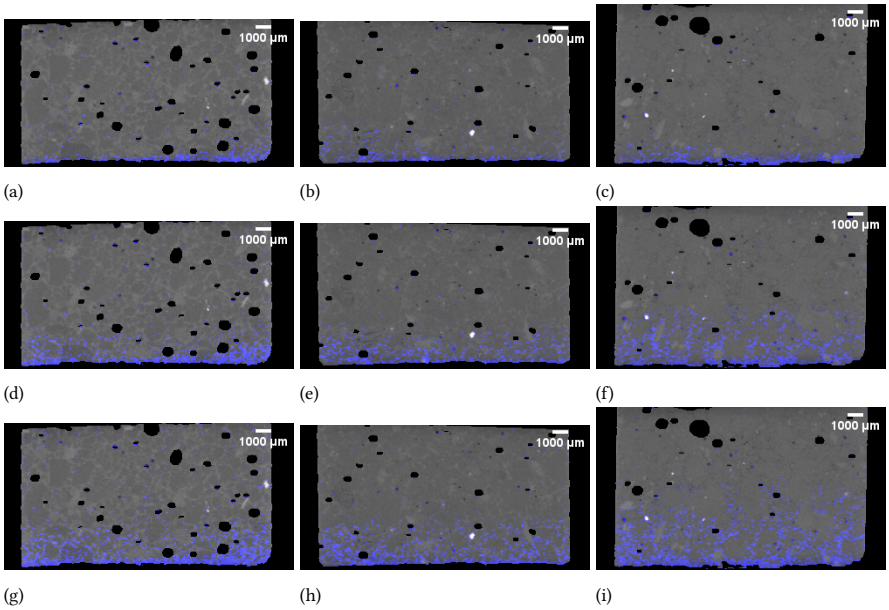

Figure 5.7: Overlay of moisture (in blue) and mortar vertical slices (in GV) after 1, 30 and 60 minutes, respectively of capillary water absorption for mortars R0.35 (a, d and g), R0.45 (b, e and h) and R0.55 (c, f and i)

ones during the whole experiment. Ultimately, the simulated wetting front is 1 mm behind the experimental one after 60 minutes of capillary absorption. A likely reason for this discrepancy could be that the initial moisture content was mistakingly measured as only one sample was used. How the initial moisture content can affect the progressive position of the wetting front will be addressed in the next section. Another possibility would be the presence of inhomogeneities on the moisture content inside the sample.

Influence of porosity and initial moisture content

Despite the three series of mortars being conditioned in the same way prior to the capillary absorption experiment, due to their different pore structures the initial moisture content was different for each of them. As a result, the hydraulic diffusivities of R0.35 and R0.45 were very close as well as the position of the wetting front over time, notwithstanding the difference in pore structure. To better understand the influence of the porosity and of the initial moisture content by separate on the results analyzed in the previous section, the numerical model was used.

In Table 5.5 the input transport properties for simulating the sole influence of initial moisture content on the capillary moisture uptake of mortar are reported. A few points can be highlighted from the comparison between vertical moisture profiles shown in Figure 5.8a for the samples in this series. For samples with same transport properties but increasing initial moisture content, the hydraulic diffusivity increases and thus the position of the wetting front becomes more advanced. Furthermore, the difference in penetration depth between higher and lower initial moisture content samples becomes larger as time progresses during the capillary water absorption simulations. The latter does not apply

when the moisture absorption is influenced by the sample boundaries, like in the case of longer exposure times in the studied samples, which in these simulations occurred between 2 and 4 hours. Finally, for the sample R0.55, this means that if a measurement error on the initial moisture content was to be responsible for the discrepancy between experimental and simulated moisture profiles, the correct initial moisture content would be around 0.23.

Table 5.5: Input transport properties for simulating the sole influence of initial moisture content on the capillary moisture uptake of mortar.

θ_0	p [-]	S_0 $[mm/min^{1/2}]$	D_0 $[mm^2/min]$
0.178	0.18	0.05579	11.3×10^{-4}
0.19	0.18	0.05644	11.9×10^{-4}
0.21	0.18	0.05763	13.0×10^{-4}
0.23	0.18	0.060203	14.3×10^{-4}

The input parameters for simulating the influence of porosity alone on the capillary moisture uptake of mortar are reported in Table 5.6. By imposing a null initial moisture content, a total independence from the initial saturation on the capillary moisture uptake is obtained. In Figure 5.8b the vertical moisture profiles are shown of samples with different porosity. The trend seems to be that increased porosity translates into a faster advance of the wetting front. The difference is quite remarkable when comparing the curve for a porosity of 0.18 to those with porosity of 0.12 and 0.14. However this is mainly due to the higher sorptivity rate encountered for R0.55. When comparing R0.35 and R0.45 no differences in the positions of the wetting front are encountered for each time step for the chosen mesh size. Regarding the differences in saturation levels at each time step, this also increases for samples with increased porosity. Again, the latter is more evident between the curve with porosity of 0.18 and the rest of the curves due to the differences in sorptivity rates, but it is also present when comparing the curve corresponding to porosity of 0.14 to 0.12 despite the close sorptivity values of R0.45 and R0.35, respectively.

Table 5.6: Input transport properties for simulating the sole influence of porosity on the capillary moisture uptake of mortar.

p [-]	θ_0	S_0 $[mm/min^{1/2}]$	D_0 $[mm^2/min]$
0.12	0	0.0205	2.02×10^{-4}
0.14	0	0.0232	2.17×10^{-4}
0.18	0	0.0475	5.52×10^{-4}

Presence of Superabsorbent Polymers

In Figure 5.9, the cumulative absorption, normalized to the exposed surface position of the F0.5 samples is presented against the square root of time which can be used to analyze the global behaviour of the composite mortar. The separation of the different phases allows for a better understanding of the transport properties of the matrix, as well as of the absorption

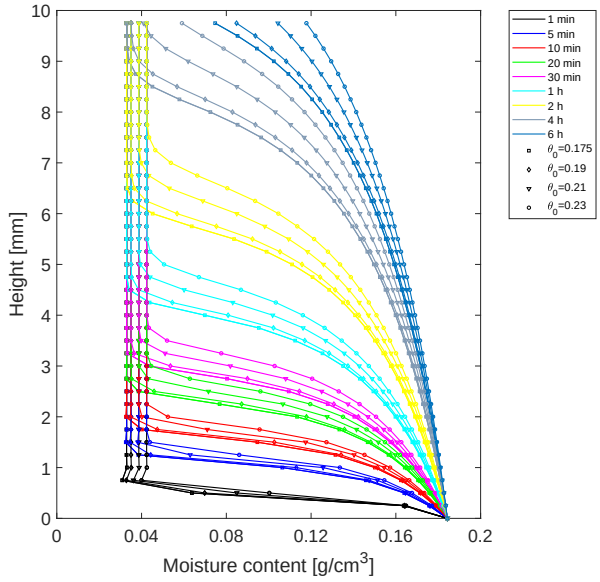

(a)

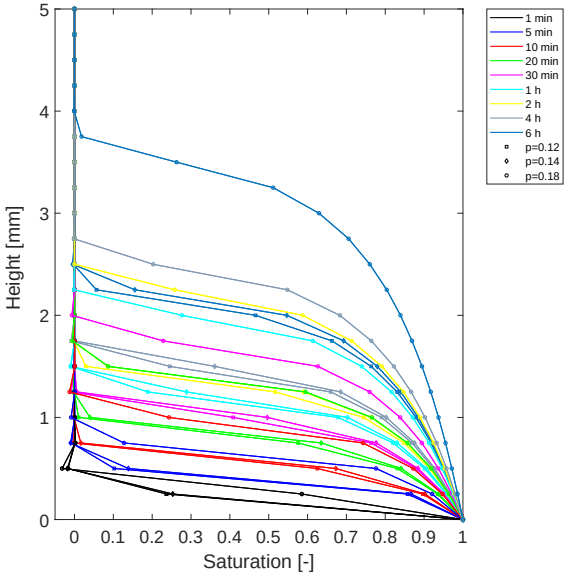

(b)

Figure 5.8: Simulated vertical moisture profiles for studying the sole influence of a) initial moisture content and b) porosity.

kinetics of the SAP. It can be seen that the mortar matrix presents similar sorptivity as the reference mortar R0.45 (Figure 5.5) albeit slightly higher. It is worth noticing that the absorption of the used SAP was carefully determined through the emulation of similar workability in the mortar when compared to the reference R0.45 which ensured that the effective water-to-cement ratio of F0.5 was 0.45 as well. A small discrepancy on the effective water-to-cement ratio from the mix design may be the reason behind the aforementioned small difference. As in the plain mortars, which results were analyzed previously, a steep water uptake was registered in the first 5 to 10 minutes, which can be associated to the high noise to signal ratio in the mortar phase at the beginning. Regarding the SAP absorption (normalized to the whole exposed surface), it can be observed that a big jump in absorption is obtained in the first minute. In this case, the signal to noise ratio is higher because the SAP phase can absorb a great deal of water per voxel. The cumulative absorption of water in the SAP does not change significantly until about 30 minutes where a steep water uptake is again observed, although less than in the first minute. A plateau is reached after 40 minutes of water absorption until the stop of the experiment at 60 minutes. Lastly, by observing the total absorption of the series F0.5 it can be deduced that the average behaviour of F0.5 samples was intermediate between the references R0.45 and R0.55. Whereas the maximum values along the curve approach the behaviour of R0.55.

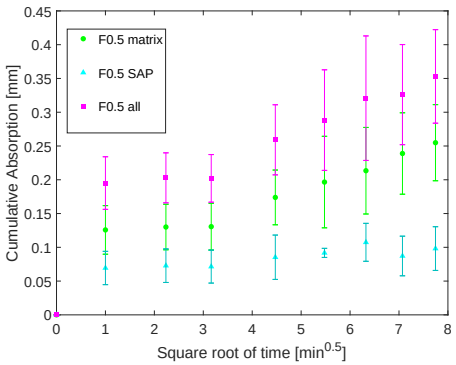

Figure 5.9: Measured cumulative water absorption vs. square root of time in the mortar alone, SAPs alone and overall in samples of series F0.5 via X-ray micro tomography.

To study the local behaviour of the mortar with SAP, the vertical moisture content profiles are reported in Figure 5.10, with distinction between the mortar Figure 5.10a and the SAP profiles Figure 5.10b. To better visualize the moisture distribution over time, the renders obtained from the XμCT are shown in Figure 5.11.

If we look at the vertical moisture content profile of the mortar phase, it can be noticed that the moisture content is in average lower than both R0.45 and R0.55, probably because in addition to the volume of nonsorptive aggregates there is the volume of SAP which contribution was left out in this specific profile. Also, the oscillations on the moisture content value along the height are similar to those found in R0.45. This confirms that these waves along the height of the sample may be the consequence of the distribution along the height of "rows of aggregates". In relation to the position of the wetting front, the

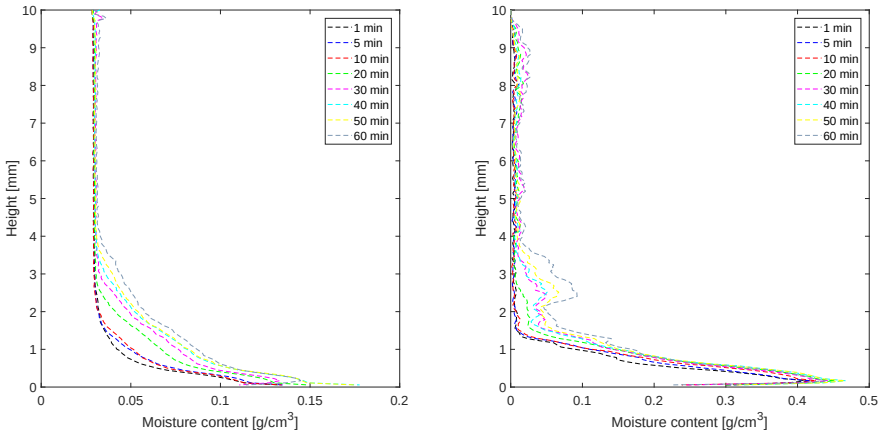

Figure 5.10: Vertical moisture profiles for one F0.5 sample for a) only the mortar and b) only the SAP.

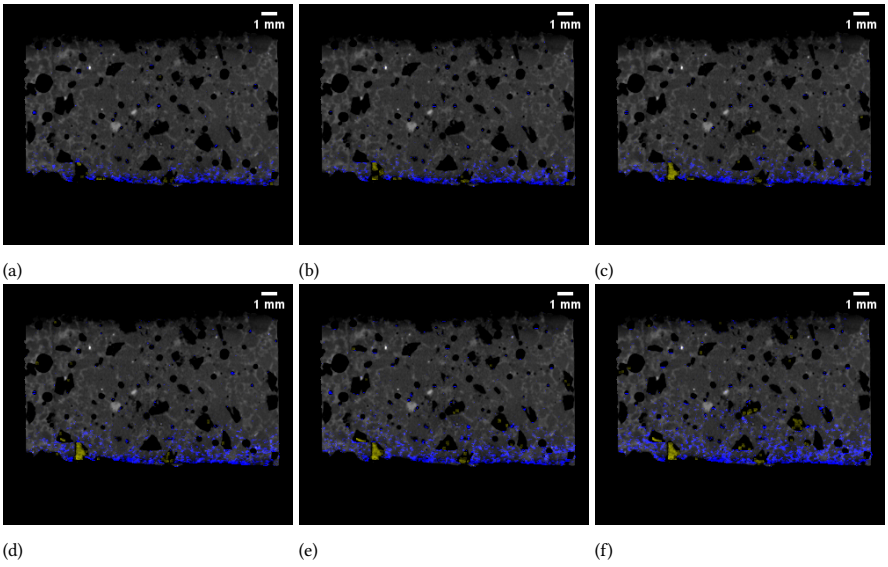

Figure 5.11: Overlay of moisture (segmented in blue), mortar (GV) and SAP (segmented in yellow) vertical slices after 1, 5, 10, 20, 30 and 60 minutes, respectively of capillary water absorption for a sample of mortar F0.5.

mortar profiles are slightly ahead of R0.45 (with a gap of around 0.25 mm after 60 minutes of capillary absorption), which corresponds well with the increased sorptivity found in the mortar phase of F0.5 when compared to R0.45.

It is especially interesting to observe the vertical moisture content profile of the SAP phase. It can be noticed that the SAP enclosed within the macropores in contact with the water pool seem to reach a dimensional equilibrium after 10 minutes as observed from Figures 5.11a to 5.11c. This seems to be irrespective of the moisture transported through the surrounding mortar matrix, which is barely different from the initial moisture content at the summit of the tallest SAP in the render. In theory, the pristine SAP used herein absorbs 332 g_{water}/g_{SAP} in 22 seconds. Yet, for the imaged SAP, these have been exposed to different cycles of absorption and desorption from the moment of casting. First, absorption of water from the wet mortar occurred, then as the samples hardened the SAPs released the absorbed water. During this cycle, it has been shown in the literature that SAP also absorbes calcium ions from the cement slurry, which results in complexation of the gel. This phenomenon is not irreversible but several cycles of absorption of water and desorption are needed to return the SAP to its initial swelling capacity [94]. During moist curing the pores are usually saturated with alkaline pore solution, so even though the ionic concentration of calcium is not as high as in the cement slurry during casting, the SAP are not likely to recover their absorption capacity fully. During preconditioning in the oven prior to the capillary absorption experiment, the SAP probably absorb calcium ions due to the increase in concentration in the pore solution due to the drying. Ultimately, prior to the capillary absorption experiment, the shrunk SAP presents a filament-like appearance, as during hardening of the mortar certain points at the swollen SAP surface were permanently interlocked with the surrounding mortar (Figure 5.12). Thus it is likely that almost full recovery of the swelling and absorbing capacity of the SAP at the bottom could take place in 10 minutes. Some SAP macropores in contact with the water pool seem to no longer contain SAP and no absorption activity is observed during the experiment. This is probably the result of sample handling during sawing of the samples which was performed in a fully saturated state of both matrix and SAP. This may be the main reason why the average absorption by SAP at the bottom of the sample is around 40 % despite the presence of fully swollen SAP after 10 minutes. As time goes by, the wet front comes into contact with SAP which had no access to the water pool at the bottom of the sample. This starts occurring after 20 minutes of elapsed capillary absorption as can be observed from the increased moisture content above the 1 mm mark. Afterwards, new SAP particles are reached by the wet front and start absorbing water. However, in general the absorption of water by the SAP not in contact with the water pool occurs very slowly with an average absorption of around 10 % after 30 minutes of being reached by the wetting front. The latter is the consequence of a depressed moisture content in those locations. Another possible conclusion is that those SAP have less water to undo the complexation achieved during the preconditioning cyle prior to the experiment.

5.3.2 Absorption in cracked mortar

Influence of crack characteristics

In Table 5.7 the average morphological characteristics of the cracks for series C175 and C300 are reported. For the evaluation of the roughness, both the arithmetical mean deviation (R_a)

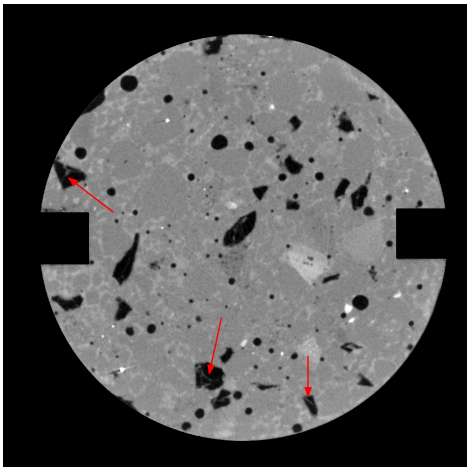

Figure 5.12: Dry SAP filaments in dry F0.5 mortar.

and the root mean squared (R_q) of the crack surface are reported. First of all, it is observed that using the crack generation methodology described in Section 5.2.1 the obtained average crack width quite differ from the nominal widths, though in a systematic way (relatively low standard deviation). Nevertheless, the method is successful in maintaining a similar crack width difference between the two experimental series, which is appropriate for the purpose of this study. From the measurements it seems that the average tortuosity of the crack paths are very similar independently of the crack width, although C300 shows a more tortuous path. Regarding the roughness of the crack surfaces, both indicators point out that the samples with wider cracks present consistently rougher surfaces.

Table 5.7: Average morphological properties of the crack surfaces.

Sample	Crack width [μm]	Roughness [μm]	
		R_a	R_q
C175	252 ± 20	235 ± 25	297 ± 27
C300	404 ± 53	324 ± 9	398 ± 9

In Figure 5.13 the simulated and experimental horizontal profiles of one sample per each series (C175 and C300) are reported. Same domain, mesh properties and time step used in Section 5.3.1 were used for the simulations. From the imaged stacks, the crack was segmented and an overlay procedure was used as described before. In the presented profiles, both experimental and simulated, each transversal slice (in planes perpendicular to the cracks surface) was centred with respect to the crack midline in order to average the moisture content along equidistant positions to the crack.

Looking at the experimental results alone, one can see that the advance of the wetting fronts perpendicular to the cracks (for samples with average crack width of 252 μm or 404 μm) are very similar regardless of the crack width. On the other hand differences were found on the average moisture content at equillibrium of the horizontal profiles of samples

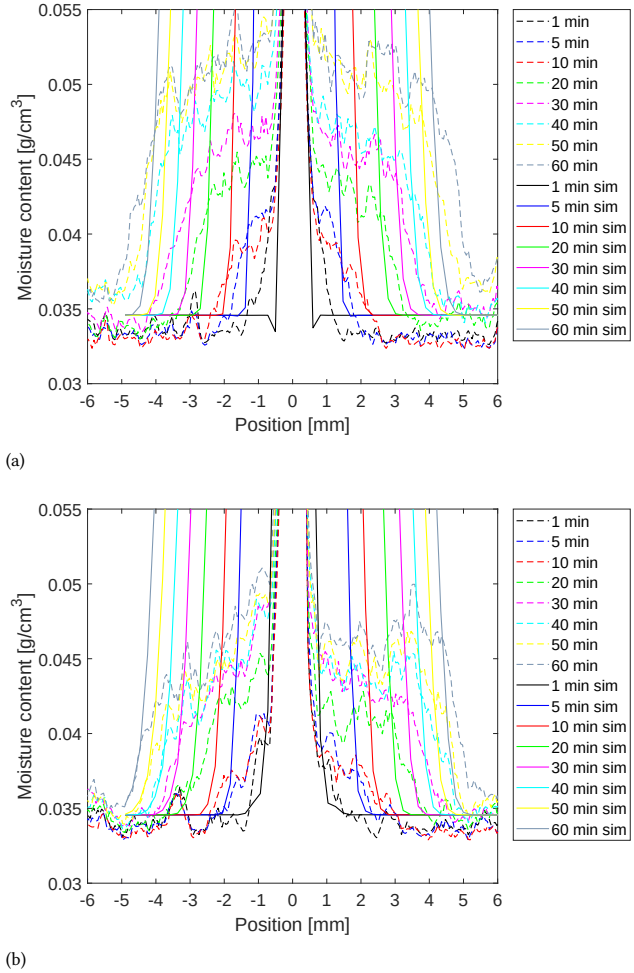

Figure 5.13: Horizontal moisture profiles for two cracked samples: C175 a) and C300 b).

with different crack width, at all studied time steps. Despite the same initial pore structure of the samples, a narrower crack width consistently led to higher average moisture contents of the mortar beyond the crack surface directly exposed to the crack water. This can be observed also in the renders reported in Figure 5.14. To the best of this author knowledge, no other studies in the literature have reported such results. A possible explanation is that the hydrostatic pressure of the water in the crack is higher for narrower cracks and thus in addition to the capillary potential also the water pressure plays a role on the moisture transport within the mortar. Circumstantially, narrower cracks resulted in smoother crack surfaces (as reported in Table 5.7) which may have affected the water absorption through them.

When comparing the results of simulations alone for the two different samples with

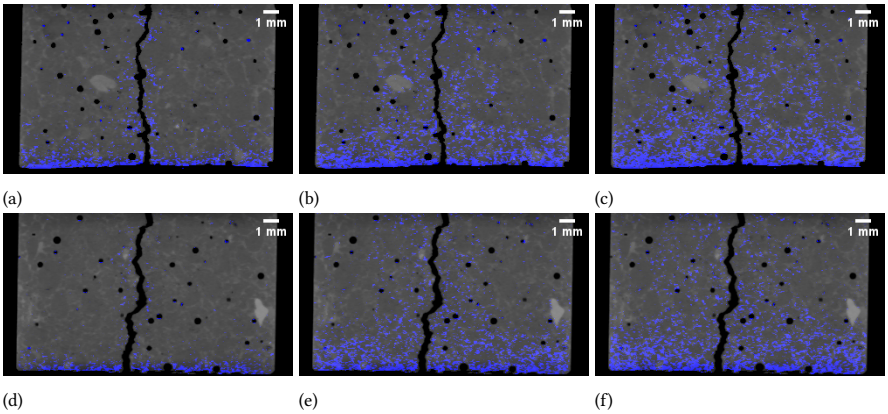

Figure 5.14: Overlay of moisture and mortar vertical slices after 1, 30 and 60 minutes, respectively of capillary water absorption for mortars C175 (a, b and c) and C300 (d, e and f).

diverse crack widths, the average saturation is slightly higher and the position of the wetting front is slightly ahead in samples with larger cracks, which is the opposite of what was found in the experiments. The latter result is due to the diffusivity calculation used herein, for which the diffusivity is proportional to the cube of the crack width. Furthermore, the differences in average moisture content are comparatively small with respect to those in the experimental results.

The correspondence between simulated and experimental position of the wetting front over time was much better for the sample with average crack width of 404 μm. Whereas for the narrower crack (average crack width of 252 μm), the simulated results lagged slightly behind the experimental horizontal profiles. This can be explained again by the cracked diffusivity equation which assumes slower transport in narrower cracks. Regarding the average moisture content, the same phenomenon as in the uncracked samples was observed: a higher average moisture content was found from the modelling results. The simulations were done on homogeneous mortar presenting uniform transport properties, whereas in the experiment the presence of heterogeneities induces local effects on the observed moisture transport.

5.4 Conclusions

In this chapter, the combination of time-resolved X-ray micro Tomography and lattice transport modelling was used for the first time to investigate moisture transport in sound mortar, with or without SAP, as well as in cracked plain mortar. First, the capillary water absorption in sound samples of mortars with different w/c ratios was experimentally monitored, and numerically modelled. Then the validated model was used to study the role of porosity and initial moisture content on the moisture transport in the mortar. A mortar with SAP was also monitored via the dynamic X-ray micro tomography, which allowed to separate mortar matrix moisture distribution, from that of the embedded SAP. Furthermore, cracked samples of different crack widths were likewise studied. The conclusions of this study are outlined as follows:

- Increasing w/c ratio in mortar results in different kinetics of the moisture movement within the material. In particular, it is shown from the experimental results that the water penetration rate is progressively faster, although much more between w/c=0.45 and w/c=0.55 than between w/c=0.35 and w/c=0.45. The latter reflects well on the differences between the diffusivity values, which encompass the influence of porosity and initial moisture content, in addition to the sorptivity. Parametric numerical simulations of this range of porosities but same initial moisture content show similar outcome regarding the water penetration depth rate of advance. From the experiments, differences in moisture content and saturation degree values between the mortars with allegedly different porosities were noticeable, with markedly increasing saturation degree distribution along the sample height for increasing w/c ratio.
- A parametric numerical study on the influence of initial moisture content on the advance rate of the water front in plain sound mortar highlighted the sensitivity of this parameter to correctly predict the penetration depth over time. For instance, a 20 % measurement error on this parameter may yield a penetration depth prediction error of up to 50%.
- The slump flow methodology to calibrate the water absorbed by the SAP during mortar mixing was validated. It can be speculated that the microstructure of the SAP mortar is similar to the reference with same effective w/c ratio (R0.45) at least regarding the transport poperties. This suggests that for this specific type of SAP, given that moist curing conditions have been used, the transport properties of the reference mortar designed as previously explained, are exchangeable with those of the matrix in the mortar with SAP.
- Complexation of the SAP is likely to be present, as the swelling kinetics of SAP exposed at the bottom of the samples need almost 30 times the equilibrium time measured on pristine SAP particles in another study. From the experiment it is also shown that embedded SAP particles can successfully absorb moisture from the partially saturated surrounding matrix, albeit more slowly than when in contact with continuous water supply (i.e. like SAP at the bottom of the samples). Due to the short duration of the experiment when compared to the time needed for full saturation, it is not possible to say what is the new absorption capacity of the embedded SAP particles.
- The horizontal water penetration rate is not directly impacted by the crack width as can be observed from the experiments. It is on the saturation level at equilibrium that the samples with different cracks widths differ the most. Such discrepancy may be associated with the differences in roughness of the crack surfaces or the hydrostatic pressure of the water in the crack due to the crack width.
- The equation used to describe the diffusivity in the crack leads to good prediction of moisture kinetics perpendicular to the crack walls. Yet, this methodological choice does not reflect how crack width differences affect the moisture content at equilibrium (and thus the saturation). As such, any conclusions regarding saturation or moisture content values based on the simulations may not be accurate.

6

Numerical modelling of crack self-sealing in cement-based materials with SAP

All knowledge is connected to all other knowledge.
The fun is in making the connections.
Arthur C. Aufderheide

Recently the concept of crack self-sealing has been investigated as a method to prevent degradation and/or loss of functionality of cracked concrete elements. To obtain self-sealing effect in the crack, water swelling admixtures such as superabsorbent polymers (SAP) are added into the cementitious mix. In order to design such self-sealing systems in an efficient way, the capillary absorption model presented in the previous chapter was expanded to simulate capillary absorption of water in sound and cracked cement-based materials containing SAP. The model choices regarding SAP absorption and swelling kinetics, as well as their interaction with the surrounding mortar matrix, are based on the observations made from the experimental results presented in Chapter 5. The numerical results yield the moisture content distribution in cracked and sound domain, as well as the absorption and swelling of SAP embedded in the matrix and in the crack. The performance of the model was validated by using the results and supplementary data of an experiment available from the literature, as well as experimentally-informed input parameters. The validated model was then used to investigate the role of SAP properties and dosage in cementitious mixtures, on the water penetration into the material from cracks. Furthermore different crack widths were considered in the simulations. The model shows good agreement with experimental results. From the numerical investigation, guidelines are suggested for the design of the studied composites.

Parts of this chapter have been published in Cement and Concrete Composites, 2019.

6.1 Introduction

The presence of a connected network of capillary pores in cementitious composites allows moisture to act as a carrier for aggressive species (i.e. chlorides, sulfates, CO_2, etc.) that may degrade the material. This process is further accelerated when cracking occurs. Cracks increase the surface area of the concrete element and therefore also the vulnerability of the material to the penetration of moisture and dissolved substances. As a consequence, corrosion of the reinforcement or expansive reactions might occur, generating further cracking within and further decreasing the durability of the element. To block water penetration into the matrix when cracks are present, superabsorbent polymers (SAP) have been proposed in the literature to obtain a self-sealing effect in the crack [39]. Self-sealing effect, in this context, refers to any reduction of the water flow in the cracks and consequently mitigated water penetration into the cementitious matrix.

Many experimental studies have been performed regarding hydrogel formation inside cracks in cementitious materials. In a work by Snoeck et al. [157] Neutron Imaging was performed during permeability tests in mortars with 1 % of SAP by weight of cement and using different types of SAP. The results presented in the study show slower depletions of the initial waterhead for mortars with SAP particles with respect to the plain reference mortar suggesting the desired self-sealing effect. Such mixtures had no additional water, therefore the differences in initial moisture content and transport properties of the mortar matrices might have influenced the results. Permeation tests performed by Hong and Choi [71] on SAP-containing mortars showed reductions of 75% and 63% of the water flow rates for crack widths of 250 and 350 μm, respectively, on mortars with 1% of SAP by weight of cement. In the former study, the swollen spherical SAP in the crack were observed by means of X-ray micro Computerized Tomography (μCT) and it was concluded that the majority of the particles filled only the macropore and portion of the crack within. In a work from Lee et al. [185] rather large dosages of SAP were used ($4-13$% by weight of cement) but the authors obtained cumulative flows well below 15 % of the reference ones for up to 300 μm cracks in cement paste, mortar and concrete. When observing through light microscopy the upstream surface of mortar samples subjected to permeability tests the authors could observe the hydrogel filling a significant portion of the visible crack. The authors also emphasized the need for limiting the initial swelling of SAP during mixing in order to obtain a larger sealing effect in the cracks.

Some analytical formulations have been proposed for the prediction of the self-sealing effect. In [186] the authors attempted to estimate the reduction of flow rates during permeation tests in mortar with spherical SAP. In the proposed formulation a fitting parameter was proposed to match modelled and experimental flow curves as the SAP dosage was increased in the material. Nevertheless, the authors could not assign a physical meaning to it and therefore, the use of the model remains limited to the type and percentages of SAP tested. Lee et al. [185] employed stereology to estimate the crack volume reduction due to SAP swelling as crack width and dosage, size and nominal swelling ratio of SAP are changed. Yet, the evaluated reduction could not be directly correlated to the water blocking effect.

Modelling-type experimentation could be advantageous for the optimization of self-sealing performance in cement-based materials with SAP while at the same time may offer insights into the mechanisms. However, it is of primary necessity that such models

are representative of service life conditions and that input and output parameters are measurable and physically meaningful for all the composite phases. On the other hand, the aforementioned effect of SAP on promotion of self-healing of cracks in cement-based materials is strongly coupled with the short-term effect which is self-sealing. Therefore self-sealing models could be used as a basis for modelling mineral precipitation in cracks.

In this chapter, a numerical model is proposed to simulate capillary water absorption in unsaturated sound and cracked cementitious materials with SAP particles. This model is an extension from the transport model described in the previous section. The outputs of the model are the spatial moisture content distribution over time during capillary absorption experiments, as well as the amount of water absorbed by SAP and their swelling evolution. The Richards equation [310] is the governing equation which is coupled with the exponential equation describing the hydraulic diffusivity change with moisture content in building materials and with the water absorption kinetics law for SAP particles modeled as sink terms. A lattice-type approach was used for the spatial discretization of the domain. Heterogeneity of transport properties is explicitly modeled with this method, not only through the discrete distinction between SAP and mortar phases. The model was validated using experimental results and experimentally-informed input parameters available from literature and from additional experiments described in this chapter. A parametric investigation is then performed to study the influence of SAP absorption capacity and dosage in the mortar for different crack widths.

6.2 SAP WATER ABSORPTION AND SWELLING KINETICS

In this section, an equation for the swelling kinetics of a single spherical SAP particle is reported. Such equation will be later coupled to the capillary-driven moisture transport governing equations discussed in Chapter 5 to extend such transport model to simulate the presence of water-absorbing admixtures, such as SAP, in mortar.

In [323, 324] the swelling kinetics of spherical SAP particles are described as a diffusion-governed process depending only on their diameter, provided a certain ionic composition of the solution and a certain type of SAP. The model has been validated by monitoring the change of SAP's diameters in time [323]. The differently sized particles were immersed in a micro-bath and observed under an optical microscope. The author [323] assumed the hydrostatic pressure of the microbath negligible to the swelling pressure and a constant particle density to calculate the water uptake.

The swelling law proposed in [323] is presented in Equation 6.1 in terms of the swelling capacity at equilibrium of one individual SAP particle, $V_{SAP,max}$, and at any given time t, V_{SAP}.

$$\frac{dV_{SAP}}{dt} = k(V_{SAP,max} - V_{SAP}(t)) \tag{6.1}$$

The rate constant k depends on the particle diameter d_{SAP} , as shown in Equation 6.2.

$$k = r_1 d_{SAP}^{-r_2} \tag{6.2}$$

The constants r_1 $[L^{-r_2}/T]$ and r_2 $[-]$ depend on the swelling medium and the SAP type under consideration. Their values should be fitted from experiments carried out like in the work mentioned above while monitoring as well the amount of absorbed water.

Herein it is implicitly assumed that the volume of the particle at equilibrium, $V_{SAP_m,max}$, can be calculated as follows:

$$V_{SAP_m,max} = \frac{Ab_{sol}\rho_{dry}}{\rho_{sol}} V_{SAP,dry} \tag{6.3}$$

Where Ab_{sol} is the absorption capacity of the SAP in the relevant solution, defined as the ratio between the weight of absorbed solution and the weight of dry polymer. ρ_{dry} and ρ_{sol} are the densities of the dry SAP and the solution, respectively and $V_{SAP,dry}$ is the volume of the dry irregular SAP particle.

6.3 Numerical and experimental methods

In this section, I explain the numerical methods used to model the problem of water absorption in unsaturated mortar with distributed sinks. In addition, a description of the simulated experiments is offered, as well of the experimental input parameters used in the simulations.

6.3.1 Mesoscale Lattice Network Model

In Section 3.3, the generalities about the domain discretization methodology employed in the lattice model were described at length. One of the advantages of lattice-type models for unsaturated flow in cement-based materials is the explicit implementation of heterogeneities in the material. Sound cement paste, cracked domain, aggregates, SAP particles, Interfacial Transport Zone (ITZ) and other interfaces can be assigned different lattice phases and corresponding transport properties.

In this work the Anm model [20] was used for parking sand-shaped SAP into an initially empty prismatic container with non-periodic boundaries. The simulated SAP particles had the dimensions of the macropores left behind by SAP due to desorption during hardening of the mortar. Next, a material overlay procedure is used: nodes in the lattice mesh are identified by overlapping them with the material mesostructure obtained with the Anm model (i.e. SAP and mortar phases). Similarly, beam elements with nodes belonging to the same phase are tagged as such, while elements bridging both phases are distinguished as interface elements. Schematics of the 2D procedure can be observed in Figure 6.1. Since the transport properties of the interface zone between SAPs and the surrounding mortar were unknown, similar properties to the mortar were assigned with good approximation since the SAPs provide internal curing.

Water absorption by superabsorbent polymers

On one hand, SAPs are regarded as sinks for the current physical problem. The volume of water absorbed by the node i belonging to the particle m at the current time step u, expressed as contribution to the forcing vector described in Chapter 5, is reported as:

$$f^u_{i,SAP_m} = \frac{k_{SAP_m}(V_{m,max} - V_m^{u-1})}{\sum_{i\in m} V_{cell,i}} V_{cell,i} \tag{6.4}$$

Where $V_{cell,i}$ is the volume of the Voronoi cell associated to node i.

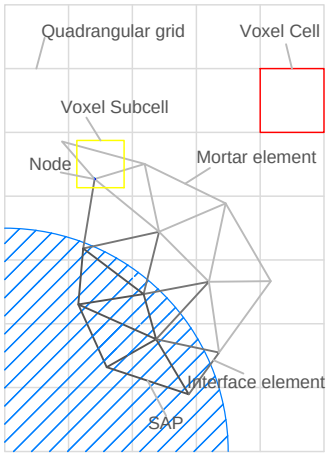

Figure 6.1: Schematics of spatial discretization and mesostructure overlay procedure for the 2D case (modified from [260]).

On the other hand, from the moment that SAPs are considered as another phase in the modeled mortar, transport properties need to be assigned to the the beam elements corresponding to the SAP domain. The hydraulic diffusivity of SAP beam elements for the current time step was then estimated as:

$$D^{u}_{ij,SAP_m} = \frac{k_{SAP_m}(V_{m,max} - V_m^{u-1})}{l_{ij}} \tag{6.5}$$

Self-sealing of cracks by SAP

The water - blocking effect of the individual SAP in the crack is considered in this model through three mechanisms. The hydraulic diffussivity of SAP elements decreases through Equation 6.5 as the SAP particle absorbs water and approaches its swelling equilibrium, eventually becoming an impermeable inclusion. At the same time, the crack width of SAP elements is reduced as the individual SAP swells and occupies more volume within the cracked macropore. Lastly, the former mechanisms are extended to other elements in the crack as the SAP swells beyond the macropore.

Procedurally, the swelling of SAP particles in the crack is actuated as follows. Firstly, the individual SAP swells to fill the macropore volume. When the cracked elements within the macropore are completely sealed the swelling beyond the macropore starts: an amount of cracked elements, contiguous to the individual SAP, are randomly tagged as such, which total volume corresponds to the volume of water absorbed at each time step. The new SAP elements are assigned transport properties corresponding to that specific SAP particle.

In implementing the aforementioned mechanisms, it was assumed that the single SAP particle grows from within every element of the macropore.

6.3.2 Experimental input parameters

In order to validate the use of the modified law of water absorption by SAP embedded in mortar (Equation 6.4-6.5), experimental results described in [54] were used. The author measured gravimetrically the capillary uptake of water in 28 days old sound mortars with SAP admixtures and in the corresponding reference plain mortars at different times during several days of absorption. The resulting absorptions for the first 6 hours of the test were reported as sorptivity values for the studied mortars. Also the initial moisture content, θ_0, and the porosity accessible to water, p, were measured on the same specimens prior to the sorptivity test and after saturation, respectively. From these experiments, the mortars containing SAP type B were simulated because of the large availability of additional experimental data. In Table 6.1 the nomenclature used for the studied mixtures is summarized.

The same mortars containing water swelling admixtures and their references were reported to have closely similar capillary pore structures in [325]. Thus herein the sorptivity values obtained for the reference mortars were used to calculate the hydraulic diffusivity of the mortar matrix of corresponding SAP mortars. Nevertheless, it is largely known that the initial moisture content of porous materials influences the measured values of sorptivity. Many researchers proposed formulations to adjust measured sorptivity taking into consideration an initial uniform moisture content of the samples [326, 327]. For low initial moisture saturations ($\theta_0 \leq 0.4$) the proposed formulations differ little, therefore in this work the simpler expression by Phillips [326] was employed (See Equation 6.6). Furthermore, the measured values of θ_0 were employed as initial conditions and the values of p were used for the calculation of the absolute water uptake obtained from the simulations. The input parameters used in the simulations, taken from [54], are summarized in Table 6.1.

$$S_0 = \frac{S}{(1-\theta_0)^{\frac{1}{2}}} \tag{6.6}$$

With respect to the superabsorbent polymers used in the experiments described in [54], their input parameters for the simulations were obtained from previous works [328, 329]. The average largest dimension of SAP B particles at the dry state was reported to be $477 \pm 53\ \mu m$. The absorption capacity of the particles was 8.9 g_{wat}/g_{SAP} during mixing of the mortar and the resulting macropores were sized $877 \pm 98\ \mu m$. In demineralized water the particles absorbed 283 g_{wat}/g_{SAP}. The particles density resulted 700 kg/m^3. In addition, the constants describing the swelling rate of SAP B in demineralized water were fitted as

Table 6.1: Studied mortar mixtures, identifying SAP dosage $m_{SAP}\%$ (in mass of cement), total and effective water-to-cement ratios and transport properties.

Mixture	$m_{SAP}\%$	w/c_{tot}	w/c_{eff}	$D_0[\frac{mm^2}{min}]$	p	θ_0
R0.50	0	0.50	0.50	0.0027	0.0077	0.16
R0.41	0	0.41	0.41	0.0012	0.044	0.277
B1.0	1.0	0.50	0.41	0.00085	0.064	0.19

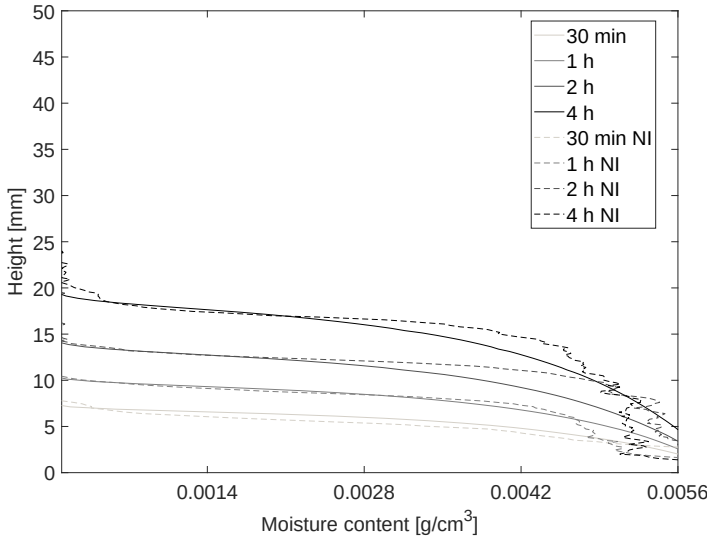

Figure 6.2: Comparison of experimental and simulated results on capillary water absorption by B1.0 mortar with $D_0 = 0.006\ \frac{mm^2}{min}$: experimental and simulated vertical moisture profiles at 30, 60, 120 and 240 min.

in Esteves [323] yielding the following formulation for the rate k where d_{SAP} is expressed in μm: $k = 112075\ d_{SAP}^{-1.828}$.

For the validation of the crack self–sealing model, the experimental results described in [157] were used. The authors used Neutron Imaging (NI) to monitor water transport in cracked B1.0 mortar specimens sized $100 \times 100 \times 28\ mm^3$. They correlated the self-sealing effect provided by SAP particles in the crack to the water penetration not only in the crack but specially into the mortar in perpendicular direction to the crack surfaces. Unfortunately, the input parameters were not available for the curing regime which the tested samples were subjected to. Nevertheless, in this thesis a fitting procedure was implemented to estimate the hydraulic diffusivity of R0.41 from the vertical moisture profiles obtained in [157] for B1.0 samples and the initial moisture content was assumed as 0.19 as measured from [54, 330] for same B1.0 mortar and different curing regimes. A lattice with characteristic voxel size of 0.25 mm was used for the simulations. The mesh had dimensions of $25 \times 28 \times 3\ mm^3$, for a total of 134400 nodes and 955337 lattice elements. In Figure 6.2 simulated moisture profiles over a period of 4 hours and radiograph after 60 minutes of simulated absorption for a value of $D_0 = 0.006\ \frac{mm^2}{min}$ are shown and compared to the experimental results.

6.3.3 Experimental methods

MicroCT was performed at the Centre for X-Ray Tomography of Ghent University of crack self-sealing in mortar at equilibrium. This experiment was used to assess the extent of swelling of single SAP particles present in the crack.

The experimental setup HECTOR [331] consisted of a 240 kV X-ray tube from X-RAY WorX operated at 150 kV and 74 μA. For each scan 2400 projection images were recorded using a PerkinElmer 1620 flat-panel detector. The Source-Detector-Distance was 1167 mm

and the Source-Object-Distance was 65 *mm* resulting on a voxel size after reconstruction of 11 μm. The obtained images were reconstructed using the Tescan XRE reconstruction software Octopus Reconstruction© and the data analysis was performed with the open source software ImageJ [222].

The mortar mixture B1.0 was cast in grooved cylindrical moulds and cured until the age of 7 days at 21°C and 95 % of Relative Humidity. The cylinders had a diameter of 16 *mm*, with two diametrically parallel prismatic grooves of 2 *mm* side, and a height of 15 *mm*. At the age of 7 days the moist samples were wrapped with adhesive tape and splitted on a Brazilian Splitting configuration by means of a small compression/tension press. The two halves were kept together because of the wrapping in order to avoid loss of material during the splitting. Artifical crack widths of 200 μm were generated within the groove of the splitted samples as follows. The two halves of the discs are fixed together by gluing them at the edges of the grooves. The desired crack width was steered by inserting prismatic bars with width equal to the groove width plus the desired crack width. The cracked cylinders were immersed in distilled water for another 3 days and later throughout the scan.

The swollen SAP particles in the crack were segmented using a Trainable Weka Segmentation (TWS) plugin [223] due to the similarity in Gray Values of water and swollen SAP in the crack. In Figure 6.3 an example is shown of a swollen SAP in the crack from a resulting tomography and segmented by using TWS. The SAP macropores embedded in the sound matrix were segmented through simple thresholding operation. The volume of each macropore was estimated through 3D Object Counter and the probability density function of the volumes were estimated by fitting the volume data to a normal Kernel Density (KD) distribution. The obtained KD was used to generate 10000 samples with size equal to the number of segmented SAP particles in the crack. The total volume of macropores of each of the 10000 samples was used to calculate an average ratio between swollen SAP gel volume and macropore volume, equivalent to the ratio between swelling capacity of the SAP in the crack and that during mixing. Throughout this chapter, we call this ratio swelling ratio, S_{cr}/S_{mix}. The resulting value, 1.37, was used as input for the model as per limiting the swelling of SAP type B in the crack.

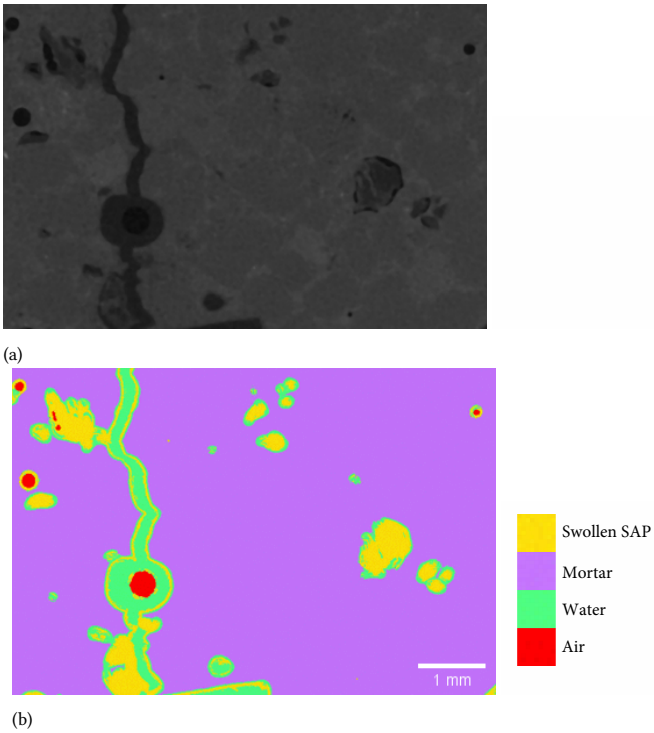

Figure 6.3: Gray value image (a) and segmentation (b) of SAP in the crack and embedded in the matrix through Trainable Weka Segmentation plugin.

6.4 Model Validation

6.4.1 Capillary absorption of water in sound mortar

The capillary uptake of water by undamaged mortar with SAP admixtures, B1.0, was simulated in this section. Also the reference mortars R0.41 and R0.50 were simulated. The mesh had dimensions of $40 \times 10 \times 10\ mm^3$, for a total of 128000 nodes and 942877 lattice elements. In Figure 6.4 a comparison is shown between experimental and simulated results of the mortars above. The simulated curve of B1.0 reports the average of three simulated mesostructures. The absorption I is normalized as:

$$Absorption(t) = \frac{m_{water}(t)}{A\rho_{water}} \tag{6.7}$$

Where $m_{water}(t)$ is the uptaken mass of water at the time t, A is the area exposed to water and ρ_{water} is the density of water at $20^{\circ}C$.

In general, the simulated water absorptions agree well with the experimental ones for the studied mixtures. Mortar R0.50, with the highest water-to-cement ratio and transport properties, presented the highest bulk water absorption. On the other hand the mortar containing SAP particles, B1.0, presented considerably higher values of absorption when compared to its reference mortar R0.41 despite the smaller values of D_0. In the simulations,

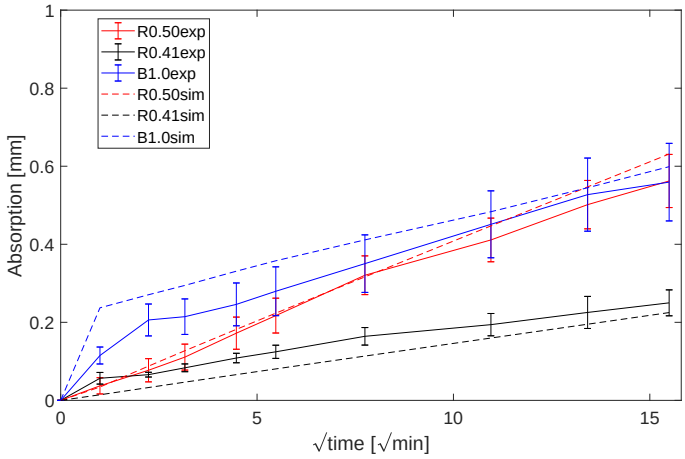

Figure 6.4: Simulated and experimental capillary water uptake in mortars R0.50, R0.41 and B1.0.

this is due to the presence of distributed discrete SAP particles modelled as sinks which absorb water rapidly when reached by the water front. Similar results were also obtained experimentally by [332] because during capillary absorption the SAP (also present at the surface) quickly absorbs and retains the absorbed water, leading to a higher observed mass.

The absorption curve of B1.0 presented a marked nonlinear behaviour as in the experiments which deviates from the typical linear behaviour found for plain mortars. This is attributed to the contrast in transport properties of mortar and SAP phases, especially at the start of the absorption when the value of D_0 is minimum for the mortar and maximum for the SAP.

In experiments, initial fast uptakes of water during sorptivity tests are commonly found in mortar with high macroporosity at the surface subjected to saturation [273]. One could argue that the surplus in absorption of water is an effect of the presence of macropores rather than of the presence of embedded SAP. Nevertheless, in a work of [333] where the authors studied the effect of different levels of air entrainment in concrete on the sorptivity, no clear trend was found to correlate the percentage of air voids with the mild increases or decreases of the sorptivity with respect to the reference samples. Furthermore, specimens preconditioned in the oven at $50^{\circ}C$, like in the results used for the validation, the sorptivity decreased for increasing percentages of air entrainment. Moreover these decreases were not greater than 10 % with respect to the reference sorptivity.

6.4.2 Self-sealing of cracks by superabsorbent polymers in mortar

Three mesostructures were used to simulate fracture in a Wedge Splitting Test (WST) configuration through lattice fracture model. The modeled mesostructures contained 1 % of SAP by weight of cement in the mortar, which results approximately in 5 % of SAP macropores by volume of simulated mortar specimen. Lattices with characteristic voxel size of 0.25 *mm* were used for the spatial discretization. The meshes had dimensions of

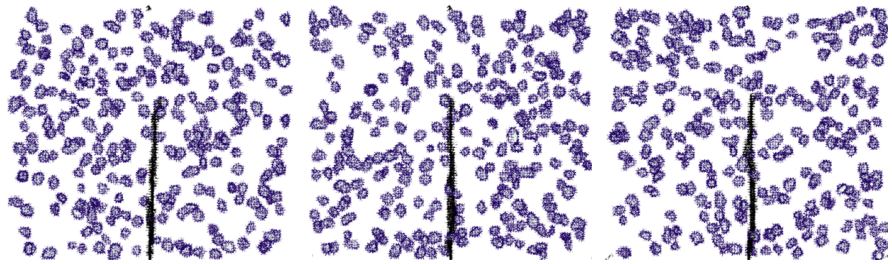

(a) (b) (c)

Figure 6.5: Simulated mesostructures and crack patterns from WST simulations.

$25 \times 28 \times 3$ mm^3, for a total of 134400 nodes and 955337 lattice elements. Although the input parameters for the fracture model such as the actual micromechanical properties of the cement paste in the mortar, aggregates and interfacial transition zone were unknown, the authors assigned lower mechanical properties to elements corresponding to SAP macropores and interface phases than to the (hypothetically homogenoeus) mortar phase as suggested in [334]. In this way more realistic crack patterns were obtained for the capillary water absorption simulations. In the literature, it is found that SAP act as crack initiator and are available upon liquid intrusion [335, 336]. The resulting cracked elements were assigned crack widths of 200 μm as the ones measured at the tip by Snoeck et al. [157]. This implies a mismatch of 40 μm in internal crack width between experimental specimens at a crack depth of 16 mm and the simulated 16 mm-deep crack, for a cracked volume difference of 9 %. Thereafter the damaged lattice elements were assigned transport properties calculated following the formulation explained in Equation 5.12.

The horizontal water profiles measured through Neutron Imaging in three cracked mortar samples from mix design B1.0 were compared to the simulated results at 1, 5, 15, 30 and 60 minutes of capillary water absorption in Figure 6.6. The experimental profiles were measured at heights not in correspondence of the reinforcement where the porosity of the material at the mortar-reinforcement interface may be different from the bulk matrix porosity. In the simulated profiles as well as in the NI profiles, the data points correspond to the moisture content averaged through the thickness of the mortar. Therefore localized anomalies on the horizontal water penetration due to the presence of superabsorbent polymers are smoothed and partially lost.

From the comparison between the profiles, there seems to be a very close agreement between experimental and simulated profiles. The penetration of the wetting front perpendicular to cracks as well as the moisture content distribution are captured well by the model. In the model the retardation of the water front penetration is due to swollen SAP in the cracks as well as those embedded in the matrix. To discriminate the role of hydrogel formation in the crack on the retardation of the water penetration perpendicular to cracks in Figure 6.7 a comparison is reported of three simulated results in: cracked mortar without SAP (REF), cracked mortar with matrix-embedded SAP only (REFs) and cracked mortar with embedded and in-the-crack SAP (B1.0). The three of them are simulated with same input parameters D_0, p and θ_0 so that the transport in the cementitious matrix occurs in the same fashion.

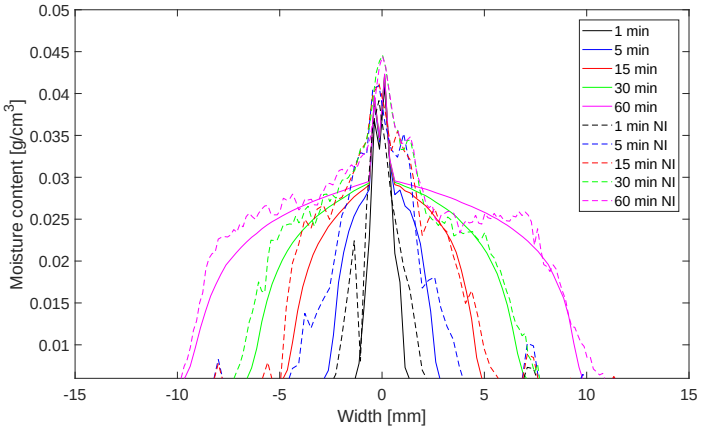

Figure 6.6: Horizontal water profiles in B1.0 at 1, 5, 15, 30 and 60 minutes of capillary absorption of water, measured through NI and simulated.

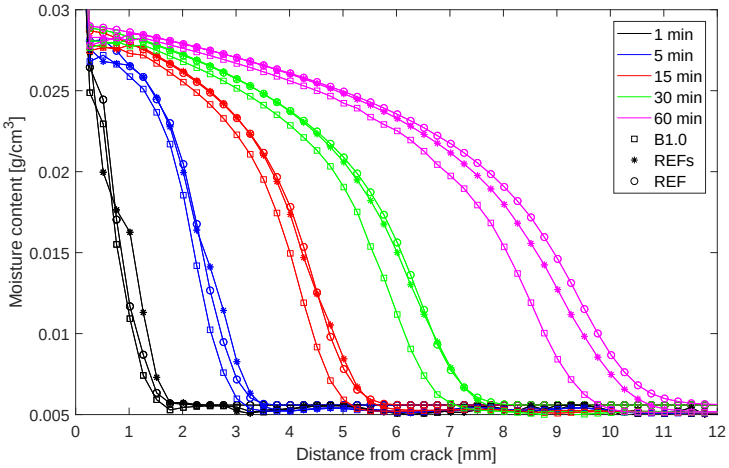

Figure 6.7: Simulated horizontal moisture profiles of cracked mortar: without SAP (REF), with matrix-embedded SAP only (REFs) and with embedded and in-the-crack SAP (B1.0).

Modest but tangible differences can be noticed in water penetration and moisture contents between B1.0 samples and the reference mortar with no admixtures (REF) since the beginning of the simulation, which are accentuated over time as seen at 60 *min*. The contribution of the embedded SAP on delaying the penetration of the water front is subtler and can be just observed after 60 minutes of capillary absorption of water for the matrix transport properties studied herein. For practical implications it can be considered negligible.

It can be observed from the results shown in Figure 6.6 and Figure 6.7 that the self-sealing performance of B1.0 was modest when compared to a reference plain mortar with same transport properties and initial conditions. The authors of this experimental study

[157] noticed that their results were somehow different from their estimates which were obtained by assuming an absorption capacity of the SAP upon contact with tap water of 148.9 g_{wat}/g_{SAP} while in the simulations we use a value of 12.193 g_{wat}/g_{SAP}.

6.5 Parametric study of crack self-sealing and discussion

In this section, parameters such as absorption capacity of the superabsorbent polymers under constraint, their dosage in the cementitious material and the crack width are studied through simulations with the developed model. In all the simulations the transport properties of the mortar matrix are invariants, as well as their relative input parameters, with values as described in the previous section. The objective is to discuss the influence of these factors on crack self-sealing and to provide recommendations for the design of cement-based materials with SAP for self-sealing purposes.

6.5.1 Influence of SAP absorption capacity in the crack

When visualizing the swollen gel in the crack from different experimental studies it is obvious that the self-sealing effect provided by these polymers depends strongly on their absorption capacity under constraint. Lee and co-authors [185] found generous formation of hydrogel in the cracks coming from highly irregular SAP particles as observed through light microscopy while Hong and Choi [71] employed X-ray tomography to observe the swelling of spherical SAP particles and concluded that this was limited to the volume ascribed by the cracked macropore. Spherical SAP possess a high surface tension due to the polymerization technique through which they are produced (inversion polymerization). Irregular, bulk polymerized SAP, seem to be more flexible.

Furthermore, this swelling capacity fluctuates when subjected to wetting–drying cycles as demonstrated in a study by Lee et al. [94] where the authors explain the reduction of swelling capacity not only due to calcium ions binding in the polymeric chains but also the eventual recovery due to ion exchange in alkaline solutions. Hence, the influence of different levels of swelling capacity in the crack on the mechanism is also simulated in this section.

Figure 6.8 shows the moisture contours and swollen gel in the crack in mortar for different absorption capacities of the SAP. In the model this is accounted for by setting a cuttoff to the maximum absorption of water and subsequent swelling by the particles.

The moisture contours show that the water penetration from the crack becomes slower as the amount of swollen gel increases. Furthermore, the distribution of the moisture content changes dramatically. The zones with higher degree of saturation 0.8-1.0 become narrower and correspondingly the zones with saturation levels between 0.6 and 0.8 become wider. This effect is probably related to the fact that as the swollen gel volume increases in the crack, bigger portions of the crack surfaces come into contact with gel and locally water penetration from those surfaces is slowed down. As a consequence, there exist gradients of moisture along the crack walls and not only perpendicular to them. As the swollen gel increases in volume the latter effect becomes more severe in localized zones around the SAP (see Figure 6.8d).

The re-swelling capacity of the SAP particles in the crack is not straight forward to

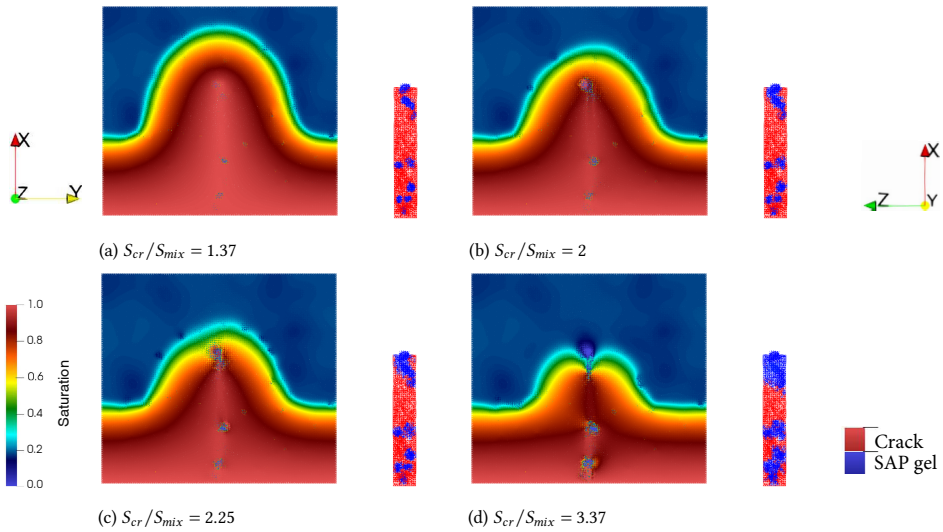

Figure 6.8: Moisture contours and respective swollen gel in the crack after 60 min of water absorption in mortar with 1.0 % of SAP by weight of cement, crack width of 200 μm and different swelling ratios of the SAP in the crack: a) 1.37, b) 2, c) 2.25 and d) 3.37.

6

measure, especially when coupled with the absorption of water under pressure of the SAP. Some guidelines have been summarized in [337].

6.5.2 Influence of SAP dosage

Perhaps the most obvious way of increasing the likelihood of obtaining self-sealing effect is to increase the amount of SAP in the cementitious mixture. The presence of increasing evenly distributed macropores leads to stress concentrations around them and therefore to a higher chance of exposing more of these macropores along the crack path [334]. Nevertheless, at the levels of incorporation of SAP for the purpose of self-sealing, typically between 0.5 % and 1.0 % by weight of cement, decreases of the compressive strength in the order of 20 % to 40 % are generally obtained in mixtures with relatively high water-to-cement ratio [71, 328]. The latter effect is explained in the literature as due to the role of SAP as crack initiator, demonstrated by the observed swelling of the particles when exposed to moisture uptake. The negative effects on the mechanical properties of the material are unwanted because on one hand we have a material with high crack self-sealing capacity whereas on the other hand it is more prone to crack formation.

In Figure 6.9a, 6.9b and 6.9c three simulated mesostructures of SAP mortar are shown with 0.5 %, 1.0 % and 1.5 % by weight of cement. The SAP particles were parked randomly with Anm model by using the same seed. Thereafter, fracture lattice simulations were performed to obtain the cracked meshes. Figure 6.9d, 6.9e and 6.9f show the moisture contours after 60 minutes of capillary absorption simulations on these cracked meshes, whereas Figure 6.9d, 6.9e and 6.9f show the cracked space of the respective mesostructures and the volume occupied by SAP gel. A fixed ratio between absorption capacity of the SAP

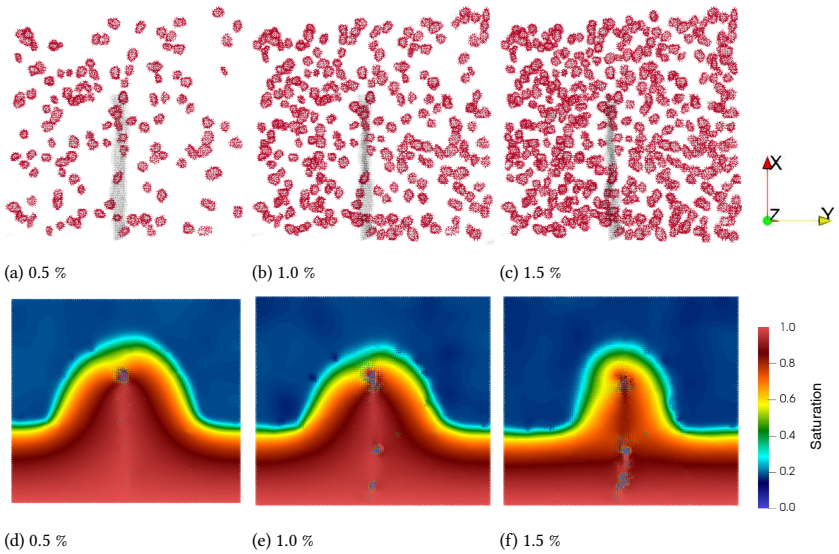

Figure 6.9: Cracked mesostructures -a, b, c-, and moisture contours -d, e, f- of mortar with SAP in dosages 0.5 %, 1.0 % and 1.5 % by weight of cement, after 60 minutes of capillary water absorption. Crack width was kept as 200 μm and swelling ratio of 2.25.

in the crack and during mixing of 2.25 was used in the three simulations. Input parameters for the simulations were identical.

Noticeable differences can be observed by comparing the simulated results of mortars with different SAP dosages. The role of embedded SAP in the capillary absorption of water in the matrix can be studied from the vertical water penetration. In a study from [320], the authors noticed that for certain transport properties of the matrix, embedded SAP could actually behave as impervious inclusions after complete swelling in the macropore. Similar to how aggregates influence the transport of moisture in concrete [338], such inclusions might delay the wetting front penetration with respect to a reference mortar with same transport properties and no SAP. For increasing number of embedded SAP, this effect was expected to be accentuated. Notwhithstanding in the simulations, this effect accounts only for a small contribution on the retardation of the wetting front as well as for the water content distribution. This contribution is also present as the wetting front advances horizontally yet the influence of the transport in the crack is still present even when the dosage is kept constant as shown previously in Figure 6.7.

The moisture contours show decreasing penetration depths of the water front for increasing dosages of SAP in the mortars and therefore higher amounts of SAP particles in the crack. This does not come as a surprise since it is expected that a higher volume of hydrogel forming in the crack contributes to decreasing the flow of water in the crack. Ideally, a plug of hydrogel would form at a certain height along the crack depth and completely stop the flow of water upwards. In the simulations shown in Figure 6.9, this happens only for the mortar containing 1.5 % of SAP by weight of cement. In the other cases, although hydrogel is formed they form separate clusters which locally prevent the

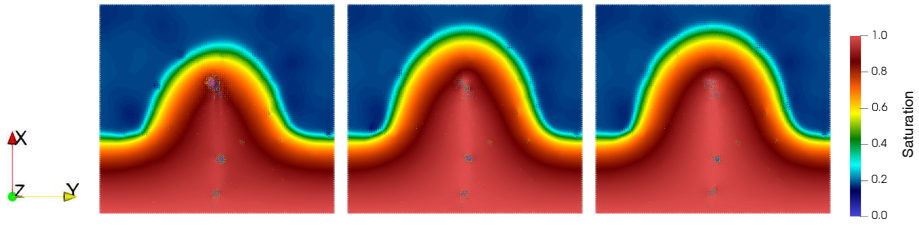

(a) $w_{cr} = 200\ \mu m$ (b) $w_{cr} = 300\ \mu m$ (c) $w_{cr} = 500\ \mu m$

Figure 6.10: Moisture contours of cracked mortar with SAP for different crack widths -a) 200 μm, b) 300 μm, c) 500 μm- after 60 minutes of capillary water absorption. Dosage and swelling ratio were kept constant as 1.0 % and 2.25, respectively

penetration of water into the matrix , while capillary rise of water in the crack still occurs.

As seen in the case of increasing swelling ratios of the SAP, here too the zones with saturation in the range 0.8-1 decrease in area for higher dosages of SAP in the simulated mortars.

6.5.3 Influence of crack width

The choice of SAP size, dosage and swelling and absorption capacity during mixing and in neutral to acidic solutions govern the crack–sealing capacity of the cementitious system. Yet, this sealing capacity will be limited as the crack widths under consideration are increased. It is important thus to evaluate how the self-sealing effect of SAP in the crack, in terms of water penetration into the cementitious matrix, changes with increasing crack widths.

Capillary absorption of water is again simulated for cracked mortar with SAP. Three different crack widths are used in the simulations: 200 μm, 300 μm and 500 μm. It is assumed that the transport properties of cracked elements is not affected by the crack width and just the proportion between cracked volume and swollen gel influences the variation in water permeation into the matrix. The aforementioned assumption would not be appropriate for crack widths above 500 μm since the capillary rise in the crack and thus the hydraulic diffusivity of the cracked elements would certainly be lower as shown in [339], which is not accounted for in Equation 5.12.In Figure 6.10 an example of such changes arising from the simulations results at $t = 60\ min$ are shown. The swelling in the crack to swelling during mixing ratio was 2.25 and the SAP dosage was 1.0 %.

As expected, the simulation results show that for wider cracks, there is less blockage of water in the crack and therefore water can penetrate more readily into the matrix. In particular, almost indistinguishable differences where found when the crack is wider than 300 μm for these specific material parameters. Also the anomalies in the moisture content distribution are gradually lost with an increase of the crack width.

6.5.4 Discussion

Figure 6.11 reports the horizontal water penetration depth in cracked mortar with SAP normalized to the penetration depth of its reference without water swelling admixtures,

h_{pen} (Equation 6.8), as a function of the chosen SAP dosage and ratio of swelling capacity in the crack to swelling capacity during mixing.

$$h_{pen} = \frac{d_{REF} - d_{SAP}}{d_{REF}} \tag{6.8}$$

According to the above definition h_{pen} valued 1 translates to a fully blocked crack water flow, while a value of 0 means that no difference is found between the reference mortar and the SAP mortar in terms of water front penetration. Therefore h_{pen} can be interpreted as a crack self-sealing efficiency. In the graphs in Figure 6.11, h_{pen} is reported for different crack widths (200 μm -a-, 300 μm -b- and 500 μm -c-).

If we compare the surface plots corresponding to simulations with different crack widths some observations can be made. Whereas 100 % sealing can be obtained in mortar with crack width of 200 μm and for a dosage of 1.5 % SAP and swelling ratio of 3.37, as the crack width increases from 200 μm to 300 μm and 500 μm, the obtained healing promptly decreased to 50 % and 30 %, respectively for the same parameters. Likewise, fewer combinations of those parameters yield substantial reductions in water penetration as cracks widen. However in this parametric analysis the self-sealing capacity of mortar with SAP is underestimated for wedge-like cracks since the error computed in the calculation of cracked space volume increases for rising values of the crack tip as discussed in Section 6.4.2.

By studying the surface plot corresponding to a crack width of 200 μm in 6.11a we can observe that for small values of the swelling ratio, such as the ones found for SAP B,1.37, increasing the dosage in the mortar from 0.5 m% to 1.5 m% does little to increase the self-sealing efficiency, resulting in an improvement from 4.5 % to only 10.2 %. On the other hand, for mortars containing as little as 0.5 m% of SAP, an increase on swelling ratio from 1.37 to 3.37 results in an improved self-sealing capacity that goes from 4.5 % to 21.6 %. This behaviour seems to become less important as the crack width increases where the only combinations of dosage and swelling ratio yielding above 10 % sealing efficiency are those higher than 1.0 m% and 2.25, respectively. In general, within the chosen range of analyzed parameters, increasing the swelling ratio results in more efficient improvements on the swelling capacity than increasing the dosage within the suggested range. This observation implies that when choosing appropriate SAP for the purpose of crack self-sealing attention should be focused on the reduction of the absorption capacity during mixing as much as possible, that bulkly polymerized SAP are to be preferred to spherical ones because of the higher elastic properties and better deformation capacity and/or that the swelling capacity in neutral or acidic of the polymer be boosted. The capacity of swelling and absorption of SAP are properties which depend mainly on their composition and employed production method. Therefore their design can be steered for the purpose of self-sealing in cement-based materials according to what has been discussed in this section.

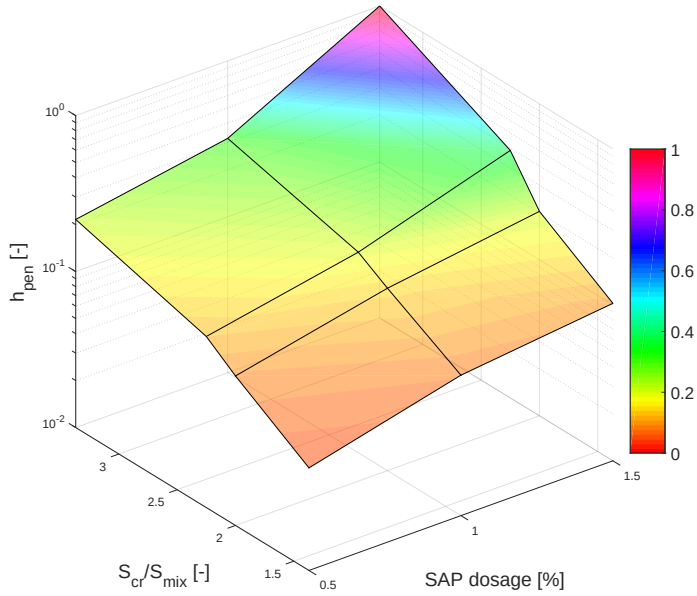

(a) $w_{cr} = 200\ \mu m$

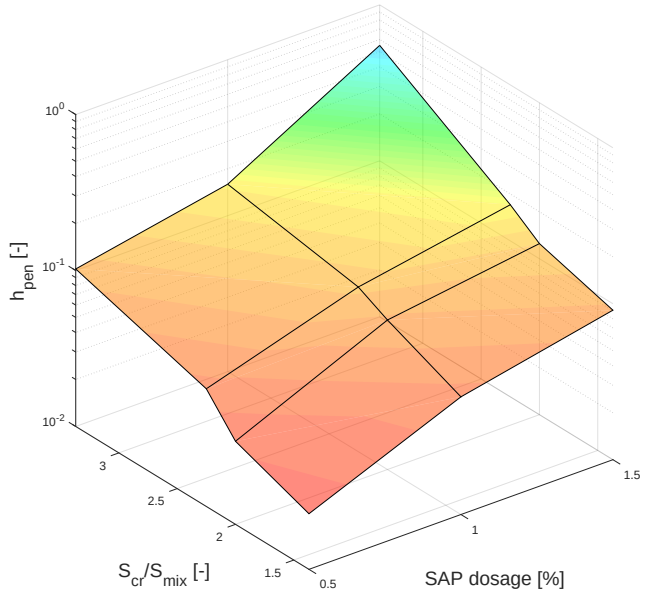

(b) $w_{cr} = 300\ \mu m$

Figure 6.11: Parametric analysis of h_{pen} as a function of SAP dosage and swelling ratio for crack widths 200 μm a), 300 μm b) and 500 μm c).

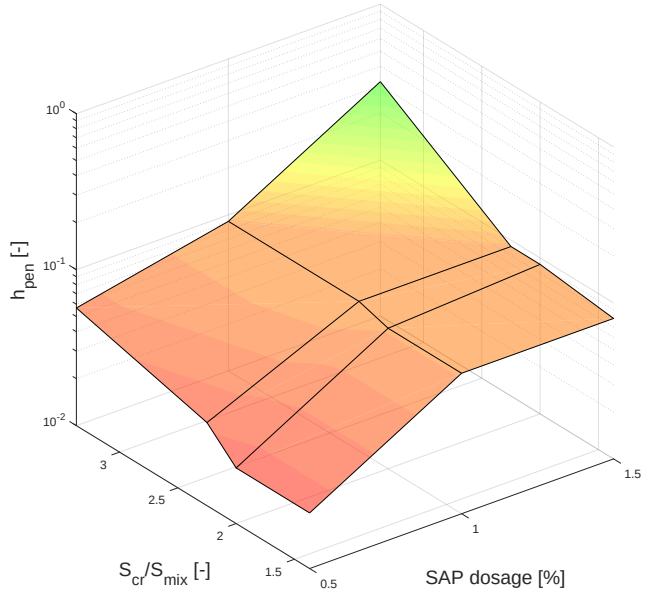

(c) $w_{cr} = 500\ \mu m$

Figure 6.11: Parametric analysis of h_{pen} as a function of SAP dosage and swelling ratio for crack widths 200 μm a), 300 μm b) and 500 μm c).

6.6 Conclusions

A numerical model is proposed in this chapter to simulate capillary water absorption in unsaturated sound and cracked cementitious materials with SAP. The results of the simulations yield the spatial moisture content distribution in the mortar during capillary absorption, as well as the water absorption of SAP in the matrix and in the crack and their swelling evolution. The model couples the Richards equation for liquid transport in porous media, the exponential equation describing the hydraulic diffusivity as a function of moisture content in porous building materials and the water absorption kinetics law for SAP particles modeled as sink terms. Lattice-type FEM was used to model the aforementioned mathematical problem. Distinction of transport properties was made explicitly between sound matrix, cracked domain and SAP particles. In the paper, the proposed model was validated first using experimental results and experimentally-informed input parameters available from literature or from experiments performed herein. The validated model was then used to investigate the influence of SAP absorption capacity and dosage in the mortar for different crack widths.

The following conclusions can be drawn from the comparison between experimental and simulated results and from the parametrical analysis performed herein:

- If reswelling capacity of the SAP particles embedded in the matrix is considered completely recovered, SAP particles provoke two main anomalies in the moisture transport within a cementitious material i) the sorptivity of the composite increases

because water uptake in the SAP occurs much faster than in the matrix and the polymer can absorb more water by unit volume than the plain mortar and ii) delays in the penetration depth of the wetting front are obtained due to the presence of almost impervious swollen gel, similar to the effect provoked by aggregates in concrete [320, 338].

- When reducing the nominal water absorption capacity of the SAP particles in the crack according to X-Ray tomography results, simulated results of capillary water absorption in cracked mortar with SAP matched very well the experimental ones. The poorer swelling capacity of the SAP in the crack can be explained more likely by the further cross linking and strong complexation in the polymer during mixing due to absorption of calcium ions [94, 328]. In this regard current practices to estimate the necessary dosage of SAP, based on measured absorption capacity of SAP in the crack must be modified i.e. by subjecting the polymers to cement filtrate absorption for a certain amount of time and only then to water absorption. Another cause of this deviation from measured free water swelling capacity of SAP can also be due to the constraint of the polymer between the crack walls.
- The validation of the model with experimental results allowed to look into detail at the effects of crack-self-sealing during capillary water absorption in cracked mortar via the simulations . There seems to be two main effects on the water transport from the cracks into the matrix: i) the penetration depth of the wetting front is delayed when hydrogel forms in the cracks and ii) moisture content distribution changes dramatically and zones with high degree of saturation are decreased. The latter can be explained by the localized covering of the crack surface with hydrogel and the existence of moisture gradients along the crack walls and not only predominantly perpendicular to them.
- The blockage of capillary rise in the crack only happens when there is a hydrogel plug occupying a cracked volume all across the specimen at a certain height, otherwise only the effects as described above are noticed. The occurrence of complete blockage of the capillary rise in the crack was, as expected, increased with increasing amount of SAP in the mixture and with a higher ratio of swelling capacity in the crack to swelling capacity during mixing.
- When designing a cementitious mix with SAP, simulated results show that choosing appropriate SAP admixtures results in a more efficient crack self-sealing performance rather than increasing SAP dosage in the mix design. The choice of SAP to be used for crack self-sealing and (allegedly) self-healing, must be based upon increasing the swelling ratio. An option could be to limit the absorption and swelling of the polymer during mixing of the cement-based materials not only for the aforementioned reason but also to control the reduction of the mechanical properties. Nevertheless, this limit should not be accompanied by complexation in the polymer due to the intake of calcium ions not to affect the swelling of the particles in the incoming crack water. A second option would be to select SAP with higher swelling capacity in neutral to acidic media. In any case, bulkly polymerized SAP should be preferred to spherical ones.

IV

Conclusions

7

Conclusion

In vain have you acquired knowledge
if you have not imparted it to others.
Deuteronomy Rabbah

In this chapter, a retrospection into the research done within the present dissertation is given. Afterwards, the general conclusions and the contributions of this research are outlined and discussed. Finally, recommendations are offered for future studies and applications.

7.1 Retrospection

In recent years, the use of self-healing cementitious systems has been proposed as alternative to or at least aid for traditional concrete repair, as well as to increase the service life of concrete structures. Several types of mechanisms for the achievement of autonomous crack sealing have been studied in the literature, for the most from an experimental standpoint. Because the functioning of these composite materials is the result of complex physico-chemo-mechanical processes, experimental investigations often lack exhaustiveness regarding the parameters governing the efficiency of the specific self-healing mechanism. The use of models for the study and optimization of such self-healing cement-based materials can then complement existing research to ultimately accelerate the design of these materials for their prompt application in engineering practice.

In this work, a modelling framework is proposed to study capsule-based self-healing cement-based systems. Although the models used herein are applied and validated to specific self-healing cement-based materials of this sort, is rather the methodology that can be feasibly extrapolated to other specific materials. Furthermore, general guidelines regarding capsule-based self-healing cementitious materials can also be used for more than one of these materials. The main work is divided in three subjects, each encompassing specific stages of the typical capsule-based self-healing process. Namely, a first stage in which the mechanical triggering of capsules is numerically studied, as well as the dual role of the capsules in the overall mechanical behaviour of the composite. The second stage regards (time-dependent) self-healing efficiency assessment through simulations of capillary water absorption in the cracked material. Finally, the last stage regards the modelling of a self-healing process itself.

In Chapter 1, the background and motivation for the current dissertation are given. The objectives and the scope of the research are then layed out based on the latter. A general description of the research methodology used throughout is also reported. Finally, the dissertation outline is presented to guide the reader.

In Chapter 2, a review of the literature regarding the main aspects of self-healing concrete is presented. Furthermore, a critical review is also performed of the existing literature on modelling of mechanically triggered healing and of the healing processes. It was identified that capsule-based mineral-producing self-healing mechanisms are the most developed, versatile and promising self-healing technology thus far. Moreover, it is advised in the literature that single-parallel-walled cracks be used for the study of self-healing efficiency in cement-based materials. Although some work has been done regarding the modelling of mechanical triggering of capsules, available optimization studies do not consider the effects of capsules on the mechanical behaviour of the self-healing composite. On the other hand, few studies are available regarding the modelling of the mineral healing processes. Among the different types of models for simulating this type of healing in cracks, mechanistic modelling is the only one with predictive and descriptive capabilities.

In Chapter 3, the interface between different types of bacteria-embedded self-healing Polylactic acid (PLA) capsules and cement paste is investigated. Particularly, the changes in microstructure and mechanical properties of the interface with respect to bulk cement paste were studied. First, nanoindentation was performed to obtain maps of hardness and elastic modulus in the interfaces. Lattice modelling of uniaxial tensile test on the mapped locations was performed then to obtain the overall tensile strength and stiffness

of the interface. Moreover, hydrates assemblage and chemical composition around the PLA particles were studied through Backscattering Electron images and Energy Dispersive X-ray Spectroscopy. The results suggest that PLA can be tailored to optimize the physico-mechanical properties of the interface and hence, the mechanical behaviour and triggering efficiency of the self-healing system. The ratios between resulting tensile strength and elastic modulus of the interface with respect to bulk paste were obtained for each PLA type. The presented methodology can be used as input for fracture modelling of cement paste containing PLA capsules.

In Chapter 4, an existing 3D mesoscale lattice model is used to simulate uniaxial tensile test of a self-healing system composed of cement paste, bacteria-containing poly-lactic acid (PLA) capsules and their interface. The ratios between tensile strength and elastic modulus of the interface with respect to bulk cement paste, obtained in the previous chapter for three different PLA types, were used as input for the mesoscale model. The self-healing and reference cement pastes were imaged through X-ray micro Computed Tomography before and after fracture to obtain the capsules distribution to input in the mesoscale model and the fracture surface for validation, respectively. The experimental and simulated stress-strain curves showed very good correspondence in the elastic phase, hence validating the proposed model for that stage. An exhaustive numerical investigation of the material was performed then to analyse the influence of dosage, size and shape of the PLA capsules, as well as of the interface properties on the mechanical behaviour of the composite and the triggering of the PLA capsules. The results show that interface properties close to but lower than the cement matrix do not entail substantial losses of tensile strength and elastic modulus, whereas the amount of triggered capsules is maximized. Optimum dosage, shape and size of the PLA capsules were also obtained.

In Chapter 5, capillary water absorption in sound and cracked mortar, with and without superabsorbent poymers is investigated. A 3D lattice transport model for the simulation of capillary water absorption in sound cement-based materials is presented. The model is thought of for obtaining the cracked capillary water absorption before and after a generic healing event, thus allowing the computation of the healing efficiency related to this functionality of the material. A tailored experimental methodology, involving the use of dynamic XμCT, is used for validation and input of the previous model. Through the experiments, local effects within the moisture uptake process were observed. Furthermore, the morphological properties of the cracks and the wetting front position and water content at saturation were correlated for cracked samples. The validated model was used to perform a parametric study on the role of porosity and initial moisture content on the capillary moisture transport within the sound mortar.

In Chapter 6, the capillary absorption model presented in the previous chapter was expanded to simulate capillary absorption of water in sound and cracked cement-based materials containing SAP, in order to design such self-sealing systems in an efficient way. The model choices regarding SAP absorption and swelling kinetics, as well as their interaction with the surrounding mortar matrix, are based on the observations made from the experimental results presented in Chapter 5. The numerical results yield the moisture content distribution in cracked and sound domain, as well as the absorption and swelling of SAP embedded in the matrix and in the crack. The performance of the model was validated by using the results and supplementary data of an experiment available from the

literature, as well as experimentally-informed input parameters. The validated model was then used to investigate the role of SAP properties and dosage in cementitious mixtures, on the water penetration into the material from cracks. Furthermore different crack widths were considered in the simulations. The model shows good agreement with experimental results. From the numerical investigation, guidelines are suggested for the design of the studied composites.

7.2 Conclusions

The general conclusions evinced by the research presented in this dissertation are presented below.

1. When considering capsule-based self-healing cementitious systems, there exists the possibility that chemical and/or physicial interactions of the capsules may induce changes in the physico-mechanical properties of the interface transition zone.

   As studied here, for the case of PLA capsules in Chapter 3, even different manufacturing processes of the capsules resulted in different kinetics of hydration, hydrates assemblage, dimensions and ultimately micromechanical properties of the Portland cement paste within the interface zone (herein counterdistinguished as influence zone). Specifics onto the causes of such modifications in the case of PLA capsules, yield useful advice on designing manufacturing processes that can limit leaching of certain species from the capsules towards the surrounding matrix (such as phosphorus and chlorides). The changes in the physico-mechanical properties of the composite can be detrimental, as encountered in the aforementioned Chapter 3, where the inclusion of some capsule types directly resulted in dramatically subpar tensile strength and elastic modulus of the interface zone when compared to the bulk cement paste with decreases of up to 62 %. Furthermore, the thickness of the influence zones of the studied self-healing capsules were considerably larger than those typically found for inert inclusions and ranging between 110 to 260 μm.

2. The mechanical properties and extension of the influence zone around self-healing capsules may influence the tensile strength and elastic modulus of the overall capsule-based cementitious composite.

   As studied experimentally and numerically in Chapter 4 for the case of PLA capsules, changes in the tensile microstrength and elastic modulus of the interface zone made a difference on the overall composite strength and stiffness, which allowed the validation of the model to simulate uniaxial tensile tests on this type of heterogeneous material.

3. Lattice fracture modelling is suitable for multi-scale study of the mechanical behaviour of capsule-based self-healing systems.

   The local mechanical properties of different phases that are present at the mesoscale can be studied through experimentally-informed micro-mechanical lattice fracture simulations, as done in Chapter 3. Ultimately, also the behaviour of the overall capsule-based composite can be investigated through mesoscale lattice fracture simulations, as shown in Chapter 4. In fact, at the latter scale, not only the influence of

capsules on mechanical properties can be investigated, but also the mechanical triggering of the capsules themselves. Furthermore, the influence of several parameters could be studied such as dosage, dimensions and shape of the capsules, as well as different properties of the influence zone. As presented in Chapter 4, an exhaustive numerical campaign encompassing certain ranges of the aforementioned parameters could be carried out to understand the influence of several material design parameters on the mechanical properties at the mesoscale.

4. Dual 4D X-ray micro tomography can be used quantitatively to obtain moisture distribution in cement-based materials overtime, as well as qualitatively to understand the behaviour of mortar with/or without SAP during capillary water absorption.

   Despite the limitations in spatial resolution, attenuation differences in the same material before and after water absorption are enough to monitor said water absorption process, given certain knowledge on the material, such as porosity and initial mositure content. In fact, in Chapter 5, the differences in kinetics of the water front advance in mortars with different w/c ratios could be clearly detected and quantified by the experimental methodology. Furthermore, the dual 4D X-ray micro tomography allowed the direct observation of global and local phenomena during water absorption in mortars with SAP. Regarding the former, through segmentation of the net moisture in mortar and SAP, it was possible to quantify the transport properties of the sole mortar matrix when SAP are added, as well as the kinetics of water absorption of the embedded SAP. From the former results, it could be confirmed that mortar flow table test is appropriate to estimate the water absorbed by SAP when mixed into the mortar. From the earlier results, it was highlighted that complexation of the embedded SAP occurred, with consequently longer times for reaching swelling equilibrium. Notwithstanding, it was directly observed that completely embedded SAPs do absorbe moisture from the surrounding mortar matrix. Their absorption/swelling kinetics seemed to increase with rising saturation levels in the surrounding mortar and even faster yet when in direct contact with the water pool at the bottom of the sample.

5. Lattice transport model can be used to simulate capillary water absorption in sound and cracked mortar to predict the water penetration depth and moisture content distribution.

   In Chapter 5, while studying such phenomena in sound mortar the numerical results could be used to complement the experimental findings whereby different parameters were linked in practice (such as porosity and moisture content) to study the sole influence of one parameter change at the time. This exercise highlighted the importance of accurately inputting the initial moisture content and properly conditioning the samples prior to capillary water absorption measurements, which otherwise may result in disproportionate errors on water front position measurements/numerical predictions. In the case of simulations in cracked mortar shown in Chapter 5, it could be concluded that the chosen cubic law of moisture diffusivity in the crack successfully predicts the moisture penetration depth perpendicular to the crack for the range of crack widths herein studied. However, the crack diffusivity law does

not reflect how crack width differences affect the moisture content at equilibrium (and thus the saturation).

6. The numerical model proposed herein to model capillary moisture transport in sound and cracked mortar with SAP was validated with experimental data and shows that the addition of SAP effects changes in the sorptivity rate of the mortar, as well as on the local and global moisture distribution within the composite.

   In sound mortar, where SAP are present for the purposes of crack self-sealing, the numerical model shows slight delays in penetration depth and overall increased sorptivity rates. In the case of cracked self-sealing mortar with SAP, the numerical results show local delays in moisture penetration depth perpendicular to the crack surfaces, changes in moisture content distribution and zones with lower maximum degree of saturation if the admixtures can block portions of the crack surface and generate moisture gradients within the crack.

7. The parametric study of mortar crack self-sealing by SAP allowed for a quantitative assessment of the sealing efficiency of the composite for different crack widths, absorption by SAP in the crack relative to their absorption during mixing and dosage of SAP.

   From the parametric simulations studying different ranges of crack width, SAP dosage and swelling/absorption capacity relative to that during mixing, and their combination it is evinced that to increase the self-sealing efficiency the design of these composites must be executed based on expected crack widths and complexation degree during mixing and as the last fine-tuning resource, their dosage.

7.3 Contribution of this study

Herein, an indirect methodology to obtain the interface micromechanical properties between any given self-healing capsule and surrounding cement paste was proposed. Whereas the micromechanical testing of elastic modulus and splitting tensile strength of cement paste is (altough complex) possible, the direct measuring of the same properties at the interface between inclusions (i.e. self-healing capsules) and cement paste are more complicated due to, for example, handling during sample preparation which may influence the measured properties. In this thesis, the combination of ESEM imaging, grid nanoindentation and 2D lattice fracture modelling was used instead. The mapping of porosity and hydration degree around the capsules allowed to define the thickness of their interface within the cement paste, not only for the spatial discretization of this phase but also to identify the phase where fracture is most likely to occur. On the other hand, the grid nanoindentation methodology yielded a map of elastic modulus and hardness of the interface zone, as well as within the bulk cement paste. The latter datapoints were assigned stochastically to the lattice nodes belonging to the interface zone and the bulk cement paste, respectively. Finally, 2D lattice fracture simulations using the aforementioned input provided the valuable elastic moduli and tensile strengths of the different interphases here studied, as well as of the bulk cement paste. A similar methodology can be easily translated into other types of capsules to be used in cement-based matrices.

Experimentally-informed micromechanical properties of the different phases and the true mesostructure of a capsule-based self-healing cement paste sample were used to validate lattice fracture modelling during direct tensile test of such self-healing system. First, X-ray microtomography of a notched self-healing cement paste cube was performed before and after a direct tensile test. The obtained 3D distributions capsules, cement paste and their interface were binarized and used to overlay on the sample discretization with lattice elements. The micromechanical properties of one of the previosuly studied self-healing systems were input stochastically for each phase. To reduce the computational time a linear-elastic constitutive law was used. The validated model was then used to study the influence of several parameters such as capsule dosage, dimensions, and shape, as well as the interface properties on the elastic modulus and tensile strength of the self-healing cement paste. Guidelines for design of capsules for self-healing from a trigering standpoint were suggested.

Time-resolved X-ray microtomography was used to monitor 3D moisture transport in cracked mortar and in sound mortar with SAP. In both cases, X-ray micro tomography was performed before and during capillary water absorption in mortar samples, for which an appropriate sample cell was designed to enable the imaging of the process and the process itself. Whereas the settings of the initial scan (at the dry state) were optimized to increase resolution and capture the 3D mesostructure of the samples, wet scans settings were optimized to obtain the best possible resolution in short enough scans (18 seconds) which allowed to capture the kinetics of the process. Quantification of moisture changes was possible through the linear attenuation changes. The time and space resolution of the scans during capillary moisture absorption in mortar with SAP were useful to understand the kinetics of water absorption of SAP embedded within the mortar matrix, as well as how the kinetics of moisture transport in the matrix are affected as consequence. The joint use of the aforementioned experimental methodology and of the transport lattice model could shed light into often overlooked aspects of the kinetics of water absorption in plain mortar. Namely, the individual influence of typically linked properties, such as the initial moisture content and the porosity, was clarified.

A mechanistic numerical model was proposed to model moisture transport in sound and cracked cement-basd materials with water-absorbing admixtures (i.e. SAP). Upon validation, the results show that simulations of capillary water absorption can be used to predict crack healing efficiency. For any other cementitious self-healing systems, the model could be used when the quantification and distribution of healing products in the cracks are known i.e. 3D experimental imaging or through simulated healing.

The results of this work highlight the importance of considering all stages of a cementitious self-healing system (cracking, self-healing process, self-healing efficiency assessment) in order to understand and predict its performance.

7.4 Recommendations for further research

While carrying out the research presented in this dissertation, some new research questions have arised. The following recommendations are given for continuing the work related to experimental and modelling investigation of cementitious self-healing composites:

- Whenever mapping of the micromechanical properties of the ITZ between capsule and cementitious matrix (Chapter 3) through grid nanoindentation is not possible, other experimental methodologies should be explored in place thereof. The quantification of ITZ microdamage through microscopy and subsequent use of a calibrating damage-factor, either implicitely or explicitely, in meso-scale simulations of the composite could be an alternative. The correlation between X-ray micro CT grayvalues and nanoindentation of cement paste was demonstrated and used in [340] to map micromechanical properties three-dimensionally. Hence, X-ray micro CT could be an alternative route for mapping the micromechanical properties of ITZ.
- In order to accurately quantify the fracture energy of capsule-based self-healing cementitious composites, the use of a multilinear constitutive law for the lattice beams should be employed in the mesoscale simulations in future studies. Furthermore, to account for the heterogeneities in the cement paste matrix, also a stochastic distribution of the cement paste micromechanical properties should be used as input.
- The expansion of the lattice moisture transport model to account for the pressure of the water given a certain crack width could help understanding their influence on the saturation distribution in the matrix surrounding the crack. This can have major repercussions as saturation levels affect the kinetics of some degradation mechanisms, as well as the kinetics of healing phenomena where dissolution of portlandite or further hydration of unhydrated cement grains is involved.
- The complexation of SAP should be investigated more in depth. Furthermore, the number of absorption and desorption cycles necessary for the recovery of the SAP swelling capacity should be normalized as an important property when intended for use as self-sealing/ self-healing additives in cement-based materials.
- In the future, the SAP absorption and swelling kinetics herein proposed should be included in a multi-species advective-diffusive-reactive model to simulate the autogenous self-healing boost provided by these water-retaining admixtures.

References

[1] J. M. Crow. The concrete conundrum. *Chemistry World*, 5(3):62–66, 2008.

[2] W. Wang, J. Liu, F. Agostini, C. A. Davy, F. Skoczylas, and D. Corvez. Durability of an ultra high performance fiber reinforced concrete (uhpfrc) under progressive aging. *Cement and Concrete Research*, 55:1–13, 2014.

[3] J. Li, Z. Wu, C. Shi, Q. Yuan, and Z. Zhang. Durability of ultra-high performance concrete–a review. *Construction and Building Materials*, 255:119296, 2020.

[4] R. B. Polder, W. H. A. Peelen, and W. M. G. Courage. Non-traditional assessment and maintenance methods for aging concrete structures–technical and non-technical issues. *Materials and Corrosion*, 63(12):1147–1153, 2012.

[5] K. Van Breugel. Is there a market for self-healing cement-based materials. In *Proceedings of the first international conference on self-healing materials*, pages 1–9, 2007.

[6] N. Hearn. Self-sealing, autogenous healing and continued hydration: what is the difference? *Materials and structures*, 31(8):563–567, 1998.

[7] M. R. de Rooij, K. Van Tittelboom, N. De Belie, and E. Schlangen. *Self-healing Phenomena in Cement-Based Materials: State-of-the-Art Report of RILEM Technical Committee 221-SHC: Self-Healing Phenomena in Cement-Based Materials*. Springer Dordrecht Heidelberg New York London, 2013.

[8] Y. Yang, M. D. Lepech, E. Yang, and V. C. Li. Autogenous healing of engineered cementitious composites under wet–dry cycles. *Cement and Concrete Research*, 39(5):382–390, 2009.

[9] O. M. Jensen and P. Lura. Techniques and materials for internal water curing of concrete. *Materials and Structures*, 39(9):817–825, 2006.

[10] J. S. Kim and E. Schlangen. Super absorbent polymers to simulate self healing in ecc. In *2nd International Symposium on Service Life Design for Infrastructures, RILEM Publications SARL, Delft*, pages 849–858, 2010.

[11] D. Snoeck, K. Van Tittelboom, S. Steuperaert, P. Dubruel, and N. De Belie. Self-healing cementitious materials by the combination of microfibres and superabsorbent polymers. *Journal of Intelligent Material Systems and Structures*, 25(1):13–24, 2014.

[12] D. Snoeck and N. De Belie. From straw in bricks to modern use of microfibers in cementitious composites for improved autogenous healing–a review. *Construction and Building Materials*, 95:774–787, 2015.

[13] D. Palin, V. Wiktor, and H. M. Jonkers. Autogenous healing of marine exposed concrete: Characterization and quantification through visual crack closure. *Cement and Concrete Research*, 73:17–24, 2015.

[14] V. Wiktor and H. M. Jonkers. Quantification of crack-healing in novel bacteria-based self-healing concrete. *Cement and concrete composites*, 33(7):763–770, 2011.

[15] M. Roig-Flores, S. Moscato, P. Serna, and L. Ferrara. Self-healing capability of concrete with crystalline admixtures in different environments. *Construction and Building Materials*, 86:1–11, 2015.

[16] K. Sisomphon, O. Copuroglu, and E. A. B. Koenders. Self-healing of surface cracks in mortars with expansive additive and crystalline additive. *Cement and Concrete Composites*, 34(4):566–574, 2012.

[17] A. Danish, M. A. Mosaberpanah, and M. U. Salim. Past and present techniques of self-healing in cementitious materials: A critical review on efficiency of implemented treatments. *Journal of Materials Research and Technology*, 2020.

[18] Scopus. Analysis of search results for self-healing concrete between 1995 and 2024. https://www-scopus-com.tudelft.idm.oclc.org/term/analyzer.uri?sid=d9f469861c6e9e773388e92f42acd2af&origin=resultslist&src=s&s=TITLE-ABS-KEY%28Self-healing+concrete%29&sort=plf-f&sdt=b&sot=b&slSHpub.png=36&count=1286&analyzeResults=Analyze+results&txGid=8e8f3b88ca79d8022d974c6a14ab22a4, 2025.

[19] Scopus. Analysis of search results for self-healing concrete modelling/modeling between 1995 and 2024. https://www-scopus-com.tudelft.idm.oclc.org/term/analyzer.uri?sort=plf-f&src=s&sid=4ce1c379cefd1e4125d08d714f6aa17e&sot=a&sdt=a&sl=90&s=%28TITLE-ABS-KEY%28self+AND+healing%29+AND+TITLE-ABS-KEY%28concrete%29+AND+TITLE-ABS-KEY%28modelling%29%29&origin=resultslist&count=10&analyzeResults=Analyze+results, 2025.

[20] Z. Qian, E. J. Garboczi, G. Ye, and E. Schlangen. Anm: a geometrical model for the composite structure of mortar and concrete using real-shape particles. *Materials and Structures*, 49(1-2):149–158, 2016.

[21] K. R. Lauer. Autogenous healing of cement paste. In *Journal Proceedings*, volume 52, pages 1083–1098, 1956.

[22] N. M. Alderete, Y. A. Villagrán Zaccardi, and N. De Belie. Physical evidence of swelling as the cause of anomalous capillary water uptake by cementitious materials. *Cement and Concrete Research*, 120:256–266, 2019.

[23] M. Wu, B. Johannesson, and M. Geiker. A review: Self-healing in cementitious materials and engineered cementitious composite as a self-healing material. *Construction and Building Materials*, 28(1):571–583, 2012.

[24] K. Van Tittelboom, E. Gruyaert, H. Rahier, and N. De Belie. Influence of mix composition on the extent of autogenous crack healing by continued hydration or calcium carbonate formation. *Construction and Building Materials*, 37:349–359, 2012.

[25] T. C. Powers and T. L. Brownyard. Studies of the physical properties of hardened portland cement paste. In *Journal Proceedings*, volume 43, pages 101–132, 1946.

[26] C. Edvardsen. Water permeability and autogenous healing of cracks in concrete. In *Innovation in concrete structures: Design and construction*, pages 473–487. Thomas Telford Publishing, 1999.

[27] H. Huang. *Thermodynamics of autogenous self-healing in cementitious materials*. PhD thesis, Delft University of Technology, 2014.

[28] M. Jooss and H. W. Reinhardt. Permeability and diffusivity of concrete as function of temperature. *Cement and Concrete Research*, 32(9):1497–1504, 2002.

[29] H. Reinhardt and M. Jooss. Permeability and self-healing of cracked concrete as a function of temperature and crack width. *Cement and Concrete Research*, 33(7):981–985, 2003.

[30] H. M. Jonkers. Self healing concrete: a biological approach. In *Self healing materials*, pages 195–204. Springer, 2007.

[31] M. Roig-Flores, F. Pirritano, P. Serna, and L. Ferrara. Effect of crystalline admixtures on the self-healing capability of early-age concrete studied by means of permeability and crack closing tests. *Construction and Building Materials*, 114:447–457, 2016.

[32] P. Azarsa, R. Gupta, and A. Biparva. Assessment of self-healing and durability parameters of concretes incorporating crystalline admixtures and portland limestone cement. *Cement and Concrete Composites*, 99:17–31, 2019.

[33] L. Ferrara, V. Krelani, and F. Moretti. On the use of crystalline admixtures in cement based construction materials: from porosity reducers to promoters of self healing. *Smart Materials and Structures*, 25(8):084002, 2016.

[34] K. Sisomphon, O. Copuroglu, and E. A. B. Koenders. Effect of exposure conditions on self healing behavior of strain hardening cementitious composites incorporating various cementitious materials. *Construction and Building Materials*, 42:217–224, 2013.

[35] P. Carballosa, J. L. G. Calvo, and D. Revuelta. Influence of expansive calcium sulfoaluminate agent dosage on properties and microstructure of expansive self-compacting concretes. *Cement and Concrete Composites*, 107:103464, 2020.

[36] M. Sahmaran, G. Yildirim, and T. K. Erdem. Self-healing capability of cementitious composites incorporating different supplementary cementitious materials. *Cement and Concrete Composites*, 35(1):89–101, 2013.

[37] P. Byoungsun and C. C. Young. Investigating a new method to assess the self-healing performance of hardened cement pastes containing supplementary cementitious materials and crystalline admixtures. *Journal of Materials Research and Technology*, 8(6):6058–6073, 2019.

[38] R. Maddalena, H. Taha, and D. Gardner. Self-healing potential of supplementary cementitious materials in cement mortars: Sorptivity and pore structure. *Developments in the Built Environment*, 6:100044, 2021.

[39] H. Lee, H.S. Wong, and N.R. Buenfeld. Potential of superabsorbent polymer for self-sealing cracks in concrete. *Advances in Applied Ceramics*, 109(5), 2010.

[40] J. S. Kim and E. Schlangen. Super Absorbent Polymers To Stimulate Self Healing in ECC. In *2nd International Symposium on Service Life Design for Infrastructure*, number 1, pages 849–858, 2010.

[41] Z. Zhang, Q. Zhang, and V. C. Li. Multiple-scale investigations on self-healing induced mechanical property recovery of ecc. *Cement and Concrete Composites*, 103:293–302, 2019.

[42] V. C. Li and E. Herbert. Robust self-healing concrete for sustainable infrastructure. *Journal of Advanced Concrete Technology*, 10(6):207–218, 2012.

[43] A. El-Newihy, P. Azarsa, R. Gupta, and A. Biparva. Effect of polypropylene fibers on self-healing and dynamic modulus of elasticity recovery of fiber reinforced concrete. *Fibers*, 6(1):9, 2018.

[44] Y. Su, C. Qian, Y. Rui, and J. Feng. Exploring the coupled mechanism of fibers and bacteria on self-healing concrete from bacterial extracellular polymeric substances (eps). *Cement and Concrete Composites*, 116:103896, 2021.

[45] N. De Belie, E. Gruyaert, A. Al-Tabbaa, P. Antonaci, C. Baera, D. Bajare, A. Darquennes, R. Davies, L. Ferrara, T. Jefferson, et al. A review of self-healing concrete for damage management of structures. *Advanced Materials Interfaces*, 5(17):1800074, 2018.

[46] G. Souradeep and H. W. Kua. Encapsulation technology and techniques in self-healing concrete. *Journal of Materials in Civil Engineering*, 28(12):04016165, 2016.

[47] G. Anglani, J. Tulliani, and P. Antonaci. Behaviour of pre-cracked self-healing cementitious materials under static and cyclic loading. *Materials*, 13(5):1149, 2020.

[48] K. Van Tittelboom, E. Tsangouri, D. Van Hemelrijck, and N. De Belie. The efficiency of self-healing concrete using alternative manufacturing procedures and more realistic crack patterns. *Cement and concrete composites*, 57:142–152, 2015.

[49] K. Van Tittelboom, J. Wang, M. Araújo, D. Snoeck, E. Gruyaert, B. Debbaut, H. Derluyn, V. Cnudde, E. Tsangouri, and D. Van Hemelrijck. Comparison of different approaches for self-healing concrete in a large-scale lab test. *Construction and building materials*, 107:125–137, 2016.

[50] C. Romero Rodriguez, S. Chaves Figueiredo, B. Chiaia, and E. Schlangen. Induction healing of concrete reinforced by bitumen-coated steel fibres. In *9th International Conference on Fracture Mechanics of Concrete and Concrete Structures*, 2016.

[51] P. Minnebo, G. Thierens, G. De Valck, K. Van Tittelboom, N. De Belie, D. Van Hemelrijck, and E. Tsangouri. A novel design of autonomously healed concrete: Towards a vascular healing network. *Materials*, 10(1):49, 2017.

[52] Z. Li, L. R. de Souza, C. Litina, A. E. Markaki, and A. Al-Tabbaa. A novel biomimetic design of a 3d vascular structure for self-healing in cementitious materials using murray's law. *Materials & Design*, 190:108572, 2020.

[53] C. De Nardi, D. Gardner, and A. D. Jefferson. Development of 3d printed networks in self-healing concrete. *Materials*, 13(6):1328, 2020.

[54] D. Snoeck. *Self-healing and microstructure of cementitious materials with microfibres and superabsorbent polymers*. PhD thesis, Ghent University, 2015.

[55] L. Lv, P. Guo, F. Xing, and N. Han. Trigger efficiency enhancement of polymeric microcapsules for self-healing cementitious materials. *Construction and Building Materials*, 235:117443, 2020.

[56] V. Wiktor and H. M. Jonkers. Bacteria-based concrete: From concept to market. *Smart Materials and Structures*, 25(8):084006, 2016.

[57] T. S. Qureshi, A. Kanellopoulos, and A. Al-Tabbaa. Encapsulation of expansive powder minerals within a concentric glass capsule system for self-healing concrete. *Construction and Building Materials*, 121:629–643, 2016.

[58] G. Perez, E. Erkizia, J. J. Gaitero, I. Kaltzakorta, I. Jiménez, and A. Guerrero. Synthesis and characterization of epoxy encapsulating silica microcapsules and amine functionalized silica nanoparticles for development of an innovative self-healing concrete. *Materials Chemistry and Physics*, 165:39–48, 2015.

[59] L. Lv, Z. Yang, G. Chen, G. Zhu, N. Han, E. Schlangen, and F. Xing. Synthesis and characterization of a new polymeric microcapsule and feasibility investigation in self-healing cementitious materials. *Construction and Building Materials*, 105:487–495, 2016.

[60] L. Lv, E. Schlangen, Z. Yang, and F. Xing. Micromechanical properties of a new polymeric microcapsule for self-healing cementitious materials. *Materials*, 9(12):1025, 2016.

[61] R. M. Mors and H. M. Jonkers. Feasibility of lactate derivative based agent as additive for concrete for regain of crack water tightness by bacterial metabolism. *Industrial crops and products*, 106:97–104, 2017.

[62] T. Nishiwaki, H. Mihashi, B. Jang, and K. Miura. Development of self-healing system for concrete with selective heating around crack. *Journal of Advanced Concrete Technology*, 4(2):267–275, 2006.

[63] W. Xiong, J. Tang, G. Zhu, N. Han, E. Schlangen, B. Dong, X. Wang, and F. Xing. A novel capsule-based self-recovery system with a chloride ion trigger. *Scientific reports*, 5(1):1–6, 2015.

[64] C. Wang, Y. Bu, S. Guo, Y. Lu, B. Sun, and Z. Shen. Self-healing cement composite: Amine-and ammonium-based ph-sensitive superabsorbent polymers. *Cement and Concrete Composites*, 96:154–162, 2019.

[65] E. Gruyaert, B. Debbaut, D. Snoeck, P. Díaz, A. Arizo, E. Tziviloglou, E. Schlangen, and N. De Belie. Self-healing mortar with ph-sensitive superabsorbent polymers: testing of the sealing efficiency by water flow tests. *Smart Materials and Structures*, 25(8):084007, 2016.

[66] A. Mignon, G.. Graulus, D. Snoeck, J. Martins, N. De Belie, P. Dubruel, and S. Van Vlierberghe. ph-sensitive superabsorbent polymers: a potential candidate material for self-healing concrete. *Journal of materials science*, 50(2):970–979, 2015.

[67] B. Dong, Y. Wang, G. Fang, N. Han, F. Xing, and Y. Lu. Smart releasing behavior of a chemical self-healing microcapsule in the stimulated concrete pore solution. *Cement and Concrete Composites*, 56:46–50, 2015.

[68] Y. Zhu, Y. Ma, Q. Yu, J. Wei, and J. Hu. Preparation of ph-sensitive core-shell organic corrosion inhibitor and its release behavior in simulated concrete pore solutions. *Materials & Design*, 119:254–262, 2017.

[69] N. Xu, Z. Song, M. Guo, L. Jiang, Ho. Chu, C. Pei, P. Yu, Q. Liu, and Z. Li. Employing ultrasonic wave as a novel trigger of microcapsule self-healing cementitious materials. *Cement and Concrete Composites*, 118:103951, 2021.

[70] O. Teall, M. Pilegis, R. Davies, J. Sweeney, T. Jefferson, R. Lark, and D. Gardner. A shape memory polymer concrete crack closure system activated by electrical current. *Smart Materials and Structures*, 27(7):075016, 2018.

[71] G. Hong and S. Choi. Rapid self-sealing of cracks in cementitious materials incorporating superabsorbent polymers. *Construction and Building Materials*, 143:366–375, 2017.

[72] C. Dry and W. McMillan. Three-part methylmethacrylate adhesive system as an internal delivery system for smart responsive concrete. *Smart Materials and Structures*, 5(3):297, 1996.

[73] B. Dong, G. Fang, W. Ding, Y. Liu, J. Zhang, N. Han, and F. Xing. Self-healing features in cementitious material with urea–formaldehyde/epoxy microcapsules. *Construction and Building Materials*, 106:608–617, 2016.

[74] G. Perez, J. J. Gaitero, E. Erkizia, I. Jimenez, and A. Guerrero. Characterisation of cement pastes with innovative self-healing system based in epoxy-amine adhesive. *Cement and Concrete Composites*, 60:55–64, 2015.

[75] M. Maes, K. Van Tittelboom, and N. De Belie. The efficiency of self-healing cementitious materials by means of encapsulated polyurethane in chloride containing environments. *Construction and Building Materials*, 71:528–537, 2014.

[76] L. Sun, W. Y. Yu, and Q. Ge. Experimental research on the self-healing performance of micro-cracks in concrete bridge. In *Advanced Materials Research*, volume 250, pages 28–32. Trans Tech Publ, 2011.

[77] C. Joseph, A. D. Jefferson, B. Isaacs, R. Lark, and D. Gardner. Experimental investigation of adhesive-based self-healing of cementitious materials. *Magazine of Concrete Research*, 62(11):831–843, 2010.

[78] Z. Yang, J. Hollar, X. He, and X. Shi. A self-healing cementitious composite using oil core/silica gel shell microcapsules. *Cement and Concrete Composites*, 33(4):506–512, 2011.

[79] K. Van Tittelboom, K. Adesanya, P. Dubruel, P. Van Puyvelde, and N. De Belie. Methyl methacrylate as a healing agent for self-healing cementitious materials. *Smart Materials and structures*, 20(12):125016, 2011.

[80] J. Gilford III, M. M. Hassan, T. Rupnow, M. Barbato, A. Okeil, and S. Asadi. Dicyclopentadiene and sodium silicate microencapsulation for self-healing of concrete. *Journal of Materials in Civil Engineering*, 26(5):886–896, 2014.

[81] D. Gardner, A. Jefferson, A. Hoffman, and R. Lark. Simulation of the capillary flow of an autonomic healing agent in discrete cracks in cementitious materials. *Cement and Concrete Research*, 58:35–44, 2014.

[82] J. J. Ekaputri, F. F. Alrizal, I. Husein, and M. M. Al Bakri Abdullah. An application of rice husk ash (rha) and calcium carbonate (caco3) as material for self-healing cement. In *Key Engineering Materials*, volume 673, pages 3–12. Trans Tech Publ, 2016.

[83] H. Deng and G. Liao. Assessment of influence of self-healing behavior on water permeability and mechanical performance of ecc incorporating superabsorbent polymer (sap) particles. *Construction and Building Materials*, 170:455–465, 2018.

[84] D. Snoeck, P. Smetryns, and N. De Belie. Improved multiple cracking and autogenous healing in cementitious materials by means of chemically-treated natural fibres. *Biosystems Engineering*, 139:87–99, 2015.

[85] T. Nishiwaki, M. Koda, M. Yamada, H. Mihashi, and T. Kikuta. Experimental study on self-healing capability of frcc using different types of synthetic fibers. *Journal of Advanced Concrete Technology*, 10(6):195–206, 2012.

[86] H. Choi, M. Inoue, S. Kwon, H. Choi, and M. Lim. Effective crack control of concrete by self-healing of cementitious composites using synthetic fiber. *Materials*, 9(4):248, 2016.

[87] T. Nishiwaki, S. Kwon, D. Homma, M. Yamada, and H. Mihashi. Self-healing capability of fiber-reinforced cementitious composites for recovery of watertightness and mechanical properties. *Materials*, 7(3):2141–2154, 2014.

[88] J. Qiu, S. He, and E. Yang. Autogenous healing and its enhancement of interface between micro polymeric fiber and hydraulic cement matrix. *Cement and Concrete Research*, 124:105830, 2019.

[89] O. M. Jensen and P. F. Hansen. Water-entrained cement-based materials: Ii. experimental observations. *Cement and Concrete Research*, 32(6):973–978, 2002.

[90] V. Mechtcherine, C. Schröfl, M. Wyrzykowski, M. Gorges, P. Lura, D. Cusson, J. Margeson, N. De Belie, D. Snoeck, K. Ichimiya, S. Igarashi, V. Falikman, S. Friedrich, J. Bokern, P. Kara, A. Marciniak, H. Reinhardt, S. Sippel, A. Bettencourt Ribeiro, J. Custódio, G. Ye, H. Dong, and J. Weiss. Effect of superabsorbent polymers (SAP) on the freeze–thaw resistance of concrete: results of a RILEM interlaboratory study. *Materials and Structures*, 50(1), February 2017.

[91] G. Lefever, D. Snoeck, D. G. Aggelis, N. De Belie, S. Van Vlierberghe, and D. Van Hemelrijck. Evaluation of the self-healing ability of mortar mixtures containing superabsorbent polymers and nanosilica. *Materials*, 13(2):380, 2020.

[92] Y. Shim, G. Hong, and S. Choi. Autogenous healing of early-age cementitious materials incorporating superabsorbent polymers exposed to wet/dry cycles. *Materials*, 11(12):2476, 2018.

[93] D. Snoeck, J. Dewanckele, V. Cnudde, and N. De Belie. X-ray computed microtomography to study autogenous healing of cementitious materials promoted by superabsorbent polymers. *Cement and Concrete Composites*, 65:83–93, 2016.

[94] H.X.D. Lee, H.S. Wong, and N.R. Buenfeld. Effect of alkalinity and calcium concentration of pore solution on the swelling and ionic exchange of superabsorbent polymers in cement paste. *Cement and Concrete Composites*, 88:150–164, April 2018.

[95] H. Singh and R. Gupta. Influence of cellulose fiber addition on self-healing and water permeability of concrete. *Case Studies in Construction Materials*, 12:e00324, 2020.

[96] Y. Lee and J. Ryou. Crack healing performance of pva-coated granules made of cement, csa, and na2co3 in the cement matrix. *Materials*, 9(7):555, 2016.

[97] H. Huang and G. Ye. Numerical studies of the effects of water capsules on self-healing efficiency and mechanical properties in cementitious materials. *Advances in Materials Science and Engineering*, 2016, 2016.

[98] ACI Committee 212.3R-10. Report on chemical admixtures for concrete. Technical report, American Concrete Institute (ACI), 11 2010.

[99] E. Cuenca, S. Rigamonti, E. Gastaldo Brac, and L. Ferrara. Crystalline admixture as healing promoter in concrete exposed to chloride-rich environments: Experimental study. *Journal of Materials in Civil Engineering*, 33(3):04020491, 2021.

[100] K. Sisomphon and O. Copuroglu. Some characteristics of a self healing mortar incorporating calcium sulfo-aluminate based agents. In *Advances in Concrete Structural Durability, 2nd International Conference on Durability of Concrete Structures ICDCS2010, Sapporo, Japan*, pages 157–164. Hokkaido University Press, 2011.

[101] H. Justnes. Calcium nitrate as a multi-functional concrete admixture. *Concrete*, 44(1):34–36, 2010.

[102] G. A. Arce, M. M. Hassan, L. N. Mohammad, and T. Rupnow. Characterization of self-healing processes induced by calcium nitrate microcapsules in cement mortar. *Journal of Materials in Civil Engineering*, 29(1):04016189, 2017.

[103] J. Milla, M. M. Hassan, T. Rupnow, and W. H. Daly. Measuring the crack-repair efficiency of steel fiber reinforced concrete beams with microencapsulated calcium nitrate. *Construction and Building Materials*, 201:526–538, 2019.

[104] X. Wang, C. Fang, D. Li, N. Han, and F. Xing. A self-healing cementitious composite with mineral admixtures and built-in carbonate. *Cement and Concrete Composites*, 92:216–229, 2018.

[105] X. F. Wang, Z. H. Yang, C. Fang, W. Wang, J. Liu, and F. Xing. Effect of carbonate-containing self-healing system on properties of a cementitious composite: Fresh, mechanical, and durability properties. *Construction and Building Materials*, 235:117442, 2020.

[106] V. Bettencourt. Effect of sodium carbonate on the self-healing capacity of bio concrete. Bachelor Thesis, 1 2020. Delft University of Technology.

[107] E. Tziviloglou, K. Van Tittelboom, D. Palin, J. Wang, M. G. Sierra-Beltrán, Y. Erşan, R. Mors, V. Wiktor, H. M Jonkers, E. Schlangen, et al. Bio-based self-healing concrete: from research to field application. *Self-healing materials*, pages 345–385, 2016.

[108] H. M. Jonkers, A. Thijssen, G. Muyzer, O. Copuroglu, and E. Schlangen. Application of bacteria as self-healing agent for the development of sustainable concrete. *Ecological engineering*, 36(2):230–235, 2010.

[109] D. Palin, V. Wiktor, and H. M. Jonkers. A bacteria-based bead for possible self-healing marine concrete applications. *Smart Materials and Structures*, 25(8):084008, 2016.

[110] E. Rossi, C. M. Vermeer, R. Mors, R.and Kleerebezem, O. Copuroglu, and H. M. Jonkers. On the applicability of a precursor derived from organic waste streams for bacteria-based self-healing concrete. *Frontiers in Built Environment*, 7:2, 2021.

[111] E. Tziviloglou, V. Wiktor, H. M. Jonkers, and E. Schlangen. Bacteria-based self-healing concrete to increase liquid tightness of cracks. *Construction and Building Materials*, 122:118–125, 2016.

[112] J. Zhang, B. Mai, T. Cai, J. Luo, W. Wu, B. Liu, N. Han, F. Xing, and X. Deng. Optimization of a binary concrete crack self-healing system containing bacteria and oxygen. *Materials*, 10(2):116, 2017.

[113] J. Y. Wang, H. Soens, W. Verstraete, and N. De Belie. Self-healing concrete by use of microencapsulated bacterial spores. *Cement and Concrete Research*, 56:139–152, 2014.

[114] J. Wang, N. De Belie, and W. Verstraete. Diatomaceous earth as a protective vehicle for bacteria applied for self-healing concrete. *Journal of industrial microbiology & biotechnology*, 39(4):567–577, 2012.

[115] Y. Erşan, F. B. Da Silva, N. Boon, W. Verstraete, and N. De Belie. Screening of bacteria and concrete compatible protection materials. *Construction and Building Materials*, 88:196–203, 2015.

[116] Y. Erşan, E. Hernandez-Sanabria, N. Boon, and N. De Belie. Enhanced crack closure performance of microbial mortar through nitrate reduction. *Cement and concrete composites*, 70:159–170, 2016.

[117] R. R. Menon, J. Luo, X. Chen, H. Zhou, Z. Liu, G. Zhou, N. Zhang, and C. Jin. Screening of fungi for potential application of self-healing concrete. *Scientific reports*, 9(1):1–12, 2019.

[118] X. Zhang, X. Fan, M. Li, A. Samia, and X. B. Yu. Study on the behaviors of fungi-concrete surface interactions and theoretical assessment of its potentials for durable concrete with fungal-mediated self-healing. *Journal of Cleaner Production*, 292:125870, 2021.

[119] M. M. Pelletier, R. Brown, A. Shukla, and A. Bose. Self-healing concrete with a microencapsulated healing agent. *Cement and Concrete Research*, 2011.

[120] A. Kanellopoulos, P. Giannaros, D. Palmer, A. Kerr, and A. Al-Tabbaa. Polymeric microcapsules with switchable mechanical properties for self-healing concrete: synthesis, characterisation and proof of concept. *Smart Materials and Structures*, 26(4):045025, 2017.

[121] R. Alghamri, A. Kanellopoulos, and A. Al-Tabbaa. Impregnation and encapsulation of lightweight aggregates for self-healing concrete. *Construction and Building Materials*, 124:910–921, 2016.

[122] S. Irico, A. G. Bovio, G. Paul, E. Boccaleri, D. Gastaldi, L. Marchese, L. Buzzi, and F. Canonico. A solid-state nmr and x-ray powder diffraction investigation of the binding mechanism for self-healing cementitious materials design: The assessment of the reactivity of sodium silicate based systems. *Cement and Concrete Composites*, 76:57–63, 2017.

[123] T. Qureshi, A. Kanellopoulos, and A. Al-Tabbaa. Autogenous self-healing of cement with expansive minerals-i: Impact in early age crack healing. *Construction and Building Materials*, 192:768–784, 2018.

[124] T. Qureshi, A. Kanellopoulos, and A. Al-Tabbaa. Autogenous self-healing of cement with expansive minerals-ii: Impact of age and the role of optimised expansive minerals in healing performance. *Construction and Building Materials*, 194:266–275, 2019.

[125] R. Alghamri and A. Al-Tabbaa. Self-healing of cracks in mortars using novel pva-coated pellets of different expansive agents. *Construction and Building Materials*, 254:119254, 2020.

[126] T. Van Mullem, G. Anglani, M. Dudek, H. Vanoutrive, G. Bumanis, C. Litina, A. Kwiecień, A. Al-Tabbaa, D. Bajare, T. Stryszewska, et al. Addressing the need for standardization of test methods for self-healing concrete: an inter-laboratory study on concrete with macrocapsules. *Science and Technology of Advanced Materials*, 2020.

[127] M. Alazhari, T. Sharma, A. Heath, R. Cooper, and K. Paine. Application of expanded perlite encapsulated bacteria and growth media for self-healing concrete. *Construction and Building Materials*, 160:610–619, 2018.

[128] K. Tomczak and J. Jakubowski. The effects of age, cement content, and healing time on the self-healing ability of high-strength concrete. *Construction and Building Materials*, 187:149–159, 2018.

[129] J. Guo, J. Wang, and K. Wu. Effects of self-healing on tensile behavior and air permeability of high strain hardening uhpc. *Construction and Building Materials*, 204:342–356, 2019.

[130] B. Park and Y. C. Choi. Effect of healing products on the self-healing performance of cementitious materials with crystalline admixtures. *Construction and Building Materials*, 270:121389, 2021.

[131] B. Park and Y. C. Choi. Self-healing capability of cementitious materials with crystalline admixtures and super absorbent polymers (saps). *Construction and Building Materials*, 189:1054–1066, 2018.

[132] X. Liu, Q. Li, B. Li, and W. Chen. A high-efficiency self-healing cementitious material based on supramolecular hydrogels impregnated with phosphate and ammonium. *Cement and Concrete Research*, 144:106427, 2021.

[133] S. Fan and M. Li. X-ray computed microtomography of three-dimensional microcracks and self-healing in engineered cementitious composites. *Smart materials and structures*, 24(1):015021, 2014.

[134] D. Fukuda, Y. Nara, Y. Kobayashi, M. Maruyama, M. Koketsu, D. Hayashi, H. Ogawa, and K. Kaneko. Investigation of self-sealing in high-strength and ultra-low-permeability concrete in water using micro-focus x-ray ct. *Cement and Concrete Research*, 42(11):1494–1500, 2012.

[135] G. Fang, Y. Liu, S. Qin, W. Ding, J. Zhang, S. Hong, F. Xing, and B. Dong. Visualized tracing of crack self-healing features in cement/microcapsule system with x-ray microcomputed tomography. *Construction and building Materials*, 179:336–347, 2018.

[136] B. Dong, W. Ding, S. Qin, N. Han, G. Fang, Y. Liu, F. Xing, and S. Hong. Chemical self-healing system with novel microcapsules for corrosion inhibition of rebar in concrete. *Cement and Concrete Composites*, 85:83–91, 2018.

[137] A. R. Suleiman, A. J. Nelson, and M. L. Nehdi. Visualization and quantification of crack self-healing in cement-based materials incorporating different minerals. *Cement and Concrete Composites*, 103:49–58, 2019.

[138] F. A. Gilabert, K. Van Tittelboom, J. Van Stappen, V. Cnudde, N. De Belie, and W. Van Paepegem. Integral procedure to assess crack filling and mechanical contribution of polymer-based healing agent in encapsulation-based self-healing concrete. *Cement and Concrete Composites*, 77:68–80, 2017.

[139] D. Snoeck, L. Pel, and N. De Belie. Autogenous healing in cementitious materials with superabsorbent polymers quantified by means of nmr. *Scientific reports*, 10(1):1–6, 2020.

[140] W. Goethals, D. Snoeck, N. De Belie, and Ma. Boone. Analysing dynamic neutron tomography of self-healing concrete using piecewise constant functions. In *4th International conference on Tomography of Materials and Structures (ICTMS 2019)*, 2019.

[141] A. Al-Tabbaa, C. Litina, P. Giannaros, A. Kanellopoulos, and L. Souza. First uk field application and performance of microcapsule-based self-healing concrete. *Construction and Building Materials*, 208:669–685, 2019.

[142] H. Huang, G. Ye, and D. Damidot. Characterization and quantification of self-healing behaviors of microcracks due to further hydration in cement paste. *Cement and Concrete Research*, 52:71–81, 2013.

[143] X. Wu, H. Huang, H. Liu, Z. Zeng, H. Li, J. Hu, J. Wei, and Q. Yu. Artificial aggregates for self-healing of cement paste and chemical binding of aggressive ions from sea water. *Composites Part B: Engineering*, 182:107605, 2020.

[144] M. Luo, C. Qian, and R. Li. Factors affecting crack repairing capacity of bacteria-based self-healing concrete. *Construction and building materials*, 87:1–7, 2015.

[145] M. Seifan, Z. Sarabadani, and A. Berenjian. Microbially induced calcium carbonate precipitation to design a new type of bio self-healing dental composite. *Applied microbiology and biotechnology*, 104(5):2029–2037, 2020.

[146] H. Amer Algaifi, S. A. Bakar, A. R. M. Sam, M. Ismail, A. R. Z. Abidin, S. Shahir, and W. A. H. Altowayti. Insight into the role of microbial calcium carbonate and the factors involved in self-healing concrete. *Construction and Building Materials*, 254:119258, 2020.

[147] C. S. S. Durga, N. Ruben, M. S. R. Chand, and C. Venkatesh. Performance studies on rate of self healing in bio concrete. *Materials Today: Proceedings*, 27:158–162, 2020.

[148] W. Zhong and W. Yao. Influence of damage degree on self-healing of concrete. *Construction and building materials*, 22(6):1137–1142, 2008.

[149] G. Yildirim, A. Alyousif, M. Şahmaran, and M. Lachemi. Assessing the self-healing capability of cementitious composites under increasing sustained loading. *Advances in Cement Research*, 27(10):581–592, 2015.

[150] J. Feiteira, E. Tsangouri, E. Gruyaert, C. Lors, G. Louis, and N. De Belie. Monitoring crack movement in polymer-based self-healing concrete through digital image correlation, acoustic emission analysis and sem in-situ loading. *Materials & Design*, 115:238–246, 2017.

[151] K. Van Tittelboom, N. De Belie, F. Lehmann, and C. U. Grosse. Acoustic emission analysis for the quantification of autonomous crack healing in concrete. *Construction and Building Materials*, 28(1):333–341, 2012.

[152] W. Li, Z. Jiang, and Z. Yang. Acoustic characterization of damage and healing of microencapsulation-based self-healing cement matrices. *Cement and Concrete Composites*, 84:48–61, 2017.

[153] E. Tsangouri, J. Lelon, P. Minnebo, H. Asaue, T. Shiotani, K. Van Tittelboom, N. De Belie, D. G. Aggelis, and D. Van Hemelrijck. Feasibility study on real-scale, self-healing concrete slab by developing a smart capsules network and assessed by a plethora of advanced monitoring techniques. *Construction and Building Materials*, 228:116780, 2019.

[154] E. Tziviloglou, Z. Pan, H. M. Jonkers, and E. Schlangen. Bio-based self-healing mortar: An experimental and numerical study. *Journal of Advanced Concrete Technology*, 15(9):536–543, 2017.

[155] D. Palin, V. Wiktor, and H. M. Jonkers. A bacteria-based self-healing cementitious composite for application in low-temperature marine environments. *Biomimetics*, 2(3):13, 2017.

[156] T. Van Mullem, E. Gruyaert, B. Debbaut, R. Caspeele, and N. De Belie. Novel active crack width control technique to reduce the variation on water permeability results for self-healing concrete. *Construction and Building Materials*, 203:541–551, 2019.

[157] D. Snoeck, S. Steuperaert, K. Van Tittelboom, P. Dubruel, and N. De Belie. Visualization of water penetration in cementitious materials with superabsorbent polymers by means of neutron radiography. *Cement and Concrete Research*, 42(8):1113–1121, 2012.

[158] P. Zhang, Y. Dai, X. Ding, C. Zhou, X. Xue, and T. Zhao. Self-healing behaviour of multiple microcracks of strain hardening cementitious composites (shcc). *Construction and building materials*, 169:705–715, 2018.

[159] D. Snoeck, P. Van den Heede, T. Van Mullem, and N. De Belie. Water penetration through cracks in self-healing cementitious materials with superabsorbent polymers studied by neutron radiography. *Cement and Concrete Research*, 113:86–98, 2018.

[160] B. Šavija and E. Schlangen. Autogeneous healing and chloride ingress in cracked concrete. *Heron, 61 (1) 2016*, 2016.

[161] S. Jacobsen, J. Marchand, and L. Boisvert. Effect of cracking and healing on chloride transport in opc concrete. *Cement and Concrete Research*, 26(6):869–881, 1996.

[162] B. Van Belleghem, Y. Villagrán Zaccardi, P. Van den Heede, K. Van Tittelboom, and N. De Belie. Evaluation and comparison of traditional methods and electron probe micro analysis (epma) to determine the chloride ingress perpendicular to cracks in self-healing concrete. *Construction and Building Materials*, 227:116789, 2019.

[163] G. Pérez, J. L. Garcia Calvo, P. Carballosa, R. Tian, V. R. Allegro, E. Erkizia, J. J. Gaitero, and A. Guerrero. Durability of self-healing ultra-high-strength reinforced micro-concrete under freeze–thaw or chloride attack. *Magazine of Concrete Research*, 69(23):1231–1242, 2017.

[164] L. Ferrara, T. Van Mullem, M. C. Alonso, P. Antonaci, R. P. Borg, E. Cuenca, A. Jefferson, P. Ng, A. Peled, and M. Roig-Flores. Experimental characterization of the self-healing capacity of cement based materials and its effects on the material performance: A state of the art report by cost action sarcos wg2. *Construction and Building Materials*, 167:115–142, 2018.

[165] Y. Zhu, Y. Yang, and Y. Yao. Autogenous self-healing of engineered cementitious composites under freeze–thaw cycles. *Construction and Building Materials*, 34:522–530, 2012.

[166] K. Van Tittelboom, N. De Belie, D. Van Loo, and P. Jacobs. Self-healing efficiency of cementitious materials containing tubular capsules filled with healing agent. *Cement and Concrete Composites*, 33(4):497–505, 2011.

[167] J. Xu and W. Yao. Multiscale mechanical quantification of self-healing concrete incorporating non-ureolytic bacteria-based healing agent. *Cement and concrete research*, 64:1–10, 2014.

[168] J. Pelto, M. Leivo, E. Gruyaert, B. Debbaut, D. Snoeck, and N. De Belie. Application of encapsulated superabsorbent polymers in cementitious materials for stimulated autogenous healing. *Smart Materials and Structures*, 26(10):105043, October 2017.

[169] A. Kanellopoulos, P. Giannaros, and A. Al-Tabbaa. The effect of varying volume fraction of microcapsules on fresh, mechanical and self-healing properties of mortars. *Construction and Building Materials*, 122:577–593, 2016.

[170] T. Han, X. Wang, D. Li, D. Li, F. Xing, J. Ren, and N. Han. Stress-strain behaviour and pore structure of microcapsule-based self-healing cementitious composite under triaxial tests. *Construction and Building Materials*, 241:118009, 2020.

[171] V. Papadopoulos and M. Impraimakis. Multiscale modeling of carbon nanotube reinforced concrete. *Composite Structures*, 182:251–260, 2017.

[172] E. Weinan. *Principles of multiscale modeling*. Cambridge University Press, 2011.

[173] M. S. Quayum, X. Zhuang, and T. Rabczuk. Computational model generation and rve design of self-healing concrete. *Frontiers of Structural and Civil Engineering*, 9(4):383–396, 2015.

[174] P. Gumbsch and R. Pippan. *Multiscale modelling of plasticity and fracture by means of dislocation mechanics*, volume 522. Springer Science & Business Media, 2011.

[175] F. A. Gilabert, K. Van Tittelboom, E. Tsangouri, D. Van Hemelrijck, N. De Belie, and W. Van Paepegem. Determination of strength and debonding energy of a glass-concrete interface for encapsulation-based self-healing concrete. *Cement and Concrete Composites*, 79:76–93, 2017.

[176] F. A. Gilabert, D. Garoz, and W. Van Paepegem. Macro-and micro-modeling of crack propagation in encapsulation-based self-healing materials: Application of xfem and cohesive surface techniques. *Materials & Design*, 130:459–478, 2017.

[177] L. M. Mauludin and C. Oucif. Interaction between matrix crack and circular capsule under uniaxial tension in encapsulation-based self-healing concrete. *Underground Space*, 3(3):181–189, 2018.

[178] L. Muhammad Mauludin, C. Oucif, and T. Rabczuk. The effects of mismatch fracture properties in encapsulation-based self-healing concrete using cohesive-zone model. *Frontiers of Structural and Civil Engineering*, 14(3):792–801, 2020.

[179] L. M. Mauludin, X. Zhuang, and T. Rabczuk. Computational modeling of fracture in encapsulation-based self-healing concrete using cohesive elements. *Composite Structures*, 196:63–75, 2018.

[180] E. Schlangen and J. G. M. Van Mier. Simple lattice model for numerical simulation of fracture of concrete materials and structures. *Materials and Structures*, 25(9):534–542, 1992.

[181] J. E. Bolander, S. Choi, and S. R. Duddukuri. Fracture of fiber-reinforced cement composites: effects of fiber dispersion. *International journal of fracture*, 154(1-2):73–86, 2008.

[182] B. Šavija, J. Feiteira, M. Araújo, S. Chatrabhuti, J. Raquez, K. Van Tittelboom, E. Gruyaert, N. De Belie, and E. Schlangen. Simulation-aided design of tubular polymeric capsules for self-healing concrete. *Materials*, 10(1):10, 2017.

[183] L. Lv, H. Zhang, E. Schlangen, Z. Yang, and F. Xing. Experimental and numerical study of crack behaviour for capsule-based self-healing cementitious materials. *Construction and Building Materials*, 156:219–229, 2017.

[184] H. Huang, G. Ye, and Z. Shui. Feasibility of self-healing in cementitious materials–by using capsules or a vascular system? *Construction and Building materials*, 63:108–118, 2014.

[185] H.X.D. Lee, H.S. Wong, and N.R. Buenfeld. Self-sealing of cracks in concrete using superabsorbent polymers. *Cement and Concrete Research*, 79:194–208, January 2016.

[186] G. Hong and S. Choi. Modeling rapid self-sealing of cracks in cementitious materials using superabsorbent polymers. *Construction and Building Materials*, 164:570–578, March 2018.

[187] H. Huang and G. Ye. Simulation of self-healing by further hydration in cementitious materials. *Cement and Concrete Composites*, 34(4):460–467, 2012.

[188] G. Ye. *Experimental Study and Numerical Simulation of the Development of the Microstructure and Permeability of Cementitious Materials.* Phd dissertation, TU Delft, 2003.

[189] A. S. Chitez and A. D. Jefferson. A coupled thermo-hygro-chemical model for characterising autogenous healing in ordinary cementitious materials. *Cement and Concrete Research*, 88:184–197, 2016.

[190] A. Chitez. *Coupled thermo-hygro-chemical modelling of self-healing processes in cementitious materials.* PhD thesis, Cardiff University, 2014.

[191] J. Jiang, X. Zheng, S. Wu, Z. Liu, and Q. Zheng. Nondestructive experimental characterization and numerical simulation on self-healing and chloride ion transport in cracked ultra-high performance concrete. *Construction and Building Materials*, 198:696–709, 2019.

[192] J. Chen and G. Ye. A lattice boltzmann single component model for simulation of the autogenous self-healing caused by further hydration in cementitious material at mesoscale. *Cement and Concrete Research*, 123:105782, 2019.

[193] K. Van Tittelboom and N. De Belie. Self-healing in cementitious materials: A review. *Materials*, 6(6):2182–2217, 2013.

[194] B. Gérard, C. Le Bellego, and O. Bernard. Simplified modelling of calcium leaching of concrete in various environments. *Materials and Structures*, 35(10):632–640, 2002.

[195] V. G. Papadakis, C. G. Vayenas, and M. N. Fardis. Experimental investigation and mathematical modeling of the concrete carbonation problem. *Chemical Engineering Science*, 46(5-6):1333–1338, 1991.

[196] A. Aliko-Benítez, M. Doblaré, and J. A. Sanz-Herrera. Chemical-diffusive modeling of the self-healing behavior in concrete. *International Journal of Solids and Structures*, 69:392–402, 2015.

[197] H. Ranaivomanana and N. Benkemoun. Numerical modelling of the healing process induced by carbonation of a single crack in concrete structures: Theoretical formulation and embedded finite element method implementation. *Finite Elements in Analysis and Design*, 132:42–51, 2017.

[198] S. V. Zemskov, H. M. Jonkers, and F. J. Vermolen. A mathematical model for bacterial self-healing of cracks in concrete. *Journal of Intelligent Material Systems and Structures*, 25(1):4–12, 2014.

[199] H. A. Algaifi, S. A. Bakar, A. R. M. Sam, A. R. Z. Abidin, S. Shahir, and W. A. H. AL-Towayti. Numerical modeling for crack self-healing concrete by microbial calcium carbonate. *Construction and Building Materials*, 189:816–824, 2018.

[200] B. Hilloulin, F. Grondin, M. Matallah, and A. Loukili. Modelling of autogenous healing in ultra high performance concrete. *Cement and Concrete Research*, 61:64–70, 2014.

[201] G. Di Luzio, L. Ferrara, and V. Krelani. Numerical modeling of mechanical regain due to self-healing in cement based composites. *Cement and Concrete Composites*, 86:190–205, 2018.

[202] S. Zhou, H. Zhu, J. W. Ju, Z. Yan, and Q. Chen. Modeling microcapsule-enabled self-healing cementitious composite materials using discrete element method. *International Journal of Damage Mechanics*, 26(2):340–357, 2017.

[203] T. Selvarajoo, R. E. Davies, B. L. Freeman, and A. D. Jefferson. Mechanical response of a vascular self-healing cementitious material system under varying loading conditions. *Construction and Building Materials*, 254:119245, 2020.

[204] C. Oucif, G. Z. Voyiadjis, and T. Rabczuk. Modeling of damage-healing and nonlinear self-healing concrete behavior: Application to coupled and uncoupled self-healing mechanisms. *Theoretical and Applied Fracture Mechanics*, 96:216–230, 2018.

[205] X. Zhuang and S. Zhou. The prediction of self-healing capacity of bacteria-based concrete using machine learning approaches. *Computers, Materials & Continua 59 (2019), Nr. 1*, 2019.

[206] A. Ramadan Suleiman and M. L. Nehdi. Modeling self-healing of concrete using hybrid genetic algorithm–artificial neural network. *Materials*, 10(2):135, 2017.

[207] M. Chaitanya, P. Manikandan, V. P. Kumar, S. Elavenil, and V. Vasugi. Prediction of self-healing characteristics of ggbs admixed concrete using artificial neural network. In *Journal of Physics: Conference Series*, volume 1716, page 012019. IOP Publishing, 2020.

[208] Z. Li, L. R. de Souza, C. Litina, A. E. Markaki, and A. Al-Tabbaa. Feasibility of using 3d printed polyvinyl alcohol (pva) for creating self-healing vascular tunnels in cement system. *Materials*, 12(23):3872, 2019.

[209] W. Li, Z. Jiang, Z. Yang, and H. Yu. Effective mechanical properties of self-healing cement matrices with microcapsules. *Materials & Design*, 95:422–430, 2016.

[210] G. Anglani, T. Van Mullem, X. Zhu, J. Wang, P. Antonaci, N. De Belie, J. Tulliani, and K. Van Tittelboom. Sealing efficiency of cement-based materials containing extruded cementitious capsules. *Construction and Building Materials*, 251:119039, 2020.

[211] G. Anglani, P. Antonaci, J. Tulliani, K. Van Tittelboom, J. Wang, and N. De Belie. Self-healing efficiency of cement-based materials containing extruded cementitious

hollow tubes filled with bacterial healing agent. In *Final Conference of RILEM TC 253-MCI: Microorganisms-Cementitious Materials Interactions*, volume 2, pages 425–431. RILEM Publications, 2018.

[212] J. Wang, K. Van Tittelboom, N. De Belie, and W. Verstraete. Use of silica gel or polyurethane immobilized bacteria for self-healing concrete. *Construction and building materials*, 26(1):532–540, 2012.

[213] R. Mors and H. Jonkers. Effect on concrete surface water absorption upon addition of lactate derived agent. *Coatings*, 7(4):51, 2017.

[214] L. Mercuri, C. Romero Rodriguez, Y. Xu, S. Chaves Figueiredo, R. Mors, E. Rossi, G. Anglani, P. Antonaci, B. Šavija, and E. Schlangen. On the role of soft inclusions on the fracture behaviour of cement paste. In *Proceedings of the 10th International Conference on Fracture Mechanics of Concrete and Concrete Structures*, 2019.

[215] B. Hilloulin, K. Van Tittelboom, E. Gruyaert, N. De Belie, and A. Loukili. Design of polymeric capsules for self-healing concrete. *Cement and Concrete Composites*, 55:298–307, 2015.

[216] S. V. Zemskov, H. M. Jonkers, and F. J. Vermolen. Two analytical models for the probability characteristics of a crack hitting encapsulated particles: Application to self-healing materials. *Computational materials science*, 50(12):3323–3333, 2011.

[217] M. Luković, B. Šavija, H. Dong, E. Schlangen, and G. Ye. Micromechanical study of the interface properties in concrete repair systems. *Journal of Advanced Concrete Technology*, 12(9):320–339, 2014.

[218] Basilisk self healing concrete. Material safety data sheet concrete healing agent pla based (cha-pla). `https://www.basiliskconcrete.com/wp-content/uploads/2019/12/20181019_HA_MSDS_Material-Safety-Data-Sheet.pdf`, 2018.

[219] T. Allen. *Particle size measurement*. Springer, 2013.

[220] M. Megalla. Bacteria based self-healing concrete. Master's thesis, Delft University of Technology, the Netherlands, 2017.

[221] W. C. Oliver and G. M. Pharr. Measurement of hardness and elastic modulus by instrumented indentation: Advances in understanding and refinements to methodology. *Journal of Materials Research*, 19(1):3–20, 2004.

[222] J. Schindelin, I. Arganda-Carreras, E. Frise, V. Kaynig, M. Longair, T. Pietzsch, S. Preibisch, C. Rueden, S. Saalfeld, B. Schmid, et al. Fiji: an open-source platform for biological-image analysis. *Nature methods*, 9(7):676–682, 2012.

[223] I. Arganda-Carreras, V. Kaynig, C. Rueden, K. W. Eliceiri, J. Schindelin, A. Cardona, and H. Sebastian Seung. Trainable weka segmentation: a machine learning tool for microscopy pixel classification. *Bioinformatics*, 33(15):2424–2426, 2017.

[224] N. W. M. Ritchie. Getting started with nist* dtsa-ii. *Microscopy Today*, 19(1):26–31, 2011.

[225] M. Vandamme, F. Ulm, and P. Fonollosa. Nanogranular packing of c–s–h at substochiometric conditions. *Cement and Concrete Research*, 40(1):14–26, 2010.

[226] M. Luković, E. Schlangen, and G. Ye. Combined experimental and numerical study of fracture behaviour of cement paste at the microlevel. *Cement and Concrete Research*, 73:123–135, 2015.

[227] B. Šavija, H. Zhang, and E. Schlangen. Micromechanical testing and modelling of blast furnace slag cement pastes. *Construction and Building Materials*, 239:117841, 2020.

[228] E. Schlangen and J. G. M. Van Mier. Experimental and numerical analysis of micromechanisms of fracture of cement-based composites. *Cement and Concrete Composites*, 14(2):105–118, 1992.

[229] G. Lilliu and J. G. M. van Mier. 3d lattice type fracture model for concrete. *Engineering Fracture Mechanics*, 70(7-8):927–941, 2003.

[230] E. Schlangen and Z. Qian. 3d modeling of fracture in cement-based materials. *Journal of Multiscale Modelling*, 1(02):245–261, 2009.

[231] H. Zhang, Y. Xu, Y. Gan, E. Schlangen, and B. Šavija. Experimentally validated meso-scale fracture modelling of mortar using output from micromechanical models. *Cement and Concrete Composites*, page 103567, 2020.

[232] Z. Qian. *Multiscale modeling of fracture processes in cementitious materials*. PhD thesis, Delft University of Technology, 2012.

[233] M. Hlobil, V. Šmilauer, and G. Chanvillard. Micromechanical multiscale fracture model for compressive strength of blended cement pastes. *Cement and Concrete Research*, 83:188–202, 2016.

[234] H. Zhang, B. Šavija, S. Chaves Figueiredo, M. Lukovic, and E. Schlangen. Microscale testing and modelling of cement paste as basis for multi-scale modelling. *Materials*, 9(11):907, 2016.

[235] H. Zhang, Y. Xu, Y. Gan, Z. Chang, E. Schlangen, and B. Šavija. Combined experimental and numerical study of uniaxial compression failure of hardened cement paste at micrometre length scale. *Cement and Concrete Research*, 126:105925, 2019.

[236] N. B. Singh, S. Prabha, and A. K. Singh. Effect of lactic acid on the hydration of portland cement. *Cement and Concrete Research*, 16(4):545–553, 1986.

[237] R. J. Schultz. A discussion of the paper effect of lactic acid on the hydration of portland cement by nb singh, s. prapha singh and ak singh. *Cement and Concrete Research*, 17(2):365–366, 1987.

[238] P. Juilland, E. Gallucci, R. Flatt, and K. Scrivener. Dissolution theory applied to the induction period in alite hydration. *Cement and Concrete Research*, 40(6):831–844, 2010.

[239] Standard Test Method for Microscopical Determination of Parameters of the Air-Void System in Hardened Concrete. Standard, ASTM, 1998.

[240] D. P. Bentz, P. E. Stutzman, and E. J. Garboczi. Experimental and simulation studies of the interfacial zone in concrete. *Cement and concrete research*, 22(5):891–902, 1992.

[241] J. Xiao, W. Li, Z. Sun, D. A. Lange, and S. P. Shah. Properties of interfacial transition zones in recycled aggregate concrete tested by nanoindentation. *Cement and Concrete Composites*, 37:276–292, 2013.

[242] A. A. Tabikh and F. M. Miller. The nature of phosphogypsum impurities and their influence on cement hydration. *Cement and Concrete Research*, 1(6):663–678, 1971.

[243] M. Singh. Treating waste phosphogypsum for cement and plaster manufacture. *Cement and Concrete Research*, 32(7):1033–1038, 2002.

[244] J. J. Hughes and P. Trtik. Micro-mechanical properties of cement paste measured by depth-sensing nanoindentation: a preliminary correlation of physical properties with phase type. *Materials characterization*, 53(2-4):223–231, 2004.

[245] S. Gautham and S. Sasmal. Recent advances in evaluation of intrinsic mechanical properties of cementitious composites using nanoindentation technique. *Construction and Building Materials*, 223:883–897, 2019.

[246] H. Zhang, B. Šavija, and E. Schlangen. Towards understanding stochastic fracture performance of cement paste at micro length scale based on numerical simulation. *Construction and Building Materials*, 183:189–201, 2018.

[247] C-J. Haecker, E. J. Garboczi, J. W. Bullard, R. B. Bohn, Z. Sun, S. P. Shah, and T. Voigt. Modeling the linear elastic properties of portland cement paste. *Cement and Concrete Research*, 35(10):1948–1960, 2005.

[248] G. Constantinides and F. Ulm. The effect of two types of csh on the elasticity of cement-based materials: Results from nanoindentation and micromechanical modeling. *Cement and Concrete Research*, 34(1):67–80, 2004.

[249] M. Luković, H. Dong, B. Šavija, E. Schlangen, G. Ye, and K. van Breugel. Tailoring strain-hardening cementitious composite repair systems through numerical experimentation. *Cement and Concrete Composites*, 53:200–213, 2014.

[250] T. Han, X. Wang, D. Li, D. Li, F. Xing, N. Han, and Z. Li. Uniaxial deformation characteristics and mechanical model of microcapsule-based self-healing cementitious composite. *Construction and Building Materials*, 274:121227, 2021.

[251] J. Milla, M. M. Hassan, and T. Rupnow. Evaluation of self-healing concrete with microencapsulated calcium nitrate. *Journal of Materials in Civil Engineering*, 29(12):04017235, 2017.

[252] H. Xu, J. Lian, M. Gao, D. Fu, and Y. Yan. Self-healing concrete using rubber particles to immobilize bacterial spores. *Materials*, 12(14):2313, 2019.

[253] X. Wang, P. Sun, N. Han, and F. Xing. Experimental study on mechanical properties and porosity of organic microcapsules based self-healing cementitious composite. *Materials*, 10(1):20, 2017.

[254] J. G. M. van Mier. *Fracture of concrete under complex stress*. Faculty of Civil Engineering, Delft University of Technology, 1986.

[255] J. G. M. Van Mier and M. B. Nooru-Mohamed. Fracture of concrete under tensile and shear-like loadings. *Fracture Toughness and Fracture Energy-Test Methods for Concrete and Rock.(eds. Mihashi, H., Takahashi, H. & Wittmann, FH), Balkema, Rotterdam*, pages 549–516, 1989.

[256] J. Blaber, B. Adair, and A. Antoniou. Ncorr: open-source 2d digital image correlation matlab software. *Experimental Mechanics*, 55(6):1105–1122, 2015.

[257] H. Zhang. *Experimentally validated multi-scale fracture modelling scheme of cementitious materials*. PhD thesis, Delft University of Technology, 2019.

[258] A. Arslan, R. Ince, and B. L. Karihaloo. Improved lattice model for concrete fracture. *Journal of Engineering Mechanics*, 128(1):57–65, 2002.

[259] C. Romero Rodríguez, F. França de Mendonça Filho, L. Mercuri, Y. Gan, E. Rossi, G. Anglani, P. Antonaci, E. Schlangen, and B. Šavija. Chemo-physico-mechanical properties of the interface zone between bacterial pla self-healing capsules and cement paste. *Cement and Concrete Research*, 138:106228, 2020.

[260] B. Šavija, J. Pacheco, and E. Schlangen. Lattice modeling of chloride diffusion in sound and cracked concrete. *Cement and Concrete Composites*, 42:30–40, 2013.

[261] P. K. Mehta and P. J. M. Monteiro. *Concrete: microstructure, properties, and materials*. McGraw-Hill Education, 2014.

[262] R. A. Guyer and P. A. Johnson. *Nonlinear mesoscopic elasticity: the complex behaviour of rocks, soil, concrete*. John Wiley & Sons, 2009.

[263] H. F. W. Taylor et al. *Cement chemistry*, volume 2. Thomas Telford London, 1997.

[264] K. Otsuka and H. Date. Fracture process zone in concrete tension specimen. *Engineering fracture mechanics*, 65(2-3):111–131, 2000.

[265] V. Mechtcherine. Fracture mechanical behavior of concrete and the condition of its fracture surface. *Cement and Concrete Research*, 39(7):620–628, 2009.

[266] H. Zhang, Y. Gan, Y. Xu, S. Zhang, E. Schlangen, and B. Šavija. Experimentally informed fracture modelling of interfacial transition zone at micro-scale. *Cement and Concrete Composites*, 104:103383, 2019.

[267] S. Brischetto and R. Torre. Tensile and compressive behavior in the experimental tests for pla specimens produced via fused deposition modelling technique. *Journal of Composites Science*, 4(3):140, 2020.

[268] N. S. Klein, L. A. Lenz, and W. Mazer. Influence of the granular skeleton packing density on the static elastic modulus of conventional concretes. *Construction and Building Materials*, 242:118086, 2020.

[269] S. H. Chu. Effect of paste volume on fresh and hardened properties of concrete. *Construction and Building Materials*, 218:284–294, 2019.

[270] S. Erdem, A. R. Dawson, and N. H. Thom. Influence of the micro-and nanoscale local mechanical properties of the interfacial transition zone on impact behavior of concrete made with different aggregates. *Cement and Concrete Research*, 42(2):447–458, 2012.

[271] T. Akçaoğlu, M. Tokyay, and T. Çelik. Assessing the itz microcracking via scanning electron microscope and its effect on the failure behavior of concrete. *Cement and Concrete Research*, 35(2):358–363, 2005.

[272] C. G. Rocco and M. Elices. Effect of aggregate shape on the mechanical properties of a simple concrete. *Engineering fracture mechanics*, 76(2):286–298, 2009.

[273] C. Hall and W. D. Hoff. *Water Transport in Brick, Stone and Concrete*, volume 25. Spon Press, 2nd edition, 2009.

[274] P. Zhang, F. H. Wittmann, P. Lura, H. S. Müller, S. Han, and T. Zhao. Application of neutron imaging to investigate fundamental aspects of durability of cement-based materials: a review. *Cement and Concrete Research*, 108:152–166, 2018.

[275] F. C. De Beer, J. J. Le Roux, and E. P. Kearsley. Testing the durability of concrete with neutron radiography. *Nuclear Instruments and Methods in Physics Research Section A: Accelerators, Spectrometers, Detectors and Associated Equipment*, 542(1-3):226–231, 2005.

[276] W. Li, M. Pour-Ghaz, P. Trtik, M. Wyrzykowski, B. Münch, P. Lura, P. Vontobel, E. Lehmann, and W. J. Weiss. Using neutron radiography to assess water absorption in air entrained mortar. *Construction and Building Materials*, 110:98–105, 2016.

[277] S. Xue, P. Zhang, E. H. Lehmann, J. Hovind, and F. H. Wittmann. Neutron radiography of water exchange across the interface between old and fresh mortar. *Measurement*, 183:109882, 2021.

[278] C. Schröfl, V. Mechtcherine, A. Kaestner, P. Vontobel, J. Hovind, and E. Lehmann. Transport of water through strain-hardening cement-based composite (shcc) applied on top of cracked reinforced concrete slabs with and without hydrophobization of cracks–investigation by neutron radiography. *Construction and Building Materials*, 76:70–86, 2015.

[279] D. Snoeck, S. Steuperaert, K. Van Tittelboom, P. Dubruel, and N. De Belie. Visualization of water penetration in cementitious materials with superabsorbent polymers by means of neutron radiography. *Cement and Concrete Research*, 42(8):1113–1121, 2012.

[280] K. Van Tittelboom, D. Snoeck, P. Vontobel, F. H. Wittmann, and N. De Belie. Use of neutron radiography and tomography to visualize the autonomous crack sealing efficiency in cementitious materials. *Materials and structures*, 46(1):105–121, 2013.

[281] P. Van den Heede, B. Van Belleghem, N. Alderete, K. Van Tittelboom, and N. De Belie. Neutron radiography based visualization and profiling of water uptake in (un) cracked and autonomously healed cementitious materials. *Materials*, 9(5):311, 2016.

[282] C. Schroefl, V. Mechtcherine, P. Vontobel, J. Hovind, and E. Lehmann. Sorption kinetics of superabsorbent polymers (saps) in fresh portland cement-based pastes visualized and quantified by neutron radiography and correlated to the progress of cement hydration. *Cement and Concrete Research*, 75:1–13, 2015.

[283] D. Dauti, A. Tengattini, S. Dal Pont, N. Toropovs, M. Briffaut, and B. Weber. Analysis of moisture migration in concrete at high temperature through in-situ neutron tomography. *Cement and Concrete Research*, 111:41–55, 2018.

[284] E. H. Lehmann. Neutron imaging facilities in a global context. *Journal of Imaging*, 3(4):52, 2017.

[285] C. Hall. Water sorptivity of mortars and concretes: a review. *Magazine of concrete research*, 41(147):51–61, 1989.

[286] B. J. Balcom, J. C. Barrita, C. Choi, S. D. Beyea, D. J. Goodyear, and T. W. Bremner. Single-point magnetic resonance imaging (mri) of cement based materials. *Materials and structures*, 36(3):166–182, 2003.

[287] L. Stelzner, B. Powierza, T. Oesch, R. Dlugosch, and F. Weise. Thermally-induced moisture transport in high-performance concrete studied by x-ray-ct and 1h-nmr. *Construction and Building Materials*, 224:600–609, 2019.

[288] D. Smyl. Electrical tomography for characterizing transport properties in cement-based materials: A review. *Construction and Building Materials*, 244:118299, 2020.

[289] M. Hallaji, A. Seppänen, and M. Pour-Ghaz. Electrical resistance tomography to monitor unsaturated moisture flow in cementitious materials. *Cement and Concrete Research*, 69:10–18, 2015.

[290] D. Smyl, M. Hallaji, A. Seppänen, and M. Pour-Ghaz. Three-dimensional electrical impedance tomography to monitor unsaturated moisture ingress in cement-based materials. *Transport in Porous Media*, 115(1):101–124, 2016.

[291] D. Smyl, R. Rashetnia, A. Seppänen, and M. Pour-Ghaz. Can electrical resistance tomography be used for imaging unsaturated moisture flow in cement-based materials with discrete cracks? *Cement and Concrete Research*, 91:61–72, 2017.

[292] A. Voss, M. Pour-Ghaz, M. Vauhkonen, and A. Seppänen. Electrical capacitance tomography to monitor unsaturated moisture ingress in cement-based materials. *Cement and Concrete Research*, 89:158–167, 2016.

[293] A. Voss, P. Hosseini, M. Pour-Ghaz, M. Vauhkonen, and A. Seppänen. Three-dimensional electrical capacitance tomography–a tool for characterizing moisture transport properties of cement-based materials. *Materials & Design*, 181:107967, 2019.

[294] K. Wan and Q. Xu. Local porosity distribution of cement paste characterized by x-ray micro-tomography. *Science China Technological Sciences*, 57(5):953–961, 2014.

[295] S. Roels and J. Carmeliet. Analysis of moisture flow in porous materials using microfocus x-ray radiography. *International Journal of Heat and Mass Transfer*, 49(25-26):4762–4772, 2006.

[296] B. Van Belleghem, R. Montoya, J. Dewanckele, N. Van Den Steen, I. De Graeve, J. Deconinck, V. Cnudde, K. Van Tittelboom, and N. De Belie. Capillary water absorption in cracked and uncracked mortar - A comparison between experimental study and finite element analysis. *Construction and Building Materials*, 110:154–162, 2016.

[297] M. Luković, G. Ye, E. Schlangen, and K. Van Breugel. Moisture movement in cement-based repair systems monitored by x-ray absorption. *Heron*, 62:21, 2017.

[298] B. Šavija, M. Luković, and E. Schlangen. Influence of Cracking on Moisture Uptake in Strain-Hardening Cementitious Composites. *Journal of Nanomechanics and Micromechanics*, 7(1):04016010, March 2017.

[299] L. Yang, Y. Zhang, Z. Liu, P. Zhao, and C. Liu. In-situ tracking of water transport in cement paste using x-ray computed tomography combined with cscl enhancing. *Materials Letters*, 160:381–383, 2015.

[300] T. Oesch, F. Weise, D. Meinel, and C. Gollwitzer. Quantitative in-situ analysis of water transport in concrete completed using x-ray computed tomography. *Transport in Porous Media*, 127(2):371–389, 2019.

[301] B. Powierza, L. Stelzner, T. Oesch, C. Gollwitzer, F. Weise, and G. Bruno. Water migration in one-side heated concrete: 4d in-situ ct monitoring of the moisture-clog-effect. *Journal of Nondestructive Evaluation*, 38(1):1–11, 2019.

[302] A. Katchalsky and I. Michaeli. Polyelectrolyte gels in salt solutions. *Journal of Polymer Science*, 15(79):69–86, January 1955.

[303] S. Vervoort. *Behaviour of hydrogels swollen in polymer solutions under mechanical action.* Phd dissertation, Ecole Nationale Superieure des Mines de Paris, 2006.

[304] E. Gruyaert, B. Debbaut, D. Snoeck, P. Díaz, A. Arizo, E. Tziviloglou, E. Schlangen, and N. De Belie. Self-healing mortar with pH-sensitive superabsorbent polymers: testing of the sealing efficiency by water flow tests. *Smart Materials and Structures*, 25(8):084007, August 2016.

[305] M. Dierick, D. Van Loo, B. Masschaele, J. Van den Bulcke, J. Van Acker, V. Cnudde, and L. Van Hoorebeke. Recent micro-ct scanner developments at ugct. *Nuclear Instruments and Methods in Physics Research Section B: Beam Interactions with Materials and Atoms*, 324:35–40, 2014.

[306] T. Bultreys, M. A. Boone, M. N. Boone, T. De Schryver, B. Masschaele, D. Van Loo, L. Van Hoorebeke, and V. Cnudde. Real-time visualization of Haines jumps in sandstone with laboratory-based microcomputed tomography. *Water Resources Research*, 51(10):8668–8676, October 2015.

[307] T. Bultreys, M.A. Boone, M.N. Boone, T. De Schryver, B. Masschaele, L. Van Hoorebeke, and V. Cnudde. Fast laboratory-based micro-computed tomography for pore-scale research: Illustrative experiments and perspectives on the future. *Advances in Water Resources*, 95:341–351, 2016. Pore scale modeling and experiments.

[308] M. Boone, T. De Kock, B. Masschaele, T. De Schryver, L. Van Hoorebeke, and V. Cnudde. 4d mapping of fluid distribution in porous sedimentary rocks using x-ray micro-ct differential imaging. In *21st General meeting of the International Mineralogical Association (IMA 2014)*, pages 292–292. Geological Society of South Africa; Mineralogical Association of South Africa, 2014.

[309] D. Cui, W. Sun, Q. Wang, and C. Gu. Use of tomography to estimate the representative elementary volume in mortars stained with potassium iodide. *Materials & Design*, 147:80–91, 2018.

[310] L. A. Richards. Capillary conduction of liquids through porous mediums. *Physics*, 1(5):318–333, 1931.

[311] A. Szymkiewicz. *Modelling Water Flow in Unsaturated Porous Media*, volume 9. Springer, 2013.

[312] D. Lockington, J-Y. Parlange, and P. Dux. Sorptivity and the estimation of water penetration into unsaturated concrete. *Materials and Structures*, 32(5):342, 1999.

[313] L. Wang, J. Bao, and T. Ueda. Prediction of mass transport in cracked-unsaturated concrete by mesoscale lattice. *Ocean Engineering*, 127(August):144–157, 2016.

[314] Y. Mualem. A new model for predicting the hydraulic conductivity of unsaturated porous media. *Water resources research*, 12(3):513–522, 1976.

[315] M. T. Van Genuchten. A closed-form equation for predicting the hydraulic conductivity of unsaturated soils 1. *Soil science society of America journal*, 44(5):892–898, 1980.

[316] P. Grassl and J. Bolander. Three-dimensional network model for coupling of fracture and mass transport in quasi-brittle geomaterials. *Materials*, 9(9):1–18, 2016.

[317] D. Asahina, K. Kim, Z. Li, and J. E. Bolander. Flow field calculations within discrete models of multiphase materials. *Composites Part B: Engineering*, 58:293–302, 2014.

[318] M. Luković, B. Šavija, E. Schlangen, G. Ye, and K. van Breugel. A 3D lattice modelling study of drying shrinkage damage in concrete repair systems. *Materials*, 9(7), 2016.

[319] A. M. Brandt, J. Olek, M. A. Glinicki, C. K. Y. Leung, and J. Lis. Influence of specimen size on results of concrete sorptivity measurements. In *Proceedings of 11th International Symposium on Brittle Matrix Composites*, pages 141–149, 2015.

[320] C. Romero Rodríguez, S. C. Figueiredo, E. Schlangen, and D. Snoeck. Modeling water absorption in cement-based composites with sap additions. In *Computational Modelling of Concrete Structures: Proceedings of the Conference on Computational Modelling of Concrete and Concrete Structures (EURO-C 2018), February 26-March 1, 2018, Bad Hofgastein, Austria*, page 295. CRC Press, 2018.

[321] Q. Zeng, K. Li, T. Fen-Chong, and P. Dangla. Analysis of pore structure, contact angle and pore entrapment of blended cement pastes from mercury porosimetry data. *Cement and Concrete Composites*, 34(9):1053–1060, 2012.

[322] R. He, H. Ma, R. B. Hafiz, C. Fu, X. Jin, and J. He. Determining porosity and pore network connectivity of cement-based materials by a modified non-contact electrical resistivity measurement: Experiment and theory. *Materials & Design*, 156:82–92, 2018.

[323] L. P. Esteves. Superabsorbent polymers: On their interaction with water and pore fluid. *Cement and Concrete Composites*, 33(7):717–724, 2011.

[324] T. Sweijen, C.J. van Duijn, and S.M. Hassanizadeh. A model for diffusion of water into a swelling particle with a free boundary: Application to a super absorbent polymer particle. *Chemical Engineering Science*, 172:407–413, 2017.

[325] D. Snoeck, L.F. Velasco, A. Mignon, S. Van Vlierberghe, P. Dubruel, P. Lodewyckx, and N. De Belie. The effects of superabsorbent polymers on the microstructure of cementitious materials studied by means of sorption experiments. *Cement and Concrete Research*, 77:26–35, November 2015.

[326] J. R. Philip. The theory of infiltration: 5. the influence of the initial moisture content. *Soil Science*, 84(4):329–340, 1957.

[327] W. Brutsaert. The concise formulation of diffusive sorption of water in a dry soil. *Water Resources Research*, 12(6):1118–1124, 1976.

[328] D. Snoeck, L. F. Velasco, A. Mignon, S. Van Vlierberghe, P. Dubruel, P. Lodewyckx, and N. De Belie. The effects of superabsorbent polymers on the microstructure of cementitious materials studied by means of sorption experiments. *Cement and Concrete Research*, 77:26–35, 2015.

[329] D. Snoeck. Zelfhelend beton door combinatie van microvezels met reactieve stoffen. Master's thesis, Universiteit Gent, Ghent, 2011.

[330] C. Romero Rodriguez, S. Chaves Figueiredo, D. Snoeck, B. Šavija, and E. Schlangen. Modelling strategies for the study of crack sefl-sealing in mortar with superabsorbent polymers. In *Symposium on Concrete Modelling (CONMOD2018)*, pages 333–341. RILEM Publications, 2018.

[331] B. Masschaele, M. Dierick, D. Van Loo, M. N. Boone, L. Brabant, E. Pauwels, V. Cnudde, and L. Van Hoorebeke. Hector: A 240kv micro-ct setup optimized for research. In *Journal of Physics: Conference Series*, volume 463, page 012012. IOP Publishing, 2013.

[332] H. W. Reinhardt and A. Assmann. Enhanced durability of concrete by superabsorbent polymers. In *Proc. BMC*, volume 9, pages 291–300, 2009.

[333] H.S. Wong, A.M. Pappas, R.W. Zimmerman, and N.R. Buenfeld. Effect of entrained air voids on the microstructure and mass transport properties of concrete. *Cement and Concrete Research*, 41(10):1067–1077, October 2011.

[334] D. Liu, B. Šavija, G. E. Smith, P. E. J. Flewitt, T. Lowe, and E. Schlangen. Towards understanding the influence of porosity on mechanical and fracture behaviour of quasi-brittle materials: experiments and modelling. *International Journal of Fracture*, 205(1):57–72, May 2017.

[335] Y. Yao, Y. Zhu, and Y. Yang. Incorporation superabsorbent polymer (sap) particles as controlling pre-existing flaws to improve the performance of engineered cementitious composites (ecc). *Construction and Building Materials*, 28(1):139–145, 2012.

[336] D. Snoeck, T. De Schryver, and N. De Belie. Enhanced impact energy absorption in self-healing strain-hardening cementitious materials with superabsorbent polymers. *Construction and Building Materials*, 191:13–22, 2018.

[337] C. Schröfl, D. Snoeck, and V. Mechtcherine. A review of characterisation methods for superabsorbent polymer (SAP) samples to be used in cement-based construction materials: report of the RILEM TC 260-RSC. *Materials and Structures*, 50(4), August 2017.

[338] X. Li, S. Chen, Q. Xu, and Y. Xu. Modeling the three-dimensional unsaturated water transport in concrete at the mesoscale. *Computers & Structures*, 190:61–74, October 2017.

[339] D. Gardner, A. Jefferson, and A. Hoffman. Investigation of capillary flow in discrete cracks in cementitious materials. *Cement and Concrete Research*, 42(7):972–981, July 2012.

[340] H. Zhang, B. Šavija, M. Lukovic, and E. Schlangen. Experimentally informed micromechanical modelling of cement paste: An approach coupling x-ray computed tomography and statistical nanoindentation. *Composites Part B: Engineering*, 157:109–122, 2019.

Acknowledgements

Without a doubt, the acknowledgments are the most widely and most eagerly read part of any thesis.

Moritz Beller

To the social animal that I am, going down this road felt, at times, the loneliest of all adventures by me undertaken. Fortunately, for most of the path, I had the support and encouragement of truly wondrous people from the before times or that I was lucky enough to encounter along this journey. To you all goes my eternal gratitude. Be warned, because in true Claudia fashion, this is about to get extremely lengthy and uncomfortably personal.

I would like to thank my promotor **Erik**. Our collaboration goes back to when when I was a young master's student from Italy, and you received me with open arms in your Microlab. You have no idea what your unabashed trust and encouragement meant to me. Having discovered a passion for research under your guidance, made me embark in this PhD. I will remember fondly our micromechanics group meetings and attending conferences to all the coolest places in the world together. Of course it was not all good times, but during the occasional hard times of the PhD, your patient, nurturing ways gave me the confidence to tackle most challenges and I could always find in you a listening ear to my rants.

I had the incredible luck to have **Branko** as a mentor, role model and friend. Working with you was nothing short of inspiring. Your empathy, clever suggestions and emotional support made problems much easier to handle. I will never not be in awe of your out-of-this-world reading speed. Thanks also for lunch and coffee breaks every work day for 4 years: it was a blast.

I feel honored to have worked with **Henk** on the topic of self-healing concrete and to have contributed a little bit to the body of research in this topic.

It is also a great honor to have such a group of brilliant and accomplished academics in my PhD committee: **Sandra Erkens**, **Santiago Garcia**, **Elke Gruyaert** and **Tony Jefferson**. Your feedback has been invaluable for the completion of this dissertation.

The unsung heroes of academic research, technicians are! I would like to declare my undying gratitude to **Ton**, **John**, **Ellen** and **Wim**. Without your support in the lab/CT room, I would have not been able to complete this research. As such, the DEMO team was also ≪instrumental≫ (pun intended) to the execution of my PhD research: **Kees**, **Paul** and **Giorgos**, thank you for making even the most crazy of experimental setups a reality. And last but absolutely not least, I would like to acknowledge the contribution of **Maiko**, not only to this work, but to my life in general. You made life during my PhD fun and magical. Not only were your concrete wisdom and practical expertise fundamental to the sucess of many of my experiments, but working in the lab with you was a blast every single time. I am so thankful for you and Daniele, hosting me for your epic BBQs, christmas and garden hangouts: it made me feel part of your beautiful family.

Thank you also to **Jacqueline** for always being the kindest: I appreciate the dedication and empathy that you put into your work everyday.

When it comes to this all-encompassing journey, few people contributed more (emotionally and scientifically) to my PhD than my beloved **Concretenest**, the best office mates I could ask for. **Marija**, bestfriend extraordinaire: It is fair to say that your friendship was one of the best gifts this TU Delft journey brought me. Your kindness, your passion for science and your hard work made me a better person and a better scientist. Ultimately, this thesis would have not been finished without your cheers, which at times made me really believe that I got this. I would like to express my infinite gratitude to **Stefan**, who taught me the lab and research ropes when I was doing my MSc thesis and then kept being my sounding board for all things brainstorming well into my PhD. Your honest feedback and incredible curiosity helped improve my experimental and modelling strategies. PSOR drinks, city center dinners, home parties, late lab co-working: doing all of this together cemented our friendship forever. And **Yading**, your bat-like tendencies halved our overlapping time in the office, but your company more than made up for that. Thank you for your sharp bantering and for always being ready to roast everything and everyone, which made our Concretenest the most fun. You know you have a Smashots membership, for life. To **Bianca**, the honorary concretenest member who may have not been salaried by TU Delft, but was through and through always there for each of us. I will always be thankful for your love through these (often) hard times, ready to feed me the best Brazilian delicacies or to dance it off, whichever I needed most. Thank you **Patrick**, you were an honorary The Office (concretenest edition) cast member and as such, offered me your support and camaraderie. I could always count on you for a laugh or two, but also for the serious talks.

I am so thankful to have been part of the Microlab troup of students, PhD's, postdoc's and professors who made working there a true joy. The amount of wonderful, kindred-spirited, curious, passionate, driven, smart folk per capita was a thing of records. Thank you **Renee**, **Xu Ma**, **Boyu**, **Yidong**, **Yask**, **Albina**, **Boyu**, **Hongzhi** , **Zhenming**, **Jiayi**, **Shizhe**, **Amir**, **Annelinde**, **Emanuele**, **Yu Chen**, **Ameya**, **Xu Shi**, **Marija Krstic**, **Ze**, for the laughs, sometimes the cries, but specially for inspiring me to be better. I would like to thank you, **Oguzhan**, for your wisdom and stories of hope, but you know that the single thing I am most thankful for, is bringing back my (now) husband from his French exile. My appreciation goes also to my MSc students **Luca**, **Rui** and **Anmol**. Each of you taught me so much. Your contribution to this work was invaluable and know it was the honor of a lifetime to initiate you in the magic realm of scientific research.

Collaborating with other researchers from other departments and institutions was one of the most rewarding parts of this journey. Harnessing their expertise, learning their ways and of course, using their unique experimental setups enriched my research enormously. My thanks go to **Lili** and **Aikaterini** for their support with dynamic vapor sorption experiments. I would also like to thank **Veerle**, **Maxim** and **Stefanie** for welcoming me into their Geology department at Ghent University. We had very limited time to tackle a challenging experiment and you made it all happen. Thank you for sharing your CT knowledge and facilities with me, but also for making me feel part of your amazing research group. **Didier**'s monumental amount of research data was paramount to some chapters of this dissertation (Chapter 5 and 6) and the way he made all of that available to me is what open science dreams are made of. Thank you Didier, I appreciate you and your work.

I would like to thank my friend and fellow alumnus, **Giovanni** for his contribution to my PhD. Fate put us together again after ignoring eachother for years during undergrad studies. Sharing this PhD journey at the same time was a true gift. Thank you also **Paola**, for your camaraderie during conferences and your invaluable feedback to Chapter 3.

I feel so thankful for you, **Carien**. Certainly my Dutch has yet to improve, but becoming friends was by far the best outcome of our taalmaatje arrangement. Thanks for keeping this STEM gal in touch with the art scene around the Netherlands. **Alexia** and **Giuseppe**, thanks for our hours long aperitivi and for keeping me connected to Italy. I wholeheartedly want to thank **Jan**, **Bruno** and **Rob** from Weber, for being amazingly supportive and at a certain point, big motivators for me to finish this dissertation. You did not have to, but you did and that made a all the difference in the world.

I feel so full of gratitude for my poorkies, my chosen family, my bubble for life, who made the most difficult of times during the PhD, at last, happy. **Kubita**, I'm so thankful for you. Not only were you essential for after lab hangouts but your friendship quickly became irreplaceable in my life. Thanks for always being down for silly or deep talks, for boardgames and parties alike, for away trips and home trips. I am so glad that you allowed me to drag you to Eindhoven with me. **Gina**, words cannot begin to describe what your friendship means to me, but I can try. You arrived in a moment of my life, where the all-consuming intensity of a PhD can make or break you. It is safe to say, that you are one of the reasons I did not break. I promise to always be your "las fit" partner and honorary SoLow date. **Gaby**, we were thrown together by the loneliness of the pandemic and academic despair but the NBA, tacos and margaritas made us friends for life. I never not feel supported and accepted by you, so thank you for providing the safest haven to my perennial oversharing. **Juanito**, I am so appreciative of your friendship over these years, for always being able to count on you for companionship in good and bad times alike, but specially when I felt homesick and needed to remember who I was and where I came from. Our familia is one of the most precious things in my life and I can't wait to enact our joint retirement plan. And of course, thank you to my **Lore**, **Thomas** and **Menno** who cheered me up countless times and whose friendships I treasure greatly.

Thank you **Dennis**, for your unwavering friendship that spans almost a decade. Know that I do not take for granted the support and the affection that you bestow upon me. I feel so much appreciation for you, **Mapa**. Our timely scheduled dinner nights are a treasure that I am hoping to keep looking forward to for the rest of our lives.

I don't know what I would have done withou you **Nalie** and I would never want to find out. Neither do I know what I did to deserve your love and loyalty, but I sure am thankful that I met you and that you became my sister. Thank you for providing me with your own PhD learnings, for teaching me to advocate for myself, for English-proofing my papers, I owe you soooo much. And **Hannes**, I am thankful to have you in my life. Your friendship and selfless (diy) support all these years mean a great deal to me. But within the context of this thesis, let it be known that without you, there would not be a thesis to speak of, quite literally. Thank you for being your computer genius self and fishing out the data in that ol' dying corrupted hard disk.

I need to express my appreciation for my old friends, from the before times, who shaped this lump of clay and who keep being present through the big moments, good or bad: **Omi**, **Alo**, **Claudia**, **Monica**, **Ferni**, **Javie**, **Kiara** and **Jessy**.

Living away from family has never been easy, but during my PhD, this almost became unbearable. I am thankful that I had my in-laws, **Alique**, **Vera** and **Fernando**, who accepted me and welcomed into their Mendonça dynasty since moment one. I treasure every Christmas and holidays together. And an in-law in everything but blood, **Julio**, thank you for extending your brotherhood with Fernando to include me. Ultimately, thank you for being my CAD savior for this dissertation figures and cover.

My eternal gratitude goes to my abuelita **Alejandrina**, whose trickle down love is the single one cause for having the most supportive family I could wish for. You taught me love and kindness in a way that I am not ready to put into words yet, and to the core, that has made me into the person that I am and is why I do what I do. I feel, oh so lucky, to have had my aunt **Tamy**'s support my whole life. Thank you for teaching me that the "love what you do" trope could be real. I do not remember one single time in which you did not excel at whatever you put your mind into, be it engineering, accountancy, motherhood or notary's. And I suspect that a big part of it was the passion you devote to all you do and that I since try to live by. I am indebted for life to my aunt **Nory**, whom I've looked up to, since I can remember. Though being my role model does not even begin to scratch the surface of your influence in my life. You gifted me with the power of books, with a thirst for learning, for exploring the world. Later in life you took a bet on me and sponsored my education abroad. This thesis is your accomplishment as much as it is mine. I would also like to acknowledge my abuela **Alba**, thank you for all you have done for me. I remember fondly your support during those stressful days of applying to Polito, very much at the origin of this PhD journey. I would also like to thank my little sister, **Karla**, for our spontaneous phone calls and neverending texts that are a real testament to your support along these years. Thank you for hopping aboard a plane to see me when I needed it the most.

Words are not sufficient to express the recognition that my parents, **Erdis** and **Morayma**, deserve and that brought me to this very moment in life. Since I was little, you have made me believe that I could achieve anything that I wished for. Maybe because of placebo effect, circumstances or naivety, but your blind thrust gave me all the confidence I needed to at least try, and trying I keep doing. Thank you for making me into the hopeless optimist that I am.

And finally, the most heartfelt thank you goes to **Fernando**, my husband. You have been in this journey with me from the very beginning, our relationship growing in parallel to this dissertation. Your contribution to this thesis is incommensurable: from your expert advice and help with ESEM and image analysis, to single-handedly keeping me sane. Even in the most desperate of times, I had this nagging certainty that everything would turn out alright because we were together. I am so lucky to have you by my side and on my side every step of the way then, now and forever.

Claudia
Eindhoven, February 2025

Curriculum Vitæ

Claudia Romero Rodriguez

1991/05/04	Born in Havana, Cuba

Education and Work experience

2006-2009	Instituto Preuniversitario Vocacional de Ciencias Exactas Felix Varela Melena del Sur, Cuba
2011-2016	BSc & MSc student Politecnico di Torino, Italy
2016-2017	Junior researcher MgAubel, Delft, the Netherlands
2017-2025	PhD student Delft University of Technology, Delft, the Netherlands
2022-Present	R&D Project leader Saint-Gobain Weber Beamix, Eindhoven, the Netherlands

List of Publications

Journal Publications

1. **Rodríguez, C. R.**, Figueiredo, S. C., Deprez, M., Snoeck, D., Schlangen, E. & Šavija, B.: Numerical investigation of crack self-sealing in cement-based composites with superabsorbent polymers. Cement and Concrete Composites, 104, 103395 (2019).

2. **Rodríguez, C. R.**, de Mendonça Filho, F.F., Mercuri, L., Gan, Y., Rossi, E., Anglani, G., Antonaci, P., Schlangen, E. & Šavija, B.: Chemo-physico-mechanical properties of the interface zone between bacterial PLA self-healing capsules and cement paste. Cement and Concrete Research, 138, p.106228 (2020).

3. **Rodríguez, C. R.**, de Mendonça Filho, F.F., Figueiredo, S. C., Schlangen, E., & Šavija, B.: Fundamental investigation on the frost resistance of mortar with microencapsulated phase change materials. Cement and Concrete Composites, 113, p.103705 (2020).

4. Figueiredo, S. C., **Rodríguez, C. R.**, Ahmed, Z. Y., Bos, D. H., Xu, Y., Salet, T.M., Çopuroğlu, O., Schlangen, E., & Bos, F. P.: An approach to develop printable strain hardening cementitious composites. Materials & Design, 169, 107651 (2019).

5. Zhang, H., **Rodríguez, C. R.**, Dong, H., Gan, Y., Schlangen, E. & Šavija, B.: Elucidating the effect of accelerated carbonation on porosity and mechanical properties of hydrated portland cement paste using X-ray tomography and advanced micromechanical testing. Micromachines, 11(5), p.471 (2020).

6. Figueiredo, S. C., **Rodríguez, C. R.**, Ahmed, Z. Y., Bos, D. H., Xu, Y., Salet, T.M., Çopuroğlu, O., Schlangen, E., & Bos, F. P.: Mechanical behavior of printed strain hardening cementitious composites. Materials, 13(10), p.2253 (2020).

7. Ng, D.S., Paul, S.C., Anggraini, V., Kong, S.Y., Qureshi, T.S., **Rodríguez, C. R.**, Liu, Q.F. & Šavija, B.: Influence of SiO2, TiO2 and Fe2O3 nanoparticles on the properties of fly ash blended cement mortars. Construction and Building Materials, 258, p.119627 (2020).

8. Chen, Y., Jansen, K., Zhang, H., **Rodríguez, C. R.**, Gan, Y., Çopuroğlu, O. & Schlangen, E.: Effect of printing parameters on interlayer bond strength of 3D printed limestone-calcined clay-based cementitious materials: An experimental and numerical study. Construction and Building Materials, 262, p.120094 (2020).

9. Chen, Y., **Rodríguez, C. R.**, Li, Z., Chen, B., Çopuroğlu, O. & Schlangen, E.: Effect of different grade levels of calcined clays on fresh and hardened properties of ternary-blended cementitious materials for 3D printing. Cement and Concrete Composites, 114, p.103708 (2020).

10. Gan, Y., **Rodríguez, C. R.**, Zhang, H., Schlangen, E., van Breugel, K. & Šavija, B.: Modeling of microstructural effects on the creep of hardened cement paste using an experimentally informed lattice model. Computer - Aided Civil and Infrastructure Engineering, 36(5), pp.560-576 (2021).

11. Gan, Y., **Rodríguez, C. R.**, Schlangen, E., van Breugel, K. & Šavija, B.: Assessing strain rate sensitivity of cement paste at the micro-scale through micro-cantilever testing. Cement and Concrete Composites, 121, p.104084 (2021).

12. Chen, Y., Çopuroğlu, O., **Rodríguez, C. R.**, de Mendonça Filho, F.F. & Schlangen, E.: Characterization of air-void systems in 3D printed cementitious materials using optical image scanning and X-ray computed tomography. Materials Characterization, 173, p.110948 (2021).

13. Singla, A., Šavija, B., Sluys, L.J. & **Rodríguez, C. R.**: Modelling of capillary water absorption in sound and cracked concrete using a dual-lattice approach: Computational aspects. Construction and Building Materials, 320, p. 125826 (2021).

14. Rossi, E., **Rodríguez, C. R.**, Jonkers, H.M. & Çopuroğlu, O.: Assessment of the self-healing capacity of cementitious materials through active thin sections. Journal of Microscopy (2021).

15. de Mendonça Filho, F.F., **Rodríguez, C. R.**, Schlangen, E. & Çopuroğlu, O.: Surface effects of molten slag spills on calcium aluminate cement paste. Materials & Design, 217, p. 110623(2021).

16. de Mendonça Filho, F.F., **Rodríguez, C. R.**, Schlangen, E. & Çopuroğlu, O.:Plutonic Rocks as Protection Layers to Concrete Exposed to Ultra-High Temperature. Materials, 15 (10), p. 3490 (2022).

Book Editorship

1. Schlangen, E., De Schutter, G., Šavija, B., Zhang, H. & **Rodríguez, C. R.**: Proceedings of the Symposium on Concrete Modelling (CONMOD2018), RILEM Publications S.A.R.L., Vol. 127 (2018).

2. Ye, G., Yuan, **Rodríguez, C. R.**, Zhang, H. & Šavija, B.: Proceedings of the 4th International Conference on Service Life Design for Infrastructure (SLD4), RILEM Publications S.A.R.L., Vol. 125 (2018).

Conference Proceedings

1. **Rodríguez, C. R.**, Figueiredo, S.C., Chiaia, B. & Schlangen, E.: Induction healing of concrete reinforced by bitumen-coated steel fibres. In 9th International Conference on Fracture Mechanics of Concrete and Concrete Structures (FraMCoS-IX) (2016).

2. **Rodríguez, C. R.**, Figueiredo, S.C., Schlangen, E. & Snoeck, D.: Modeling water absorption in cement-based composites with SAP additions. In Computational Modelling of Concrete Structures (pp. 295-304). CRC Press (2018).

3. **Rodríguez, C. R.**, Figueiredo, S.C., Snoeck, D., Šavija, B. & Schlangen, E.: Modelling strategies for the study of crack self-sealing in mortar with superabsorbent polymers. In Symposium on Concrete Modelling (CONMOD2018) (pp. 333-341), RILEM Publications (2018).

4. **Rodríguez, C. R.**, Figueiredo S. C., de Mendonça Filho, F.F., Schlangen, E. & Šavija, B.: Frost Damage Progression Studied Through X-Ray tomography In Mortar With Phase Change Materials. In 10th International Conference on Fracture Mechanics of Concrete and Concrete Structures (FraMCoS-X) (2019).

🏆 5. **Rodríguez, C. R.**, Deprez, M., de Mendonca Filho, F.F., Van Offenwert, S., Cnudde, V., Schlangen, E. & Šavija, B.: X-ray micro tomography of water absorption by superabsorbent polymers in mortar. In International Conference on Application of Superabsorbent Polymers & Other New Admixtures Towards Smart Concrete (pp. 29-37). Springer, Cham (2019).

🏆 6. **Rodríguez, C. R.**, Ye, R., Varveri, A., Rossi, E., Anglani, G., Antonaci, P., Schlangen, E. & Šavija: Accelerated carbonation of ordinary portland cement paste and its effects on microstructure and transport properties. In International Rilem Conference on Microstructure Related Durability of Cementitious Composites, RILEM Publications (2020).

7. **Rodríguez, C. R.**, Gan, Y., Zhang, H., Schlangen, E. & Šavija, B.: Investigation of the micromechanical properties of the interface between PLA self-healing capsules and cementitious matrix. In International Conference Resilient Materials 4 Life (RM4L) (2020).

8. Mercuri, L., **Rodríguez, C. R.**, Xu, Y., Figueiredo S. C., Mors, R., Rossi, E., Anglani, G., Antonaci, P., Šavija, B. & Schlangen, E.: On the role of soft inclusions on the fracture behaviour of cement paste. In 10th International Conference on Fracture Mechanics of Concrete and Concrete Structures (FraMCoS-X) (2019).

🏆 Won a best paper award or proposal grant.